



저작자표시-비영리-변경금지 2.0 대한민국

이용자는 아래의 조건을 따르는 경우에 한하여 자유롭게

- 이 저작물을 복제, 배포, 전송, 전시, 공연 및 방송할 수 있습니다.

다음과 같은 조건을 따라야 합니다:



저작자표시. 귀하는 원저작자를 표시하여야 합니다.



비영리. 귀하는 이 저작물을 영리 목적으로 이용할 수 없습니다.



변경금지. 귀하는 이 저작물을 개작, 변형 또는 가공할 수 없습니다.

- 귀하는, 이 저작물의 재이용이나 배포의 경우, 이 저작물에 적용된 이용허락조건을 명확하게 나타내어야 합니다.
- 저작권자로부터 별도의 허가를 받으면 이러한 조건들은 적용되지 않습니다.

저작권법에 따른 이용자의 권리는 위의 내용에 의하여 영향을 받지 않습니다.

이것은 [이용허락규약\(Legal Code\)](#)을 이해하기 쉽게 요약한 것입니다.

[Disclaimer](#)

**A THESIS
FOR THE DEGREE OF DOCTOR OF PHILOSOPHY**

**Smart Sensors and Neuromorphic Resistive Memory Devices
for Intelligent Wearable Electronics**

Muhammad Umair Khan

**Department of Ocean System Engineering
GRADUATE SCHOOL
JEJU NATIONAL UNIVERSITY**

February 2022

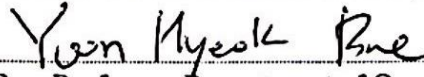
Smart Sensors and Neuromorphic Resistive Memory Devices for Intelligent Wearable Electronics

Muhammad Umair Khan
(Supervised by Professor Jinho Bae)

A thesis submitted in partial fulfillment of the requirement for the degree of PhD

2021. 12

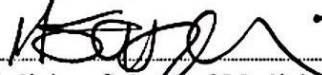
The thesis has been examined and approved by



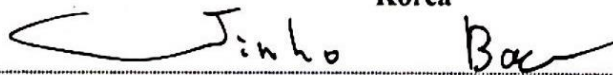
Thesis Director, Yoon Hyeok Bae, Professor, Department of Ocean System Engineering, Jeju National
University South Korea



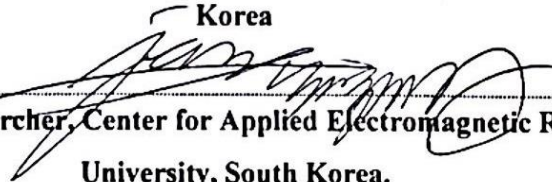
Chong Hyun Lee, Professor, Department of Ocean System Engineering, Jeju National University South
Korea



Min Joo Choi, Professor, Department of Medicine, School of Medicine, Jeju National University South
Korea



Jinho Bae, Professor, Department of Ocean System Engineering, Jeju National University South
Korea



Young Pyo Jeon, Senior Researcher, Center for Applied Electromagnetic Research, Seoul National
University, South Korea.

Dec-2021
Date

Department of Ocean System Engineering

GRADUATE SCHOOL
JEJU NATIONAL UNIVERSITY
REPUBLIC OF KOREA



*Dedicated to my beloved grandparents, parents, sisters, and
brother without whom I would not be where I am today*

*I missed my grandparents this entire long journey who always
did proud of me. I believe you have seen all my success and
journey from the Heaven, and you will still feel proud of me.*

*(Miss you Grandparents: Dost Muhammad &
Shahjahan Bibi)*



“Don’t be satisfied with stories, how things
have gone with others. Unfold your own
myth.”

Jalal ad-Din Muhammad Rumi

Acknowledgements

I would like to present my humble gratitude to Almighty ALLAH who bestowed me courage and skill to complete the doctoral studies with quite satisfaction and contentment. At this vital occasion when I am going to get the highest educational degree, I acknowledge my parents for their encouragement and every kind of support during my studies from the first day of my school until now. Especially the prayers of my mother and her believe in me have always been a source of courage during my entire life.

I am heartily thankful to my supervisor Prof. Jinho Bae whose guidance and every kind of support from the start to the end of my Ph.D. studies were there for me in the completion of this research work. Who polished my skills not only to grow as a quality researcher but also as an instructor, independent and innovative thinker. I would like to pay my heartiest thanks with best regards to Prof. Jinho Bae, who put his full efforts to give me confidence, access over all the resources in the laboratory and hire external resources as well to accomplish the task. During my Ph.D. studies, Prof. Bae provided me shelter against all kinds of crisis from morally depraved conditions to financial problems.

I am especially grateful to Dr. Shawkat Ali who introduced me to my supervisor Prof. Jinho Bae for postgraduate studies at OISE Lab, Jeju National University. I am extremely grateful to Dr. Gul Hassan my mentor during master's studies at Jeju National University. I am thankful to all my teachers who taught me from my elementary school to the highest educational degree.

I would like to thank my colleagues at OISE Lab in the Jeju University Jungmin Kim, Mahesh Yashavant Chougale, Qazi Muhammad Saqib, Rayyan Ali Shaukat. I would also like to thank my colleagues at NUCES-FAST Islamabad, Chungbuk National University and Hongkong University of Science and Technology for their encouragement to pursue my Ph.D. studies Mr. Tahseen Elahi Chattha, Dr. Muhammad Awais, Dr. Arshad Hassan, Sobia Ali Khan, Mehr Khalid Rahmani, and Chaudhry Muhammad Furqan.

I would love to present my tribute to my grandparents (Dost Muhammad and Shahjahan Bibi), father (Jahanzeb khan), Mother (Dilshad bibi), Sisters (Shaista Jahanzeb, Sidra Shahzad and Saadia Nabeel) and Brother (Muhammad Uzair Khan) for their support and care when I was busy in my studies and could not give them much time. All of my family has always been a source of appreciation and admiration

throughout my life either in my professional career or student life. I would like to disclose that Almighty ALLAH bestowed me such a noble and dominating figures in my life, without whom I could not have predicted myself to accomplish this task.

In the end, I would like to acknowledge and promise myself to be bind by the golden tips of life as positive thinking, hard work and consistency in execution of the idea.

Muhammad Umair Khan

Abbreviations and Notations

ZnO	Zinc Oxide
GaN	Gallium Nitride
DMF	N,N-dimethyl-formamide
FESEM	Field Emission Scanning Electron Microscope
Fe ₂ O ₃	Iron (III) Oxide
PAA: Na ⁺	Poly acrylic Acid Partial Sodium Salt Solution
NaOH	Sodium Hydroxide
LRS	Low Resistance State
GeO ₂	Germanium Dioxide
Ag@AgCl	Ag@AgCl core shell particles
HRS	High Resistance State
ITO	Indium Tin Oxide
I-V	Current-Voltage
STDP	Spiking Time Dependent Plasticity
SRDP	Spike Rate Dependent Plasticity
Memristor	Memory Resistor
MIM	Metal Insulator Metal
FTIR	Fourier-transform infrared spectroscopy
XRD	X-ray Powder Diffraction
PET	Polyethylene terephthalate
ReRAM	Resistive Random Access Memory
BMIM FeCl ₄	butylmethylimidazolium tetrachloroferrate
MoSe ₂	Molybdenum diselenide
SCLC	Space Charge Limited Current
STDP	Spike Timing Dependent Plasticity
TCLC	Trap Charge Limited Current
XPS	X-ray Photoelectron Spectroscopy
Raman	Raman Spectroscopy
IDEs	Inter Digital Electrodes
RH	Relative Humidity
R _{OFF}	High Resistance State
R _{ON}	Low Resistance State
V _{th}	Threshold Voltage
IESM	Inner Egg shell Membrane
T _{res}	Response Time
T _{rec}	Recovery Time
SUT	Sensor Under Test

List of Figures

Figure 1.1. Printed electronics applications.....	2
Figure 1.2. Schematic diagram of the DMP-3000 along main components.....	4
Figure 1.3. Schematic diagram of the screen printing showing main components.	5
Figure 1.4. (a) Spin coater schematic diagram. (b) Simple spin coating process	5
Figure 2.1. The diagram shows the six binary relations between the four fundamental circuit.	8
Figure 2.2. Amplitude dependent unipolar resistive switching.....	10
Figure 2.3. Polarity dependent bipolar resistive switching	10
Figure 2.4. Fabrication process of asymmetric resistive memory device using spin coating technology and showing fabricated image and cross-sectional image of fabricated device with 100 nm magnification.....	14
Figure 2.5. (a) Surface morphology of a top electrode based on Ag at 10 μm . (b) Element detection showing Ag peaks and (c) EDS mapping of Ag. (d) The 2D and 3D nano-profiles show the top electrode of 80 μm \times 80 μm with electrode roughness \sim 99.96 nm and (e) the height profile with the thickness of 180 nm, respectively. (f) The microscopic image of the top electrode	16
Figure 2.6. (a) Surface morphology of Fe_2O_3 is analyzed with TESCAN MIRA 3 at magnification level of 1 μm , (b) EDS spot profile confirms the presence of following peaks Fe and O, and (c) EDS mapping of Fe_2O_3 showing (d) O K series image, (e) Fe K series image at 10 μm , and (f) FTIR of Fe_2O_3 . (g) The 2D and (h) 3D nano-profile of Fe_2O_3 . (i) XRD of Fe_2O_3	17
Figure 2.7. (a) STEM of ZnO with magnification level of 1 μm , (b) EDS spot profile confirms the presence of Zn and O peaks, and (c) EDS mapping of ZnO showing d zinc mapped image and e oxygen mapped image at 1 μm . (f) Raman spectrum of Fe_2O_3 . (g) The 2D and (h) 3D nano-profile of ZnO. (i) XRD of ZnO.....	18
Figure 2.8. (a) Asymmetric I–V characterization of ITO/ZnO/ Fe_2O_3 /Ag and (b) its semi-log graph to show device passing from 0 V. (c) Roff/Ron graph	19
Figure 2.9. (a) Charge trapping mechanism. Schematic illustration of the proposed asymmetric resistive switching mechanism in ZnO/ Fe_2O_3 (n-type/p-type) heterojunction showing oxygen ion migration in (b) forward bias and (c) reverse bias.....	21
Figure 2.10. (a) Device stability for 300 cycles. (b) Device continuity test between HRS and LRS at read voltage of \sim 0.10204. (c) The reliability test of the proposed device with PDMS encapsulation for 30 days and (d) its retention stability between HRS and LRS.	22
Figure 2.11. Bending test of memory device on (a) flat condition. (b) Bending test on 20 mm diameter. (c) Bending test on minimum curvature of 1 mm diameter using mechanical bending machine. (d) Bending test from 40 to 1 mm diameter	22
Figure 2.12. (a) Fabrication of a cylindrical microchannel IL memory device and (b) the experimental setup.	25
Figure 2.13. (a) Effects of different 1: 0, 1: 0.5, and 1: 1.5 (PAA- Na^+ : H_2O):(NaOH) composites on the complementary resistive switching of the memory device and (b) $R_{\text{off}}/R_{\text{on}}$ ratio comparison of different blending ratios of (PAA : Na^+ : H_2O) and NaOH	26
Figure 2.14. (a) I–V characteristics of the proposed IL resistive switching device and (b) its $R_{\text{off}}/R_{\text{on}}$ resistance ratios for various read voltages	26
Figure 2.15. Ionic mechanism of the proposed memory device	27
Figure 2.16. (a) Endurance of the proposed device with respect to HRS and LRS and (b) its I–V plots. (c) IL retention time at a voltage read of 0.15 V and (d) the corresponding I–V plots.	27
Figure 2.17. Schematic presenting the complementary resistive switching mechanism, and the corresponding semi-log I–V curve.	29
Figure 2.18. Photographs of the proposed IL resistive memory device in (a) unbent and (b) bent states. (c) Their I–V curves.	30

Figure 3.1. The memory computing architecture can be related to human-brain-spiking system with future technology based on neural networking to process robotic technology. (b) Vertical structure of single memristor cell. (c) The Layered atomic structure of ZnO and GaN. (d) Cross-sectional SEM image **33**

Figure 3.2. The Raman spectrum of (a) ZnO and (b) GaN. XPS core level spectra peaks fitting of (c) Zn 2p_{3/2}, (d) O 1s, (e) Ga-3d and (f) N 1s **36**

Figure 3.3. (a) I-V curve ITO/ZnO/Ag Schottky diode. (b) Pulsed modulated DC sputtered XRD of GaN. (c) I-V curve of ITO/ZnO/GaN/Ag, (d) semi-log I-V curve showing asymmetric behavior. (e) The device endurance between HRS and LRS and (f) 500 I-V sweep cycles. (g) The bandgap diagram showing energy levels..... **37**

Figure 3.4. (a) Resistive synapse in GaN/ZnO heterojunction illustrating the synaptic response similar to biological synapses. (b) DC Sputtered XRD of GaN. (c) The triangular voltages response to investigate the device tunability. The I-V of (d) positive and (e) negative voltage sweep showing multistate resistive switching behavior. (f) The synaptic plasticity against pulse train of 45 long-term potentiation pulses of 4 V and long-term depression pulses of -1.5 V with a pulse of 1 ms..... **38**

Figure 3.5. (a) The synaptic behavior of the device for different pulse intervals, and (b) the ΔI plotted with the different pulse intervals to calculate PPF and PTP. (c) PPF index (%) as a function of interval time. (d) The stimuli response different pulse voltage and (e) the ΔI calculated from different pulse heights, to calculate PPF and PTP. (f) PPF index (%) as a function of voltage. (g) The brain learning and forgetting mode are based on STM and LTM. (h) The STP under consecutive 10 pulses and the LTP under consecutive 45 pulses to observe the change in conductance to observe the forgetting behavior. (i) The experimental STDP results showing antisymmetric Hebbian..... **40**

Figure 3.6. Switching mechanism model for a neuromorphic-based device (ITO/ZnO/GaN/Ag) **42**

Figure 3.7. (a) Device endurance and stability performance. (b) The synaptic plasticity of LTP and LTD. (c) Analog device behavior of nonlinear weight update data, which represents the normalized conductance against a normalized number of pulses. (d) The neural network with a 2-fully-connected layer for neurosim simulation. (e) Simulation accuracy based on real and ideal devices **43**

Figure 3.8. (a) Schematic of flexible artificial synaptic memristor with ITO/GeO₂/Ag structure. (b) Schematic diagram of biological neurons and synapses. The synapse is the connection between a pre-synaptic neuron and a post-synaptic neuron. (c) The photograph proposed a synaptic memory device on the flexible substrate. (d) Cross-sectional scanning electron microscopy (SEM) image of the proposed Ag/GeO₂/ITO device. XPS of Germanium dioxide showing (e) Ge-3d series in binding energy 30-36 and (f) O-1s series in binding energy 528-536 **45**

Figure 3.9. (a) The FTIR, (b) Raman, and (c) XRD analysis of GeO₂. The SEM of the GeO₂ in different magnification, (d) 10 μ m, (e) 1 μ m, and (f) 200 nm. (g) The EDS mapping of GeO₂. (h) The surface morphology of GeO₂ at 100 μ m. EDS mapping showing (i) O K series and (j) Ge L Series..... **48**

Figure 3.10. (a) I-V characteristics on different current compliance. (b) Multistate behavior on the different applied voltage. (c) The I-V curves on different frequencies. (d) The hysteresis area and memory window of the device on different frequencies. (e) The endurance performance of different frequencies. (f) Logarithmic I-V characteristics of GeO₂ memory device positive region. (g) Filamentary conduction mechanism of the GeO₂ memory device. (g) The photograph of bending test. (i) The performance of memory device during bending showing semi log I-V characteristics for 100 repetitive cycles and (j) endurance results **50**

Figure 3.11. (a) The potentiation of the by applying the different pulse amplitude. (b) The ΔI calculate the increasing current (ΔI) for different pulse amplitude, $I_n - I_1$ where $n = 1, 2, 3, \dots, 30$. (c) PPF index % of the device on different voltages. The experimental STDP results show (d) antisymmetric Hebbian and (e) antisymmetric anti-Hebbian learning rules. (f) LTP and LTD of the proposed device. (g) Simulation process of the device by using CNN network. (h) Real and ideal CNN accuracy of the proposed synaptic device... **53**

Figure 3.12. (a) Illustrating the synaptic response between the presynaptic neuron and the postsynaptic neuron and ionic memristor interface with future technology. (b) Fabricated PDMS mold with channel length of 15 mm, (c) and channel width of 1.5 mm. (d) Optical image of realized device, (e) zoom image of electrode spacing ~ 0.5 mm. (f) Synthesis of ionic liquid BMIM FeCl₄. (g) Raman and (h) FTIR of BMIM FeCl₄. The XPS of (i) carbon, (j) nitrogen, (k) chlorine, and (l) iron regions of BMIM FeCl₄ **56**

Figure 3.13. (a) Basic mechanism schematic for the electrical manipulation of ion and liquid transport in

discrete channel. The I-V of (b) positive and (c) negative voltage sweep. The five cycles of triangular voltages with time on (d) positive and (e) negative voltage region. (f) Plasticity characteristics of the artificial synapse with different pulse widths of, 400 μ s, 600 μ s, 800 μ s, and 1 ms. (g) The different pulse amplitude response at 1.5 V, 1.2 V, 0.9 V, 0.7 V and 0.3 V. (h) Frequency response at 1.1 Hz, 2.4 Hz, 4.6 Hz, and 7.8 Hz. (i) The STM retention of the neuromorphic device **59**

Figure 3.14. The synaptic plasticity of (a) unbending, (b) bending, and (c) stretching device under continuous pulse train with a pulse with of 1 ms. (d) Diagram of neural networks for recognition of cifar-10 data. (e) Simulated accuracy ideal and real device. (f) Device endurance performance. (g) Schematic waveform for STDP. (h) The synaptic weights (%) change with respect to time difference (Δt) **61**

Figure 3.15. Ink preparation method of Ag@AgCl core-shell IL electrolyte and fabrication of soft and flexible memory cells for neuromorphic computing **64**

Figure 3.16. (a) SEM image, (b) EDS spot profile, and (c) FTIR analysis of the core shell. XRD pattern of (d) Ag and (e) Ag@AgCl **66**

Figure 3.17. (a) Ion conduction mechanism. (b) Semilog I-V curve of Cu/FeCl₃/Cu. (c) Device dose-response with time, (d) charge-flux property of the device, and (e) device flux response with time. (f) 100 I-V sweep cycles and (g) device cycle-to-cycle endurance at a voltage read of 0.15 **68**

Figure 3.18. (a) Multistate I-V curve of Cu/Ag@AgCl/Cu in a negative voltage region and (b) positive voltage region. The (c) current and (d) conductance response of the device for a pulse width of 1 ms with a reading pulse amplitude of -1.5 V on negative and 1.5 V on positive voltage region. The triangular pulse response in (e) negative and (f) positive voltage regions **71**

Figure 3.19. (a) Plasticity characteristics of the artificial synapse with different pulse widths of 200 μ s, 400 μ s, 600 μ s, 800 μ s, and 1 ms. (b) Frequency response at 1.1, 2.4, 4.5, and 7.8 Hz. (c) The different pulse amplitude responses at 1.5, 1.0, 0.7, and 0.5 V. (d) The forgetting curve of the neuromorphic device. (e) Bending test of the device under a continuous pulse train **73**

Figure 3.20. (a) The convolutional neural network. (b) Synaptic plasticity under a continuous pulse train. (c) Simulated accuracy of each epoch during training **74**

Figure 3.21. The working mechanism of the core-shell soft ionic liquid neuromorphic device **75**

Figure 4.1. (a) The Processing of the IESM. (b) The wave shape of printing nozzles of the Fujifilm DMP-3000 inkjet printer. (c) Dimension of the IDEs and Printed IDEs on the surface of the IESM using inkjet printer. **77**

Figure 4.2. (a) Structural image of hen egg. (b) FESEM image of IESM. (c) Microscopic image of printed IDEs showing electrode width of 100 μ m and electrode spacing of 100 μ m. 2D surface roughness of 197.33 nm and (d) 3D surface nano profile with thickness of 1.77 μ m. (e) Histogram of height for nano profile of IDEs. (f) SEM image of the IDEs **80**

Figure 4.3. (a) Cross sectional image of IESM. (b) FTIR of the IESM. (c) Surface morphology of the IESM using TESCAN MIRA 3. (d) The EDS representation of the IESM and insert image showing element composition of the IESM **81**

Figure 4.4. (a) EDS mapping SEM image of IES. (b) EDS layer image, and element mapping of the IESM representing as (c) C K series, (d) O K series, (e) S K series, and (f) Na K series **81**

Figure 4.5. Realized image of the humidity setup using Arduino UNO, DHT21D humidity sensor, sensor under test (SUT), KEYSIGHT LCR meter, humidifier, dry nitrogen (N₂), LCD, and PC **83**

Figure 4.6. Impedance response of the sensor 1 at (a) 1 kHz and (b) 10 kHz. Impedance response of the sensor 2 at (c) 1 kHz and (d) 10 kHz **83**

Figure 4.7. Images of the fabricated sensor on IESM transferred to various shaped as a substrate: (a) plant stem as a substrate with 5.53 mm diameter, (b) computer mouse with diameter 10 mm, and (c) round shape conical flask with diameter 13.1 mm. (d) Impedance response of IESM on transferred to arbitrary surface. (e) FESEM of IDEs after transferred to arbitrary surface. (f) EDS spot profile shows the presence of Ag in FESEM **84**

Figure 4.8. Capacitance response of the sensor 1 at (a) 1 kHz and (b) 10 kHz. Capacitance response of the sensor 2 at (c) 1 kHz and (d) 10 kHz **85**

Figure 4.9. Transient response of (a) sensor 1 and (b) sensor 2. Stability on 0% RH, 40% RH (open air), and 90% RH of (c) sensor 1 and (d) sensor 2	86
Figure 4.10. (a) Sensing mechanism of the IESM showing adsorption of water molecules and resulting ionic current flow through the thin film. (b) Cross sectional image of the IESM at 50 μm magnification, and (c) 2D and (d) 3D nano profile of IESM. (e) Histogram of IESM	87
Figure 4.11. Impedance response hysteresis curve of (a) sensor 1 and (b) sensor 2 showing adsorption and desorption from RH 0–90% at 1 kHz. Capacitance response hysteresis curve of (c) sensor 1 and (d) sensor 2 showing adsorption and desorption cycle with humidity range from 0 to 90% at 1 kHz.....	88
Figure 4.12. Schematic illustration of fabrication process of humidity sensor	92
Figure 4.13. (a) STEM GaN layer, (b) nitrogen K series, (c) Ga L series, (d) STEM IDEs (e) silver L series, (f) carbon K series, nano-profile (g) GaN, and (h) IDEs.....	93
Figure 4.14. GaN sensing layer (a) Overall general scan spectrum, (b) Ga 3d band, (c) N 1s Band, and (d) O1s band, (e) XRD, and (f) Raman spectrum	94
Figure 4.15. (a) Humidity test setup, (b) measured and simulated impedance and capacitance response at 1 kHz. (c) Impedance response and recovery. (d) Capacitance response and recovery. (e) Impedance stability, and (f) capacitance stability	96
Figure 4.16. (a) chemical adsorption of water molecules on GaN sensing layer. (b) capacitance response w.r.t temperature variations. Hysteresis (c) impedance at 1 kHz, (d) capacitance at 1 kHz	97
Figure 4.17. (a) Picture of sensor attached at lower side of plant leaf and cross-sectional view of leaf with sensing mechanism and (b) real time monitoring of capacitive response towards plant transpiration after water from 1 to 5 days. Meat freshness test: (c) Amino acids structure and decomposition mechanism and (d) current response w.r.t. time and freshness states.	99
Figure 4.18. (a) The schematic of Red-tongue viper snake species gloydius ussuriensis. (b) Unfolded and (c) folded snakeskin shed membrane showing its flexibility. The schematic device structure of (d) triboelectric and (e) piezoelectric nanogenerator. The SEM image of snakeskin shed membrane at magnification level of (f) 100 μm , (g) 50 μm and (h) 20 μm . (i) The cross-sectional image of piezoelectric nanogenerator showing deposition of Ag electrodes on both sides of snakeskin shed membrane using RF sputter and, we can see the thickness of membrane \sim 10 μm	102
Figure 4.19. (a) The surface morphology of the snakeskin shed membrane analyzed by the SEM with a magnification of 25 μm . (b) EDS analysis of the snakeskin shed film. The insert figure presented its elemental composition. The EDS layered image of the snakeskin shed showing the (c) C K series, (d) O K series, (e) S K series, (f) Na K Series, (g) Si K Series, (h) Cl K series, and (i) K K series, respectively. The structural analysis for the snakeskin shed film. c) 2D and d) 3D nano-profile presenting the highly porous structure. e) FTIR analysis of the snakeskin shed, showing the existence of different functional groups.	104
Figure 4.20. The output (a) of open circuit voltage and (b) short circuit current comparison using different electronegative layer (cellulose, Lignin, PRT, PDMS, PTFE) and snakeskin shed membrane used as electropositive layer. The output of (c) open circuit voltage and (d) short circuit current comparison using PTFE as electropositive layer and with and without snakeskin shed membrane as electronegative layer. (e) Output power of snakeskin shed membrane with PTFE at different external load resistances, (f) The charging of 10 μF , 4.7 μF , and 1 μF capacitors using snakeskin shed piezoelectric nanogenerator, (g) The charging and discharging curve of 10 μF capacitor employing snakeskin shed piezoelectric nanogenerator. (h) The current stability for more than 7300 sec.....	106
Figure 4.21. The different size of piezoelectric nanogenerators to examine the (a) open circuit voltage and (b) short circuit current. The rectification effect is examined of the snakeskin shed membrane piezoelectric nanogenerator to monitor the (d) open circuit voltage and (d) short circuit current. (e) Dependence of output current and power of piezoelectric nanogenerator of snakeskin shed membrane at different external load resistances, (f) The charging of 10 μF , 4.7 μF , and 0.1 μF capacitors using snakeskin shed piezoelectric nanogenerator, (g) The charging and discharging curve of 10 μF capacitor employing snakeskin shed piezoelectric nanogenerator. (h) The current stability for more than 5000 sec.....	107
Figure 4.22. The(a) triboelectric and (b) piezoelectric nanogenerator mechanism shed piezoelectric nanogenerator	108
Figure 4.23. (a) The schematic circuit of TENG connections with a stopwatch and the realized image of	

internal connections and powering up low power stopwatch. (b) The schematic circuit of TENG connections with LEDs and Lighting of LEDs using GUA-based TENG. The bio-mechanical force excitation for piezoelectric nanogenerator. (c) Finger tapping, (d) Hand tapping and (e) Palm tapping.109

Figure 4.24. Materials preparation and step by step fabrication process. (a) Preparation of the graphene and magnetic iron oxide nano-composite and polyurethane substrate. (b) Inkjet materials printer DMP-3000 and its schematic diagram. (c) The proposed strain sensor113

Figure 4.25. SEM Analysis of the active layer. (a) SEM image of graphene film, (b) SEM image of magnetic iron oxide film, and (c) SEM image of self-healing nano-composite film of graphene and magnetic iron oxide. (d) 3D morphology of the active layer on engineered polyurethane substrate. (e) The fabricated strain sensor based on graphene and magnetic iron oxide nanocomposite.....114

Figure 4.26. Strain detection mechanism of the proposed self-healing strain sensor. (a) Schematic illustration of the strain sensing with 0%. (b) Schematic illustration of the strain sensing with 5%, with increasing the stretching strain, the overlapping area between graphene flakes decrease those results in the increase in resistance. (c) Schematic illustration of the strain sensing with 15%, along the decreasing overlapping area between graphene flakes, small micro cracks also appear that results in the increase in the resistance of the strain sensor. (d) SEM image of the active composite film with 0% stretching. (e) SEM image with 5% stretching. (f) SEM image with 15% stretching. (g) SEM image with 20% stretching. (h) SEM image with 35% stretching. (i) SEM image with 40% stretching. (j) SEM image with 50% stretching. (k) SEM image with 54.5% stretching. (l) EDS elemental mapping after 54.5% stretching.116

Figure 4.27. Characterization of a strain sensor based on just graphene active layer. (a) Sensors attached on a glove to record the fingers motion. (b) I–V curves by different bending diameter as shown in the inset image. (c) Bending and relaxing cycles of the sensor. (d) The response and recovery time of the sensor. (e) Sensitivity and maximum stretching % along graphene and iron oxide composite blending ration118

Figure 4.28. Characterization of the self-healing strain sensor with graphene and magnetic iron oxide composite film. (a) Current and resistance changes along different bending diameters as the inset image. (b) Current and resistance changes along different stretching % as the inset image. (c) 10,000 bending/relaxing cycles. (d) Normalized current variation along the stretching cycle of the proposed strain sensor. (e) Hysteresis curve of bending and relaxing.120

Figure 4.29. Electrical characterization of the self-healing strain sensor before and after the cutting. (a) I–V curves of the proposed self-healing strain sensor at different bending diameter. (b) Bending and relaxing cycles before cutting the proposed sensor. (c) Bending and relaxing after first cutting and the sensor recovers its 94% efficiency. (d) Bending and relaxing after 2nd time cutting and still the proposed sensor is recovered after healing.....121

Figure 4.30. Cutting and healing of the proposed strain sensor. (a) Images of the cutting sensors. (b) Images of the sensors after self-healing and we can see that the sensors are fully healed (it can see in supplementary movie). (c) SEM image of the sensor after self-healing. (d) Cross section SEM images of the sensor after cutting it. Here, we can see both the graphene flakes as well magnetic iron oxide. (e) SEM image analysis of self-healing of the strain sensor. Here, the thread like structure and magnetic property of the magnetic iron oxide is the main reason of self-healing as shown in the SEM image.....122

Figure 4.31. Comparison of the SEM of the films without and with Fe₂O₃. (a) SEM of the film without Fe₂O₃, where, in this SEM image, we can see the graphene flakes, clearly. (b) SEM image after cutting the film. Here, we can see the layered structure based on graphene flakes without Fe₂O₃. (c) SEM image of the composite film can clearly see graphene and Fe₂O₃. Here, in this image, the green arrows present the graphene flakes covered with Fe₂O₃. (d) SEM image of the composite film can also clearly see graphene and Fe₂O₃. Here, we can see the graphene flakes and the red arrows shows the Fe₂O₃.123

List of Contents

Abstract.....	xvi
Chapter 1 Introduction	1
1.1 Printed of Electronics.....	1
1.2 Technologies Utilized for Device Fabrications.....	3
1.2.1. Inkjet Printing	4
1.2.2. Screen Printing.....	4
1.2.3. Spin Coating.....	5
1.3 Objective of the Thesis.....	6
1.3.1. Outline of Thesis.....	6
Chapter 2 Memristors.....	8
2.1 Memristor.....	8
2.2 Types of Memristors	9
2.2.1 Unipolar Memristors	9
2.2.2 Bipolar Memristors	10
2.3 Memristors Mechanisms	11
2.3.1 Bulk Effect.....	11
2.3.2 Interface Effect.....	11
2.3.3 Redox Process Induced Cation Migration.....	11
2.3.4 Redox Process induced Anion Migration	12
2.3.5 Formation and Disruption of Metal Oxide.....	12
2.4 Asymmetric Resistive Switching Memory based on ZnO/Fe ₂ O ₃ Heterojunction.....	12
2.4.1 Materials and Methods.....	14
2.4.2 Characterization	15
2.4.3 Result and Discussion	19
2.4.4 Summary	23
2.5 Soft Ionic Liquid Based Resistive Memory in a Cylindrical Channel.....	23
2.5.1 Materials and Methods.....	24
2.5.2 Result and Discussion	25
2.5.3 Summary	30
Chapter 3 Neuromorphic Resistive Memories	31
3.1 Introduction.....	31
3.2 One Directional Engineered GaN Resistive Memory Device for Electronic Synapses.....	31
3.2.1 Materials and Methods.....	33
3.2.2 Characterization	34
3.2.3 Result and Discussion	36

3.2.4	Summary	44
3.3	Multistate Resistive Memory Device based on GeO ₂ for Electronic Synapses	44
3.3.1	Materials and Methods	46
3.3.2	Characterization	46
3.3.3	Result and Discussion	48
3.3.4	Summary	54
3.4	Ionic Liquid Multistate Resistive Switching Device for Neuromorphic Computing.....	54
3.4.1	Materials and Methods	55
3.4.2	Characterization	56
3.4.3	Result and Discussion	58
3.4.4	Summary	62
3.5	Soft and Flexible: Core-shell Ionic Liquid Resistive Memory for Electronic Synapses	63
3.5.1	Materials and Methods	65
3.5.2	Characterization	65
3.5.3	Result and Discussion	67
3.5.4	Summary	75
Chapter 4	Sensors	76
4.1	Biocompatible Organic Humidity Sensor Based on Natural Inner Eggshell Membrane.....	76
4.1.1	Materials and Methods	78
4.1.2	Characterization	79
4.1.3	Result and Discussion	82
4.1.4	Summary	89
4.2	Printable Highly Stable and Superfast Humidity Sensor Based on 2D MoSe ₂	89
4.2.1	Materials and Methods	91
4.2.2	Characterization	92
4.2.3	Result and Discussion	95
4.2.4	Summary.....	100
4.3	Self-Powered Tribo and Piezo Electric Nanogenerator using Snakeskin shed Membrane..	100
4.3.1	Materials and Methods	103
4.3.2	Characterization	104
4.3.3	Result and Discussion	105
4.3.4	Summary	110
4.4	Inkjet Printed Self Healable Strain Sensor Based on Graphene and Magnetic Iron Oxide.	111
4.4.1	Materials and Methods	112
4.4.2	Characterization	115
4.4.3	Result and Discussion	115
4.4.4	Summary	124

Chapter 5 Conclusions and Future Work.....	125
5.1 Overview and General Conclusions	125
5.2 Future Work	127
Annex-A Journal Papers	128
Annex-B to be Submitted Papers	130
Annex-C Conference Papers.....	131
Annex-D References	132

Abstract

Recently there has been a growing interest in the realization of smart sensors and neuromorphic resistive memory devices by process from the field of printed electronics with low cost, and high-throughput printing techniques. These devices can easily be integrated and interfaced with Human machine interface (HMI) and have the potential to revolutionize the spread of electronic applications. Printed Electronics has emerged as one of the most promising alternative manufacturing technologies because of its ambient manufacturing processing. This thesis focuses on the fabrication of Printed, flexible, and stretchable electronic devices by utilization of printed techniques. Materials are synthesized to make it printable through printed techniques for the realization of electronic devices and circuits. The printed techniques used in device manufacturing are Spray Coating, Inkjet material printing, Screen Printing, and spin coating. In this work, I have used different substrates according to the manufacturing process requirement in glass substrate and flexible and stretchable substrate. The main substrates utilized in fabrication of devices are glass, PDMS, PET and biomaterials. The fabricated devices were characterized against their electrical, mechanical, optical, and chemical behavior to verify the device fabrication approach and performance.

Resistive random-access memory (RRAM) devices are receiving increasing extensive attention due to their enhanced properties such as fast operation speed, simple device structure, low power consumption, and are currently considered to be one of the next-generation alternatives to traditional memory. I have fabricated different memristors based on device structure ITO/ZnO/Fe₂O₃/Ag to solve sneak current problem in a crossbar array and soft and flexible resistive memory device Cu/(PAA-Na⁺:H₂O): (NaOH)/Cu to improve retention time, on/off ratio and endurance cycles.

Neuromorphic computing has emerged as a promising avenue towards building the next generation of intelligent computing systems. It has been proposed that memristive devices, which exhibit history-dependent conductivity modulation, could efficiently represent the synaptic weights in artificial neural networks. I have fabricated solid state and liquid based neuromorphic computing resistive memory devices. The solid-state structure is based on structure ITO/ZnO/GaN/Ag and ITO/GeO₂/Ag are fabricated using spin coating and RF sputtering technology. These works show the memory importance to block sneak current in a crossbar array. On the same time the Neuromorphic behavior has been explored to show its importance to implement hardware based artificial intelligence system. On the other hand, soft and liquid based neuromorphic resistive memory devices are emerging field, which helps to open a gateway for soft circuits. To introduce simple device structure to perform neuromorphic computing we fabricated discrete channel device, which helps to improve our understanding towards soft neuromorphic computing devices using

structure Cu/BMIM FeCl₄: H₂O/Cu. The large-scale integration of soft memory devices can be enabled by introducing soft and flexible device structure in a crossbar array structure Cu/Ag@AgCl/Cu. These results open a gateway for the implementation of soft and flexible brain like miking systems.

Several types of printed devices are fabricated and discussed in this thesis includes: Humidity Sensor, Piezo and Triboelectric Nanogenerator, and its stretchability achieved up to 54.5%. To measure humidity in a wide range with high sensitivity, an inkjet printing, Screen-printing and spin coating technique are utilized to fabricate humidity sensor, which helps to monitor real time humidity applications using inner eggshell membrane, and GaN. The snake shad is used to fabricate the Piezoelectric and Triboelectric nanogenerator for energy harvesting to power electronic devices. Inkjet printed self-healable strain sensor based on Graphene and Magnetic Iron Oxide on polyurethane substrate. The prototype of printed electronic devices and circuits fabricated by utilizing solution-processed materials are good achievements and a way to future printed flexible and stretchable electronics

Chapter 1 Introduction

1.1 Printed Electronics

Printed electronics is a new branch of electronics where functional materials are directly deposited through printing techniques on substrates to make operational electronic devices and systems. Printed electronics is rapidly grooming because of its ample advantages over conventional rigid electronics such as Silicon or Gallium Arsenide, which are fabricated in clean-room environments at wafer-size level[1]. This type of electronics starts to find severe limitations to satisfy the demands imposed by new applications, especially those requiring large area, mechanical flexibility, or compatibility with biological systems. On the other hand, printed electronics full-fill the missing gaps of conventional electronics with more dynamic style including easy fabrication, environmentally friendly, low cost, low temperature, and ambient conditions processing. Within the printed electronics, organic electronics, polymer electronics or plastic electronics consist of using organic materials as the substrate or active material in electronic circuits and systems[1, 2]. Some of the organic electronic devices have reached a level to find a place in the consumer electronics market for large- area applications such as, organic thin film transistors (OTFTs) or especially organic LEDs (OLEDs), already used on modern displays and TVs[2]. As a natural expansion of the field, the development of low-cost ubiquitous flexible sensors, biomedical stretchable and implantable devices or intelligent surfaces are currently gaining a lot of interest. These devices require all the use of polymers as supportive substrate[1, 3]. Using polymers substrates as substrates for electronic systems is then opening new opportunities in the field of micro engineering. Polymers have the potential of making electronics very low-cost, environmentally friendly, disposable, biocompatible or biodegradable[2, 4]. Moreover, they can bring benefit to electronic systems especially in those applications where optical opacity, weight or mechanical rigidity is limiting factors[1]. Some polymers are also able to stretch or deform into arbitrary shapes without losing their properties[2]. The fact that they are inexpensive and compatible with large-scale production though roll-to-roll or sheet-to- sheet process make them the perfect complement to be used with printing technologies, rather than with standard clean-room techniques such as photolithography, lift-off or etching; to the point that the term printing electronics often implies the use of a plastic or paper substrate. Some of the applications of printed electronics are shown in Fig. 1.1.

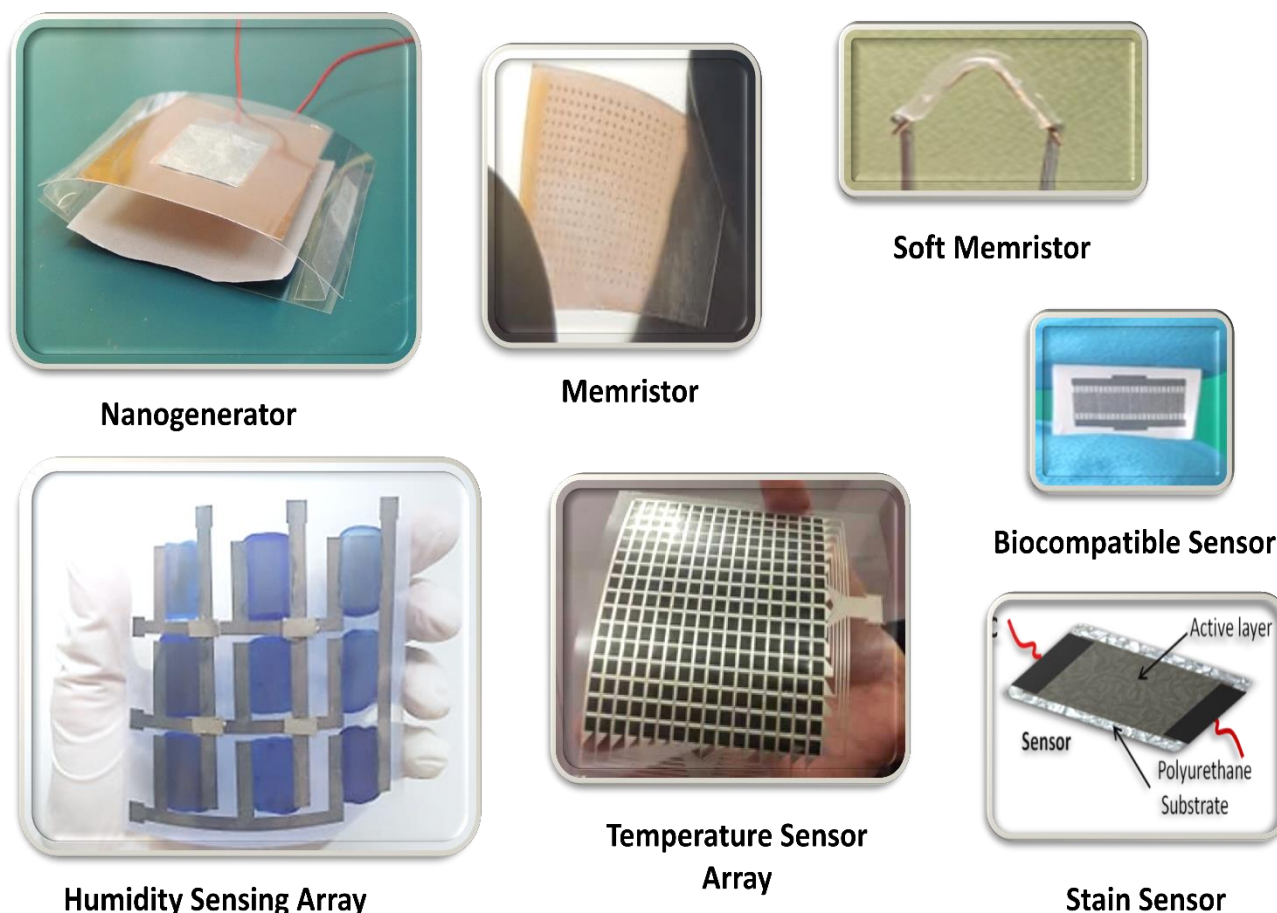


Figure 1.1. Printed electronics applications.

Flexible circuits have been one of the fastest growing market segments for interconnection products in the last several years, which is due to the wide range of applications enabled by flexibility. Like conventional rigid circuit boards, flexible circuits can be single-sided, double-sided, or multilayered. Applications of flexible circuits can be roughly divided into two categories: (1) dynamic and (2) flex-to-fit. In dynamic applications, flexibility enables movement and changing form factors, whereas in flex-to-fit applications flexibility is needed only in the assembly phase to fit circuit board in such form factor, which is not possible with rigid planar boards[1].

Printed electronics allow the manufacturing of stretchable electronics as the processing temperature is low where polymeric substrate can work. Making the stretchable electronic devices there are two choices available, first method is to use intrinsically stretchable materials, like conductive polymers or organic semiconductors, which have relatively poor electrical performance compared to conventional inorganic electronic materials[5, 6].

The second method is to use conventional electronic materials and make the system stretchable[6]. This way good electrical performance is achieved, but the stretching is more challenging, since conventional semiconductors like silicon are hard and brittle[7]. If rigid areas with silicon-based semiconductors are kept small and the interconnections between them are made stretchable, resulting system appears stretchable macroscopically. Stretchable interconnects are usually made by exploiting out-of-plane deformation or planar patterning which help to reduce stresses caused by stretching. The actual length of conductors is increased while dimensions along one or two axes are preserved. Consequently, this converts stretching to bending for strains between the actual length of conductor and the relaxed state of conductor. Other methods for producing stretchable interconnects rely on thin films and forming of microscopic cracks, which serve as strain relief and form a conductive network.

1.2 Technologies Utilized for Device Fabrications

Recent years have seen a great demand in the field of printed electronics because their light weight, environment-friendly, low-cost manufacturing, ease of fabrication, and the availability of inexpensive substrates such as papers, textiles, and plastics which make flexible electronics an attractive candidate for the next generation of consumer electronics[8].

For the fabrication of printed electronic devices, a variety of fabrication techniques is available in which some are matured and commercialized whereas some techniques are still under research. Main task of the printed electronics techniques is to deposit the functional materials on a substrate with precision and high accuracy where the thickness and uniformity of the film is main concern. In the history of thin films deposition, various techniques have been adopted including. The different printing techniques including chemical bath, spin-coating, dip coating, doctor blade, metering rod, slot casting, spray coating, screen printing, inkjet printing and aerosol jet. Other than these techniques, electrostatic spray deposition (ESD) and electro hydrodynamic (EHD) use for the deposition of thin films, where material is deposited through electrostatic field.

All fabrication techniques have their advantages and disadvantages. Some of them need vacuum chambers, heat, and a special environment to process the fabrication of a device. Some materials require special environment such as specific temperature, pressure, humidity, light and vacuum, therefore the fabrication techniques are adopted accordingly. In this thesis work, for the fabrication of devices and circuits ink jet, spray coating, spin coating and screen printing are used. These techniques are discussed in detail in the forthcoming sections

1.2.1. Inkjet Printing

Inkjet printing is a liquid deposition technique where the droplets of the ink are ejected with the same volume and printed on the substrate. It is a low cost, material conserving, non-contact, additive patterning, and mask less approach with the scalability to large area manufacturing[9, 10]. Digital photograph of the DMP-3000 schematic diagram is shown in Fig. 1.2, where main components are shown includes high-resolution camera, monitor, PC control system, jet driver, 16 nozzles head, ink reservoir, pressure controller, strove LED, temperature controller and moveable stage. These components mainly contribute to printing process. The features of DMP-3000 printer are print area 300x300mm, substrate thickness 0.05 to 30 mm, system position accuracy $\pm 5 \mu\text{m}$, repeatability is $\pm 1 \mu\text{m}$, and platen temperature from room 25 to 60 °C.

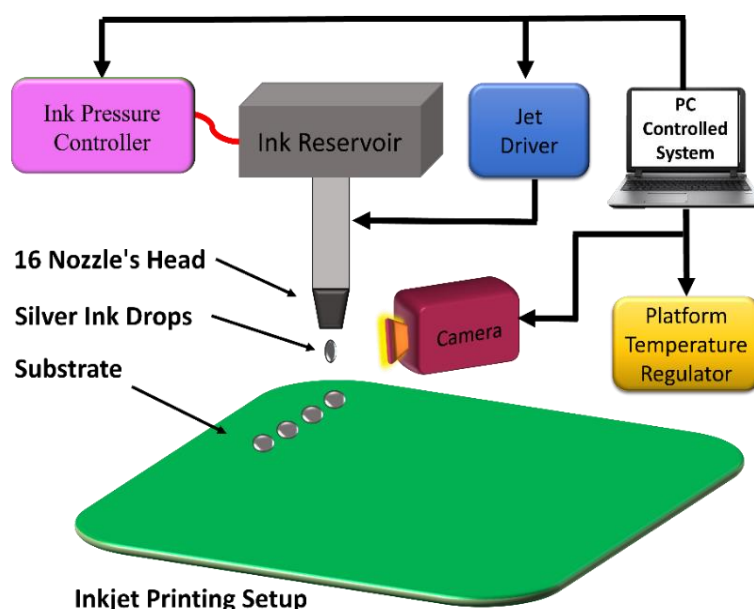


Figure 1.2. Schematic diagram of the DMP-3000 along main components.

1.2.2. Screen Printing

screen printing is the process of transferring a stenciled design onto a flat surface using a mesh screen, ink, and a squeegee. Fabric and paper are the most commonly screen-printed surfaces[11, 12]. The basic method involves creating a stencil on a fine mesh screen, and then pushing ink (or paint, in the case of artwork and posters) through to create an imprint of your design on the surface beneath. The screen-printing schematic diagram is shown in Fig. 1.3.

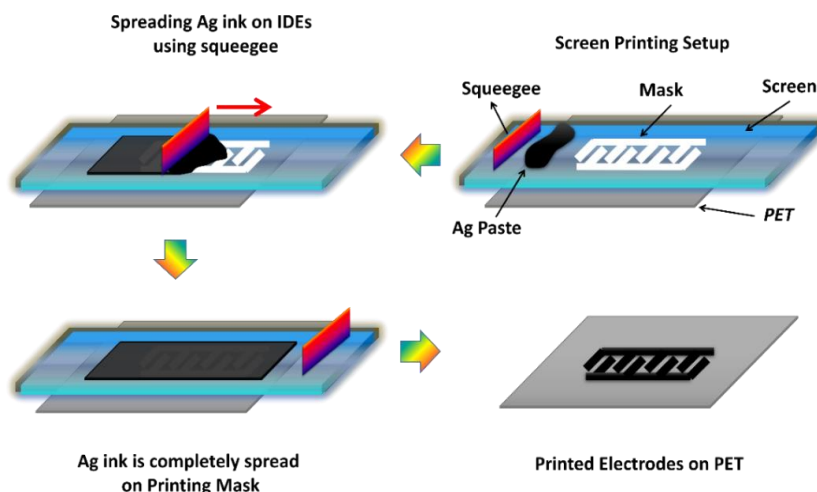


Figure 1.3. Schematic diagram of the screen printing showing main components.

1.2.3. Spin Coating

Spin coating has been used for several decades for the fabrication of thin films. A typical process involves depositing a small puddle of a fluid resin onto the center of a substrate and then spinning the substrate at high speed (typically measured in revolution per minute rpm). Centripetal acceleration will cause the resin to spread to, and eventually off, the edge of the substrate leaving a thin film of resin on the surface. Final film thickness and other properties will depend on the nature of the resin such as, viscosity, drying rate, percent solids, surface tension, etc. and the parameters chosen for the spin process. Factors such as final rotational speed, acceleration, and fume exhaust contribute to how the properties of coated films are defined[13, 14]. Schematic diagram of a spin coater along with main components is shown in Fig. 1.4a and a very simple process of spin coating flow chart is shown in Fig. 1.4b.

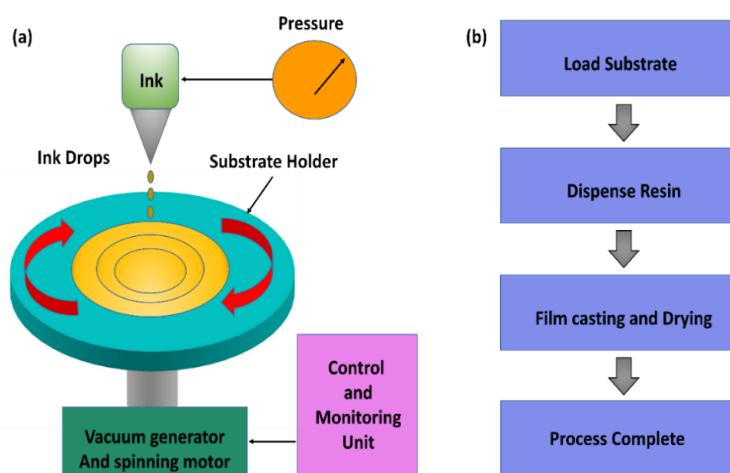


Figure 1.4. (a) Spin coater schematic diagram. (b) Simple spin coating process.

1.3 Objective of the Thesis

Printed electronics is new emerging field that allow low cost, large area, flexible and environmentally friendly applications. Some devices are matured and already have been used in electronic applications such as OLED display, RFID tags and biomedical sensors etc. Since printed electronics is new field there is big room yet in the advancement of the printed electronics. Among the recent challenges of the printed electronics are the fabrications techniques, encapsulation, and reliable materials. The main objective of thesis is to address these challenges by exploring new functional materials to fabricate the electronic devices such as memristors, neuromorphic resistive memory devices, humidity sensors, strain sensors and nanogenerators, etc.

Current passive crossbar memories (ReRAM) are suffering from inherent problem of sneak currents. This problem is minimized by introducing new device structures and materials to achieve asymmetric memristors. Apart from this, the fully memristive neural network is emerging as a game-changer in the artificial intelligence competition. Artificial synapses and neurons, as two fundamental elements for hardware neural networks, have been substantially implemented by different devices with memory and threshold switching (TS) behaviors, respectively. However, obtaining controllable memory and TS behaviors in the same memristive material system is still a considerable challenge that holds great potential for realizing compatible artificial neurons and synapses. We have reported controllable neuromorphic resistive memory device for the implementation of neural network. On the other hand, we have investigated the development of smart sensors based on self-power devices to monitor humidity, nanogenerator, strain sensor and tribo and piezoelectric nanogenerator using low cost, ambient conditions manufacturing techniques are studied and utilized for the fabrication of these devices. The optical, chemical, mechanical, and electrical characteristics and statistical analysis has been carried out to make sure the reliability and direct printability of the electronic device.

1.3.1 Outline of thesis

The thesis is organized into five chapters as under:

Chapter 2 deals with the memristor working, fabrication and characterization of Zinc Oxide Iron Oxide ZnO/Fe₂O₃ heterojunction on PET substrate and soft and flexible discrete channel devices using partial sodium salt solution and sodium hydroxide (PAA-Na⁺:H₂O):(NaOH).

These devices are fabricated with solution processed techniques. Resistive switching properties and resistive switching mechanism are investigated in the fabricated devices. This chapter also describes the fabrication of flexible resistive switch.

Chapter 3 deals with the neuromorphic resistive memory devices. The one directional resistive memory devices have importance to reduce sneak current and the analog behavior helps to perform neuromorphic computing. To achieve both properties we have utilized ZnO/GaN heterojunction and GeO₂. The soft and flexible liquid based neuromorphic resistive memory devices are fabricated using ionic liquid BMIM FeCl₄ and Ag@AgCl. These liquid devices structures show promising performance for the implementation of the hardware based neural network system. These devices are fabricated with solution processed techniques and characterized for electrical and surface morphology.

Chapter 4 describes humidity, Piezoelectric and triboelectric nanogenerator, and Photosensor which are fabricated through screen printing, inkjet printing, and spin coating at ambient conditions. The humidity sensor sense % RH from 0-100 %. For sensing the humidity, the sensor utilizes Inner Eggshell membrane, and Gallium Nitride (GaN). The biocompatible and biodegradable snake shad membrane is utilized for the fabrication of piezoelectric and triboelectric nanogenerator. The Inkjet Printed Self Healable Strain Sensor Based on Graphene and Magnetic Iron Oxide is used to detect stretching performance up to 54.5% strain.

Chapter 5 presents conclusion of the thesis and future work.

Chapter 2 Memristors

2.1 Memristor

In the classical electronics, there are only three fundamental 2-terminal passive circuit elements the resistor, the inductor, and the capacitor. Based on simple symmetry arguments Leon Chua claimed that a fourth fundamental 2-terminal passive circuit element is necessary to complement the other three[15]. More specifically, Chua realized that out of the six possible pairwise combinations between the four fundamental circuit variables, namely, the current, voltage, charge, and flux-linkage, only five had been identified. He therefore postulated mathematically the memristor as the element relating the charge and the flux-linkage to establish the missing link (see Fig. 2.1). In 2008, HP lab demonstrated the first physical memristor based on resistive switching in doped TiO_2 [16]. In 2010 Chua confirmed that every resistive switching device is a memristor[17]. Memristor can be switched between two resistive states, low resistance state (LRS) and high resistance state (HRS) through external voltage bias[18]. This feature makes it a transistor less switch that can be fabricated in very small size. Since that, it researched widely in the electronics field for the future non-volatile memory applications[19].

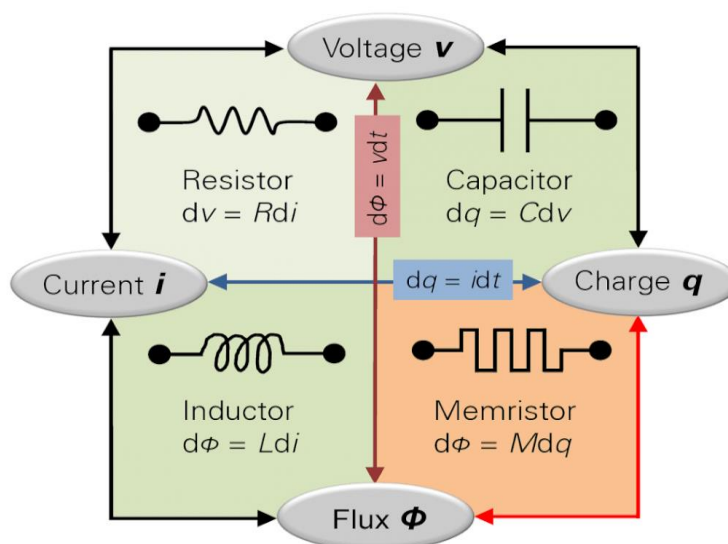


Figure 2.1 The diagram shows the four fundamental circuit elements.

Resistive crossbar passive memories (ReRAMs) based on resistive switching is considered the next generation non-volatile memory (NVM) because of its ample advantages over the flash memory[20].

As CMOS technology is reaching its limits in sense of materials, device size, fabrication plants and economics, ReRAM is the only hope to counteract the upfront challenges to the electronic industry. Resistive switches (transistor less) considered as a justified replacement for the memory devices and electrical switching elements have been researched productively for many[21]. Solid electrolyte sandwiched between two metallic electrodes is considered to elucidate the reversible resistive switching characteristics[22]. The sandwiched structures exhibit at least two distinct states when are being forced with opposite polarity. The change in the resistance is then exploited for the electrical switching and memory applications[23]. The resistive switching devices are fabricated by simply sandwiching some metal oxide, polymer-based material, perovskite material, or even a vacuum nano-gap etc between two conducting electrodes[24]. The resistive switch provides great data storage density due to its simple device structure. The sandwiched type structures are more reliable because these devices are resistance based so they keep their state unchanged even when the power absence[25].

2.2 Types of Memristors

As described in the previous section that as compared to an ordinary electrical resistor, memristor can be programmed or switched in different resistive states based upon the history of the voltage signal applied to the device[26]. This phenomenon can be understood in a current-voltage (I-V) curve[22]. Resistive switching are categories into two main types based upon the voltage polarity needed to the device operation.

2.2.1 Unipolar Memristors

If switching of the resistive switch is independent of the polarity of the voltage/current source and is dependent on the amplitude of the voltage/current, then the switching is categorized as unipolar resistive switching as shown in Fig. 2.2. As noticed in the I-V curve, set and reset of the device is happening irrespective of the polarity of forcing node. A device in an HRS state can be switched to LRS state by a threshold voltage (V_{th}) and the current is limited by compliance current to avoid hard break down in the switching layer of the device. Resetting back to ON-state happens at a same polarity below its V_{th} . A much higher current can be observed in retting state of the device[27]. Application of CC is not needed in retting of the device. Therefore, both the transition of setting and resetting are possible on both sides of the polarity.

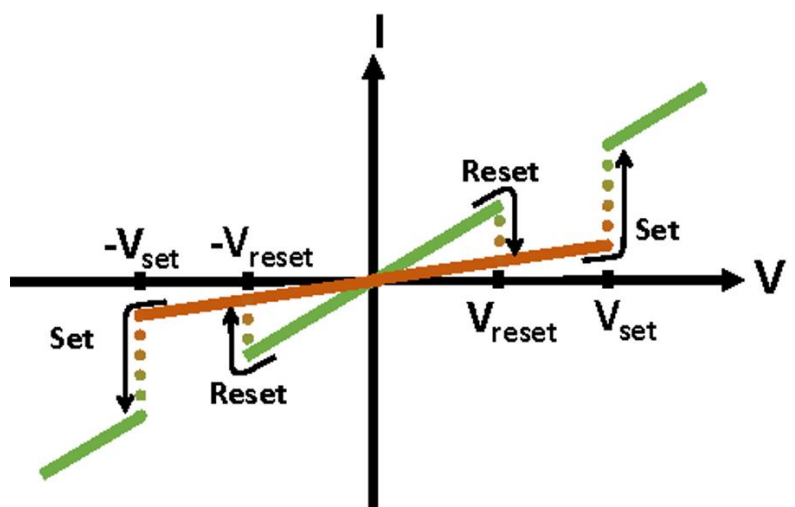


Figure 2.2. Amplitude dependent unipolar resistive switching.

2.2.2 Bipolar Memristors

The behavior of the device in which setting and retting of the device appeared at different sides of the polarity is termed as bipolar resistive switching. In this type of resistive switching, ON-state of the device occurs at some V_{TH} and OFF-state of the device occurs at some specific V_{TH} on the opposite side of the voltage polarity as shown in Fig. 2.3. Bipolar resistive switching is also called polarity dependent resistive switching[26, 28]. Current observes in bipolar resistive is much lower as compared to that of unipolar resistive switching.

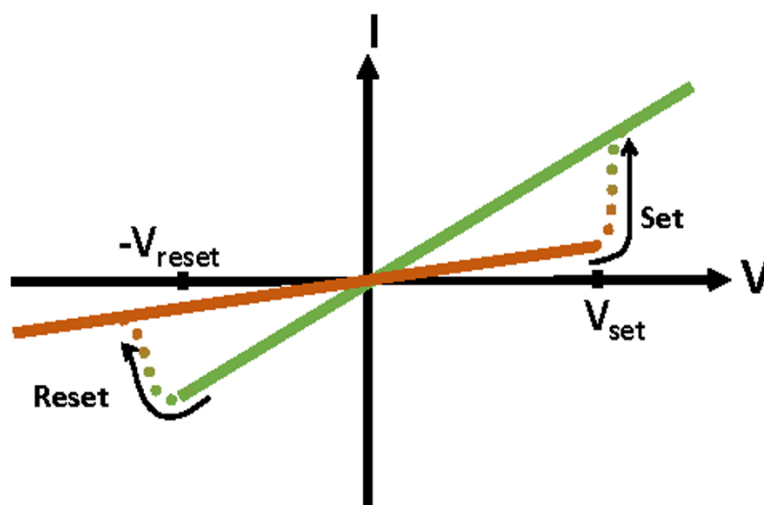


Figure 2.3. Polarity dependent bipolar resistive switching.

2.3 Memristors Mechanisms

Several studies have been conducted for memristive mechanisms involved in metal oxides and polymers based sandwiched structures (Waser and Aono 2007, Sawa 2008, Akinaga and Shima 2010, Lee and Chen 2012, Cho et al. 2011, and Ling et al. 2008). Broadly, the proposed mechanisms are categorized into two classes: the bulk effect and the interface effect.

2.3.1 Bulk Effect

The memristive effect that is caused by formation and rupturing of the conductive filaments due to joule heating in the sandwiched material between the two electrodes is termed as bulk effect or thermal effect[29]. Bulk effect is observed common in unipolar resistive switching devices. Forming voltage is usually needed in these types of resistive switching. The filaments are formed by the voltage induced partial dielectric breakdown[29]. These filaments may be composed of electrode material transported into the sandwiched layer, local degradation of the organic film or decomposed insulator material such as sub-oxides[29]. During the resetting state of the device, the filaments are undergone into the rupturing phase hence the device change its LRS into HRS.

2.3.2 Interface Effect

Interface effect is common in bipolar devices. Different models are involved to explain the interface effect in bipolar resistive switching devices[30]. Some common models are explained with the charge injection and trapping of charges in the traps in the insulator/oxide switching material[30]. Traps play an important role when the interface between metallic/conducting electrode and insulator/oxide is Schottky. When external potential is provided then the injected charges are trapped in the interface between conducting electrode and insulator. When sufficient number of charges are gathered in the trap site eventually the scenario overcomes the barrier between metal-insulator interface and large current starts to flow through the interface. Contrary when the biasing is reversed then again, the Schottky barrier establishes and changes the device state to its original HRS.

2.3.3 Redox Process Induced Cation Migration

This model is based on the redox reaction of the metallic electrode. When one of the electrodes is chemically reactive while the other conducting electrode is inert then cations migrate in the ionic conductor. Chemically reactive electrode (Ag or Cu etc.) undergoes oxidation reaction when force with some potential. The drift of cations (such as Ag^+ or Cu^+ etc.) in the ion-conducting layer and

their discharge at the counter electrode forms a highly conductive path results in setting the device into the ON state. When the polarity is reversed, the conductive path undergoes into the electrochemical dissolution and resetting the device into the OFF state[31].

2.3.4 Redox Process induced Anion Migration

Anion migration model is based on the chemical redox reaction of insulator/oxide. This is the mechanism in which resistive switching takes place by the migration of anion/oxygen ion towards anode or better described by the migration of oxygen vacancies towards cathode. This model is also termed as oxygen vacancy migration resistive switching model. The migration of anion (oxygen ion) or oxygen vacancy leads to the change in stoichiometry and a valance change of the cation sub lattice. Eventually the state of the device changes to the LRS by the change in the electronic conductivity of the oxide/insulator[32].

2.3.5 Formation and Disruption of Metal Oxide

In some of the reports, the resistive switching effect was attributed to the formation and disruption of the metal oxide between the metallic electrode and oxide interface. When a potential is applied to the device, metal oxide formed due to the electrochemical reaction between the electrode material and sandwiched layer[33].

2.4 Asymmetric Resistive Switching Memory Based on ZnO/Fe₂O₃ Heterojunction

Since the advancement in complementary metal oxide semiconductor (CMOS) technologies has quickly reaching physical and economical limits[34]. To overcome this problem researchers are exploring nonvolatile memory devices with low power consumption and higher integration density as compared to dynamic random-access memory (DRAM)[35]. In these expectation, theoretical concept of resistive memory device is explained by Lean Chua in 1971[36], and in 2008, Hewlett Packard (HP) laborites group has released resistive memory device and recognized as fourth fundamental circuit element of electronics components[37]. After this breakthrough, numerous memory devices are explored with the hope of a next generation of the nonvolatile resistive memory device[38]. A single resistive memory cell consists of metallic top and bottom electrode and sandwiched active layer based on 2D materials, biomaterials, metal oxide, soft materials, phase change material, and composite of two different materials[39].

However, the stability of these resistive memory devices has strong dependency on following parameters, low power consumption, long endurance cycles, high retention time, high resistance state (HRS), low resistance state (LRS), high current density, and high integrating density[39].

To fabricate a novel multifunctional resistive memory device, researchers are proposing different structures like active layers based on single material, composite of two different materials, heterojunction of two materials based on following mechanisms like oxygen ion migration mechanism, filament formation mechanism, and charge trapping mechanism[40]. The single bit nonvolatile resistive switching memory cell can be applied in the numerous applications in real life like neuromorphic computing, programmable analog circuits, and many more[41]. Crossbar resistive switching array architectures for a high integrating density are facing numerous issues, which include unnecessary power consumption and read error by sneak current problem[42]. In the case of increasing the area of the device, bendability is also more important in the wearable electronics. For this reason, the micro-cracks and mechanical fractures in a device repeatedly occur under repeated deformation. The performance of a device is susceptible to the structure damage, and this damage may cause the loss of its functionality.

Therefore, it is necessary to introduce a device with an enduring recovery property to maintain its function under a bending situation. For the sneak current problem, several researchers are proposing different memristor architectures which include Schottky diode-based resistive switching memory device, anti-serial memristor complementary nonvolatile resistive switching device, one diode one resistor memory device, and passive crossbar array memristor with highly asymmetric current–voltage characteristics and its mathematical model[43]. Although these proposed architectures have addressed to overcome the sneak current problem, further investigations for the wearable electronics are required to improve the various problems as flexibility and low power consumption including the sneak current.

In this paper, we propose a highly bendable asymmetric resistive switching memory device using n-type zinc oxide (ZnO) and p-type magnetic iron oxide (Fe_2O_3). There is high electron concentration effect in ZnO with high forward and reverse current ratio in a Schottky barrier between ITO/ZnO. The n-type ZnO has band gap of $E_g \sim -3.2$ eV with LUMO ~ -4.3 eV and HOMO ~ -7.5 eV. The p-type Fe_2O_3 is magnetic recording media with multivalent oxidation states. It enhances the hole mobility, and the high band gap of Fe_2O_3 $E_g \sim -2.1$ eV with LUMO ~ 4.9 eV and HOMO ~ -7.0 eV, which helps to enhance the Schottky diode function between ITO/ZnO into the asymmetric resistive memory function using ITO/ZnO/ Fe_2O_3 /Ag.

The HRS and the LRS of resistive memory device in forward current is $\sim 16.16 \text{ M}\Omega$ and $\sim 179.4 \text{ k}\Omega$, respectively, at read voltage $\sim 0.10204 \text{ V}$ with $R_{\text{off}}/R_{\text{on}}$ ratio ~ 90.1 . The HRS and LRS are recorded as $\sim 15.66 \text{ M}\Omega$ and $LRS \sim 9.23 \text{ M}\Omega$, respectively, in reverse current at read voltage $\sim -0.10204 \text{ V}$ with $R_{\text{off}}/R_{\text{on}}$ ratio ~ 1.69 . Hence, the proposed device is operated about $\sim 0.10204 \text{ V}$ under $1 \mu\text{A}$ to read the data with mainly memory operation, which is operated about $\pm 1 \text{ V}$ with $\sim 11 \mu\text{A}$ to write data. From these results, the proposed resistive switching device can be a solution for a future crossbar array in wearable electronics.

2.4.1 Materials and Methods

50 wt.% ZnO dispersion in water with nanoparticle $< 100 \text{ nm}$ in water, deionized water, N,N-Dimethyl formamide (anhydrous 99.8%), Fe_2O_3 nanoparticles 0.8–1.4% solid material basis with 0.5–0.7% Fe basis, Acetone, Ethanol were used to fabricate active layer, ITO coated PET were used as a substrate with a bottom electrode, and polydimethylsiloxane (PDMS) purchased from Sigma-Aldrich (South Korea) was used to encapsulate fabricated device. The silver (Ag) epoxy CW2400 was purchased from 4Science for the fabrication of top electrode. ZnO and Fe_2O_3 inks were prepared as; initially, 15% ink was prepared by diluting Fe_2O_3 in 5 ml acetone and ZnO ink was diluted with 10% water and both inks were placed on magnetic stirrer for 8 h at 12,000 rpm and bath sonicated by for 30 min at $60 \text{ }^\circ\text{C}$.

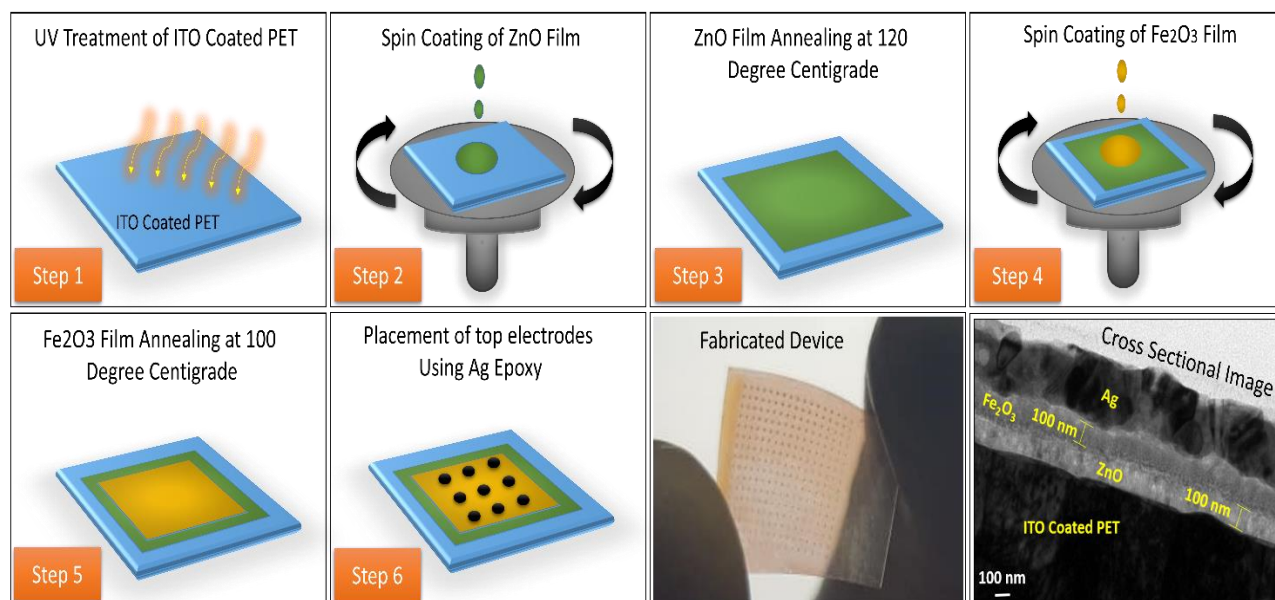


Figure 2.4. Fabrication process of asymmetric resistive memory device using spin coating technology and showing fabricated image and cross-sectional image of fabricated device with 100 nm magnification

Fabrication process is shown in Fig. 2.4, it consists of following steps; (i) ITO coated PET substrate was cleaned using acetone and ethanol for 5 min and then rinsed with deionized water and dried by a hot air and ultraviolet (UV) treatment for 5 min, (ii) the ZnO layer was deposited by using a spin coater at 1700 rpm for 60 s, (iii) then annealed for 2 h at 120 °C, (iv) the Fe₂O₃ film was also deposited by using spin coating technology at 2000 rpm for 40 s, (v) annealed for 2 h at 100 °C, and (vi) in final step, silver (Ag) epoxy as a top electrode was deposited on the fabricated heterojunction film based on ZnO/Fe₂O₃ film and cured at 120 °C for 30 min. The realized image of the fabricated device is shown in Fig. 2.4. To verify the vertical structure of the fabricated device, its cross-sectional image with magnification level of 100 nm is analyzed, which ensures that ZnO and Fe₂O₃ films are properly fabricated with a spin coating technology as shown in Fig. 2.4.

2.4.2 Characterization

The current and voltage (I–V) characterization was performed with KEYSIGHT B2902A source measuring unit. The device flexibility was analyzed with a mechanical bending machine. The surface morphology was analyzed through TESCAN MIRA 3 scanning transmission electron microscope (STEM), and their element compositions were analyzed using energy dispersive X-ray spectroscopy (EDS). The chemical and structural information of active layer film was performed with Lab Ram HR Evolution Raman spectrometer (Horiba Jobin Yvon, France) and Fourier transform infrared spectroscopy (FTIR) using Bruker IFS 66 V spectrometer, respectively. The surface roughness and film thickness were performed with NV-2000 Universal non-contact surface profiler. The crystal structure was characterized by XRD (X-ray diffractometer (Panalytical X'PERT PRO) with Ceramic Cu X-ray tube and elimination of K β (Ni filter).

The surface morphology of Ag was analyzed at 10 μ m as shown in Fig. 2.5a, which confirms that Ag nanoparticle cured at 120 °C and there is not any gap between Ag nanoparticles. The EDS spot profile of Ag is shown in Fig. 2.5b, which confirms the presence of Ag peaks. The EDS mapping of Ag is shown in Fig. 2.5c, which confirms the presence of Ag L series. The 2D nano-profile of Ag is given in Fig. 2.5d which shows the surface roughness $R_a \sim 99.96$ nm, and the covered area of top electrode is 80 μ m \times 80 μ m. The 3D nano-profile of Ag is shown in Fig. 2.5e, which shows the thickness ~ 180 nm. The microscopic image of the top electrode is shown in Fig. 2.5f with magnification level of 100 μ m.

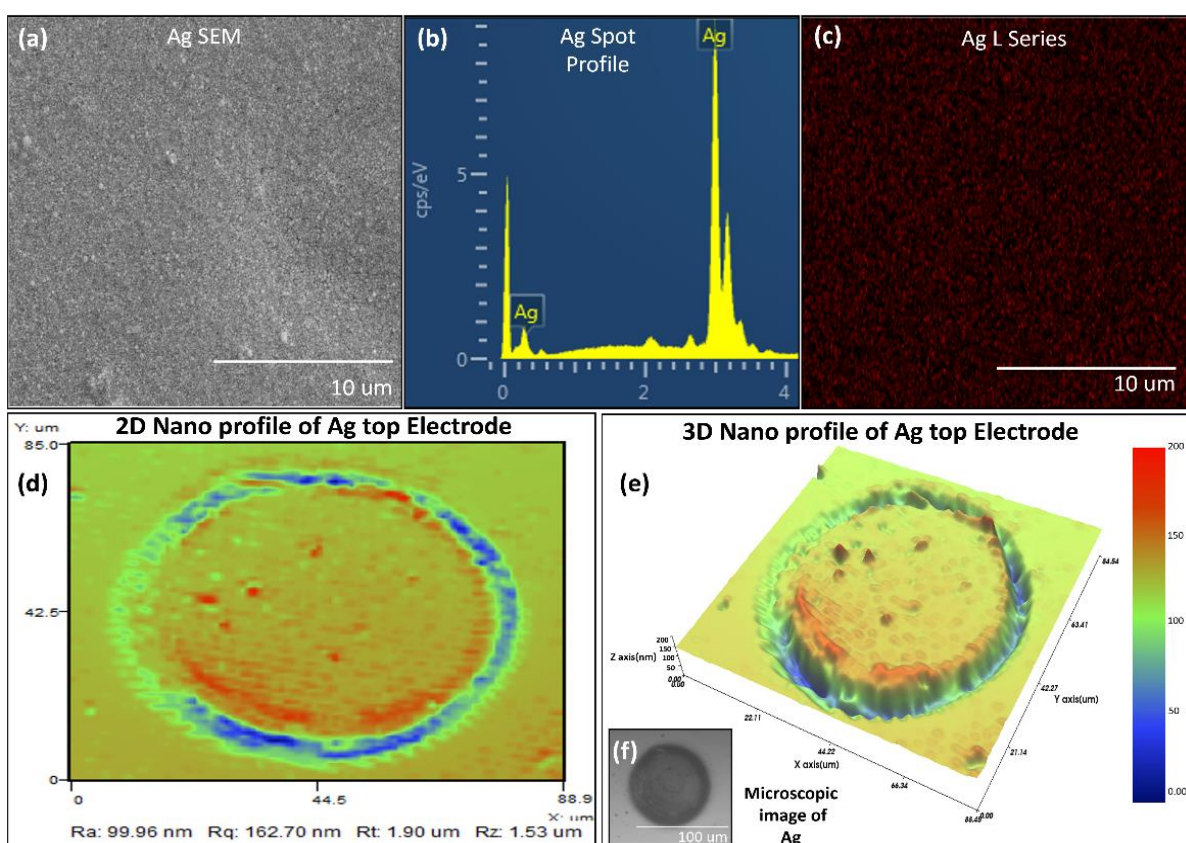


Figure 2.5. (a) Surface morphology of a top electrode based on Ag at 10 μm . (b) Element detection showing Ag peaks and (c) EDS mapping of Ag. (d) The 2D and 3D nano-profiles show the top electrode of 80 μm \times 80 μm with electrode roughness \sim 99.96 nm and (e) the height profile with the thickness of 180 nm, respectively. (f) The microscopic image of the top electrode

The surface morphology of the Fe_2O_3 is shown in Fig. 2.6a with magnification level of 10 μm . The Fe_2O_3 film is properly fabricated with spin coater. The EDS spot profile of the Fe_2O_3 is shown in Fig. 2.6b, which confirms the presence of O and Fe peaks as shown in Fig. 2.6b. The EDS mapping as shown in Fig. 2.6c confirms the presence of the oxygen (O K series) in Fig. 2.6d, oxygen (Fe K series) in Fig. 2.6e. The FTIR spectra of Fe_2O_3 show the characteristic absorption peak at 3425.86 cm^{-1} is referenced to the stretching vibration of $-\text{OH}$, 2840.86 cm^{-1} is attributed to the stretching vibration of $-\text{CH}_3$, 1684.89 cm^{-1} is assigned to the $\text{C}=\text{O}$, 1399.215 cm^{-1} is referenced to the $\text{Fe}-\text{O}$ vibration while 560.08 cm^{-1} is assigned to the $\text{Fe}-\text{O}$ stretching[44] a shown in Fig. 2.6f. The 2D nano-profile of Fe_2O_3 is shown in Fig. 2.6g, which confirms that film is high uniform with roughness $R_a \sim$ 422.53 nm. The 3D nano-profile of Fe_2O_3 shows the high profile with film thickness \sim 100 nm as show in Fig. 2.6h. Figure 2.6i shows the XRD pattern of alpha Fe_2O_3 in the range of $200 \leq 2\theta \leq 70$, which shows Hematite alpha Fe_2O_3 according to (JCPDS 33-0664). The peaks of Fe_2O_3 at $2\theta = 24.43^\circ, 32.61^\circ, 36.43^\circ, 41.92^\circ, 43.96^\circ, 49.82^\circ, 54.83^\circ, 57.82^\circ, 62.36^\circ,$ and 64.82° were assigned to (012), (104), (110), (113), (202), (024), (116), (018), (214), and (300)[44]. XRD of Hematite alpha Fe_2O_3 confirms that there are no impurities.

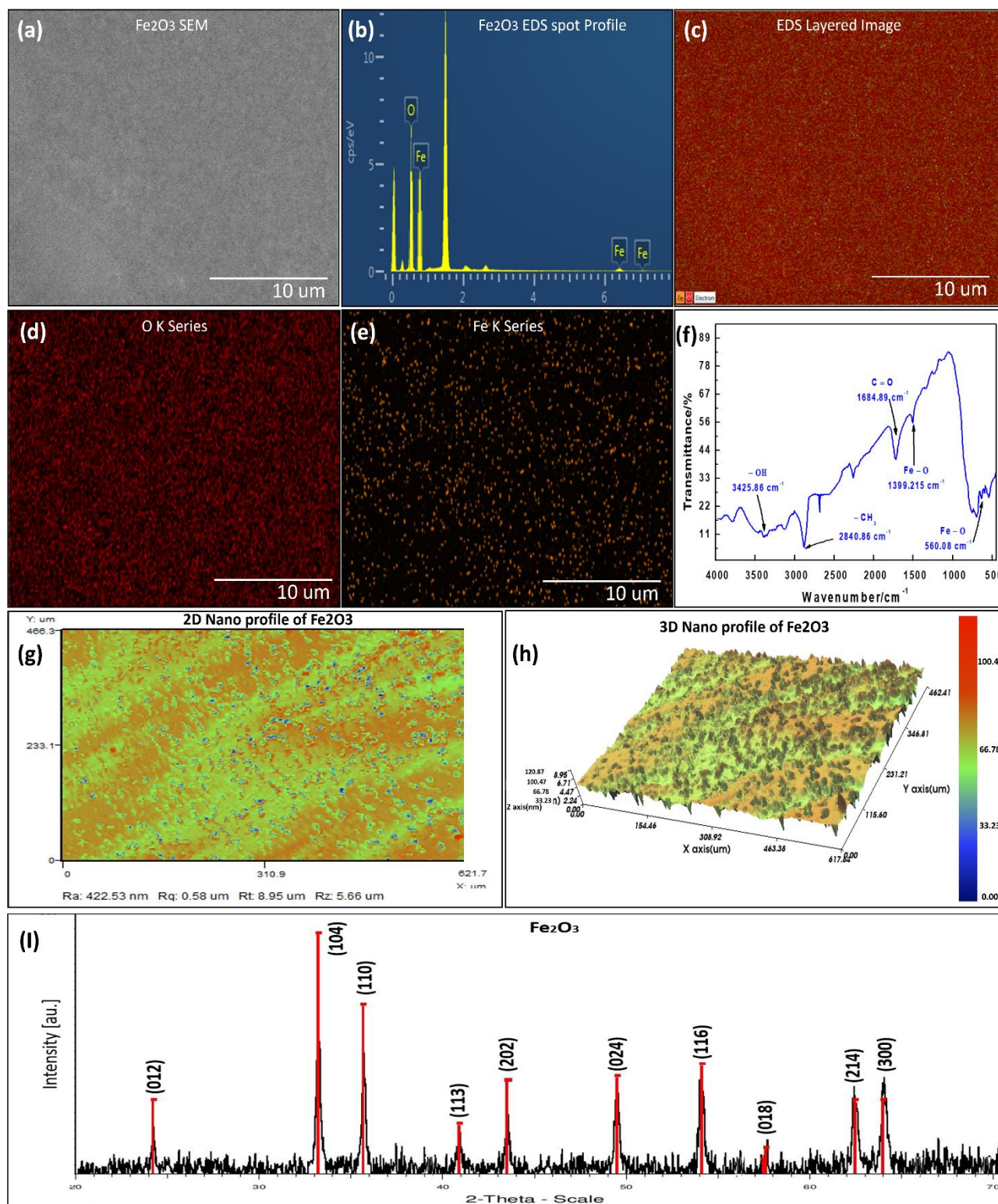


Figure 2.6. (a) Surface morphology of Fe₂O₃ is analyzed with TESCAN MIRA 3 at magnification level of 1 μm, (b) EDS spot profile confirms the presence of following peaks Fe and O, and (c) EDS mapping of Fe₂O₃ showing (d) O K series image, (e) Fe K series image at 10 μm, and (f) FTIR of Fe₂O₃. (g) The 2D and (h) 3D nano-profile of Fe₂O₃. (i) XRD of Fe₂O₃

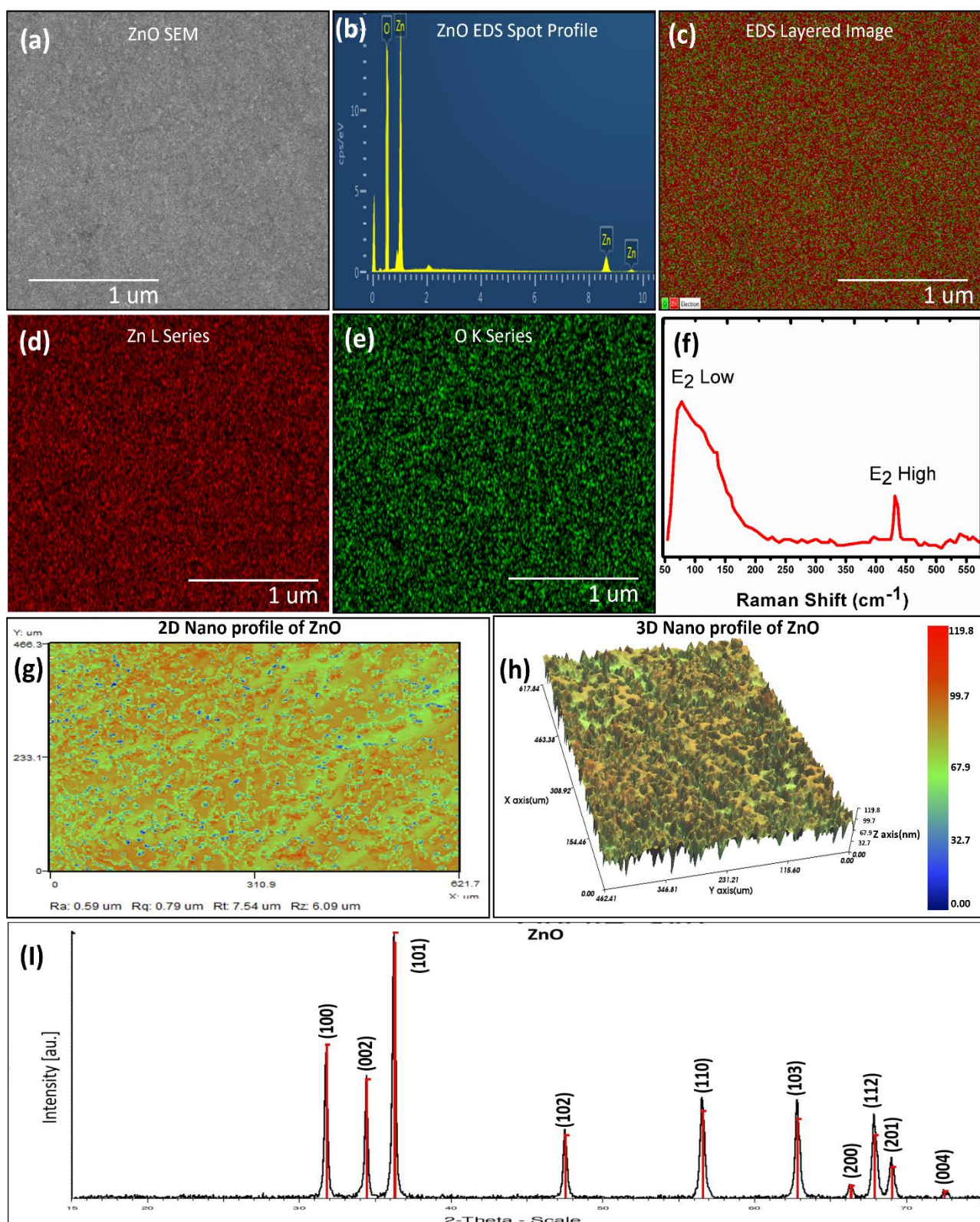


Figure 2.7. (a) STEM of ZnO with magnification level of 1 μm, (b) EDS spot profile confirms the presence of Zn and O peaks, and (c) EDS mapping of ZnO showing d zinc mapped image and e oxygen mapped image at 1 μm. (f) Raman spectrum of Fe₂O₃. (g) The 2D and (h) 3D nano-profile of ZnO. (i) XRD of ZnO

The surface morphology of ZnO is shown in Fig. 2.7a with magnification of 1 μm , which ensures that film is highly uniform due to film forming property and there is no cracks and pores on the surface of film due to proper centering at 120 $^{\circ}\text{C}$. The EDS spot profile of ZnO shows following element peaks Zn and O as shown in Fig. 2.7b. The EDS mapping of the ZnO is shown in Fig. 2.7c, which confirms the presence of the Zinc (Zn L series) and oxygen (O L series) presence in ZnO film as shown in Fig. 2.7c, d. The Raman spectra of the ZnO are given in Fig. 2.7e. In the Raman spectra of ZnO, we observed two peaks at 98.7 cm^{-1} (E2 Low) and 440.1 cm^{-1} (E2 High), which correspond to zinc atom lattice vibration and stress in the ZnO lattice, respectively. The wurtzite phase and vibration characteristics are due to lattice vibrations of the oxygen atoms in ZnO[44]. The 2D nano-profile of ZnO shows roughness $R_a \sim 0.59 \mu\text{m}$ as given in Figs. 2.7g and 3D nano-profile as shown in Fig. 2.7h confirms the device thickness $\sim 100 \text{nm}$. Figure 2.7i shows the XRD pattern of ZnO film in the range of $15^{\circ} \leq 2\theta \leq 80^{\circ}$, which shows standard hexagonal wurtzite crystal structure (Zincite, JCPDS 5-0664). The peaks of ZnO at $2\theta = 31.78^{\circ}, 34.23^{\circ}, 36.19^{\circ}, 47.52^{\circ}, 56.81^{\circ}, 62.86^{\circ}, 66.86^{\circ}, 67.52^{\circ}, 69.06^{\circ},$ and 72.52° were assigned to (100), (002), (101), (102), (110), (103), (200), (112), (201), and (004)[44]. XRD confirms that there are no impurities in ZnO.

2.4.3 Result and Discussion

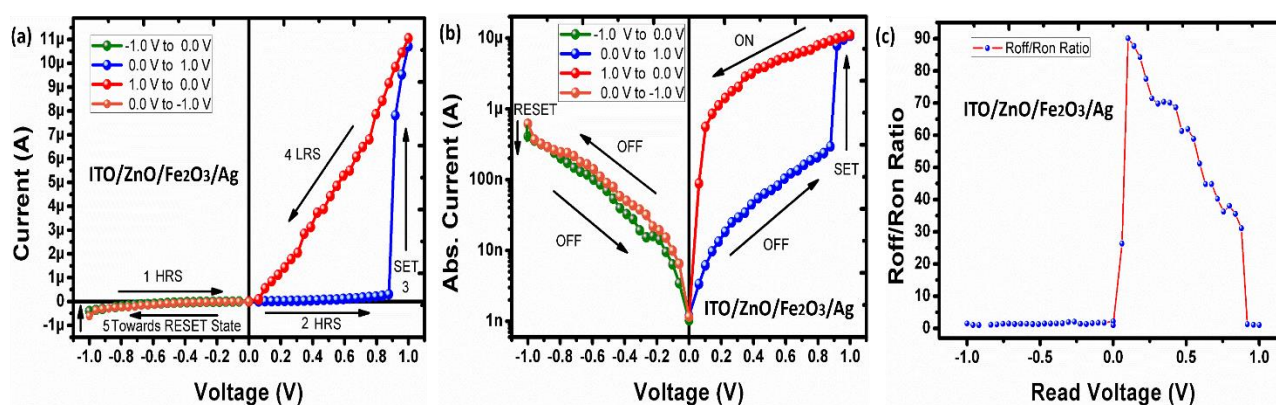


Figure 2.8. (a) Asymmetric I–V characterization of ITO/ZnO/Fe₂O₃/Ag and (b) its semi-log graph to show device passing from 0 V. (c) Roff/Ron graph

Electrical characterizations of the proposed resistive switching device were analyzed by using KEYSIGHT B2902A source measuring unit connected with probe station. To investigate the resistive switching behavior in the proposed heterojunction of ZnO/Fe₂O₃ as shown in Fig. 2.8a, it was biased with double voltage sweep from $\pm 1 \text{V}$. Initially, during positive voltage sweep from -1 to $+1 \text{V}$, a bottom electrode is biased with a positive voltage and a top electrode is biased with a negative voltage,

and the device in region 1 and 2 maintains its HRS due to presence of charge depletion region between n-type and p-type material based on ZnO and Fe₂O₃, respectively. Over 0 V, because the movement of hole and electron in forward bias helps to decrease depletion region and at threshold voltage (0.9 V), the memory device changes its state from HRS to LRS in region 3 (SET), which is also known as a state transition region. Similarly, under reverse voltage sweep from +1 to -1 V, a top electrode is a negative biased and a bottom electrode is also a negative biased as shown in Fig. 2.8a. The asymmetric resistive switching memory device remains in LRS in region 4, and after 0 V, p-n junction will increase due to reverse biased and memory device shows high resistance in region 5 and at threshold voltage ~ 1 V memory device undergoes in reset process. As the double log I-V graph shown in Fig. 2.8b, it ensures that the asymmetric memory device is passing from 0 V. From these results, we conclude that the $R_{\text{off}}/R_{\text{on}}$ ratio (~ 1.6976) decreases in the negative current region, as compared to positive voltage region $R_{\text{off}}/R_{\text{on}}$ ratio (~ 90.1), it shows an asymmetric property as shown in Fig. 2.8c. From these results, the reading voltage of the proposed resistive switching is operated about ~ 0.10204 V under 1 μA as shown in Fig. 2.8c. This is the main operation of the memory, and this reading voltage with the best resistance ratio is small value in terms of power consumption. The writing voltage is operated about ± 1 V with ~ 11 μA , and it is also lower power consumption than with ± 4 V for writing and reading data.

The conduction mechanism of the asymmetric resistive memory device based on double log I-V graph of ITO/ZnO/Fe₂O₃/Ag can be explained with the help of the charge trap-ping mechanism as shown in Fig. 2.9a. The asymmetric resistive memory device remains in HRS from -1 to +1 V, due to presence of less amount of a charge carrier. The HRS can be divided into two regions: (i) ohmic conduction region ($I \propto V$) and it is marked with red line slope fitting ~ 1.03 and (ii) child's law region and it is marked with green slope fitting ~ 2.0. In child's law region, charge carriers start increasing with applied voltage and abrupt increase of current is observed at threshold voltage 0.9 V and asymmetric resistive memory device changes its state from HRS to LRS. This region is marked with yellow slope fitting $I \propto V^n$ as shown in Fig. 2.9a. After this asymmetric resistive switching device shifts in LRS and then we applied reverse voltage sweep from +1 V to -1 V, where it governs by an ohmic conduction ($I \propto V$) as shown in Fig. 2.9a. After 0 V memory device again undergoes in HRS state. At negative threshold voltage -1 V, a filament is going to vanish, and memory device shift from LRS to HRS due to presence less amount of charge carriers in an active layer. Asymmetric resistive memory function can be explained with the help of ion migration. Initially, voltage sweep from -1 to +1 V is applied in which ITO coated PET as bottom electrode is biased with negative voltage and top electrode is based on Ag biased with positive voltage as shown in Fig. 2.9b.

The Ag^+ ion at top electrode increases with increase in the applied voltage that results in the increase of repulsion forces between Ag^+ ions. On the other hand, in ZnO and Fe_2O_3 films, the O^{2-} ion increases with increase in applied voltage and move upward due to negative charge on oxygen ions. At threshold Ag^+ ion moves toward Fe_2O_3 film and form a filament. Ag^+ ions use oxygen vacancies in Fe_2O_3 and ZnO as a trap charge and make a filament between top and bottom electrode and device changes state from HRS to LRS and the memory device undergoes in SET process due to decrease in barrier height between n-type ZnO and p-type Fe_2O_3 and abrupt increase in current is observed due to filament in an active layer. To back the resistive memory device in HRS, a reverse voltage sweep from +1 V to -1 V is applied to top and bottom electrodes as shown in Fig. 2.9c. After this, Ag^+ ions start moving upward due to positive charge on Ag ions and oxygen O^{2-} vacancies move downward due to negative charge on oxygen vacancies, and the filament will decrease due to increase in barrier height between ZnO and Fe_2O_3 , and at negative threshold voltage ~ -1 V it will break and the amount of the current will decrease, and the memory device undergoes HRS.

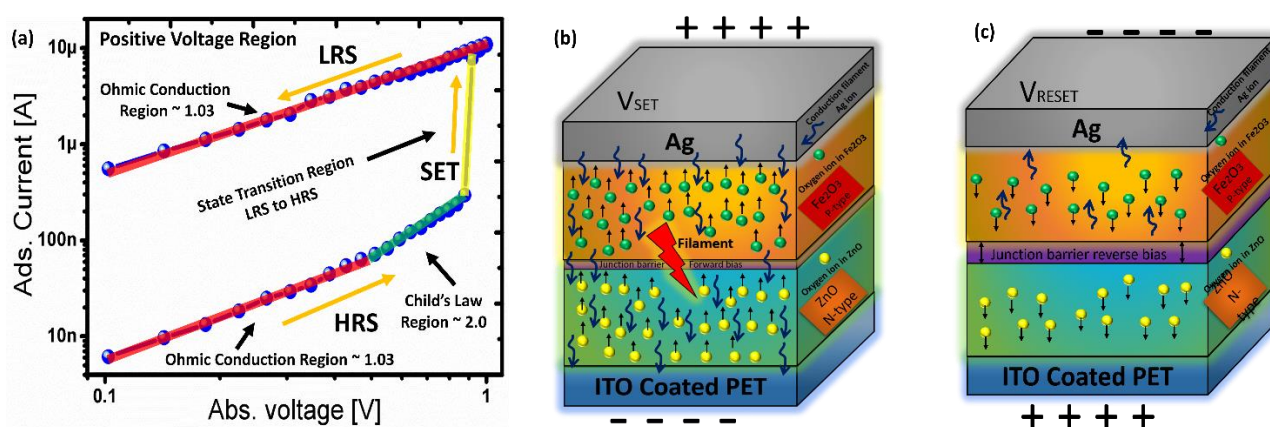


Figure 2.9. (a) Charge trapping mechanism. Schematic illustration of the proposed asymmetric resistive switching mechanism in ZnO/ Fe_2O_3 (n-type/p-type) heterojunction showing oxygen ion migration in (b) forward bias and (c) reverse bias

The stability tests of the proposed asymmetric resistive switching devices with ITO/ZnO/ Fe_2O_3 /Ag were analyzed at room temperature 28 °C. The endurance test is continuously tested for more than 300 endurance cycles as shown in Fig. 2.10a, which shows a stable HRS and LRS value at voltage read of 0.10204 V with $R_{\text{off}}/R_{\text{on}}$ ratio of ~ 90.1 as shown in Fig. 2.10b. The HRS and LRS are continuously tested for 30 days after device encapsulation with PDMS as shown in Fig. 2.10c. The asymmetric resistive memory device shows a stable switching between HRS and LRS as shown in Fig. 2.10d after device encapsulation.

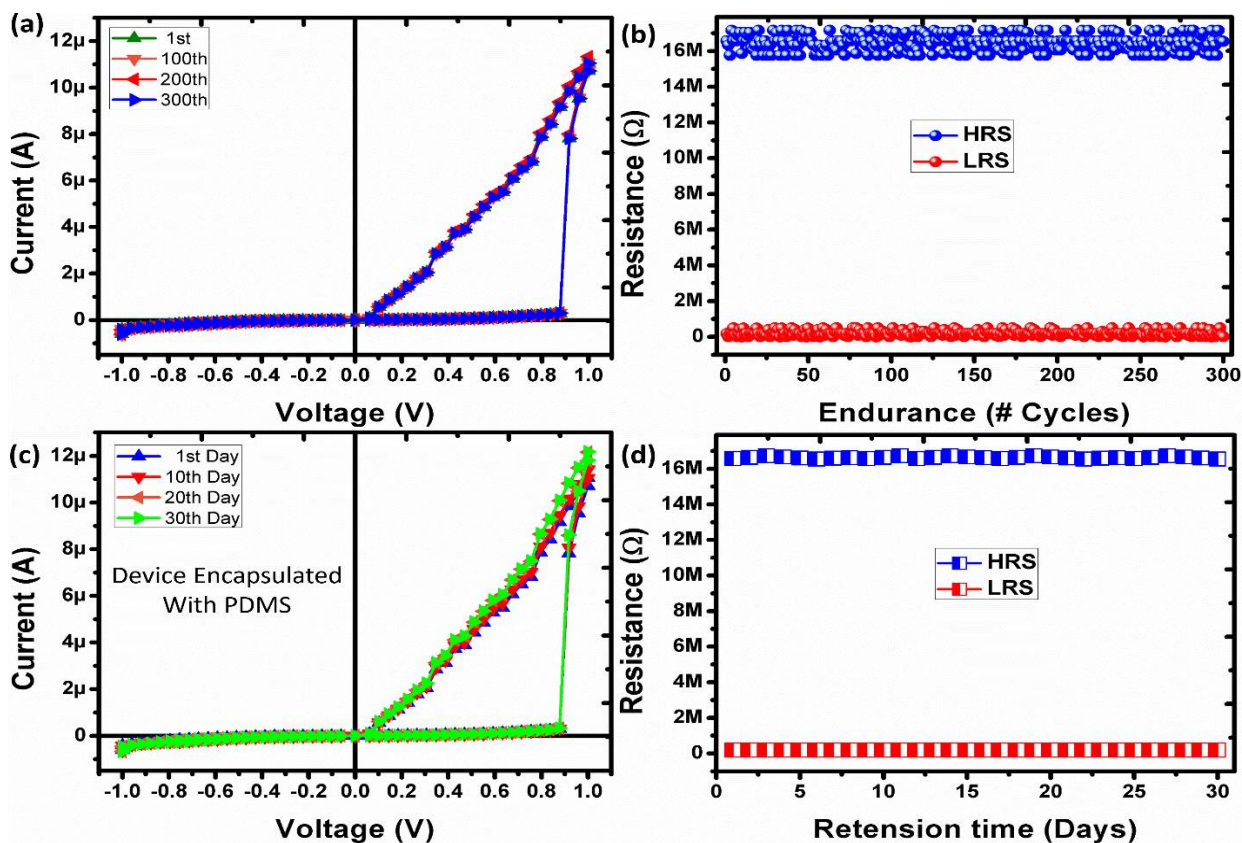


Figure 2.10. (a) Device stability for 300 cycles. (b) Device continuity test between HRS and LRS at read voltage of ~ 0.10204 . (c) The reliability test of the proposed device with PDMS encapsulation for 30 days and (d) its retention stability between HRs and LRS.

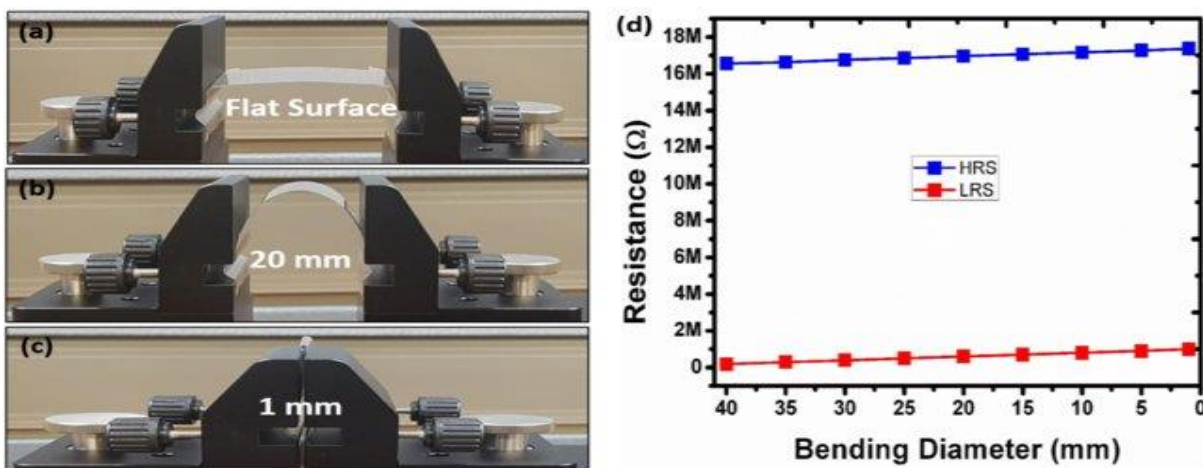


Figure 2.11. Bending test of memory device on (a) flat condition. (b) Bending test on 20 mm diameter. (c) Bending test on minimum curvature of 1 mm diameter using mechanical bending machine. (d) Bending test from 40 to 1 mm diameter.

The device flexibility is an important feature of the printed and flexible electronic devices, which helps to target wide range of application for real-life applications including flexible displays, flexible mobile phones, flexible resistive memory devices, flexible strain sensors, flexible wide band antennas, flexible thin film batteries, flexible solar cells, and flexible skin sensors. The flexibility of asymmetric

resistive switching device was evaluated by mechanical bending setup on different curvatures from flat down 40 mm to 1 mm diameter as shown in Fig. 2.11a, b, and c. This main possible reason of the higher level bending of the proposed device was due to the magnetic force property of Fe_2O_3 in an active layer, which provides a recovery function as shown in Fig. 2.11d

2.4.4 Summary

In this paper, the high bendable asymmetric resistive switching device based on ITO/ZnO/ Fe_2O_3 /Ag was proposed. Its active layer based on ZnO/ Fe_2O_3 was fabricated through the spin coater, which operated at ± 1 V. To verify the fabricated devices, the various mechanical and electrical analyses were studied. The $R_{\text{off}}/R_{\text{on}}$ ratio of ~ 90.10 was recorded in forward current with HRS and the LRS of ~ 16.16 M Ω and ~ 179.4 k Ω , respectively, at read voltage ~ 0.10204 V. The $R_{\text{off}}/R_{\text{on}}$ ratio of ~ 1.69 was recorded in reverse current with HRS and LRS of ~ 15.66 M Ω and ~ 9.23 M Ω , respectively, at read voltage ~ -0.10204 V. The proposed asymmetric resistive switching has shown a stable endurance and a long retention performance, which ensured that memory device can be highly reliable for printed electronics in different target applications. It has shown extremely stable bending performance down to 1 mm diameter. The proposed device can open a new gateway for highly bendable asymmetric resistive switching for crossbar array devices.

2.5 Soft Ionic Liquid Based Resistive Memory in a Cylindrical channel

Resistive switching device is a two terminal memory element, and its resistance (high or low) state depends on the history of an applied voltage[7]. The concept of resistive memory device is proposed in 1970s and it considered as fourth fundamental component of electronic circuits after resistor, inductor, and capacitor[45]. In recent decade, researchers are exploring numerous application area of memristor which include digital logic circuits, dynamic random access memory, signal processing, frequency selective circuits, bio sensing, and artificial intelligence[46]. Recently, many researchers are putting more efforts to mimic brain and proposing different memristor structures, which can be used as synapse device for neuromorphic computing[47]. The electrical properties of resistive memory device can be controlled by physical switching type, forming state, and using current compliance. Basic structure of resistive switching is based on metal/insulator/metal (MIM). This structure experimentally implemented by Hewlett-Packard (HP) group lead by Stan Williams using Pt/TiO₂/Pt[48].

However, many researchers observe that memristor behavior is ubiquitous and can be observed in different materials which include organic, metal oxide, biomaterials, and organic-inorganic[49]. Ionic liquids (IL) have versatile properties due to presence of organic salt[50]. Therefore, IL are used in different applications which include supercapacitors, fuel cells and biocatalyst, and ionic liquid gate transistors[51]. On the other hand, soft materials based resistive memory devices are getting enormous consideration in soft electronics due to low cost, simple solution process, simple fabrication method, and easy to realize memristor behavior based on IL using PVDF/AgNO₃[52], Ag@AgCl coreshell[53], and water/TiO₂[54]. The ionic memristors operation is based on ion transportation and polarization[54].

To improve retention time, endurance performance, and R_{off}/R_{on} resistance ratio, lot of room is available to introduce new IL materials and device structures, to achieve highly stable liquid memristors for soft electronics. In this aspect, the paper reports a soft ionic liquid resistive memory device with two terminal discrete polydimethylsiloxane (PDMS) cylindrical microchannel using composite of poly (acrylic acid) partial sodium salt (PAA-Na⁺:H₂O) gel and sodium hydroxide (NaOH). The device fabrication process consists of very simple step, which mainly consists of fabrication of microchannel in PDMS substrate, filling of ionic liquid in microchannel using syringe, and connection are provided by thin copper (Cu) wire. The Cu/(PAA-Na⁺:H₂O):NaOH/Cu IL liquid device shows highly stable performance at low operating voltage and it shows highly stable endurance and retention stability. The proposed ionic gel based liquid memory devices can be considered as potential candidate for the soft electronics.

2.5.1 Materials and Methods

The Poly (acrylic acid) partial sodium salt solution gel with (Mw) ~5000 with 50 wt.% in water (PAA-Na⁺:H₂O), 10 M sodium hydroxide solution (NaOH) in H₂O purchased from Sigma Aldrich and used without any chemical processing. The PDMS and curing agent were purchased from Dow Corning for preparation of cylindrical microchannel. Initially, PDMS mold was prepared by mixing PDMS and curing agent in 10:1 and for microchannel thin wire was placed in mold and cured for 100 °C for 80 min. After curing thin wire was removed from PDMS mold, which resulted in formation of cylindrical microchannel with diameter of 1 mm as shown in Fig. 2.12a. The PAA-Na⁺:H₂O and NaOH were mixed in 1:1. The composite was finally filled inside the channel using syringe and connection are provided by using thin copper (Cu) wire. The distance between both wires is approximately ~ 2 mm as shown in Fig. 2.12b.

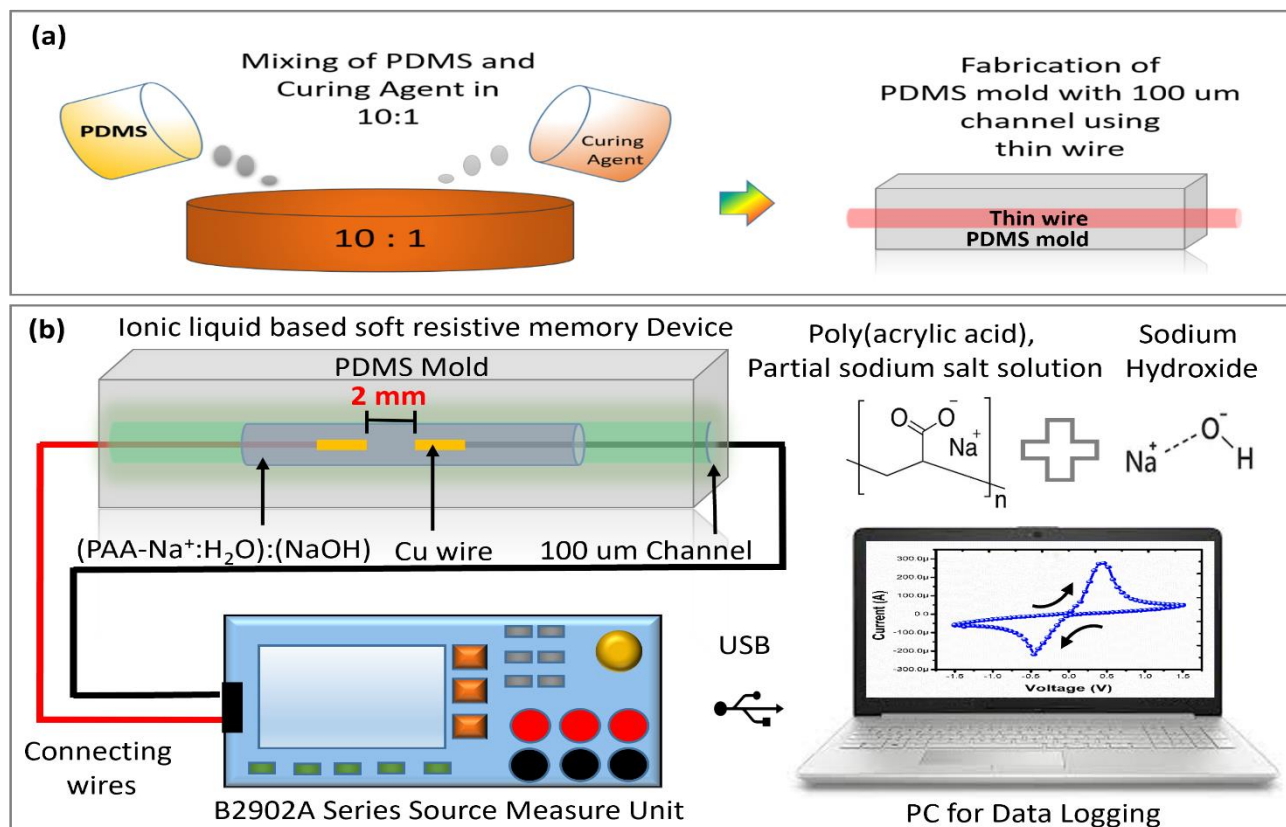


Figure 2.12. (a) Fabrication of a cylindrical microchannel IL memory device and (b) the experimental setup.

2.5.2 Result and Discussion

In this paper, I-V curve of Soft IL based resistive memory device was characterized, which featured pinched-hysteresis loop with voltage sweep of ± 1.5 V using KEYSIGHT B2902A source measuring unit. Initially, Cu/PAA-Na⁺:H₂O/Cu structure is characterized as shown in Fig. 2.13a, and it shows very low R_{off}/R_{on} resistance ratio. It is quite difficult to make very high difference between HRS and LRS of device. To improve the device stability and performance 10 M NaOH is added in different ratios in PAA-Na⁺:H₂O like 1:0, 1:0.5, 1:1 and 1:1.5 as shown in Fig 2.13a, where the optimum ratio of PAA-Na⁺:H₂O and NaOH is 1:1 as shown in Fig. 2.14. This shows stable switching performance with maximum R_{off}/R_{on} ratio. The blending ratio of PAA-Na⁺:H₂O and NaOH is shown in Fig. 2.13b. The composite of PAA-Na⁺:H₂O and NaOH are mixed in 1:1 and filled in a cylindrical microchannel to get a stable resistive switching and ± 1.5 V are applied across the device as shown in Fig. 2.14a. During forward voltage sweep in segment 1 from 0 V to 0.46 V, which illustrates ohmic region. In segment 1, the diffusion-flux help to increase current from linear region (0 V) to ohmic region (0.46 V). In segment 2 from 0.46 V to 1.5 V presents limiting resistance region. In cylindrical microchannel, diffusive flux and concentration gradient flux increases until ions are depleted on Cu electrodes.

In segment 2, ion flux saturates due to ion transportation proceed with diffusion of concentration gradient flux and decrease in current appears beyond a critical point from 0.46 V to 1.5 V. In reverse voltage sweep, segment 3 from 1.5 V to 0 V shows high resistance state due to decrease in ion flux and region become ion depleted. The sweep in the negative bias region containing segment 4, 5, and 6 showing yield of odd symmetry, which confirms the double loop hysteresis pinched at origin. The IL resistive memory device shows high R_{off}/R_{on} ratio 201.507 at 0.15 V as shown in Fig. 2.14b.

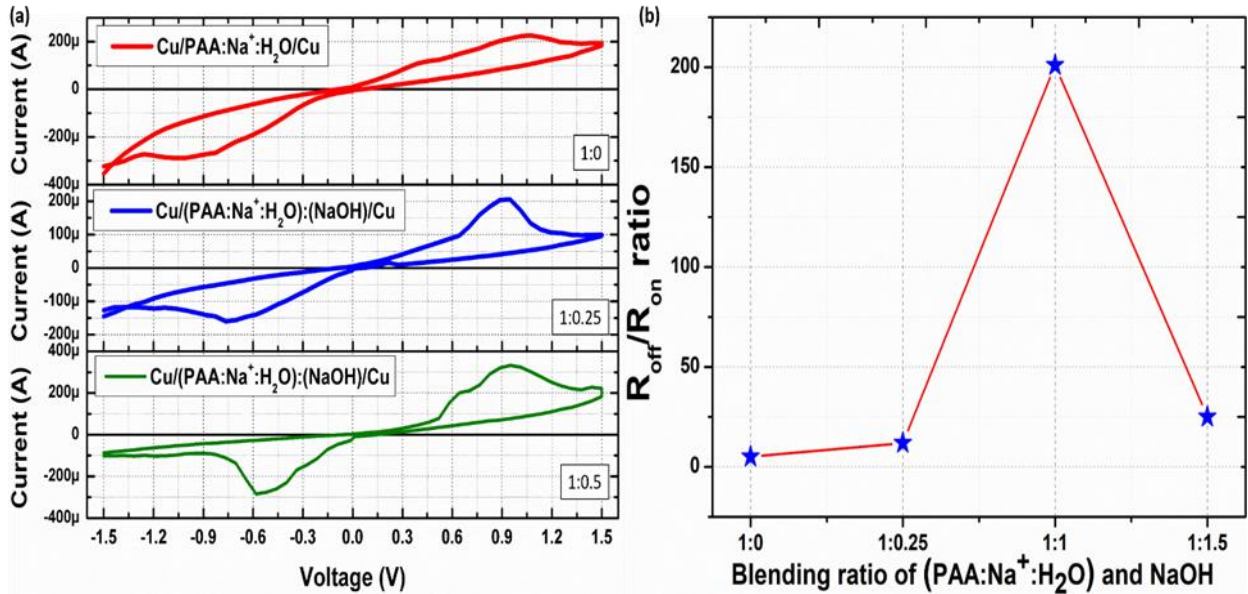


Figure 2.13. (a) Effects of different 1: 0, 1: 0.5, and 1: 1.5 (PAA-Na⁺:H₂O):(NaOH) composites on the complementary resistive switching of the memory device and (b) R_{off}/R_{on} ratio comparison of different blending ratios of (PAA : Na⁺:H₂O) and NaOH.

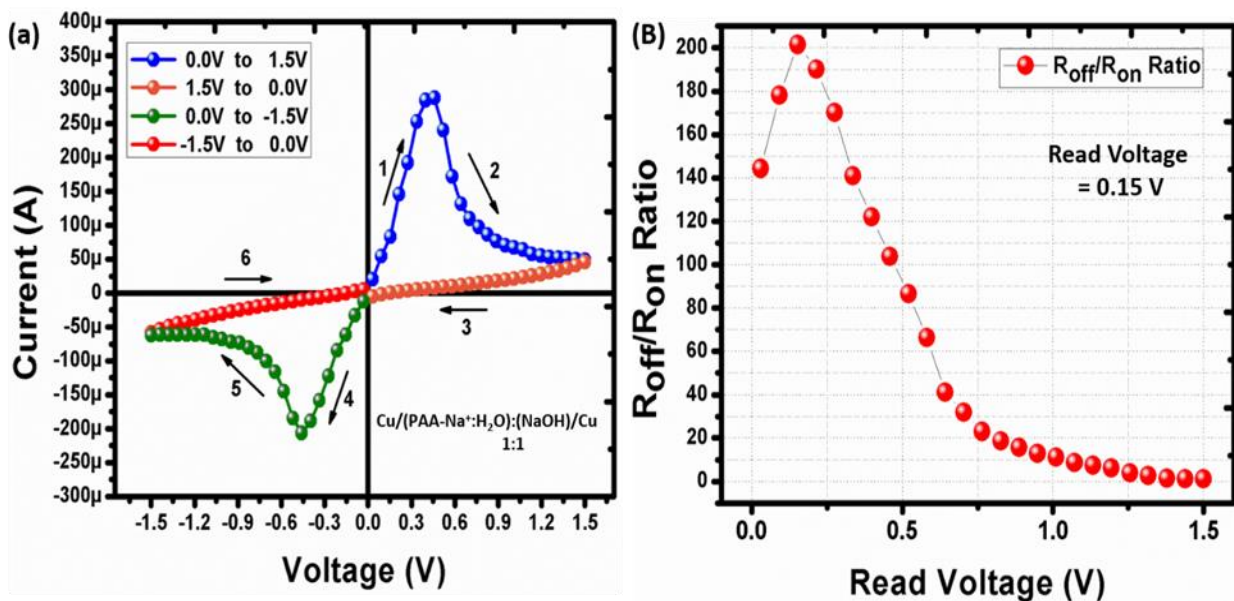


Figure 2.14. (a) I-V characteristics of the proposed IL resistive switching device and (b) its R_{off}/R_{on} resistance ratios for various read voltages.

The main reason of the resistive switching in IL microchannel device is due to electronic ion instability from one electrode to another electrode. Possible ion mechanism of IL resistive memory device explained in cylindrical microchannel using composition of IL PAA-Na⁺:H₂O and NaOH as shown in Fig. 2.15. The ion transport mechanism based on oxidation and reduction which took place at anode and cathode, respectively. During positive voltage applied on anode results in oxidation take place and Cu electrodes converts into Cu²⁺ ions. During device characterization, blue color is noticed in composite solution, which confirms the presence of Cu²⁺ instead of Cu⁺ ions. On the other hand, OH⁻ ion move toward anode and react with Cu²⁺ ion and form Cu(OH)₂. The Cu²⁺ ions further dissociates and move towards the cathode which is negatively charged. At cathode two different reactions can be observed as; first possibility is Na⁺ ions reduced to Na at cathode and in second possibility, Cu²⁺ ion reduced to Cu at cathode.

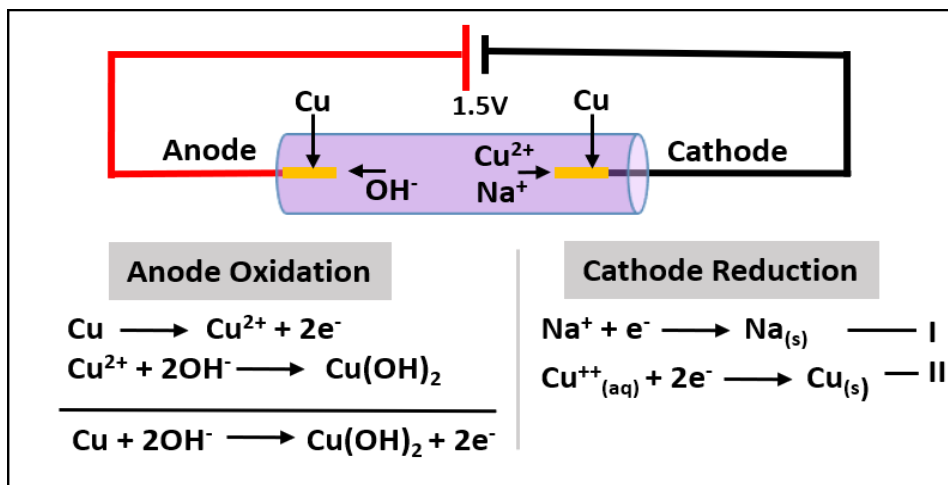


Figure 2.15. Ionic mechanism of the proposed memory device.

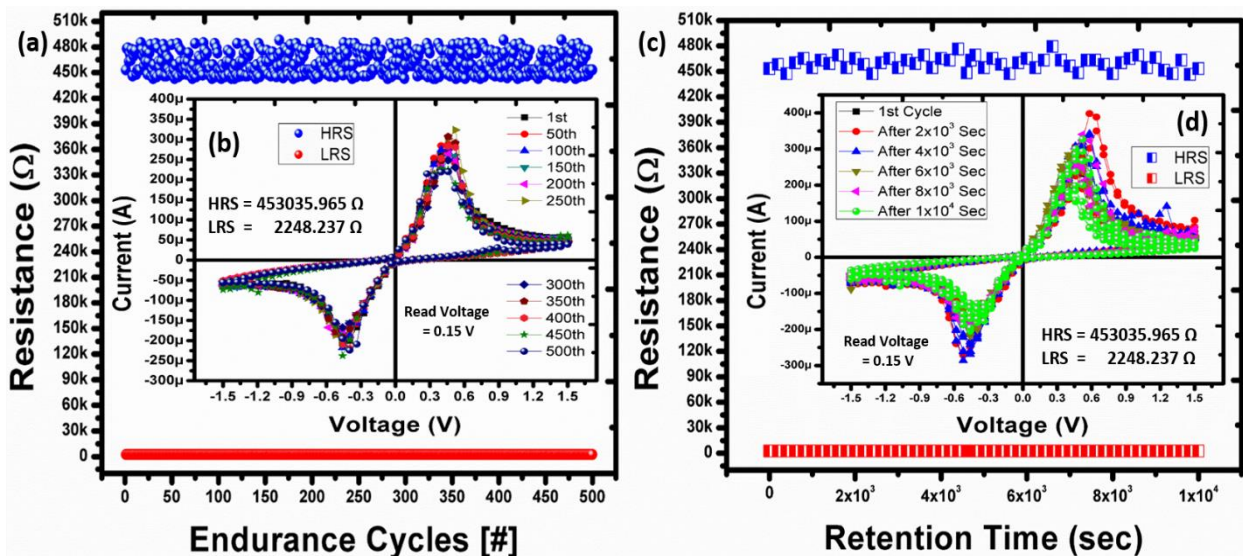


Figure 2.16. (a) Endurance of the proposed device with respect to HRS and LRS and (b) its I–V plots. (c) IL retention time at a voltage read of 0.15 V and (d) the corresponding I–V plots.

The next generation IL resistive memory devices are getting lot of attention due to their stable switching performance. The endurance and retention performance are very important feature to investigate resistive memory performance for device commercialization. In this work, the stable endurance property of the soft IL device was investigated. Fig. 2.16a shows the endurance performance of the IL device for more than 500 cycles with stable switching between HRS and LRS as shown in Fig. 2.16b at read point of 0.15 V. The retention time of the soft IL device is more than 104 sec as shown in Fig. 2.16c and current voltage curves are shown in Fig. 2.16d.

In this part of mechanism, we mainly focus only on the movement of Cu ions in ionic gel, which result in complementary resistive switching (CRS) as shown in Fig. 2.17. The migration of Cu ions can be modulated by tuning the amplitudes of externally applied voltages results in CRS. On applying positive voltage to anode sweeps of $0\text{ V} \rightarrow +1.5\text{ V} \rightarrow 0\text{ V}$ to Cu electrode by keeping cathode Cu electrode as ground and result in IL device shows CRS characteristics. In Fig. 2.17, semi-log graph showing the CRS behavior. For the mechanism of the CRS, we define different threshold voltages V_{th1} , V_{th2} , V_{th3} and V_{th4} , which are defined from Fig. 2.14a in Fig. 2.17, in which resistance states HRS or LRS changes prominently. The average voltages of V_{th1} , V_{th2} , V_{th3} and V_{th4} are 0.14 V, 1.1 V, -0.13 V, and -0.96 V, respectively. In Fig. 2.17, semi-log image shows that the device turns “ON” for the V_{th1} of $\sim 0.14\text{ V}$ and V_{th3} of $\sim -0.13\text{ V}$. The turns “OFF” at the voltages of $V > V_{th2} \sim +1.1\text{ V}$ and $V > |V_{th4}| \sim -0.96\text{ V}$ as shown in Fig. 2.17. Thus, the device is in ON state in the voltage range between $V_{th1}-V_{th2}$ (0.14 V to 1.1V) and $V_{th3}-V_{th4}$ (-0.13 V to -0.96 V). When the magnitude of sweep voltage becomes higher than $V_{th2} \sim 1.1\text{ V}$ or $|V_{th4}| \sim -0.96\text{ V}$, the device switched back to the “OFF” state. The IL based CRS device with “ON” and “OFF” states solely depend on the time during which conduction filament between anode and cathode. The “0” and “1” states mainly depend on the location of the Cu^{++} ions. During state “1”, Cu^{++} ions start entering in ionic solution and the diffusion-flux help to increase the flow of ions and ions move towards cathode and on the same time very small amount of Cu^{++} ions reacts with OH^- ions at anode and result in formation of $\text{Cu}(\text{OH})_2$ (oxidation) and releases $2e^-$. In the state “0”, the Cu^{++} ions migrate to cathode and accept $2e^-$ and result in Cu (reduction) at cathode. In this whole process, ionic flux saturates because ion transportation proceeds with diffusion of concentration gradient flux and decrease in current appears beyond a critical point. Due to this phenomenon, Cu migration increases at certain value of voltage and then ion migration decreases, which results in conduction filament get break and in the “0” state due to diffusive flux and concentration gradient flux increases until ions are depleted on Cu electrode resulting in the creation of a higher resistance value.

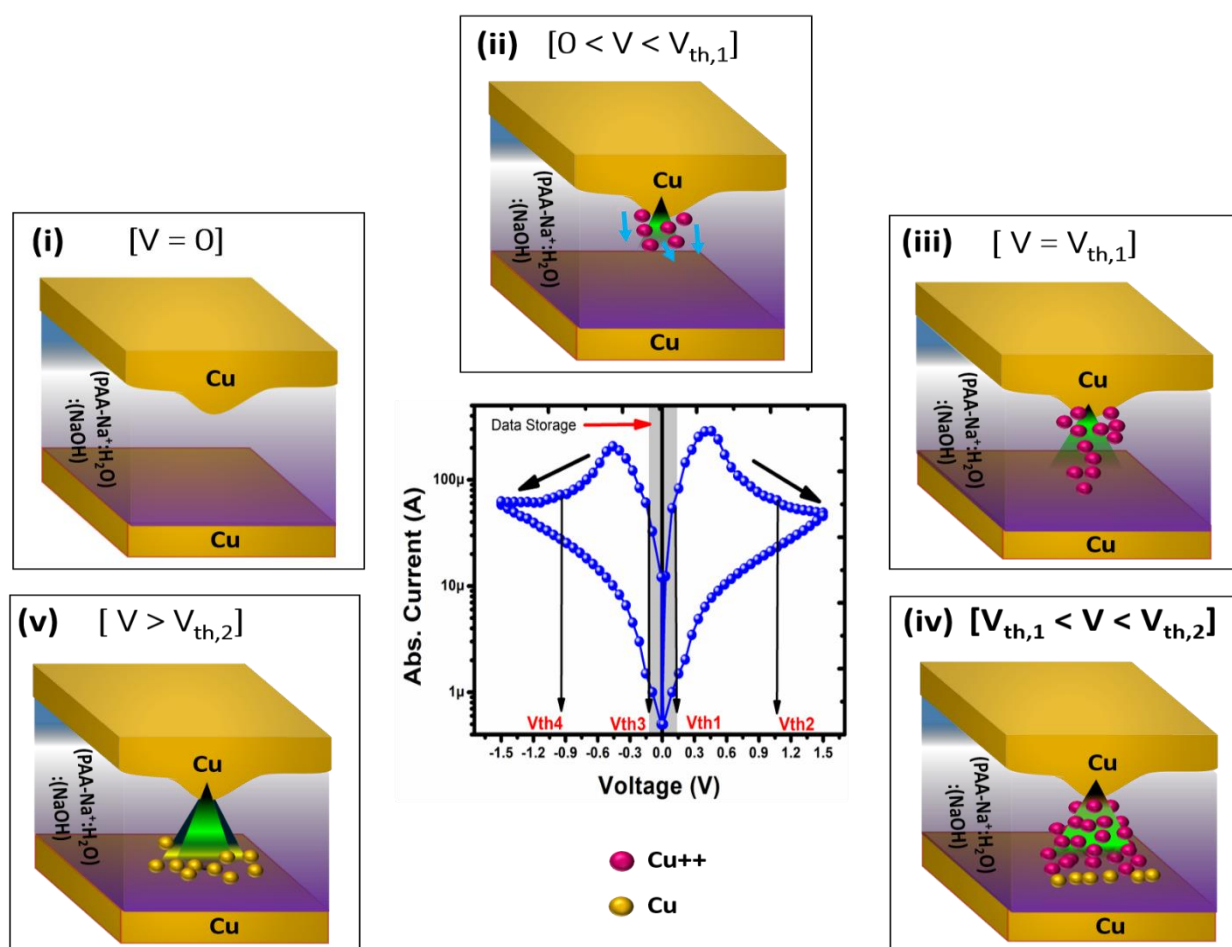


Figure 2.17. Schematic presenting the complementary resistive switching mechanism, and the corresponding semi-log I-V curve.

The flexibility is mainly due to the use of IL and soft material substrate, which can easily be bent as shown in Fig. 2.18a and 2.18b. The IL can be made in any dimension and design. The IL was filled in PDMS cylindrical microchannel, and two electrodes are sealed to avoid liquid leakage. This experiment part just based on demonstration of the device bending, which can open a gateway for future IL device structures to intergrade in soft electronics. The thickness, length, and flexibility could be designed according to device application. The Cu wire were used for electrode at both ends. The composite of PAA- Na^+ gel in 50 wt.% in water and 10 M of NaOH in water were mixed in 1:1 and filled in cylindrical microchannel as a switching medium. The soft IL device shows stable resistive switching behavior even while bent as shown in Fig. 2.18c. The traditional resistive memory devices filament is strongly depending on electrode structure. On the other hand, the soft IL resistive memory device design can be formed in different dimensions and with flexible structures in curved shape. The soft IL can be operated in different flexible design because switching medium is liquid, which provides versatility in device bending.

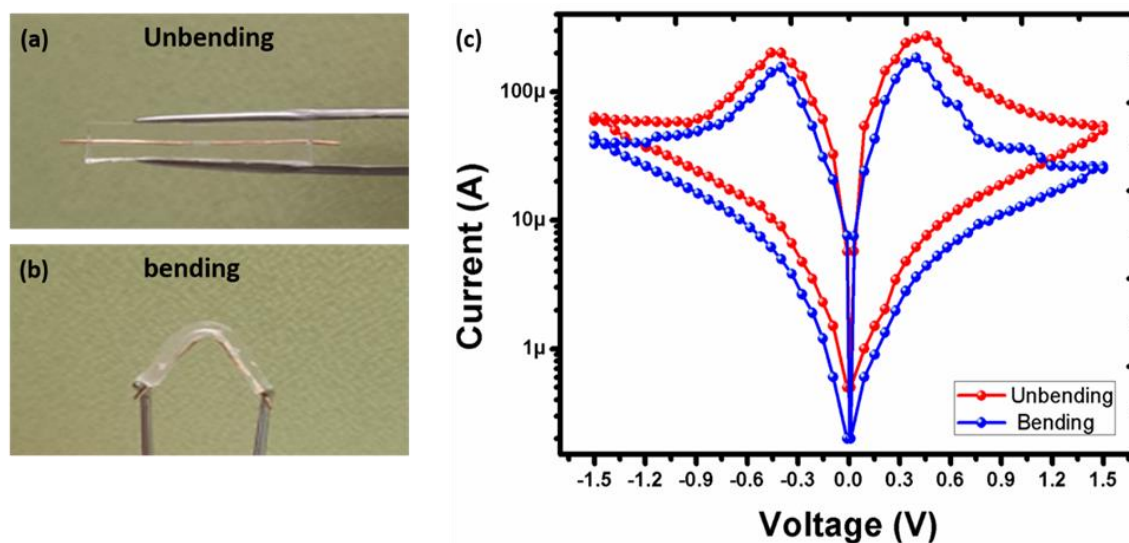


Figure 2.18. Photographs of the proposed IL resistive memory device in (a) unbent and (b) bent states. (c) Their I–V curves.

2.5.3 Summary

In the current work, an ionic-liquid-based soft resistive memory device using a cylindrical channel with a Cu/(PAA-Na⁺:H₂O):(NaOH)/Cu structure was developed. We explored the impact of electrode spacing, electrode size and blending ratio of the IL on device R_{off}/R_{on} ratio, device stability, an endurance. The mechanism of the developed device was proposed to involve ion concentration polarization, and the device mainly operated based on oxidation and reduction. The device stably operated at very low voltages of ± 1.5 V. The proposed device has demonstrated the high endurance (500 cycles) and retention time (10^4 sec) performance with R_{off}/R_{on} ratio of 201.507. According to these results, our investigation is expected to lead to the development of new soft ionic liquid devices for various applications.

Chapter 3 Neuromorphic Resistive Memories

3.1 Introduction

Novel memory device technologies hold significant promise in providing new capabilities and opportunities for synaptic devices of the neuromorphic hardware. The synaptic memory devices are required to have high integration density, fast read speed, and low power. More importantly, the device imitating the characteristics of synapses needs to be a non-volatile storage, capable of expressing multiple levels of synapse strength, and easy to implement synaptic learning[55]. Memristor devices have been widely researched because the devices have such desirable characteristics. Memristor is two terminals passive circuit element except it can change its resistance between two states HRS & LRS and retain the state in absence of power[56]. This very feature makes the memristor an attractive circuit element to perform neuromorphic computing.

3.2 One Directional Engineered GaN Resistive Memory Device for Electronic Synapses

Resistive memory device was firstly proposed by Leon Chua in 1971, which becomes an emerging technology, that plays a great role for future memory technology[56]. In 2008, memristor was the first time released by St. Williams in HP lab[54]. After this, new materials were introduced for memristor3 fabrication and optimization, including biomaterials, soft materials, 2D materials, and metal oxides[38]. Different device structures are proposed to fabricate memristor on a larger scale in a crossbar array¹⁰, including active layer based on single material, and composite or heterojunction of two materials[40, 57]. However, the crossbar array is facing a sneak current problem. To reduce the crosstalk effect in a crossbar array, different solutions are proposed which include transistor-memristor, diode-memristor, Schottky-diode memristor, and anti-serial memristor[14, 58]. Although these proposed architectures have been addressed to overcome the sneak current problem in a crossbar array, and further investigation is required to control power consumption and cross talk problem. On the other hand, one directional resistive memory devices are also very helpful to achieve a human-brain-mimicking system in a crossbar array to investigate the spike-rate-dependent plasticity (SRDP) and spike-timing-dependent plasticity STDP[59]. Synapses are the widely spread connection in the human brain as shown in Fig. 3.1a, where nerve cells communicate with each other via synapse[59].

During the learning process, different kinds of electrical activities occur among pre and post synaptic neurons and result in the generation of post-synaptic potential[60]. The flow of ions helps to adjust the synaptic weight during postsynaptic potential. The ionic flow (Na^+ , Mg^{2+} , Ca^{2+}) is the main reason for the learning and forgetting behavior. Similarly, the neuromorphic memristor (Neuromem) device must emulate the synaptic plasticity that can be tuned due to its tunable analog resistance behavior similar to the synaptic weight of biological synapses[61]. Various resistive memory devices have been investigated which including phase-change resistive memory, ferroelectric resistive memory, and resistive random-access memory (RRAM). The RRAM devices can be considered the most suitable neuromorphic candidate, with a simple device structure and easy to integrate on a large scale area[62]. The memristor changes its conductance on a specific value of input pulses, and this change is the counterpart of synaptic weight change of the synapse. Memristor can be used as a neuromorphic device, it exhibits an incremental (analog) switching instead of a digital switching[63] as shown in Fig. 3.1a. The overall efficiency of analog resistive switching in a neuromorphic application depends on operational speed, the number of resistance levels, and power consumption. Numerous materials are used to achieve neuromorphic behavior, and these devices cause unintentional leakage current paths in the crossbar array, results in a misreading within the read cells, namely the crosstalk effect. To solve crosstalk problem, one directional asymmetric memristors are preferred in a crossbar array. This means that asymmetric neuromorphic device can pass information directionally from a pre-synaptic to a post-synaptic cell[64]. The GaN is used as a resistive memory element on the top of the Schottky diode (ITO/ZnO) to achieve one directional resistive memory device as shown in Fig. 3.1b. The atomic layer wurtzite structure of ZnO and GaN is shown in Fig. 3.1c. The GaN is one of the most promising materials for power electronics with high electron mobility and band gap of ~ 3.3 eV with the lowest unoccupied molecular orbit (LUMO) ~ -3.1 eV and highest occupied molecular orbit (HOMO) ~ -6.4 eV, which can help to improve switching frequency, system volume, and energy conversion efficiency in electronic devices. The GaN film can be deposited by chemical vapor deposition (CVD), pulsed laser deposition (PLD), and molecular beam epitaxy (MBE). These deposition technologies are based on complex processes and are expensive. For this work, we have used the sputtering technique for the deposition of ZnO and GaN thin film. Among all PVD deposition, sputtering is used to make memristors in most cases because of their excellent film quality due to its simplicity, low cost, and large-scale deposition. We easily control the morphology, crystallinity, thickness, and surface roughness by tuning the sputtering parameters such as power, pressure, temperature, and gas ratio.

This work reports compliance and electroforming free asymmetric resistive memory behavior. On the other hand, the electroforming step requires a large voltage with higher power consumption and device-to-device variance is also very high and electroforming failure leads to low switchable yield. In terms of technology reliability and advancement, it is highly desirable to eliminate the electroforming step. To introduce electroforming and compliance-free with stable one directional switching performance, we report an engineered asymmetric resistive memory device[64].

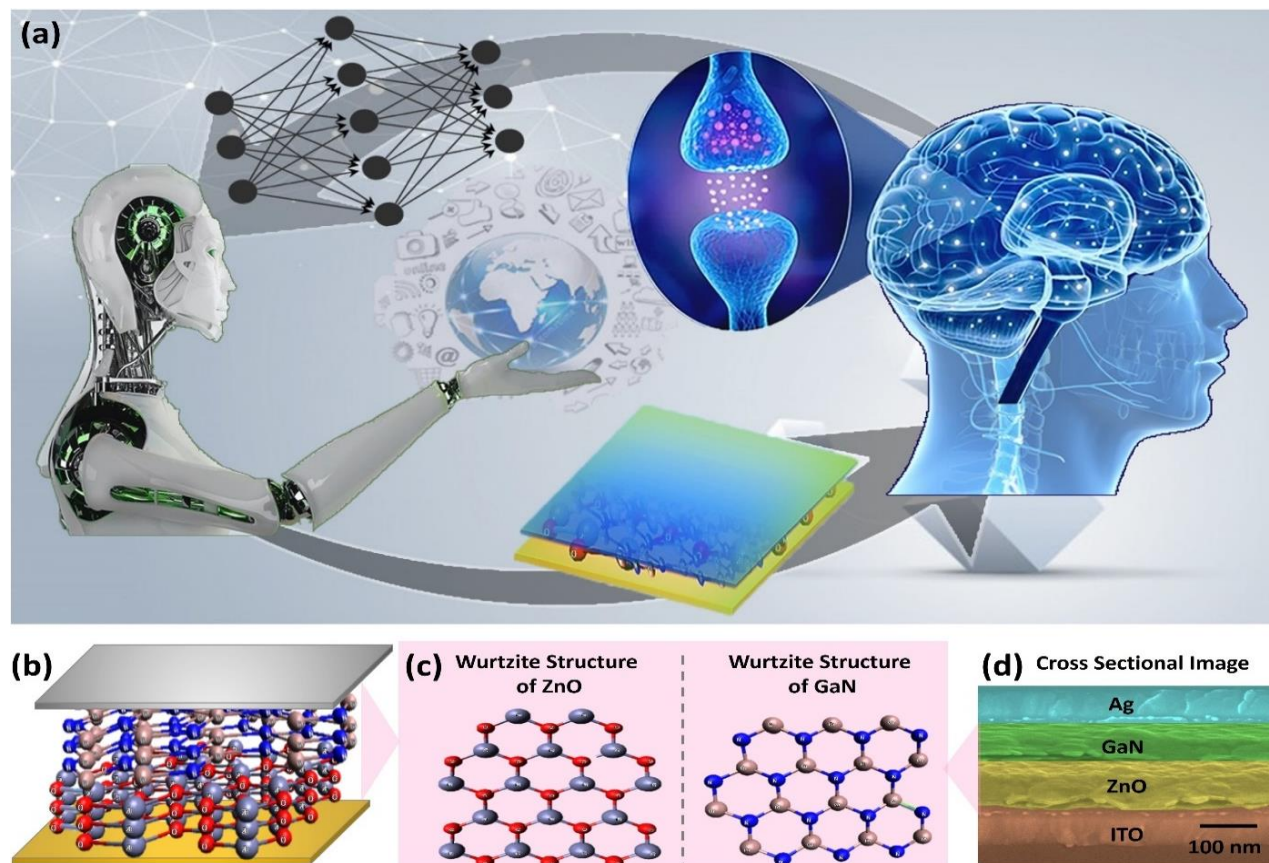


Figure 3.1. The memory computing architecture can be related to human-brain-spiking system with future technology based on neural networking to process robotic technology. (b) Vertical structure of single memristor cell. (c) The Layered atomic structure of ZnO and GaN. (d) Cross-sectional SEM image.

3.2.1 Experimental and Methods

The fabrication process of the device consists of the following steps: ITO glass served as a substrate, after going through the cleaning process, the fabrication of the device was followed by 100 nm ZnO thin film deposition by RF sputtering technique. Pure ZnO target with the gas ratio of Ar and O₂ (18:2) sccm at the maintained pressure of 3 mT by applying RF power of 120 W was used during the growth process. For the deposition of GaN here we used simple DC and Pulsed Modulated DC Magnetron Sputtering.

The liquid Gallium (Ga) target (99.9%) was utilized during the deposition and base pressure of 1×10^{-6} Torr was pumped. For the optimal growth of GaN thin film by Pulsed DC sputtering the gas flow rate of N₂ 41 sccm and Ar 9 sccm. During the sputtering process, substrate was heated at 450°C and the chamber pressure was maintained at 7.5 mT with a pulse width of 70 μs and power of 70W. For DC Sputtering, the pressure was maintained at 10 mT with the gas ratio of N₂ 45 sccm and Ar 5 sccm. The substrate temperature was maintained to 450°C with an average power of 80 W, respectively. For the deposition of Ag electrodes, RF magnetron Sputtering was used at the rate of 0.6 nm/s layers. Firstly, pumped down the sputtering chamber by creating an ultra-high vacuum. During the deposition, power of Radio Frequency (RF) source, the temperature of substrate, and gasses pressure were maintained at 240 W, 300 K, and 10^{-4} Pa.

3.2.2 Characterization

TESCAN MIRA 3 scanning transmission electron microscope (STEM) is used to investigate the surface morphology of GaN and ZnO and cross-sectional of the fabricated device. A non-contact surface profiler NV-2000 was used to analyze the height profile of the top electrode. Raman Spectrum of GaN and ZnO was measured by HORIBA LabRAM HR confocal spectrometer, the laser was shined on the surface of the sample with the excitation wavelength of 325 nm. The crystalline and polycrystalline nature of GaN was recorded by X-ray diffraction pattern (XRD) Empyrean (PANalytical) diffractometer using CuK α radiation of wavelength $\lambda=1.5406$ nm. XPS Spectrum of the memristive device was measured by PHI 5600 (Physical Electronics) with the source of Al X-ray monochromator. The I-V and neuromorphic pulse characterization was performed using the KEYSIGHT B2902A source measurement unit.

The cross-sectional SEM is shown in Fig. 3.1d, showing the thickness of the top electrode ~ 90 nm. The sputtered film of ZnO and GaN shows the thickness of 110 nm and 100 nm, respectively. Raman spectroscopy provides a detailed investigation of materials, such as the presence of phases (amorphous or crystalline) and the impact of different stress states and defects. In the hexagonal wurtzite structure of ZnO, there are four atoms per unit cell, which relates to 12 branches of phonons, consisting of three acoustic and nine optical modes. Fig. 3.2a shows the ZnO thin film pattern of Raman spectra deposited on ITO substrate. Two main Raman modes can be seen in the spectra at 436 cm^{-1} and 578 cm^{-1} , which is the presence of E₂ (high) and A₁ (LO) modes that confirm the wurtzite crystalline ZnO structure[44].

The Raman spectra of GaN show only two active phonons of E2 (high) at 567.6 cm^{-1} and A1 (LO) at 735.2 cm^{-1} as shown in Fig. 3.2b. The E2 (high) mode can help for finding the strain/stress within materials. The sputtered GaN shows a shift in the E2 (high) indicating the compressive stress in GaN thin film[65].

For the further structural investigation of GaN/ZnO bilayer, the XPS technique with depth profile scans was performed up to 250 nm with monochromatic radiation of Al K α (150 W). We are explaining here only bulk elements, the ZnO and GaN. The Zn 2p $_{3/2}$, O 1s, Ga-3d, and N 1s peaks are found in the spectra. Fig. 3.2c presents the typical XPS spectra fitting of the lower binding energy peak of ZnO that is found as Zn 2p $_{3/2}$. The little abnormality of the score line is credited to the presence of zinc excess in the film. The reported Zn 2p $_{3/2}$ core levels range is 1021.24–1021.81 eV, which is associated with Zn $^{2+}$ ions. The Zn 2p $_{3/2}$ binding energy electronic states are the same as the reported value of the bulk ZnO (1021.8 eV). As no metallic Zn peak was found, which confirms that Zn exists only in an oxidized state. Fig. 3.2d presents the XPS analysis of O 1s core-level provides the information of oxygen defect or positions of presence in the ZnO thin film. As reported, the major O1s peak in ZnO is composed of three small peaks located at 531.8 eV, 533.1 eV, and 534.4 eV. The lower binding energy peak around 531.8 eV is supposed to be the form of Zn–O bonds in the lattice oxygen of ZnO. While the second peak, located at ~533.1 eV is considered to be the generated form defects or O vacancies in the ZnO. The binding energy peak at 534.4 eV is ascribed to the adsorbed oxygen species found in the environment. On the other hand, the XPS spectra Ga-3d of GaN are shown in Fig. 3.2e. The peak of Ga 3d is comprised of three peak fitting, central peak at binding energy 20.15 eV and the other two smaller peaks are located at 17.54 eV and 20.96 eV. The central incidence peak at 20.15 eV approves the bonding between Ga elements and N atoms, forming the GaN bond. On the left side, the smallest peak at 17.54 eV signifies the existence of metallic Gallium (Ga–Ga) in the sample which did not interact with the N species. The other small peak at 20.96 eV could be credited to Ga–O bond development in GaN $_{51}$. Meanwhile, the grown GaN sample was exposed to the ZnO layer. As the device temperature was so high the oxygen on the surface of ZnO interact with Ga metals and form the Ga–O interfacial layer. The N 1s spectra peak and its fitting are shown in Fig. 3.2f. The N-1s core level shows three unlike peaks adjusted at 397.7, 395.65, and 393.06 eV. The peak binding energy at 397.7 eV is consigned to N due to bonding with Ga, while the other two peaks are recognized for Ga Auger LMM alterations[65, 66].

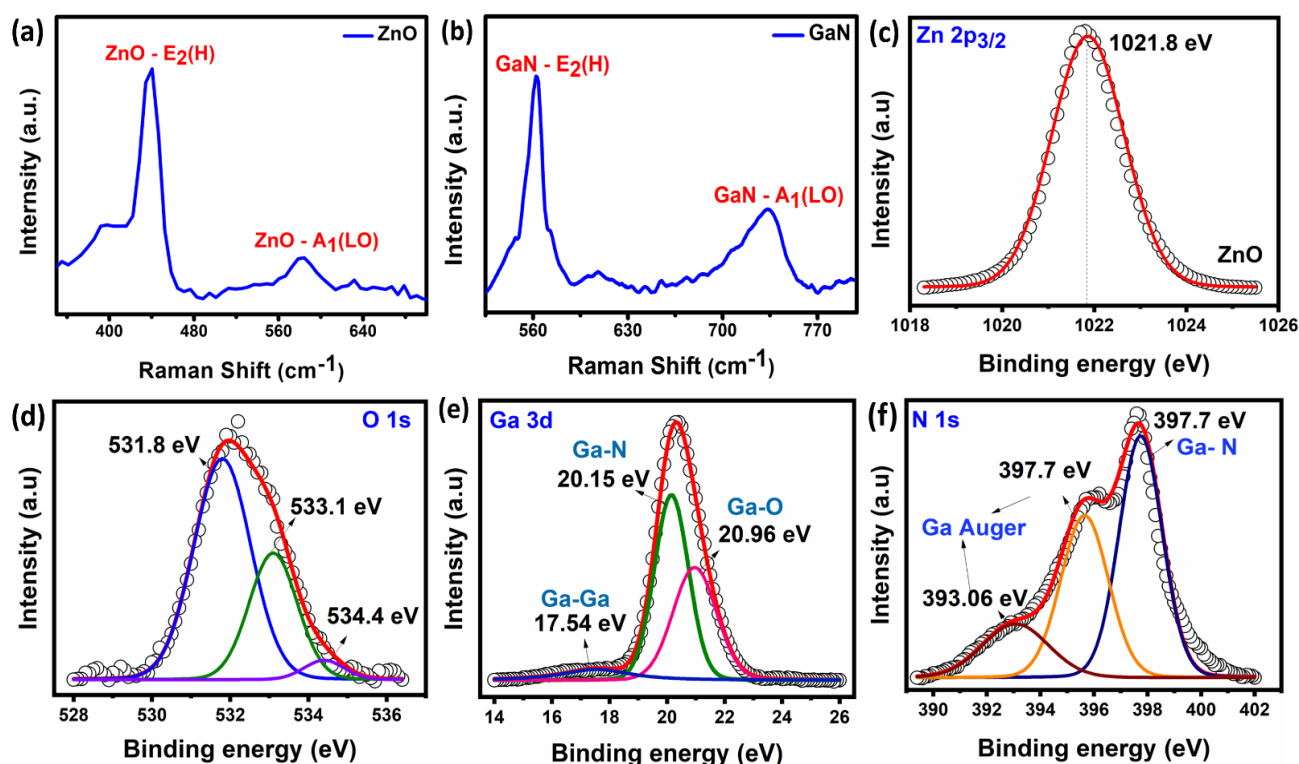


Figure 3.2. The Raman spectrum of (a) ZnO and (b) GaN. XPS core level spectra peaks fitting of (c) Zn 2p_{3/2}, (d) O 1s, (e) Ga-3d and (f) N 1s.

3.2.3 Result and Discussion

To solve sneak current problem Schottky diode (ITO/ZnO) is used as shown in Fig. 3.3a. The Schottky diode significantly helps to block the sneak current problem in the negative voltage region and at the same time helps to reduce the current flow. To block sneak current, crystalline GaN film on top of ZnO was applied. Fig. 3.3b shows Pulsed modulated DC sputtered GaN with the peaks at $2\theta = 34.47^\circ, 48.26^\circ, 63.26^\circ,$ and 68.83° indicating that the Pulsed modulated DC sputtering have higher crystalline behavior, due to sharp c-axis orientation of (002) peak with FWHM value of 0.508253. The pulsed sputtered GaN films which indicate better quality of GaN thin films like lattice strain and dislocation density values are 0.0071% and 0.0034 line/m². GaN thin film prepared by Pulsed Modulated sputtering shows less strain value and less value of dislocation length compared to DC sputtering, indicating good quality of GaN film.

To investigate symmetric resistive switching behavior to block sneak current in the ITO/ZnO/GaN/Ag device, a double voltage sweep was applied at ± 4 V as shown in Fig. 3.3c. In the positive voltage region, the device shows $R_{\text{off}}/R_{\text{on}}$ ratio ~ 81.02 at a reading voltage of $V_{\text{read}} \sim 0.89$ V, and in the negative voltage region device shows $R_{\text{off}}/R_{\text{on}}$ ratio ~ 1.2 at a reading voltage of $V_{\text{read}} \sim -0.89$ V as shown in Fig. 3d.

The asymmetric device endurance for more than 500 cycles is recorded at a reading voltage of $V_{\text{read}} \sim 0.89$ V as shown in Fig. 3.3e and insert Fig. 3.3f showing I-V sweep cycles. The ZnO and GaN heterojunction can be presented in the form of the LUMO, and HOMO as shown in Fig. 3.3g. The ZnO and GaN have different depths between HOMO and LUMO due to different depths in potential barriers. As shown in Fig. 3.3g, the LUMO and HOMO values of ZnO (-4.3 eV and -7.5 eV), and GaN (-3.1 eV and -6.4 eV) and work function of Ag and ITO -4.2 eV and -4.7 eV, respectively. The barrier height between ZnO/GaN is -1.2 eV and ITO/ZnO barrier height is 0.4 eV only, while GaN/Ag band offset is 1.1 eV as shown in Fig. 3.3g. Hence, GaN and ZnO act as donor and acceptor, respectively as result electrons will move from LUMO of the ZnO to LUMO GaN or LUMO of the GaN to LUMO of ZnO, depending on the polarity.

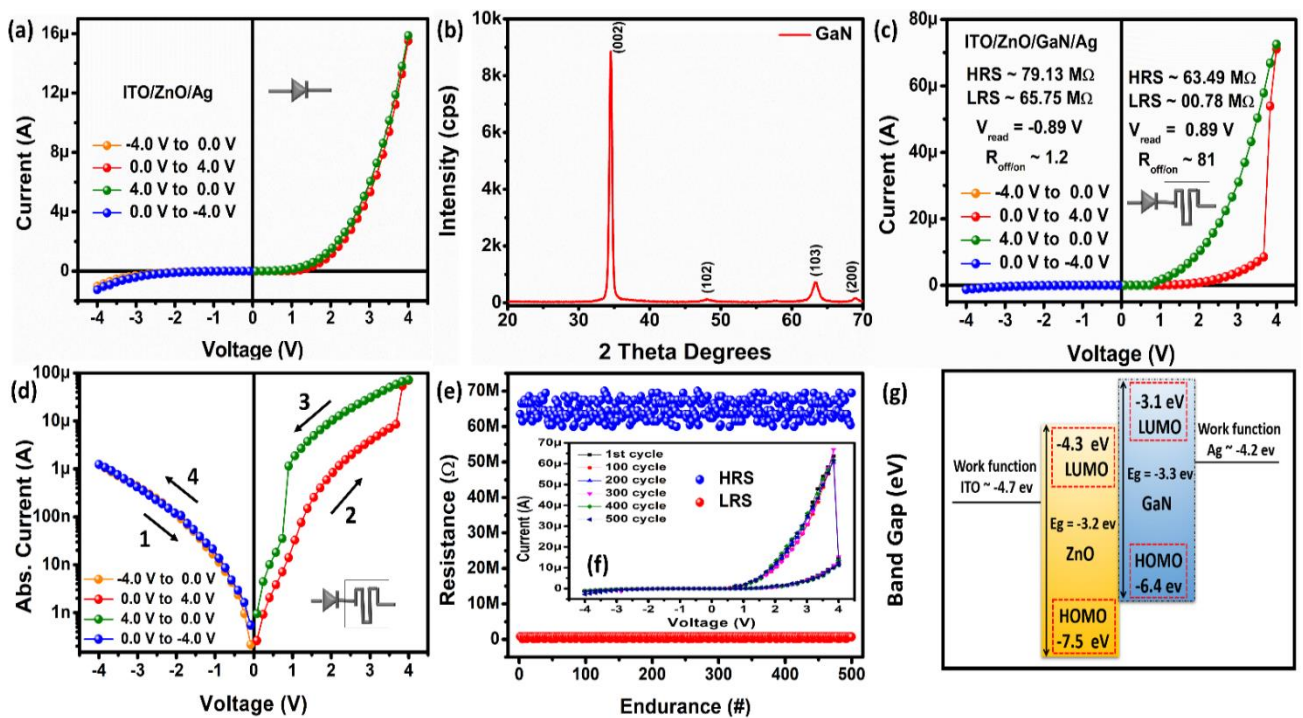


Figure 3.3. (a) I-V curve ITO/ZnO/Ag Schottky diode. (b) Pulsed modulated DC sputtered XRD of GaN. (c) I-V curve of ITO/ZnO/GaN/Ag, (d) semi-log I-V curve showing asymmetric behavior. (e) The device endurance between HRS and LRS and (f) 500 I-V sweep cycles. (g) The bandgap diagram showing energy levels.

The transmission process of the neurotransmitter in the human brain initializes the synaptic plasticity between the pre and post synaptic neuron as depicted in Fig. 3.4a. Similarly, the resistive memory device can also use to perform the electronic synapses by applying input stimuli of signal. To achieve synaptic behavior, we used polycrystalline GaN film on top of ZnO. Fig. 3.4b shows the XRD pattern of GaN with wurtzite structure, here we used the DC Sputtering technique which reveals the Polycrystalline behavior with the peaks at $2\theta = 32.32^\circ, 34.46^\circ, 36.7^\circ, 57.56^\circ,$ and 68.86° with an increase in FWHM value of 0.6588 . For simple DC sputtering, 14 nm, 0.0051 line/m², and

0.0093%, are the calculated values for average crystallite size, dislocation density, and lattice strain of 002 peaks. Polycrystalline GaN based on DC sputtering helps to create a high number charge trap in an active layer, which helps to achieve multistate resistive behavior.

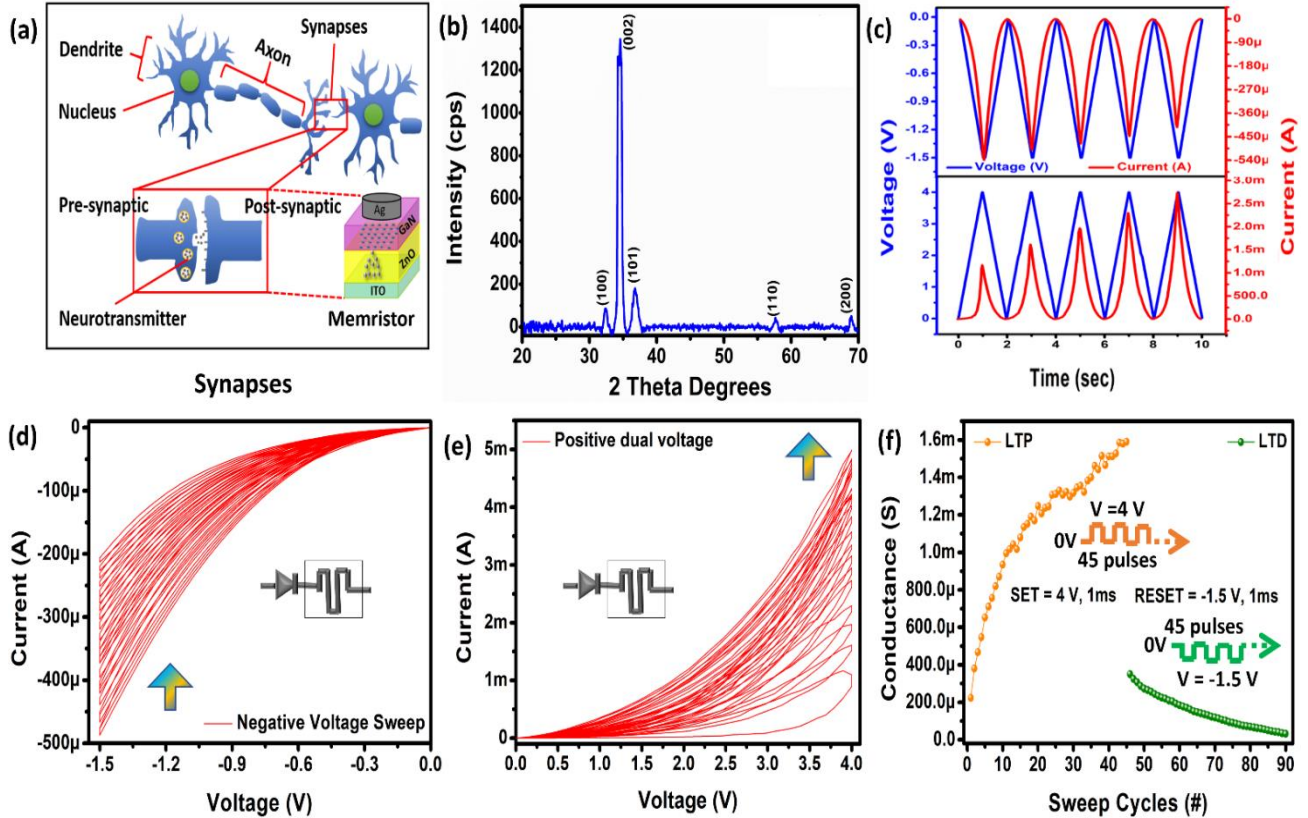


Figure 3.5. (a) Resistive synapse in GaN/ZnO heterojunction illustrating the synaptic response similar to biological synapses. (b) DC Sputtered XRD of GaN. (c) The triangular voltages response to investigate the device tunability. The I-V of (d) positive and (e) negative voltage sweep showing multistate resistive switching behavior. (f) The synaptic plasticity against pulse train of 45 long-term potentiation pulses of 4 V and long-term depression pulses of -1.5 V with a pulse of 1 ms.

Fig. 3.4c shows five triangular voltage sweeps with a period of 2 sec, which shows the increase in conducting current on positive and decreases on negative voltage sweep region. We can see that the device current nonlinearly increases on the positive and decreases on the negative voltage sweep region, respectively with the number of consecutive five triangular voltage pulses. The device under positive and negative voltage sweep shows multistate resistive switching behavior as shown in Fig. 3.4d and e. The negative dual-sweep voltage is applied from 0 V to -1.5 V to 0 V, the device shows anticlockwise multistate resistive switching behavior as depicted in Fig. 3.4d. The conductance of the device decreases, and the resistance state increases with an applied voltage sweep as shown in Fig. 3.4d. During the positive voltage sweep from 0 V to 4 V to 0 V the device shows clockwise multistate resistive switching behavior as shown in Fig. 3.4e. The conductance state increases, and the resistance of the device decrease during continuous voltage sweep as depicted in Fig. 3.4e.

The analog I-V characteristics also confirm the one directional switching behavior, in which positive voltage shows a much higher current in a range of mA, on the other hand, negative voltage region current limits to uA, due to Schottky barrier of ITO/ZnO, which helps to block cross talk effect in a crossbar array. The 45 long-term potentiation (LTP) and long-term depression (LTD) pulses with amplitude +4 V and -1.5V, respectively, are measured under pulse width and interval of 1ms, as shown in Fig. 3.4f.

Further, the time interval dependence was analyzed in device ITO/ZnO/GaN/Ag. A gradual current increase by applying 45 identical pulses with different pulse intervals of 1 ms, 5 ms, 10 ms, and 15 ms, and pulse height in each case is 4 V by keeping the constant pulse width of 1ms, in which stimulation with a time interval of 1ms shows the higher increase in current as compared to stimulation at 15 ms as depicted in Fig. 3.5a. The conducting current values are tunable according to the different pulse widths by keeping the pulse height of 4 V as shown in Fig. 3.5a. The neuron releases Na^+ , Mg^{2+} , Ca^{2+} ions during pre-synapse stimulation, which increases the synaptic transmission, and if another identical stimulation acts during relaxation time, then post synapse stimulation will be larger, and this process is known as pulse-paired facilitation (PPF). Similarly, for post-tetanic potentiation (PTP), continuous release of ions stimuli causes the increase in postsynaptic stimulation[67, 68].

The current increase (ΔI) is calculated to investigate the PPF and PTP for different pulses with different pulse intervals and constant pulse height as shown in Fig. 3.5b. The $I_n - I_1$ equation is used to calculate the increase in current (ΔI), where $n = 1, 2, 3, 4, \dots \dots 45$), where $I_2 - I_1$ is PPF and $I_{45} - I_1$ is PTP. The PPF is calculated by $I_2 - I_1$ for the pulse intervals of 1 ms, 5 ms, 10 ms, and 15 ms as following 6.25002×10^{-4} A, 1.9933×10^{-4} A, 6.0076×10^{-5} A, and 3.0372×10^{-5} A and PTP analyzed by $I_{45} - I_1$ as following 0.0055 A, 0.00308 A, 0.00149 A, and 9.12945×10^{-4} A, respectively as shown in Fig. 3.5b. The PPF index (%) trend decreases by the pulse interval from 1ms to 15 ms. The smaller pulse intervals (1 ms) have the greater value of PPF index (%) as shown in Fig. 3.5c.

Similarly, higher voltages (4 V) with the same pulse interval can give us the same trend with current modulation. The current change in pulse trains with voltage heights of 2.5 V, 3 V, 3.5 V, and 4 V by keeping the constant pulse width and interval of 1 ms as shown in Fig. 3.5d. The PPF values for the pulse height of 2.5 V, 3 V, 3.5 V, and 4 V are 6.25002×10^{-4} A, 3.0094×10^{-4} A, 1.9933×10^{-4} A, and 1.22306×10^{-4} A and the PTP values are 0.00557 A, 0.00425 A, 0.00313 A, and 0.00222 A, respectively as shown in Fig. 3.5e. The PPF index (%) trend decreases by varying the pulse voltage from 4V to 2.5V and pulse interval and width of 1ms are kept constant as shown in Fig. 3.5f.

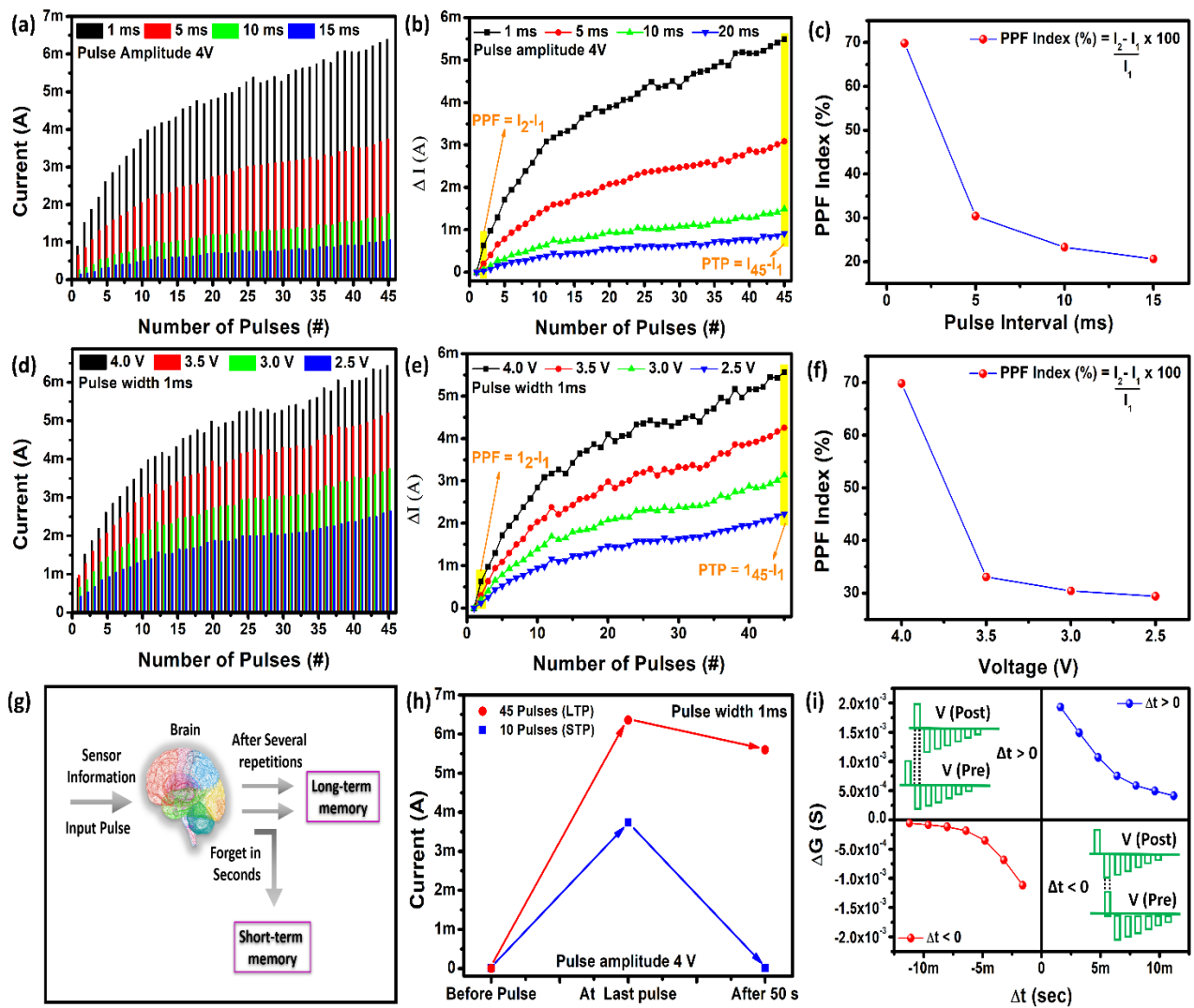


Figure 3.5. (a) The synaptic behavior of the device for different pulse intervals, and (b) the ΔI plotted with the different pulse intervals to calculate PPF and PTP. (c) PPF index (%) as a function of interval time. (d) The stimuli response different pulse voltage and (e) the ΔI calculated from different pulse heights, to calculate PPF and PTP. (f) PPF index (%) as a function of voltage. (g) The brain learning and forgetting mode are based on STM and LTM. (h) The STP under consecutive 10 pulses and the LTP under consecutive 45 pulses to observe the change in conductance to observe the forgetting behavior. (i) The experimental STDP results showing antisymmetric Hebbian.

The Atkinson and Shiffrin brain model based on long term memory and short-term memory is shown in Fig. 3.5g. The synapses of the device go through short-term plasticity (STP) at 4 V with an increase in current with weak stimulation as shown in Fig. 3.5h by applying 10 successive presynaptic stimulation with pulse width and interval of 1ms. This process results in weak stimulation and current decay down to zero in a very small-time interval and this behavior is known as short term potentiation (STP). The (higher) 45 input sequence of electric identical pulses improves SRDP for a longer time, this process gives rise to the synaptic conduction from STP to LTP as shown in Fig. 3.5h with high stability.

The practicability of the neuromorphic device can be realized with the STDP rule. We performed an anti-symmetric Hebbian rule using the pulse train consist of different amplitudes +1.2, -1.0, -0.8, -0.6, -0.4, 0.2, and -0.1 as given in Fig. 3.5i, where the pulse width is 600 μ s and pulse off interval is 1 ms. The pre and post synapse pulses combined with respective relative time intervals Δt as post - pre synapse, which results in the device conductance strengthening or weakening. During $\Delta t > 0$ synaptic weight increases, which results in potentiation, and conversely, for $\Delta t < 0$, synaptic weight decreases (depression). Fig. 3.5i shows the anti-asymmetric Hebbian rule of the resistive memory device. The STDP behavior of ITO/ZnO/GaN/Ag resistive memory device successfully performed Hebbian rule similar to biological synapses[69-71].

To understand the movement of electrons, the mechanism based on metallic ions and vacancies as a switching model is designed for neuromorphic type I-V switching of Ag/GaN/ZnO/ITO device as shown in Fig. 3.6. During the deposition process of GaN on the ZnO layer, the Ga metal from GaN combines with oxygen atoms due to high temperature and generates an interfacial layer between ZnO and GaN interface layer which causes the formation and rupture of filament. Some evidence of the chemical structure of the device is given in XPS analysis. By applying the positive voltage on the top electrode and Ag is reduced as $\text{Ag} \rightarrow \text{Ag}^+ + \text{e}^-$ and on the same time, the metallic ions move toward the bottom electrode. These ions easily pass through a minor interface barrier and arrive GaN layer to ZnO, respectively. The decrease in barrier height between Ag and GaN was due to the applied positive voltage on TE Ag. At the same time, the electrically injected electrons and the negatively charged oxygen vacancies drift from the BE ITO towards the Ag/GaN top interface layer. It is reported, the carriers injected from ITO contact at higher voltages present enough energy to overcome the potential barrier of ITO-ZnO, demonstrate the FN behaviour. According to the literature, we purposed the switching model of metallic ions and oxygen vacancies based presented in Fig. 3.6. When we apply the positive voltage to set the device, the vacancies through the BE move towards the TE and cause filament formation in the ZnO layer while Ag ions move towards the BE through the GaN traps. The attraction between ions and vacancies at the interfacial layer causes the complete filament path into the GaN/ZnO active layer through which electrons easily pass from anode to cathode. On every cycle, the Ag ions start to diffuse into the oxygen vacancies, and the remaining oxygen vacancies move through the interfacial layer towards the cathode by filling the traps in GaN one by one, and the current density increase on every cycle. Similarly, when we apply the negative charge on the TE, the Ag metallic ions attract towards the top surface and stop there while the oxygen vacancies drift towards the BE through the traps. It causes the rupture of filament at the interfacial layer of ZnO and GaN.

As the filament was very thicker till the last SET process. So, during the RESET process, the traps become unfilled one by one on every cycle, and current density decreases, as shown in Fig. 3.3f. This happens because of the diffusion of metallic ions on each cycle at the top electrode.

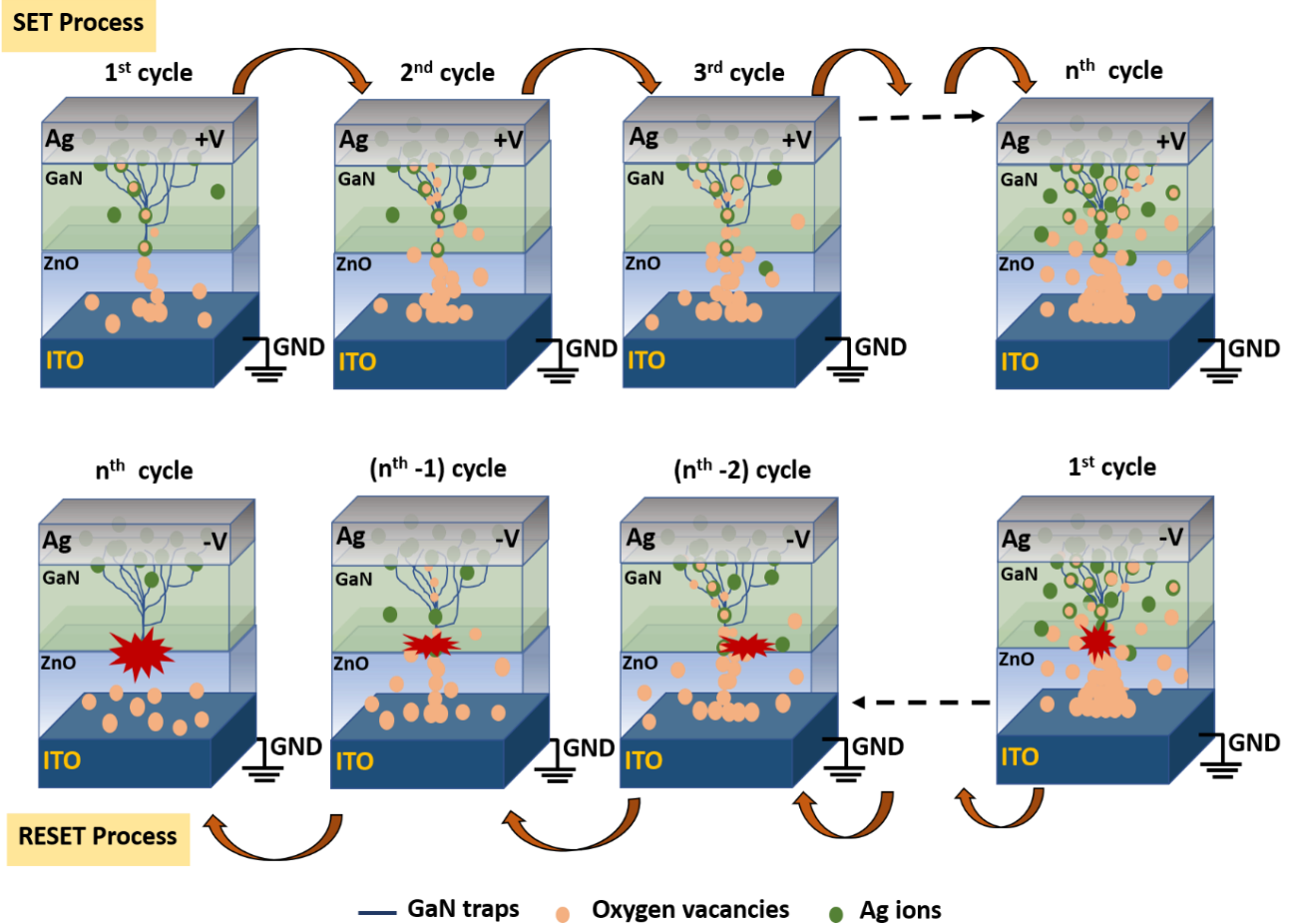


Figure 3.6. Switching mechanism model for a neuromorphic-based device (ITO/ZnO/GaN/Ag).

The device shows stable cycle-to-cycle endurance repeatability, which is one of the most important parameters for on-chip training as shown in Fig. 3.7a. The LTP and LTD data were analyzed at a read voltage of 1 V with a pulse width of 1ms and write voltage of 4 V and -4 V with a pulse with 1.5 ms, respectively, where the maximum conductance and minimum conductance are 5.20×10^{-4} and 7.18×10^{-5} , respectively as shown in Fig. 3.7b. The LTP and LTD data were applied to take MLP_Neurosim_V3.0 code for deep learning[72-74]. Here, the pursuit simulation model is a cross point with analog crossbar parallel read-out, which is composed of one memristor for each cell. Neurosim deep learning structure is composed of 2-fully-connected layers. In neurosim, device behavioral model is used to analyze nonlinear weight update. The A parameters for LTP and LTD are 0.5077 and 0.5996, respectively. the fitted lines of LTP and LTD are illustrated in Fig. 3.7c. Based on that A parameter, we estimate the analog weight nonlinearities for LTP and LTD.

The analog weight nonlinearities (NL) are approximately 2.36 for LTP and -2.03 for LTD from nonlinearity normalized value from Fig. 3.7b values. The training data is composed of MNIST (Modified National Institute of Standards and Technology database), and the epoch is 200. For a neuromorphic simulation based on these data, input data is normalized 20 x 20 cropped MNIST, the hidden layer is composed of 100 neurons and the output layer is composed of 10 neurons corresponding to 10 numbers classified[72-74] as shown in Fig. 3.7d, and training simulation is operated based on these parameters. As the simulation result shown in Fig. 3.7e, for the proposed real device, the maximum network learning accuracy is converged to 89.38%, and the epoch number converged on 86.3% is 35. In the case of the ideal device, the maximum network learning accuracy is converged to 91.85%, and the epoch number converged on 86.25% is 23 as shown in Fig. 3.7e. In the comparison, its accuracy is about 2% more than the proposed device and more fast convergence. Hence, the proposed device's performance was very close to the ideal case, although the ideal device used linear function as compared to the proposed device with non-linear function.

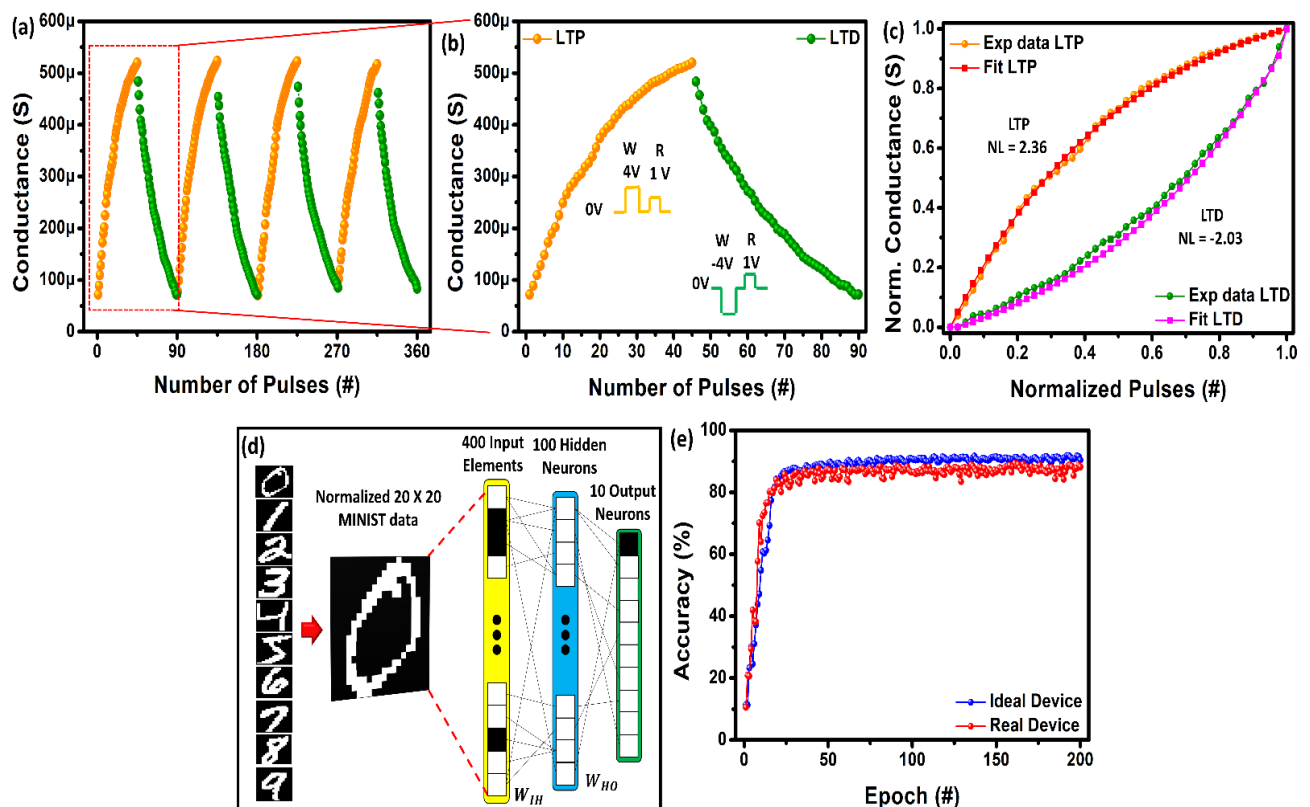


Figure 3.7. (a) Device endurance and stability performance. (b) The synaptic plasticity of LTP and LTD. (c) Analog device behavior of nonlinear weight update data, which represents the normalized conductance against a normalized number of pulses. (d) The neural network with a 2-fully-connected layer for neurosim simulation. (e) Simulation accuracy based on real and ideal devices.

3.2.4 Summary

In conclusion, this work reports engineered GaN in-situ Digital to analog resistive switching device fabricated to block sneak current in a crossbar array to perform neuromorphic computing. Under the applied voltage, the trapped charges in the active layer have migrated by hopping or tunneling from one defect to another until they reach the surface states, which resulted in multistate switching. To achieve the repeatable and stable synaptic behavior pulse was design to investigate the spike-timing-dependent plasticity. The device performance was analyzed by using neural network pattern recognition at the system level with an accuracy of 89.38%. The simulation part deepens the insight to reduce sneak current problem in a crossbar array. We are sure that these results deepen and broaden the concept of device engineering for the implementation of one-directional asymmetric deep memristive network.

3.3 Multistate Resistive Memory Device Based on GeO_2 for Electronic Synapses

A memristor is a non-volatile passive circuit element newly added into the circuit variable along with the previous resistor, inductor, and capacitor¹. The conventional charge storage-based memory devices suffer from limitations such as the current leakage issue and basic structural properties[70, 71]. Among others, the memristor is a prominent emerging candidate to replace conventional memory devices because of its easy fabrication process, good energy efficiency, and fast operation process. The non-volatile memory devices have also shown potential for applications such as smartphones, soft robotics, and wearable electronic applications[75]. Researchers report that the multistate resistive switching memory device could mimic neuromorphic computing[75]. The conductance modulation of memory device is distinguishing the potentiation and depression of the electronic synapse[71]. However, in biological neurons, the dominant neurotransmitter parameter controls the synaptic plasticity between pre-synaptic and post-synaptic neurons as shown in Fig. 3.8a. A similar resistive switching effect of the analog memory device can be seen on the application of appropriate active material sandwiched between two electrodes for performing neuromorphic computing. The analog memory device can be easily fabricated using different organic and inorganic materials, including a metal oxide, ferrites, biomaterials, and electrochemical memory devices[76]. The metal oxide materials have been widely used for various electronic applications (solar cell, memory, supercapacitor, and optoelectronic devices) due to their electrical, optical, and thermal properties[77].

On the other hand, the metal oxides show the dependency of structural and morphological properties of the materials on their electrical performance, which can be synthesized by using very low temp and cost-effective techniques besides achieving different morphological structures[77]. The resistive switching effect of the memory devices is dependent on the oxygen vacancies of the active materials and ion migration of the electrode[78]. The metal oxides having high oxygen abundance, which is helpful in the formation of filamentary conduction mechanisms[78]. Several conventional oxide materials such as TiO_2 , ZnO , etc., have already been reported for resistive memory device applications with different morphological structures[79]. Besides having the various advantages, metal oxide-based devices also have problems such as high input voltage for electroforming, low stability, and energy efficiency[33].

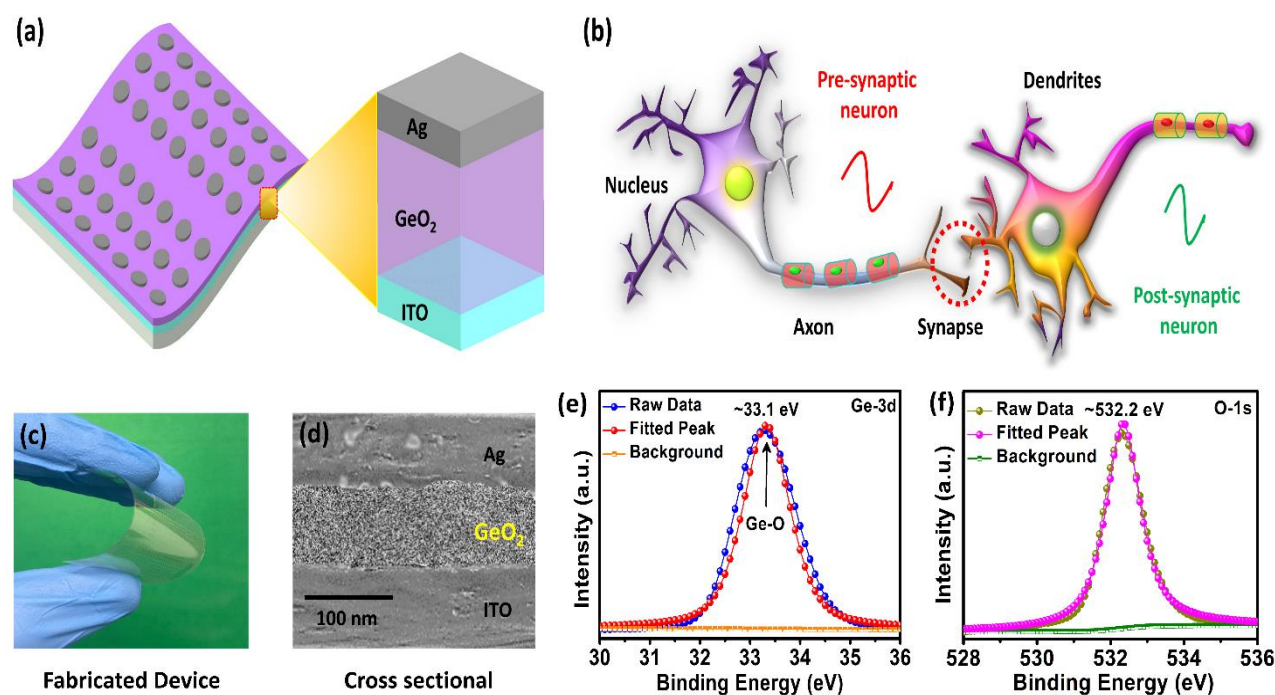


Figure 3.8. (a) Schematic of flexible artificial synaptic memristor with ITO/ GeO_2 /Ag structure. (b) Schematic diagram of biological neurons and synapses. The synapse is the connection between a pre-synaptic neuron and a post-synaptic neuron. (c) The photograph proposed a synaptic memory device on the flexible substrate. (d) Cross-sectional scanning electron microscopy (SEM) image of the proposed Ag/ GeO_2 /ITO device. XPS of Germanium dioxide showing (e) Ge-3d series in binding energy 30-36 and (f) O-1s series in binding energy 528-536.

To overcome these problems, new metal oxides are being studied to check out their performance in resistive switching memory devices. Among other metal oxides, hexagonal structured crystalline GeO_2 has exhibited excellent electrical, optical, and thermal properties[80]. In general, GeO_2 demonstrates various advantages such as low toxic and low-cost synthesis process. The abundance of Germanium and oxygen ions in GeO_2 is helpful regarding the formation of conduction filaments and redox-active reactions in resistive switching devices.

Besides these advantages, hexagonal crystalline GeO₂ also exhibits good thermal properties and high electrical stability, which are crucial for implementation in electronic devices. Herein we demonstrate Ag/GeO₂/ITO based resistive switching synaptic learning device as shown in Fig. 3.8a. The developed device demonstrated highly asymmetric resistive switching behavior and the double valued charge flux characteristic. The filamentary conduction of the device takes place due to Ag ion migration and oxygen vacancies. The stable electrical performance of the hexagonal crystalline structured GeO₂ clarifies the proposed material is a prominent candidate to develop the modern resistive switching synaptic learning devices.

3.3.1 Materials and Methods

The GeO₂ was purchased from Sigma Aldrich. The GeO₂ was dispersed into the ethanol with 10 wt% and placed on probe sonication for 10 min with 20 kHz frequency (Pulse on 1s and Pulse off 3s) to make the homogeneous solutions. ITO-coated PET substrate was cleaned by ethanol and kept into the ultraviolet (UV) treatment for 5 min to create roughness onto the ITO substrate. The dispersed germanium dioxide was deposited onto the ITO substrate by using the spin coating technique at 3000 rpm for the 30 s and then dried into the oven for 30 min at 80 °C. Finally, the top electrode of 100 μm was deposited by Ag epoxy. The cross-section view in Fig. 3.8d confirms that all layers are properly deposited.

3.3.2 Characterization

The XPS spectrum of the GeO₂ sample was measured by using PHI 5600 (Physical Electronics) with the Al K-alpha X-ray monochromator source. Raman Spectrum was measured by HORIBA LabRAM HR confocal spectrometer, equipped with 800 nm length monochromator, He-Cd laser was shined on the surface of the sample with the excitation wavelength 325 nm. The FT-IR of Germanium dioxide was analyzed through Bruker IFS 66 V. TESCAN MIRA3 STEM used to measure the SEM and EDS Mapping of GeO₂ thin film. The source measurement unit (KEYSIGHT B2902A) was used for I-V characterizations and synaptic measurements.

Fig. 3.8c shows the actual device, and the cross-sectional view of the device defines the layer structure of the proposed Ag/GeO₂/ ITO synaptic memory device in Fig. 3.8d. The GeO₂ is coated uniformly onto the ITO substrate by spin coating, and the Ag top electrode is firmly coated and well connected with the active material.

The X-ray photoelectron spectroscopy (XPS) analysis is shown in Fig. 3.9e-f. Adventitious C-1s peak was adjusted at 285.0 eV for the calibration of the absolute binding energy. Analysis of the Ge-3d core level line for the thin film signifies that full width at half maximum (FWHM) value of 1.41 eV with a dominant peak at ~33.1 eV of binding energy, and corresponds to Ge-O bonding as shown in Fig. 3.8e. Fig. 3.8f demonstrates the O-1s core-level line, which has an FWHM of 1.25 eV with the dominant peak at 532.3 eV corresponds to the adsorbed oxygen and other oxygen species to the surface of sample 39-41. Apart from chemical bonding, the analysis also describes the ratio of atomic concentration of Ga, N, O, and C (Ga: 32.13%, C: 2.77%, and O: 65.10)[81-83].

FTIR (Fourier-transform infrared spectroscopy (FTIR) analysis of GeO₂ is represented in Fig. 3.9a, and the antisymmetric vibration of the Ge-O-Ge was observed at peaks corresponding to 960 and 850 cm⁻¹ bands. The vibrational peak at 753 cm⁻¹ is assigned to the stretching of the Ge-O bond. The symmetric stretching of the GeO₂ can be observed at triplet bands corresponding to 514 cm⁻¹, 544 cm⁻¹, 581cm⁻¹ peaks[84]. Raman spectroscopic analysis of the GeO₂ was performed to confirm the formation of the material into the thin film. Fig. 3.9b represents the Raman spectra of the GeO₂. Here, the Raman spectra of GeO₂ show the most substantial first-order peaks at ~301 cm⁻¹, which relate to the crystalline Ge. Additional two more modes are detected at ~259 cm⁻¹ and ~440 cm⁻¹, and there can confirming characteristics of Raman active modes of GeO₂[85, 86]. The X-ray powder diffraction (XRD) pattern of GeO₂ is demonstrated in Fig 3.9c. The characteristic XRD peaks of the GeO₂ effectively match with already reported work[87]. The synthesized GeO₂ shows good crystallinity and phase purity in agreement with previously reported hexagonal crystalline structured GeO₂.

Scanning Electron Microscopy(SEM) analysis of the samples was carried out using TESCAN MIRA3 SEM. As SEM images of the device presented in Fig. 3.9d-f, the hexagonal structured GeO₂ sheets firmly attached can be seen from the obtained images. The high scan area shows the attachment of sheets, and the low scan area offers the hexagonal structure nanosheets of germanium dioxide. Fig. 3.9g represents the energy dispersive spectroscopy (EDS) mapping of germanium dioxide. The EDS mapping confirms that the presence of germanium and oxygen in the germanium dioxide. The absence of any other peaks into the device active layer except germanium and oxygen concludes the purity of the active layer of GeO₂. The SEM image of the GeO₂ deposited onto the ITO-coated substrate can be seen in Fig. 3.9h. The particles are seen to be firmly attached to the substrate of the ITO. Fig. 3.9i-j represents the oxygen and germanium series of EDS mapping the particles are well distributed and firmly attached with ITO substrate.

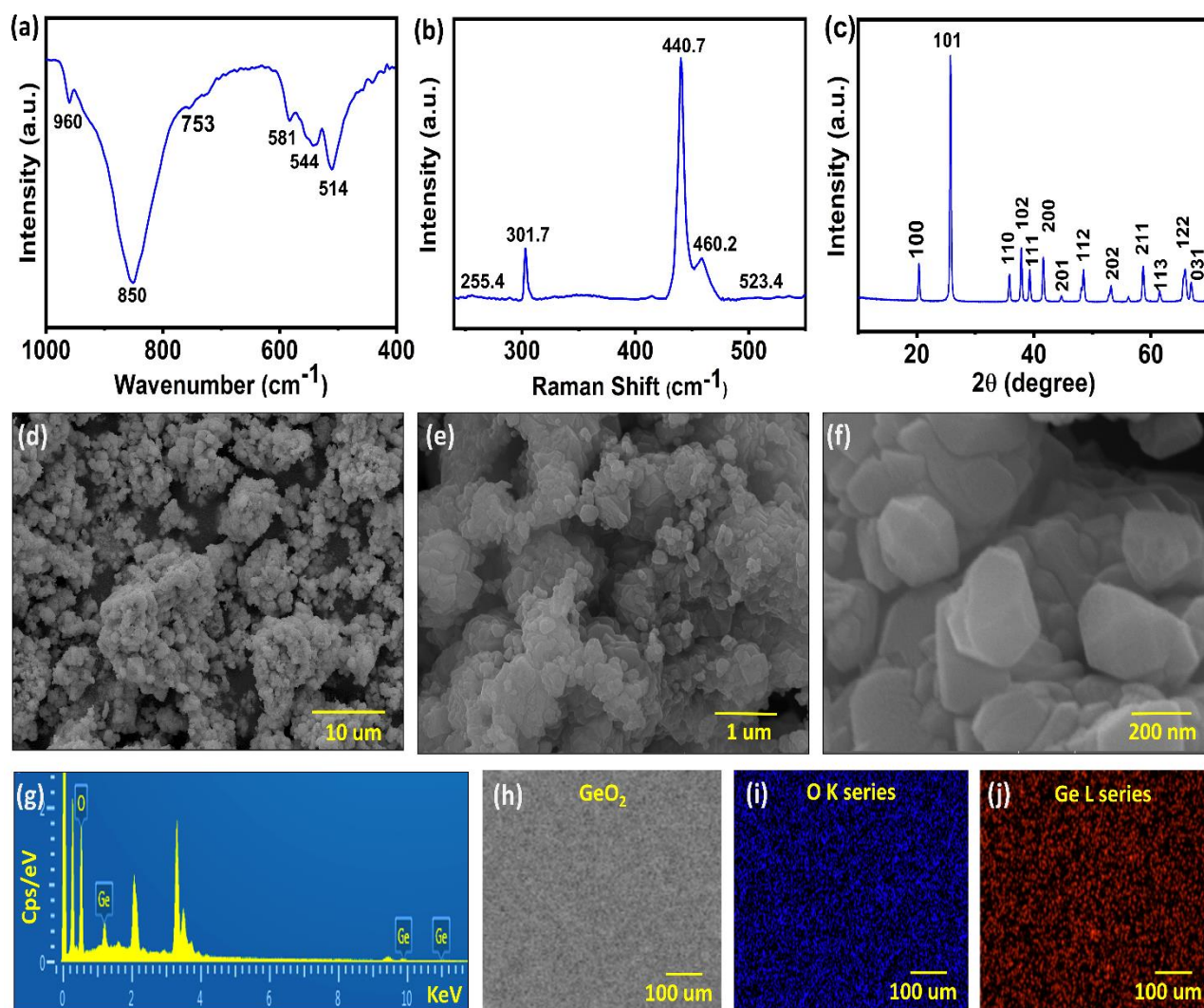


Figure 3.9. (a) The FTIR, (b) Raman, and (c) XRD analysis of GeO_2 . The SEM of the GeO_2 in different magnification, (d) $10\ \mu\text{m}$, (e) $1\ \mu\text{m}$, and (f) $200\ \text{nm}$. (g) The EDS mapping of GeO_2 . (h) The surface morphology of GeO_2 at $100\ \mu\text{m}$. EDS mapping showing (i) O K series and (j) Ge L Series.

3.3.3 Result and Discussion

The non-linear I-V characteristics with the classical hysteresis curve were analyzed to understand the device behavior¹⁴. The I-V curve of the memory device was measured by applying positive potential value on the top Ag electrode and negative potential at the bottom ITO electrode. The multistate resistive behavior of the memory devices can be achieved by controlling the current compliance (CC), voltage sweep, and varying the frequencies. Fig. 3.10a shows the tunability of memristive with increasing the current compliance level. The positive current was controlled by applying the current compliance. The LRS of the device has been changed after increasing the CC level from $100\ \mu\text{A}$ to $1\ \text{mA}$ with applying the $1.2\ \text{V}$ voltage sweep. The proposed device successfully performed the tunability of the current compliance.

On the other hand, the applied voltage sweep of the device has changed from 0.5 V to 1.4 V as shown in Fig. 3.10b. The LRS of the device has changed with increasing the voltage sweep. The change in the LRS state offers the tunability of the memory device with voltage sweep. Fig. 3.10c demonstrates the I-V characteristic of the device investigated with varying frequencies such as 0.05, 0.6, and 0.1 Hz. The zero-crossing pinched hysteresis loop of the I-V characteristics clarifies that the proposed device is a resistive switching memristive device. The device current was decreased while increasing the frequency value. The device tunability by varying the frequency is known as the limiting linear characteristic of the memory device Fig. 3.10c. The tunability in the resistance state of the memory device while applying different CC, voltage sweep and frequencies, the voltage sweep was applied in the order of ± 1.2 V. When the positive potential value was applied to the device, a minimal amount of current was passed through the device in a high resistance state (HRS) due to the charge carriers starts to migrate towards the ITO. The abrupt change in the current was observed in the device with an increase in the magnitude of sweep voltage. The device is at SET state when potential drifts from 0.5 V to 1 V. The device was at SET state when threshold voltage occurred, complete formation of conduction filaments ensued. When the polarity of the applied voltage was changed, the current starts to decrease from LRS to HRS. The negligible current shows into the RESET state of the device due to the breaking of conduction filaments. A similar magnitude of positive and negative polarity was applied on the device, but the diverse extent of the current was observed with both polarities. This demonstrated results suggest that the proposed Ag/GeO₂/ITO device has a highly asymmetric function to block the backward current.

The smooth variation observed from the SET and RESET state, which is reminiscent of the proposed device, is an analog memory device. We have calculated the device hysteresis area and memory window with different frequencies to check the effect of frequency onto the hysteresis area and memory window as shown in Fig. 3.10d. The frequency effect was also exhibited onto the hysteresis area and memory window of the device. The hysteresis area has been decreased with increasing frequency. Conversely, the memory window of the device has been improved with increasing frequency. The continuous stability of the device is the major issue in resistive switching memory devices. Here, the device was run up to continues 500 cycles. The proposed device showed stable performance up to 500 switching cycles without any degradation as shown in Fig. 3.10e. The excellent electrical stability of the hexagonal crystalline structured GeO₂ is responsible for the stable performance of the proposed Ag/GeO₂/ITO memory device. Fig. 3.10e shows the R_{off}/R_{on} ratio and endurance of the proposed memory device with different frequencies.

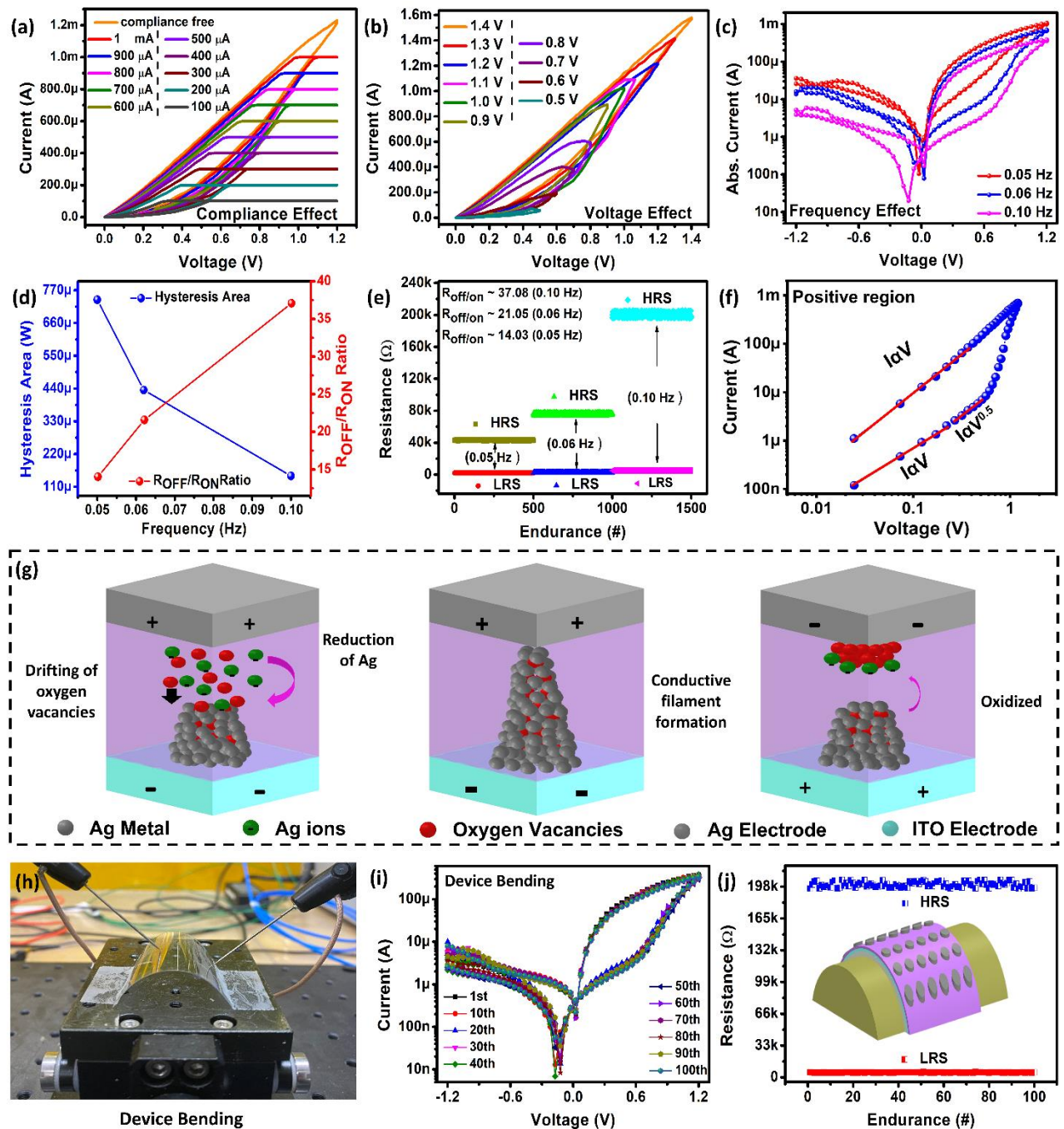


Figure 3.10. (a) I-V characteristics on different current compliance. (b) Multistate behavior on the different applied voltage. (c) The I-V curves on different frequencies. (d) The hysteresis area and memory window of the device on different frequencies. (e) The endurance performance of different frequencies. (f) Logarithmic I-V characteristics of GeO₂ memory device positive region. (g) Filamentary conduction mechanism of the GeO₂ memory device. (g) The photograph of bending test. (i) The performance of memory device during bending showing semilog I-V characteristics for 100 repetitive cycles and (j) endurance results.

Fig. 3.10f demonstrated the logarithmic I-V characteristics of positive and negative voltage regions. On the entire LRS region, the current indicates the linear relation with voltage which confirms the Ohmic conduction mechanism. On the other hand, the positive side current of the HRS state was slowly changed into the low voltage region.

The slope value of the low voltage region regions is ~ 1 , which indicates that the low voltage region of positive HRS is well fitted onto the Ohmic region. In the high voltage region of HRS, the slope value of the region is 1.23. According to the slope values, the high voltage region of both positive biased fitted the Schottky mechanism. Fig. 3.10g presents the filamentary conduction mechanism of the Ag/GeO₂/ITO synaptic device. Ag is the redox-active electrochemical component. The resistive switching behavior was observed in the proposed device due to the redox reaction of the Ag electrode and the migration of oxygen vacancies. When the positive voltage is triggered to the Ag (Top electrode), the Ag ions and oxygen vacancies of GeO₂ start to migrate towards the negatively biased bottom electrode, and the Ag ions are reduced at the bottom electrode. Since the migration oxygen vacancies of GeO₂ generated, also involved forming the conduction filaments. In the SET voltage, the device switched in ON state or LRS due to the complete formation of conduction filaments of the oxygen vacancies and Ag ions. When the RESET voltage is applied, the device is conversely switched in the OFF state, resulting from the rupture of the conduction filament. Bendability is an essential key factor in developing soft electronic device applications. Fig. 3.10h shows the realized image of the bending device. Herein, the proposed device delivers stable performance when experiments are performed in a bending state with 100 repetitive cycles as shown in Fig. 3.10i. The endurance performance of the proposed memory device in the bending form for 100 repetitive pulses Fig. 3.10j shows. The device delivers very stable performance in the bending state.

Neuromorphic memory devices are new emerging technology to develop electronic neuro synapses. The transmitter is an important key factor in mimicking the biological synapses sandwiched between pre-synaptic and post-synaptic neurons. Similar to the memory device, the active layer of the device is the key factor to tuning the synaptic plasticity in electronic neurons[70, 74]. The multistate resistive switching behavior of the memristor can perform synaptic plasticity, which is achieved by varying the frequency, voltage, and CC. The gradual modulation of conductance is the crucial parameter to understand the strengthening and weakening of the synaptic learning devices. The conductance modulation depends upon the filament formation and ion migration of the reduced electrodes that could be controlled by applied signals. To further study synaptic learning, the most suitable pulse can be helpful to mimic the synaptic plasticity. The current modulation of the device by applying the different pulse amplitude is known as spike rate-dependent plasticity (SRDP). Fig. 3.11a demonstrates the potentiation of the device by applying the different pulse amplitude from 1.8 V to 3 V. The device shows the current change while applying the same repetitive pulses.

The current of the device is increasing by applying the repetitive pulse, which is called the potentiation of the device. The 1.8 V to 3 V pulses are more suitable for performing the synaptic learning properties of the proposed memory device. This data was used to further calculations of the pulse-paired facilitation index. Synaptic weight is increasing by controlling the sequential pulse interval is known as pulse-paired facilitation (PPF). Herein, we calculated the ΔI for the different voltages which can be useful to calculate the PPF and post-tetanic potentiation (PTP) as shown in Fig. 3.11b. The increasing ΔI is calculated by the $I_n - I_1$ Where $n = 1, 2, 3, \dots, 30$. The second pulse compared with the first pulse ($I_2 - I_1$) is the PPF and the 30th current pulse compared with the first pulse ($I_{30} - I_1$) is the PTP. The PPF index of the proposed device with different voltages was plotted in Fig. 3.11c. The higher PPF index is observed onto the 3 V, and its trend decrease with decreasing the voltage value.

The spike time dependant plasticity (STDP) of the proposed memory device is correlated with biological neuro Hebbian and anti-Hebbian learning rules[69-71]. Here, we have performed the antisymmetric and antisymmetric anti-Hebbian rules as shown in Fig. 3.10d and e. The pulse scheme (1.8 V, -2 V, -1.5 V, -1 V, -0.5 V, -0.3 V, -0.1 V) was used to perform antisymmetric Hebbian and pulse scheme (-1.8 V, 2 V, 1.5 V, 1 V, 0.5 V, 0.3 V, 0.1 V) was used to perform antisymmetric anti-Hebbian with pulse width 600 μ s and pulse off interval is 1 ms as insets shown in Fig. 3.11d and e. The time interval of post- and pre-synapse is considered as the Δt . The time interval (Δt) between the pre-synaptic spike and the post-synaptic spike is known as modulation of devices conductance (ΔG). After combined of pre- and post-synapse, the resulting pulse shows a higher value than the threshold voltage values, which plays a vital role in reading the potentiation and depression of the device with respective the relative time interval. The proposed Ag/GeO₂/ITO device successfully performed the antisymmetric Hebbian and antisymmetric anti-Hebbian rules. Hence, there confirming that the proposed device is the foremost candidate for synaptic learning applications.

The LTP and LTD of the device were performed by applying the 100 repetitive pulses with 3 V and -3 V pulse amplitude, and the pulse width was 600 μ s shown in Fig. 3.11f. When the 100 repetitive 3 V positive amplitude was applied to the device, the current of the device gradually increased from 3.5 μ A to 9 μ A. The current of the device is increasing with applying the repetitive pulse, which is called the potentiation of the device. When we applied negative repetitive pulses -3 V to the device, the current of the device start to decrease. The decrease in the current with applying the repetitive pulses signifies a depression of the device.

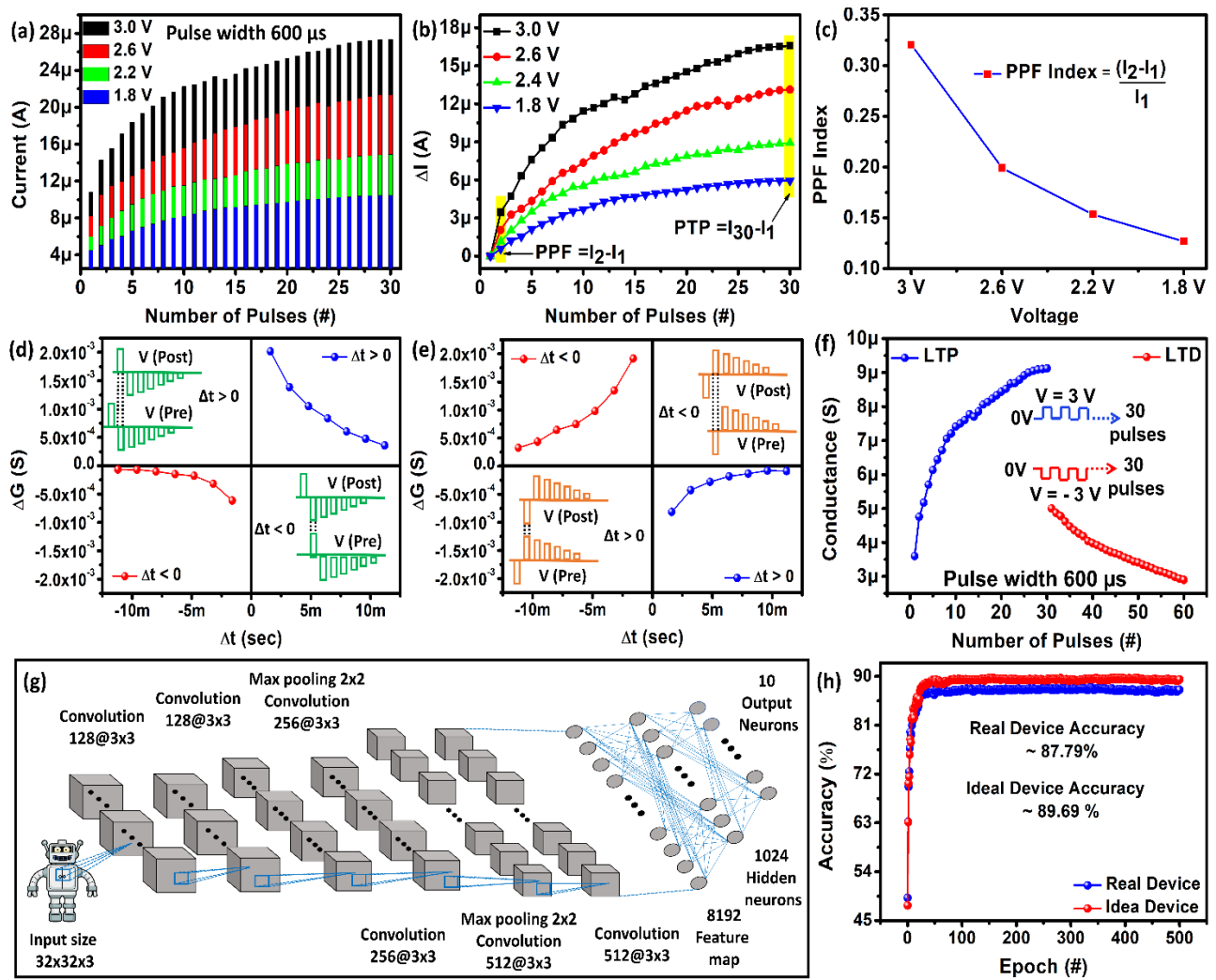


Figure 3.11. (a) The potentiation of the by applying the different pulse amplitude. (b) The ΔI calculates the increasing current (ΔI) for different pulse amplitude, $I_n - I_1$ where $n = 1, 2, 3, \dots, 30$. (c) PPF index % of the device on different voltages. The experimental STDP results show (d) antisymmetric Hebbian and (e) antisymmetric anti-Hebbian learning rules. (f) LTP and LTD of the proposed device. (g) Simulation process of the device by using CNN network. (h) Real and ideal CNN accuracy of the proposed synaptic device.

Fig. 3.11g demonstrates the convolutional neural network (CNN) illustration. Herein, the CIFAR-10 data set was used, which is composed of 6-convolutional layers and 2-fully-connected layers. The first and second convolutional layers consist of 128 convolution kernels, and their size was 3×3 . The third and fourth layers consist of the same size with 256 kernels. Furthermore, 512 kernels were included in the fifth and last layers of similar size with prior layers. The max-pooling was used with 2×2 kernel for every 2 layers. After these processes, The feature map was converted into the flatten output denoting 8192 units and connected with the 1024 Hidden layer units. However, the final output is composed of 10 units for classifying the 10 CIFAR-10 labels. The output layer was calculated using the featured map, which comes from a hidden layer, and extracted the accuracy from true value and the predicted value of the CIFAR-10 label[73, 74].

In deep learning simulation experiments, the non-linearity factor can define the non-linearity between actual and ideal linear weight function. Then non-linearity value is 3.76 for LTP and 1.61 for LTD. Also, cycle-to-cycle variation is 0.003, and the conductance ratio is 2.75. Fig. 3.11h depicts the ideal and real case accuracy of the proposed device. Herein, we have compared the ideal and real case accuracy of neural network simulation. The real case accuracy value is 87.79%, and the Ideal case is 89.69%, showing almost similar results with a negligible (2%) difference, respectively. These results suggested that the proposed non-linear synaptic device function is very closed with linear Ideal device function.

3.3.4 Summary

In summary, the hexagonal crystalline structured GeO_2 has been successfully developed the multistate resistive switching memory behavior with synaptic learning application. The device was modulated with applied amplitude from 0.4 V to 1.4 V and varying the frequencies from 0.05 Hz to 0.1 Hz. The current of the device was controlled by applying from 100 μA to 1mA. The tunability of the memory device while changing the voltage and frequency should be suggested that the proposed device is a favorable candidate to mimic the synaptic learning properties. The endurance and flexibility test have demonstrated stable performance, proving that the hexagonal crystalline structured GeO_2 is an excellent electrical durable material. The device was able to demonstrate the potentiation- depression, SRDP, and STDP. The results of the proposed study encouraging that the $\text{Ag}/\text{GeO}_2/\text{ITO}$ is a valuable memory device to develop highly stable soft and flexible electronic synapses.

3.4 Ionic liquid multistate resistive switching Device for Neuromorphic Computing

Synapses are the most elegant memory network, in which each neuron is polarized with ions (Ca^+ or K^+), which communicates and results in a release of neurotransmitters[69] as shown in Fig. 3.12a. Similarly, to realize the neuromorphic device, researchers are trying to develop the next generation computing technology by using the nonvolatile conductance property of memristive materials to emulate the synapses[67] as shown in Fig. 3.12a, which include metal oxides, 2D materials, organic materials, inorganic materials, hybrid materials, and ionic liquids (IL)[88-90]. Hence, liquid materials are getting more attention due to high flexibility, high ion conductivity, and easy device fabrication[91].

The signal transmission in biological neurons is defined between presynaptic and postsynaptic neurons[67] as shown in Fig. 3.12a. Similarly, multistate resistive switching neuromorphic device can be used to mimic synaptic function by using the discrete channel, in which IL will play an important role in the movement of cation and anion[71] as shown in Fig. 3.12a. Specifically, the ability to emulate SRDP and STDP of the soft and flexible discrete channel IL needs to be addressed to perform the electronic synapses.

However, several critical aspects of liquid based soft and flexible artificial synapses with memorable conductance tuning, under bending and stretching state required to successfully produce a functioning hardware neural network, which has rarely been reported in discrete channel systems. In this proposed work, we introduce ionic liquid (IL) BMIM FeCl₄ and H₂O into a discrete channel system and thus realize a multistate resistive switching behavior. We then emulate the analog weight change behavior SRDP and STDP of a synapse with our discrete channel memristor and evaluate its performance in a convolutional neural network pattern recognition task based on a system-level simulation. The device presents a highly stable multistate resistive switching behavior in a bending and stretching state. we are confident that, soft and flexible devices are an excellent candidate to perform neuromorphic computing in the field of artificial intelligence and brain shape mimicked robotics as shown in Fig. 3.12a.

3.4.1 Materials and Methods

FeCl₃ and BMIM Cl were purchased from Sigma Aldrich. The 2 g of BMIM Cl was dried under vacuum in a round bottom flask placed in oil bath at 120 °C. The 1.86g of FeCl₃ was dried at 120 °C and was added to the flask containing BMIM Cl. The solution was placed again in the oil bath containing BMIM Cl and FeCl₃ with a molar ratio of 1:1 and stirred under vacuum for 24 h. The final product was a ruby red liquid (BMIM FeCl₄)₁₆ and the chemical reaction of BMIM FeCl₄ is shown in Fig. 3.12f. The PDMS was purchased from Dow Corning. The curing agent and PDMS were mixed in 1:10 and mold was prepared by placing thin wire with a thickness of 1.5 mm and cured at 80 °C for 4 hours as shown in Fig. 3.12b. The length and width of the PDMS mold is 15 mm and 5 mm, respectively as shown in Fig. 3.12b. The PDMS channel with a hole size of 1.5 mm was used to hold IL as shown in Fig 3.12c. In the final step, IL BMIM FeCl₄ and H₂O was filled in PDMS mold using a syringe and two electrodes as anode and cathode used as contacts and the liquid stopper was used on both sides to prevent the leakage of IL as shown in Fig. 3.12d. The distance between both electrodes was kept 0.5 mm to perform device characterization as shown in Fig. 3.12e.

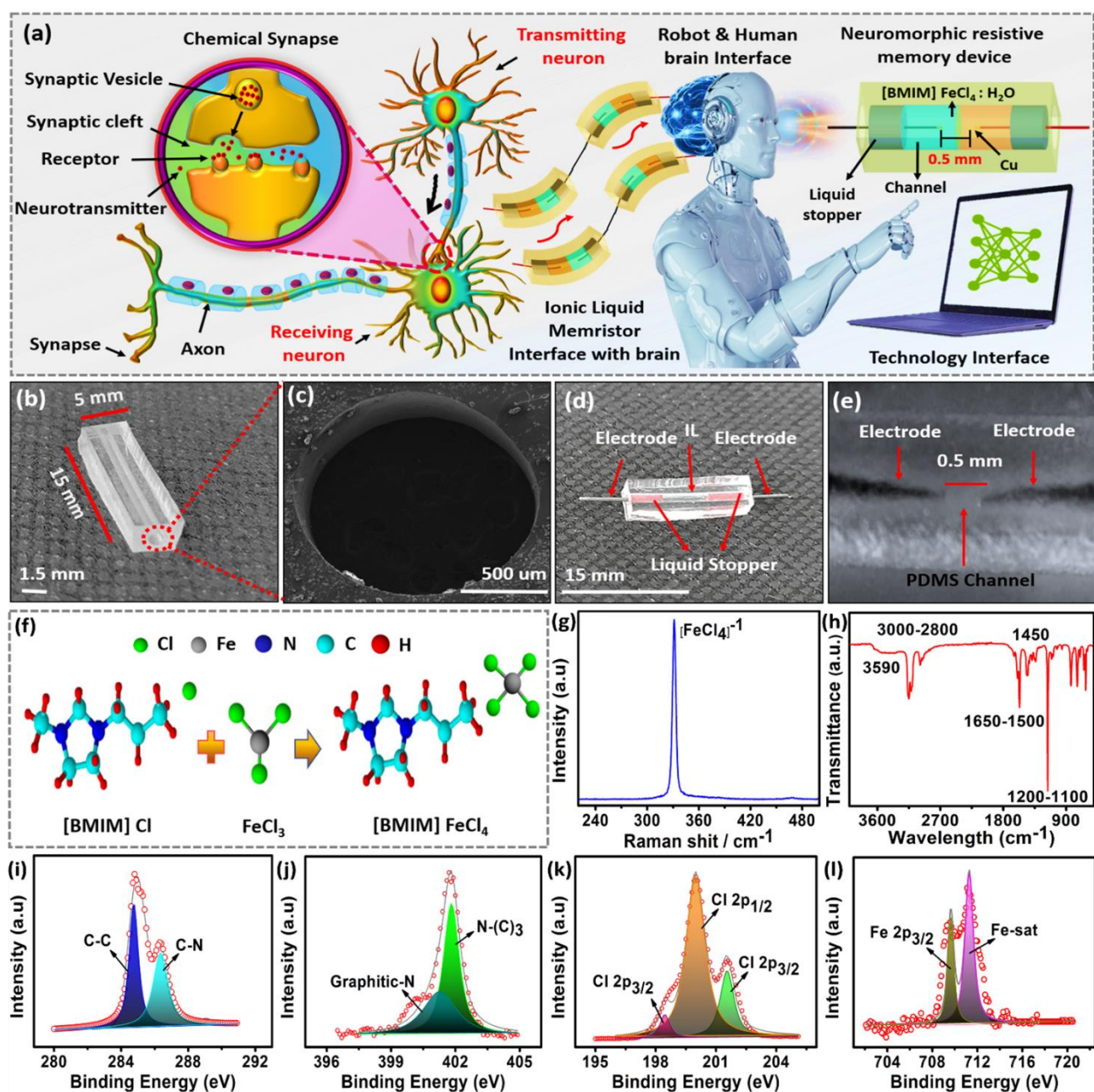


Figure 3.12. (a) Illustrating the synaptic response between the presynaptic neuron and the postsynaptic neuron and Ionic memristor interface with future technology. (b) Fabricated PDMS mold with channel length of 15 mm, (c) and channel width of 1.5 mm. (d) Optical image of realized device, (e) zoom image of electrode spacing ~ 0.5 mm. (f) Synthesis of Ionic liquid BMIM FeCl₄. (g) Raman and (h) FTIR of BMIM FeCl₄. The XPS of (i) carbon, (j) nitrogen, (k) chlorine, and (l) iron regions of BMIM FeCl₄.

3.4.2 Characterization

The neuromorphic device was analyzed with KEYSIGHT B2902A source measuring unit. The XPS spectrum was measured by PHI 5600 (Physical Electronics) with the source of Al X-ray monochromator, which uses photoelectrons excited by X-ray's emission for the surface characterizations up to a depth of 2-5 nm, FTIR using Bruker IFS 66 V spectrometer, and Raman

Spectrum was measured by HORIBA LabRAM HR confocal spectrometer, equipped with 800 nm length monochromator, He-Cd laser was shined on the surface of the sample with the excitation wavelength of 325 nm. The chemical characterization was performed by using Raman spectroscopy, FTIR, and XPS. In Raman spectroscopy, vibrational analysis of materials is analyzed at the atomic scale. Every free-standing crystal holds its own natural vibration frequency on the lattice and foundation of the material.

The Raman spectra of BMIM FeCl₄ show the strong peak at 330.2 cm⁻¹, corresponding to the symmetric Fe–Cl stretch vibration of [FeCl₄]⁻ as shown in Fig. 3.12g. We performed the FT-IR to investigate the functional groups of the BMIM FeCl₄ as shown in Fig. 3.12h. The hydroxyl group is observed in 3590 cm⁻¹ into the FTIR spectra. –C–H stretching vibrations of the imidazolium cation is observed into the peak range of the 3,105 cm⁻¹ to the 3,200 cm⁻¹. 3000–2800 cm⁻¹ peaks showing the stretching behavior of –C–H, –CH₂, and –CH₃ of the alkyl groups attached to the nitrogen atom in the imidazolium ring of the BMIM FeCl₄ ionic liquid. The vibrational peaks of the imidazole ring are observed at 1650–1500 cm⁻¹ and 1450 cm⁻¹. The metal chloride is observed into the transmission bands around the 3200–3100 cm⁻¹, 3000–2800 cm⁻¹, 1650–1500 cm⁻¹, 1450, and 1200–1100 cm⁻¹. The XPS BMIM FeCl₄ is measured for the identification of elements and their chemical bonding, respectively. C-1s peak was adjusted at 285.00 eV for the calibration of absolute binding energy and represents the deconvoluted spectra of BMIM FeCl₄, with core levels of Fe-2p, N-1s, Cl-2p and C-1s from the surface of the sample as shown in Fig. 3.12i. The dominant peaks at 284.72 eV and Lorentzian fitted peak at 286.21 eV in high resolution spectra of C1s are attributed towards the bonding of C-C and C-N, respectively as shown in Fig. 3.12i. Analysis of the N-1s core level line signifies the Lorentzian fitted peak at 401.23 eV relates to the graphitic nitrogen and other peaks at 401.83 eV shows the N-C bonding as shown in Fig. 3.12j. The high-resolution Cl-2p XPS spectrum demonstrated the doublets at 201.8 eV and 200.3 eV associated with 2p_{1/2} and 2p_{3/2} levels due to the spin-orbitals coupling, which is a typical indication of organic C–Cl covalent bond structure, further sub-peak at 198.43 eV demonstrates the coupling of 2p_{3/2} Cl orbitals, in Fig. 3.12k. The Fe-2p core level line has a FWHM of 4.12 eV and its high-resolution spectra reveal two sub peaks the dominant peak at 711.3 eV confirm the bonding of Fe-cat and other peaks at 709.86 eV correspond towards the transition of Fe-2p_{3/2} spin orbitals as shown in Fig. 3.12l.

3.4.3 Results and Discussion

The human brain is composed of interconnected neurons, where the presynaptic neuron passes information to the postsynaptic neuron and results in the transmission of neurotransmitters which control the synaptic plasticity. Similarly, the multistate resistive switching characteristics in two terminals discrete PDMS cylindrical channel can also mimic the biological synaptic plasticity by gradual variation in the resistance state by repeated pulse sequence to modulate the conduction between the interface of IL BMIM FeCl₄ and H₂O. The ion selectivity (BMIM⁺, FeCl₄⁻, H⁺, OH⁻) provides the basic mechanism for discrete channel device, in which the surface charges on the channel walls will repelling ions with the same charges and attract oppositely charged ions due to electroosmotic flow equation as given in Fig. 3.13a, where the counterions attracted to the wall surface charges in H₂O, which plays the predominant role in the transport rather than the ions in the bulk region of IL BMIM FeCl₄. The electric body force \vec{f}_e creates an imbalance between co-ions and counterions ($n_+ - n_-$), which causes a net charge under the presence of applied electric field \vec{E} on an interface between IL BMIM FeCl₄ and H₂O as shown in Fig. 3.13a. The electroosmotic flow will cause the conductance tuning in our discrete channel device to perform neuromorphic computing.

The measured multistate resistive switching as shown in Fig. 3.13b and c shows that conductance tuning can be observed with each voltage sweep. The hydration reactions hardly occur between the interface of PDMS and IL BMIM FeCl₄, the surface charges of IL BMIM FeCl₄ on the channel wall are negligible, as shown in Fig. 3.13a. Hence, we infer that a positive voltage will result in an electrical body force that exists only within the H₂O and points from the H₂O side of the device to the IL BMIM FeCl₄ side, as illustrated in Fig. 3.13a. This force pushes the H₂O against the IL BMIM FeCl₄, as shown in Fig. 3.13a, and conductance is tuned under continuous voltage sweeps, due to the smaller resistivity of the H₂O as compared to IL as shown in Fig. 3.13b and c. The above discussion indicates that the discrete channel is equivalent to an interfacial memristor, in which under negative and positive voltage region current decreases with voltage sweeps and conductance of the device decreases Fig. 3.13b and c. Thus, the electrical characteristics of the soft and flexible discrete channel device can be related to synapses in which the conductance decrease can be related to ion metallization. The measured current under a ten triangular voltage sweep with a period of 1.2 seconds and conducting current decreases with time as shown in Fig. 3.13d and e. The spike rate-dependent plasticity (SRDP) of the multistate resistive switching device in the discrete channel was examined by varying by different pulse width, pulse amplitude, and frequencies.

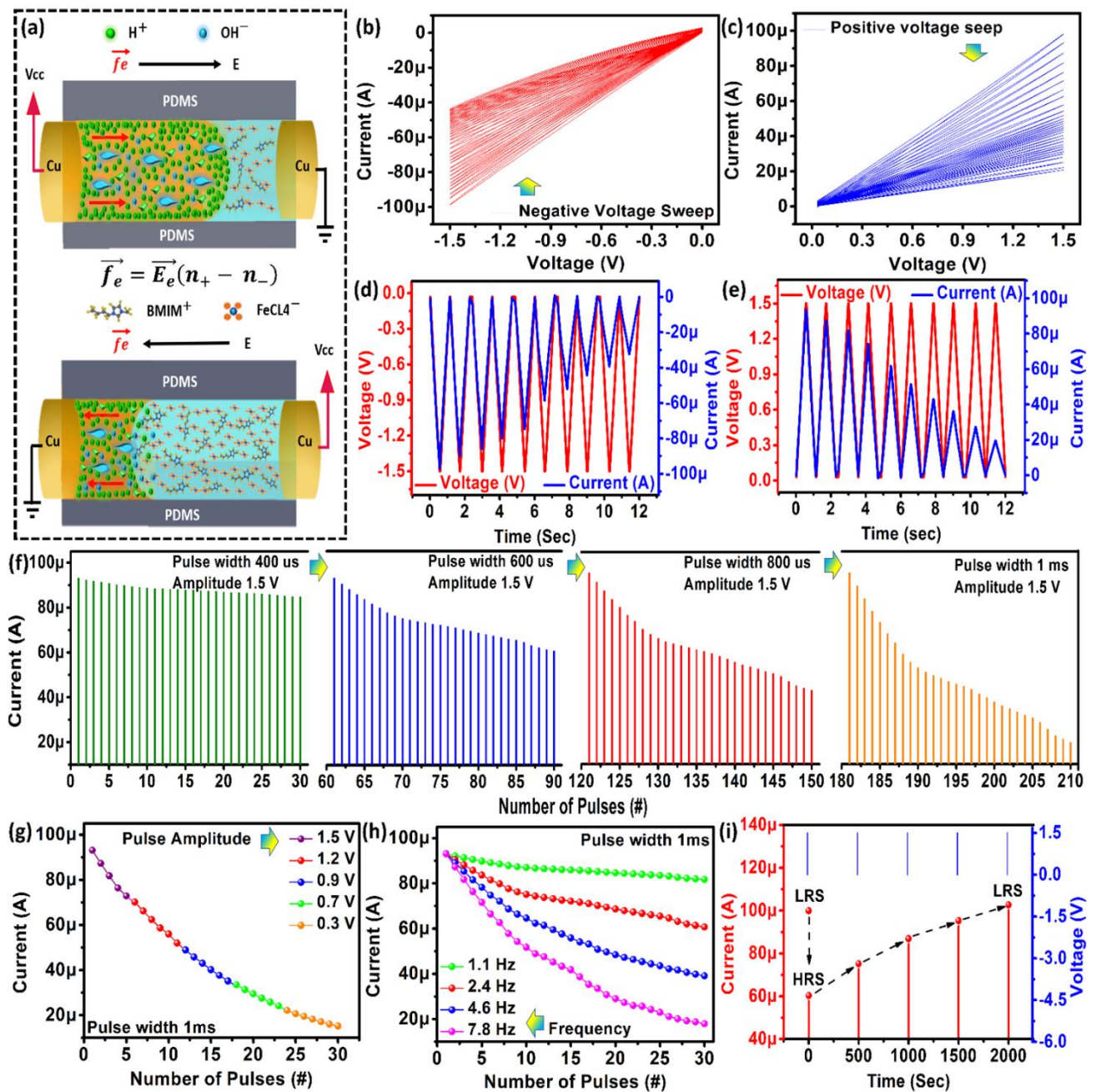


Figure 3.13. (a) Basic mechanism schematic for the electrical manipulation of ion and liquid transport in discrete channel. The I-V of (b) positive and (c) negative voltage sweep. The five cycles of triangular voltages with time on (d) positive and (e) negative voltage region. (f) Plasticity characteristics of the artificial synapse with different pulse widths of, 400 μs , 600 μs , 800 μs , and 1 ms. (g) The different pulse amplitude response at 1.5 V, 1.2 V, 0.9 V, 0.7 V and 0.3 V. (h) Frequency response at 1.1 Hz, 2.4 Hz, 4.6 Hz, and 7.8 Hz. (i) The STM retention of the neuromorphic device.

The synaptic weight can be modulated by the successive stimuli of externally applied pulses of different widths of 400 μs , 600 μs , 800 μs , and 1 ms by keep a constant pulse amplitude of 1.5 V as shown in Fig. 3.13f. The pulse width 400 μs shows no obvious decrease in the current (93 μA to 87 μA). The increase in pulse width up to 1ms, the results in current changes significantly from 93 μA to 19 μA as compared to the pulse width of 400 μs , 600 μs , and 800 μs .

The different voltage amplitude of 1.5 V, 1.2 V, 0.9 V, 0.7, and 0.3V with a pulse width of 1ms, the current decreases from 94 μ A to 12 μ A, as illustrated in Fig. 3.13g, which corresponds to lower electrical body force between the interface of IL BMIM FeCl₄ and H₂O at lower voltage as compared to a higher voltage. The frequency test is performed using a continuous pulse train on the optimized pulse width of 1ms and amplitude of 1.5 V as shown in Fig. 3.13h. The frequency range of 1.1 Hz shows very small current variation under continuous pulse train. On the other hand, by the increase the frequency range up to 7.8 Hz the current decreasing rate is larger (93 μ A to 18 μ A) as compared to the previous conditions with lower frequencies (1.1 Hz, 2.4 Hz, and 4.6 Hz), as shown in Fig. 3.13h. This experiment demonstrates the process of memory retention of the multistate resistive switching device. Initially by applying the input pulses to set device in HRS as shown in Fig. 3.13i. Then after every 500 sec, the conductivity was measured by applying the 1.5 V with pulse width of 1ms. The current increases or recovers by applying the pulses after every 500 sec. The neuromorphic device recovers to its initial state (LRS) after 2000 Sec. The device recovers its state from HRS to LRS, this phenomenon can be related to the forgetting of human memory. The short-term memory (STM) is an important feature of the human brain, which provides the information loss of the particular time. Similarly, it is an important feature to mimic forgetting behavior for the electronic synapse devices as shown in Fig. 3.13i. The switching transaction by applying input pulses to change device state from LRS to HRS is similar to the short-term depression (STD)[70].

The more sophisticated pulse scheme was implemented to mimic the SRDP, in which the current was obtained by applying 30 consecutive pulses with amplitude of ± 1.5 V and pulse width of 1 ms with duty cycle of 50% as shown in Fig. 3.14a. The gradual variation in the current with pulses is like a variable synaptic weight in bio synapses. In IL BMIM FeCl₄ and H₂O discrete channel synaptic device behave like brain neuronal activation in which a similar phenomenon also exists after inverting the polarity of voltage as shown in Fig. 3.14a. The scaling possibility of the device depends on the PDMS and ionic liquid (EMIM FeCl₄), which helps to form the device in any shape by controlling the length, width, thickness, and flexibility. This works provides a demonstration for the adoption of flexible discrete channel resistive memory architectures for neuromorphic computing. This experiment part is just based on the demonstration of the device flexibility to intergrade the discrete channel device in a brain shape mimicked robotics. The bending and the stretchability nature of the device were due to IL BMIM FeCl₄ and PDMS substrate. In bending and stretching state, the device shows stable analog resistive switching behavior and can be used for neuromorphic computing in soft robotics as shown in Fig. 3.14b and c.

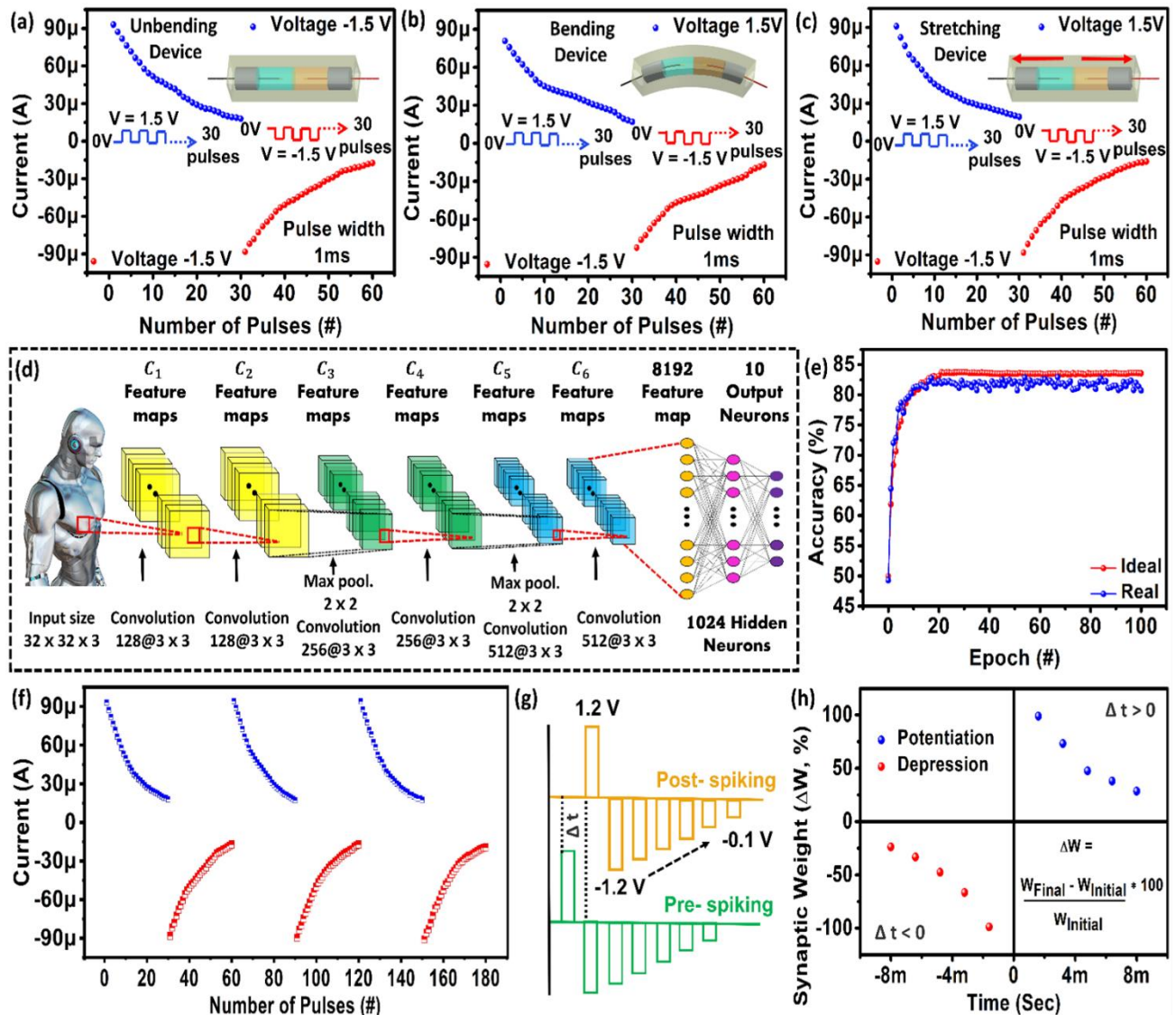


Figure 3.14. The synaptic plasticity of (a) unbending, (b) bending, and (c) stretching device under continuous pulse train with a pulse width of 1 ms. (d) Diagram of neural networks for recognition of cifar-10 data. (e) Simulated accuracy ideal and real device. (f) Device endurance performance. (g) Schematic waveform for STDP. (h) The synaptic weights (%) change with respect to time difference (Δt).

The proposed device was operated with the neuromorphic functionality, and the working data were obtained. To evaluate the proposed device, the simulation parameters for convolutional neural network (CNN) can be easily obtained from these data. Using these parameters for CNN simulation, CIFAR-10 recognition data was used in which input consist of $32 \times 32 \times 3$. The first and second convolutional layer consists of 128 convolutional kernels of size 3×3 and subsampling data with size 2×2 after using two convolutional layers. The third and fourth convolutional layer consist of 256 convolutional kernels of size 3×3 . Again, we are subsampling data with size 2×2 after using two convolutional layers. The fifth and sixth convolutional layer consists of 512 convolutional kernels of size 3×3 .

The feature map was connected to 2 fully connected layers for classification. The output layer is composed of 10 neurons to classify. In summary, 6 convolutional layers are used to extract features and the last 2 fully connected layers are used to classification features[74] as shown in Fig. 3.14d. The maximum conductance and minimum conductance of the device are $1.1400e-05$ and $1.6385e-08$, respectively with off/on ratio ~ 5.4474 and nonlinearity for positive and negative pulse data is 2.23 and 2.81, respectively. As shown in Fig. 3.14e, the accuracy of the neural network is 84% and converges 83% in epoch 20. A CNN is designed as shown in Fig. 3.14d, using 6 convolutional layers and 2 fully connected layers. The input image is CIFAR-10 data that has 10-classes. The batch size is 200, epoch is 100. Based on that data, we trained kernels and synapses in all layers to minimize the error between real output and predict output. For comparison of real case, we also simulated ideal device using linear function. As shown in Fig. 3.14e, the ideal device presents the maximum accuracy $\sim 84.23\%$ and converges 84% in epoch 20. The device shows stable cycle to cycle endurance repeatability, which is one of the most important parameters for on chip training as shown in Fig. 3.14f.

The spike time dependent plasticity (STDP) rule helps to illustrate the practicability of the neuromorphic device for biological synapses. We have designed the pulse train, which consist of different amplitudes (+1.2, -1.2, -1, -0.8, -0.6, -0.3, and -0.1) as given in Fig. 3.14g, where pulse width is $600 \mu\text{s}$ and pulse off interval is 1 ms. The pre and post synapse pulses combined together to form a resulting signal more than the threshold voltage, which results the device conductance weakening or strengthening with respective relative time interval Δt , where the device conductance (ΔW) modulation is a function of time interval (Δt) between pre and post synaptic spiking. During $\Delta t > 0$, pre-spike proceeds post-spike, which result in potentiation and conversely, for $\Delta t < 0$, synaptic weight decreases (depression), due to post-spike proceeds pre-spike. The Fig. 3.14h shows the asymmetric Hebbian rule of flexible discrete channel resistive memory device, showing conductance change as a function of time interval Δt between pre and post spiking pulse. The STDP behavior of discrete channel resistive memory device using different time intervals shows similar behavior as biological synapses[69].

3.4.4 Summary

In summary, we have addressed the key challenges in the use of soft and flexible multistate resistive switching in discrete channel device as a synapse by introducing a viscous IL BMIM FeCl₄ and H₂O for mimicking various shapes for the artificial intelligent neuromorphic system.

The working mechanism was based on the ion concentration polarization within the channel, which can be modulated through the electrical input signal. In this way, memorable conductance could be tuned by changing pulse width, frequency, and pulse amplitude. The SRDP and STDP behavior shows high stability to perform electronic synapses. The analog weight change behavior demonstrated a stable endurance performance with our discrete channel memristor. In the flexibility test, highly stable performance was archived under mechanical deformation. The proposed discrete channel synapse operating performance was evaluated using CIFAR-10 image recognition for system-level CNN simulation with an accuracy of 84%. We are sure that the paper gives insight for highly stable neuromorphic resistive memory device for wearable electronic systems.

3.5 Soft and Flexible: Core-shell Ionic Liquid Resistive Memory for Electronic Synapses

Resistive switching memory (RSM) devices show promise for next-generation memory applications due to their simple fabrication process[54], excellent stability[14], and ultrafast switching performance[35] at low operating voltages[34]. After the conceptualization of RSMs by Leon Chua in the 1970s[17], Hewlett Packard Laboratories presented the foremost solid-state memory device[37]. Then, RSMs were also widely investigated to develop next-generation neuromorphic devices to mimic the brain[53]. Synapses are the most elegant memory and artificial intelligence network, in which different kinds of learning processes occur with the electrical activities of neurons[53]. Each neuron consists of a central cell body, which consists of narrow and long extensions (axons), each of which has indirect connections[53]. The cell membrane of each neuron is polarized with sodium (Na^+) ions outside and potassium (K^+) inside the cell, which communicates and results in the release of neurotransmitters during synapses[53]. The brain synapse process generates a signal of several tens of millivolts with high efficiency and low power[53]. Currently, researchers are trying to develop an artificial memory device that can operate as power efficiently as the human brain in which resistance change depends on the applied voltage. Liquid-based soft resistive memory can be applied to mimic the brain to perform synapses[53]. Hence, researchers are applying various liquid materials, such as electrolytes, liquid metals, and ionic liquids (ILs), in RSMs due to their high flexibility, high conductivity, low cost, low viscosity, and easy device fabrication[7, 53]. In addition, liquid-based RSMs work on the principle of transportation of cations and anions[7].

Soft RSMs show electrochemical metallization behavior and result in filamentary conduction, in which active electrodes such as Cu can inject Cu^{2+} metallic cations into the IL medium[7]. These metal cations (Cu^{2+}) move to the cathode and are reduced by electrons. The precipitation of the active metals at the cathode leads to the growth of metal protrusion, which reaches the anode to form a highly conductive filament between the electrodes, and the conduction saturates due to ion polarization and results in resistive switching behavior⁹. These electrolytes will play an important role in the movement of cationic and anionic transportation to achieve neuromorphic behavior[7, 53]. This paper reports an Ag@AgCl core-shell (liquid electrolyte) synapse device with multistate resistive switching behavior, as shown in Fig. 3.15. Initially, iron (III) chloride (FeCl_3) was used as an IL electrolyte to achieve resistive switching behavior. To control the conduction current to achieve multistate resistive switching behavior, Ag is introduced in a liquid electrolyte, which results in the formation of an Ag@AgCl core shell. The presence of a core shell significantly helps to control the device performance by limiting the movement of Cu^{2+} ions. The device presents a highly stable multistate resistive switching behavior at low operating voltage. We are confident that the proposed device is an excellent candidate for soft electronics to perform synapses similar to the human brain.

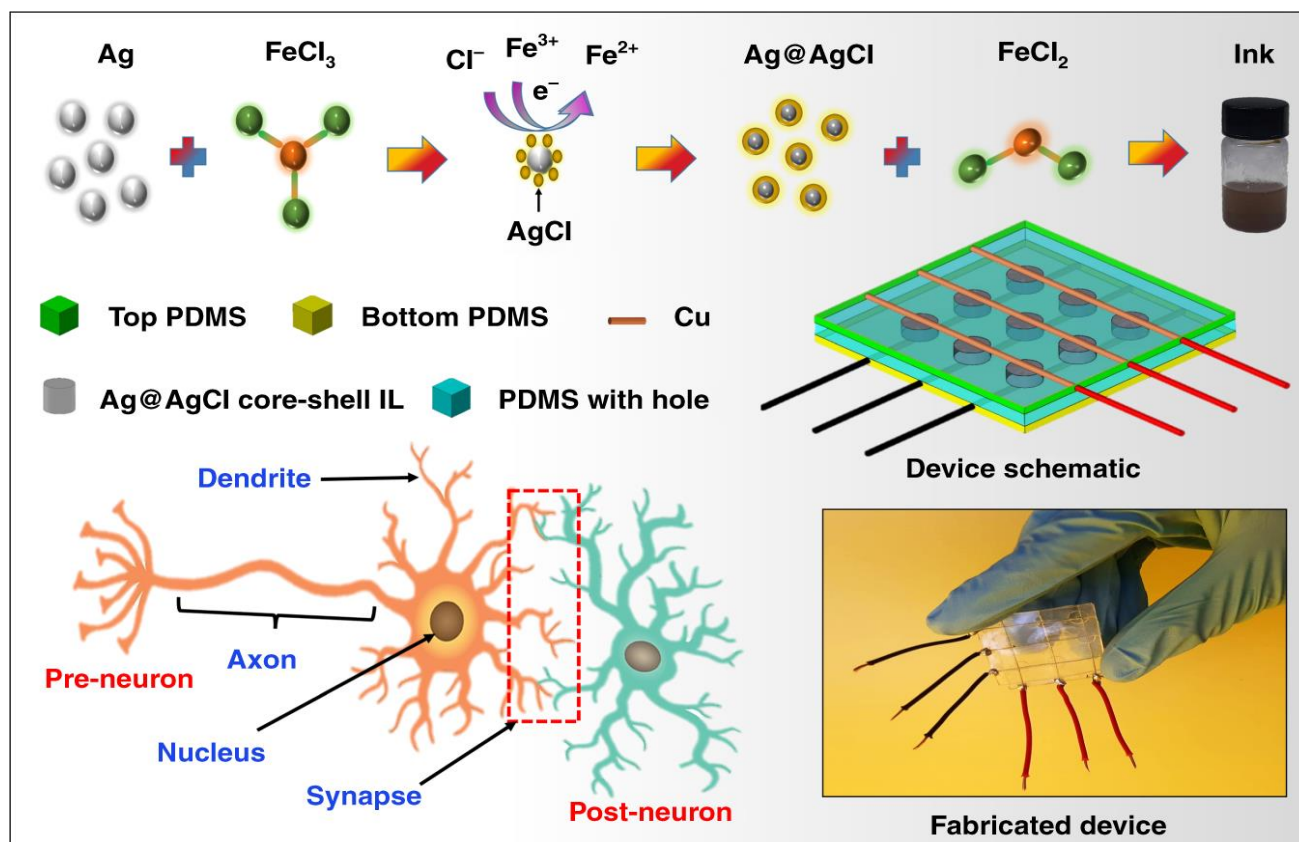


Figure 3.15. Ink preparation method of Ag@AgCl core-shell IL electrolyte and fabrication of soft and flexible memory cells for neuromorphic computing

3.5.1 Materials and Methods

FeCl₃ hexahydrate crystallized, glycerol solution, and Ag nanoparticles (50 wt%) in tetrahydrofuran (THF) solvent were purchased from Sigma Aldrich for the preparation of Ag@AgCl core shells. Ink preparation is presented in Fig. 3.15. We prepared a core shell by dropwise adding 5 wt % FeCl₃ solution to glycerol and 50 wt % Ag nanoparticle solution to THF solutions at a ratio of 1: 1. After this reaction, the mixture was kept at room temperature until its color changed from black to brown. Color changes are observed in the reaction, which confirms the Ag@AgCl core shell with iron II chloride (FeCl₂), as shown in Fig. 3.15. PDMS was purchased from Dow Corning for the preparation of the mold. The fabrication process is explained in Fig. 3.15, in which a PDMS mold is prepared by mixing curing agent and PDMS in a 1: 10 ratio and cured at 80 °C for 4 h. In the top and bottom PDMS molds, Cu wires with a thickness of 1 mm were used for electrodes at both ends (anode and cathode). A porous mold with a hole size of 3 mm was used to hold the core-shell IL with a thickness of 200 μm. In the final step, Ag@AgCl core-shell IL was used as a resistive switching medium and was filled in PDMS mold using a syringe and two electrodes as anode and cathode used as contacts, and PDMS helps to avoid liquid leakage in a channel between electrodes.

3.5.2 Characterizations

Current-voltage (I-V) and neuromorphic characterization of the device was performed with the KEYSIGHT B2902A source measuring unit. The surface morphology of Ag@AgCl core-shell nanoparticles was analyzed through TESCAN MIRA3 STEM and the core-shell element compositions were analyzed using EDS (Energy Dispersive Spectroscopy). The chemical and structural information of the Ag@AgCl core shell was investigated by FTIR using a Bruker IFS 66V spectrometer. The crystal structure of the FeCl₃, Ag, and Ag@AgCl core shell was characterized by XRD diffraction with a tube target of Cu.

Figure 3.15 shows the detailed process of the Ag@AgCl core-shell IL ink synthesis process, which is further utilized as an active material to perform biological synapses using memristive behavior. The presence of a core-shell IL controls the movement of Cu²⁺ ions, which results in multistate resistive switching behavior by applying a continuous sweep voltage and pulses with different frequencies, widths, and amplitudes. The liquid-based synapse memristive device is closer to the human neural model, which is based on the neurotransmitter, as shown in Fig. 3.15, in which two neurons are connected by a synapse[53].

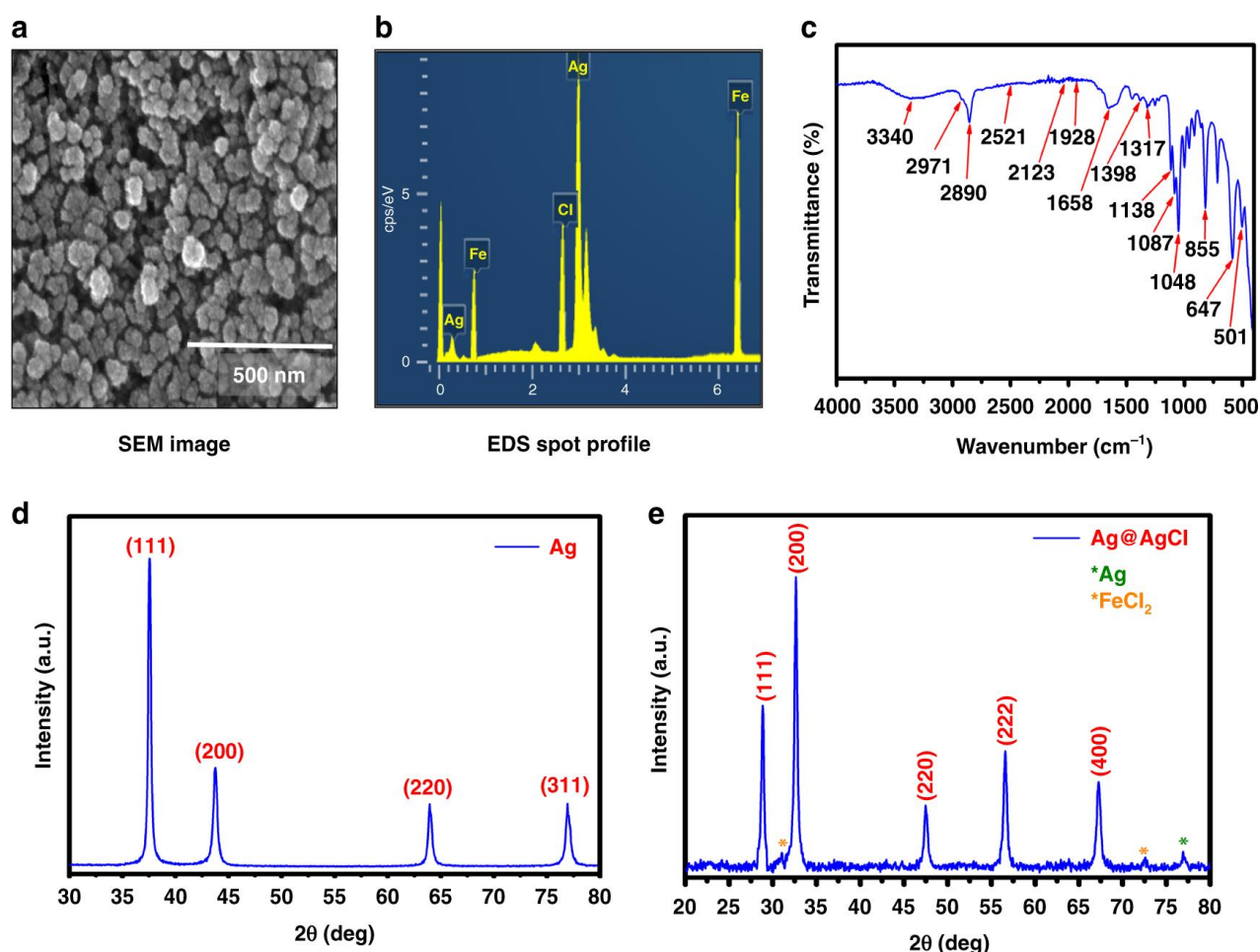


Figure 3.16. (a) SEM image, (b) EDS spot profile, and (c) FTIR analysis of the core shell. XRD pattern of (d) Ag and (e) Ag@AgCl

The preparation of the Ag@AgCl core shell can be observed using Field Emission Scanning Electron Microscope (FESEM) at a magnification scale of 500 nm, as shown in Fig. 3.16a. The average size of Ag@AgCl is ~100–120 nm. The confirmation of the core-shell structure can be observed from the energy-dispersive X-ray spectroscopy (EDS) spot profile, showing the presence of Ag, Fe, and Cl, as shown in Fig. 3.16b. Fourier-transform infrared spectroscopy (FTIR) analysis was performed to identify the presence of possible functional groups within the Ag@AgCl core shell[53], as shown in Fig. 3.16c. The major infrared absorption peaks detected in the Ag@AgCl core shell were 3340 cm^{-1} , 2971 cm^{-1} , 2890 cm^{-1} , 1658 cm^{-1} , 1398 cm^{-1} , 1317 cm^{-1} , 1138 cm^{-1} , 1087 cm^{-1} , 1048 cm^{-1} , 855 cm^{-1} , and 647 cm^{-1} . An intense band of alcohols and phenolic compounds with OH functional groups were observed at 3340 cm^{-1} , whereas aliphatic and aromatic compound side-chain vibrations of C-H stretching were observed at 2971 cm^{-1} and 2890 cm^{-1} , respectively. The peak at 1658 cm^{-1} could be assigned to protein chains with stretching vibrations of C = O and -N-H- (amide I and amide II) bonds.

Peaks located at 1317 cm^{-1} , 1138 cm^{-1} , and 1048 cm^{-1} might be attributed to the presence of stretching vibrations of amino groups, and carboxylic acids and alkyl halide stretching observed at 855 cm^{-1} . The asymmetric deformation of CH_2 and CH_3 in proteins was observed at 1398 cm^{-1} . The C-O-C bonds in polysaccharides were attributed to a peak at 1087 cm^{-1} , which was typically found in the region between 1200 and 900 cm^{-1} . The broad absorption band of the C-H bend alkyne was observed at 647 cm^{-1} .

Figure 3.16d shows the X-Ray Diffraction (XRD) patterns of silver (Ag) thin-film XRD, revealing polycrystalline behavior[53]. The overwhelmingly concentrated peak positioned at $2\theta = 38.02^\circ$ relates to the face-centered cubic structure, revealing that the (111) planes of Ag were highly adapted and parallel to the substrate. Furthermore, we evaluated the average crystallite size by implementing Debye Scherrer's equation, which was found to be 100 nm . Figure 3.16e shows the XRD analysis of Ag@AgCl with peaks centered at $2\theta = 28.5^\circ$, 32.6° , 45.7° , 55.4° , and 63.8° assigned to the (111), (200), (220), (222), and (400) planes, respectively. XRD shows some impurity peaks related to Ag and FeCl_2 compounds with slightly lower intensities and the average crystallite was found to be 32 nm .

3.5.3 Result and Discussion

To achieve a higher $R_{\text{OFF/ON}}$ resistance ratio, the FeCl_3 ink concentration in glycerol was optimized. The $0.2\text{ wt}\%$ FeCl_3 was added to glycerol, to prepare the electrolyte to investigate the resistive memory behavior. The main reason for the resistive switching in FeCl_3 based ILs is due to ion movement between the anode and cathode (such as Fe^{++} , Cu^{++} , and Cl^-). Figure 3.17a shows the possible ionic transport mechanism of FeCl_3 . When a positive voltage was applied to the anode, oxidation was observed, and the copper electrode changed to Cu^{++} . The green color in the solution indicates that the Cu^{++} ions instead of Cu^+ and 2Cl^- ions move to the anode, and copper II chloride (CuCl_2) will be formed. On the cathode, there are two possibilities: (1) Fe^{++} ions move toward the copper electrode and (2) are reduced to Fe at the cathode. During the experiment, an orange color is observed in the electrolyte and this observation indicates that Fe is reduced at the cathode. Another possibility is the formation of Cu^{++} aqueous ions in the electrolyte, as discussed in our first observation, which may reduce to Cu at the cathode, as shown in Fig. 3.17a. The FeCl_3 IL was further characterized for resistive memory characteristics, showing resistive switching behavior, and the device passes from zero, as shown in Fig. 3.17b. To understand the memristive behavior, the device flux is shown in Fig. 3.17c and the device charge is discussed in Fig. 3.17e.

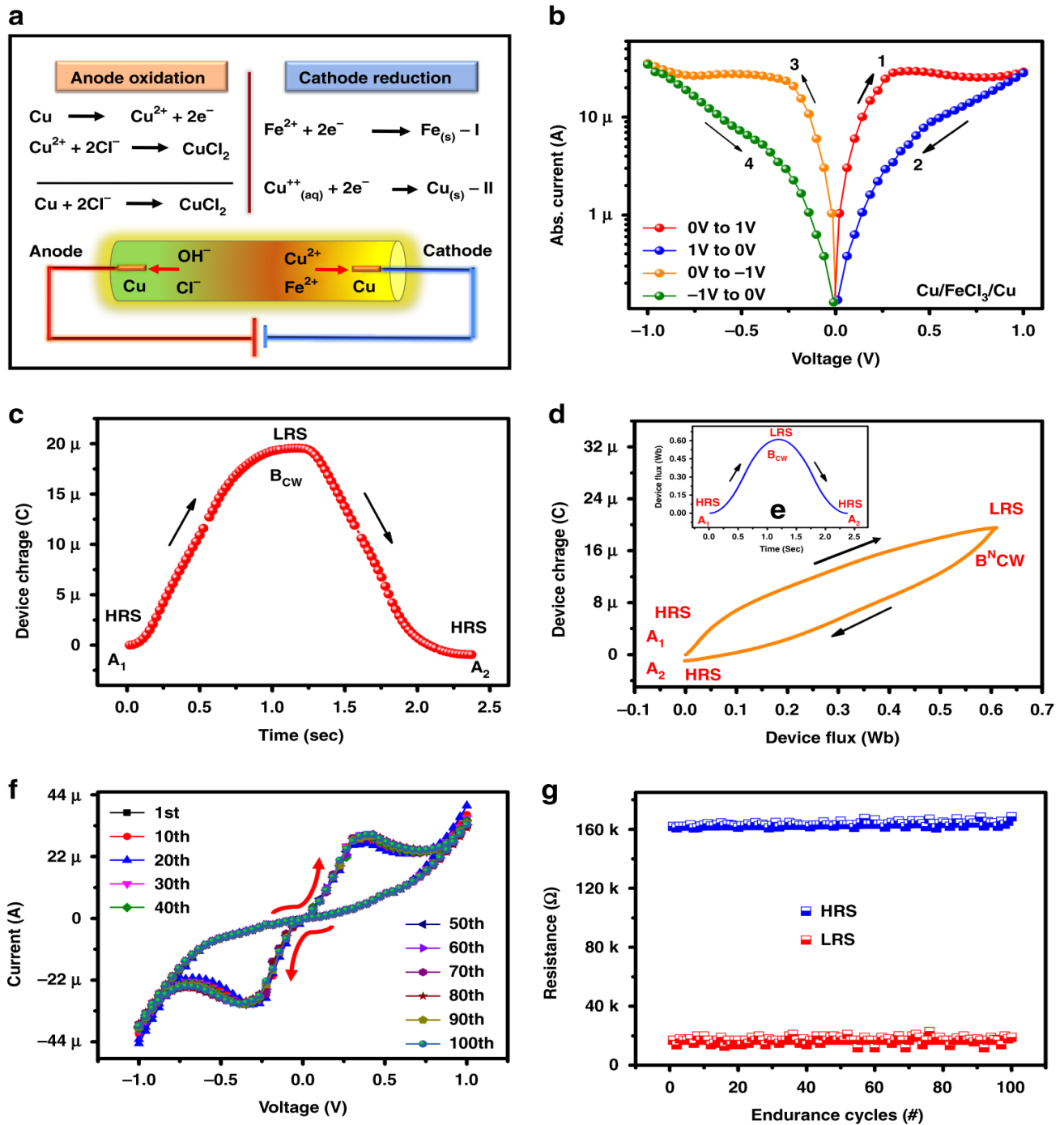


Figure 3.17. (a) Ion conduction mechanism. (b) Semi log I-V curve of Cu/FeCl₃/Cu. (c) Device dose-response with time, (d) charge-flux property of the device, and (e) device flux response with time. (f) 100 I-V sweep cycles and (g) device cycle-to-cycle endurance at a voltage read of 0.15

The ideal memristor device shows nonlinearity in the charge and magnetic flux planes and passivity in the I-V plane, which means that the current should be zero at the origin. The ideal memristor $q-\phi$ characteristics should be nonlinear and single valued. To check whether the devices developed in this work are either memristor or memristive, we calculated the $q-\phi$ characteristics, as shown in Fig. 3.17d, with the help of experimental time-dependent I-V characteristics.

The time-domain charge is given in Fig. 3.17c and flux characteristics are shown in Fig. 3.17e. The initial (A1), final-period (A2), turning (BCWN), and half-period (BCW) points represent the resistive switching states of the memristive device, as shown in Fig. 3.17c–e. The device was in the high resistance state (HRS) at points A1 and A2 and went into the low resistance state (LRS) at the BCWN point. The resistive memory device shows symmetric time-domain flux characteristics, as shown in Fig. 3.17e, because the voltage stimulus is symmetric in nature and its integration ($\varphi(t)$) must be an asymmetric function. However, the time-domain charge characteristics, as shown in Fig. 3.17c, of the FeCl_3 resistive memory device were found to be asymmetric, which indicates that the pinched hysteresis loop of the developed device was asymmetric. Similarly, the nonlinear q – φ characteristic suggests that nonideal memristor properties are observed in the FeCl_3 resistive memory device, as shown in Fig. 3.17d. Cycle-to-cycle repeatability was performed for more than 100 cycles, as shown in Fig. 3.17f, and the device showed stable repeatability. The I–V endurance is shown in Fig. 3.17g with an HRS of 161.9 k Ω and an LRS of 15.4 k Ω at a voltage read of 0.15 V with OFF/ON resistance ratio of ~ 10.51 . To achieve multistate resistive switching, Ag nanoparticles are added to FeCl_3 , which results in the formation of an Ag@AgCl core shell. The formation of a core shell helps to achieve multistate resistive switching to perform neuromorphic computing.

The human brain is composed of interconnected neurons, where the neurons communicate with each other by synaptic plasticity[53]. Synaptic plasticity between presynaptic and postsynaptic neurons is responsible for the efficient functioning of the human brain. As depicted in Fig. 3.15 the transmission process of neurotransmitters (Na^+ or Ca^{2+} ions) initiates neuronal spikes that control synaptic plasticity between presynaptic neurons and postsynaptic neurons[53]. Similarly, the memristor device can also mimic biological synaptic plasticity by gradual variation in the resistance state, using repeated pulse sequences to modulate conduction in the switching layer[53]. To achieve synaptic behavior, an Ag@AgCl core shell was used in the IL. Our core-shell soft resistive memory device synapse is equivalent to the parallel combination of a capacitor with a memristor, as shown in Fig. 3.18a, b. The capacitance[53] behavior can be observed near the origin of the positive voltage region, as shown in Fig. 3.18a, and the negative voltage region, as shown in Fig. 3.18b.

Notably, the presence of the Ag@AgCl core shell and Cu^{2+} ions have a remarkable influence on the device performance under a dual voltage sweep. Multistate resistive switching was achieved by applying dual voltage sweeps on the positive and negative voltage regions, as shown in Fig. 3.18a, b. In the positive and negative voltage regions, the current decreased with an increase in the number of voltage sweeps. Therefore, the resistance state of the Cu/Ag@AgCl/Cu device gradually increases with consecutive voltage sweeps and the conductance of the device decreases.

Thus, the electrical characteristics of the core-shell soft resistive memory device are related to the typical electrical properties of memristive devices used as synapses. The multistate resistive switching is due mainly to the presence of Ag@AgCl core-shell ions in the IL, which resists the flow of Cu^{++} ions, and second, ion metallization at the cathode and anode. The multistate characteristics of the core shell-based IL device were observed during a continuous voltage sweep of $0\text{ V} \rightarrow +1.5\text{ V} \rightarrow 0\text{ V}$. Then, the core-shell IL device shows turn-off behavior when the voltage range is 0 V . During a voltage sweep from $0\text{ V} \rightarrow +1.5\text{ V}$, Cu^{++} ions enter the ionic solution, and the diffusion flux helps to increase the flow of ions and moves toward the cathode. At the same time, a very small amount of Cu^{++} ions react with 2Cl^- ions at the anode and result in the formation of CuCl_2 (oxidation) and release of $2e^-$. However, the movement of Cu^{++} can be reduced by the Ag@AgCl core shell, which was the main reason for the multistate resistive switching. During voltage sweep from $+1.5\text{ V} \rightarrow 0\text{ V}$, the Cu^{++} ions move toward the cathode and accept $2e^-$, which results in a reduction of Cu at the cathode. In this whole process, ionic flux saturates, because ion transportation proceeds with the diffusion of concentration gradient flux, and a decrease in current appears beyond a critical point. The movement of Cu increases at a certain voltage and then the movement of ions decreases, due to which breakage of conduction filaments, and diffusive flux and concentration gradient flux increase until ions are depleted on the Cu electrode, resulting in the creation of a higher resistance value (metallization). Similarly, this sweep cycle repeats every time and results in multistate resistive switching.

To further emulate a biological system, a more sophisticated pulse scheme was implemented to mimic the spike rate-dependent plasticity (SRDP), in which the current and conductance were obtained by applying 100 repetitive pulses of different voltages with a pulse width of 1 ms to the Cu/Ag@AgCl/Cu device, as shown in Fig. 3.18c, d. The gradual variation in the current and conductance with pulses is similar to a variable synaptic weight in bio synapses. In the Ag@AgCl core-shell device, a similar phenomenon also exists after inverting the polarity on the positive or negative voltage region, as shown in Fig. 3.18c, d. These results indicate that the Ag@AgCl core-shell soft IL and flexible synaptic device behave like brain neuronal activation. Thus, the electrical characteristics are related to the typical electrical properties of memristives used as synapses. Figure 3.18e, f shows the measured current under a five triangular voltage sweep with a period of 2 s. The conducting current varied with time, as shown in Fig. 3.18e, f. We can see that the device current nonlinearly decreases in the negative and positive voltage sweep regions.

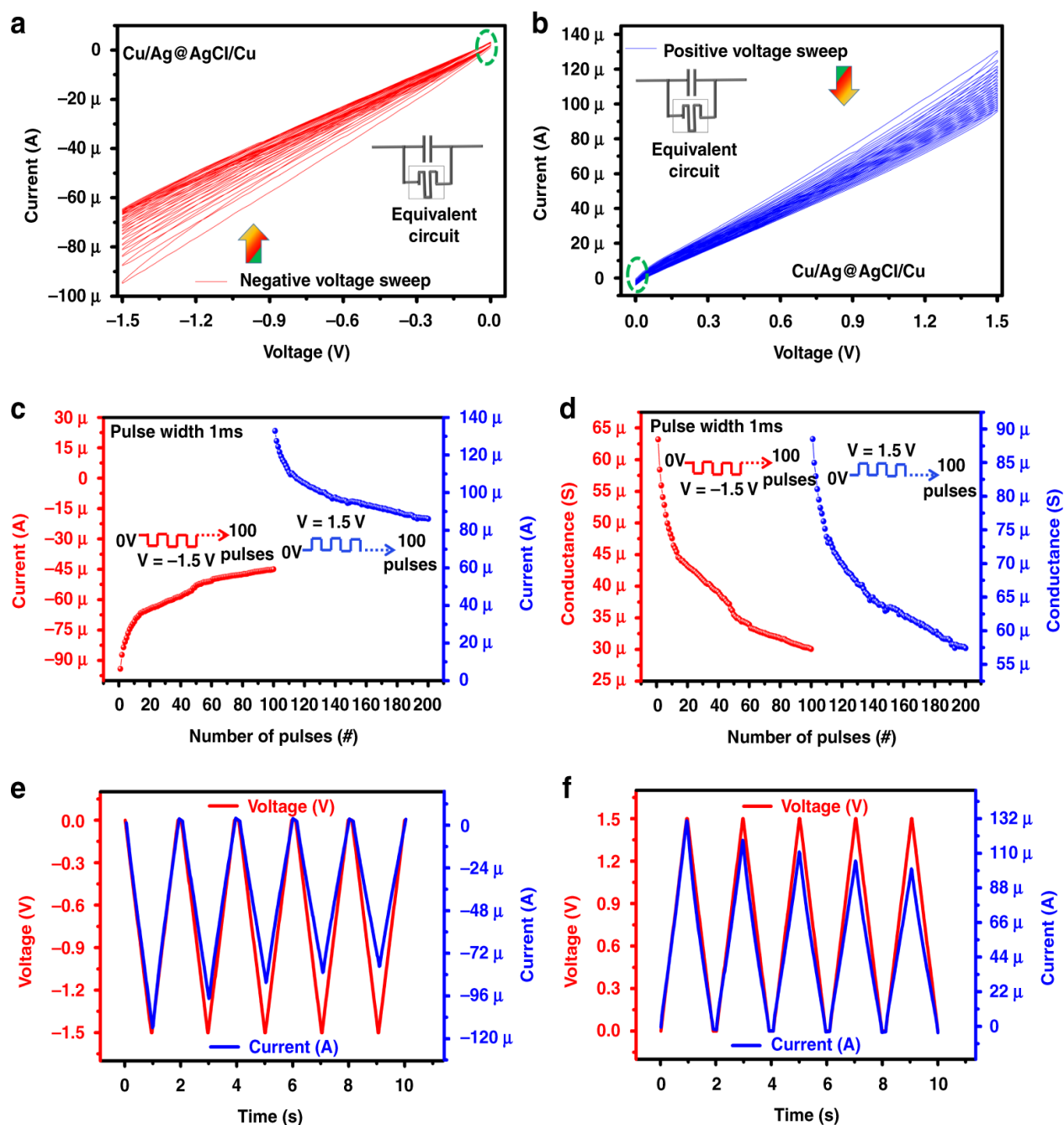


Figure 3.18. (a) Multistate I–V curve of Cu/Ag@AgCl/Cu in a negative voltage region and (b) positive voltage region. The (c) current and (d) conductance response of the device for a pulse width of 1 ms with a reading pulse amplitude of -1.5 V on negative and 1.5 V on positive voltage region. The triangular pulse response in (e) negative and (f) positive voltage regions

The synaptic weight of the Cu/Ag@AgCl/Cu core-shell IL artificial synapse device is defined by the current of the multistate switching and can be modulated by successive stimuli of externally applied pulses of different widths. Therefore, pulse widths of $200\ \mu\text{s}$, $400\ \mu\text{s}$, $600\ \mu\text{s}$, $800\ \mu\text{s}$, and $1\ \text{ms}$ were investigated by applying 100 consecutive synaptic pulses with an amplitude of $1.5\ \text{V}$, as shown in Fig. 3.19a.

In the case of a pulse width of 200 μs with 100 consecutive pulses, no obvious decrease in the current was observed. However, by increasing the pulse width to 1 ms, the synaptic current changes significantly from 136 to 97 μA compared to a pulse width of 200, 400, 600, and 800 μs . This phenomenon is basically due to better ionic diffusion at higher pulse widths, which provides a higher change in current.

The SRDP of the soft core-shell resistive memory device was examined by varying the frequency, as shown in Fig. 3.19b, and different amplitudes of the pulses, as shown in Fig. 3.19c. For 100 consecutive pulses with an amplitude of 1.5 V and a width of 1 ms, there is almost no increase in the response current at a given frequency of 1.1 Hz. However, when the frequency increases to 7.8 Hz, the current decreasing rate (135–95 μA) is larger than the current decreasing rate of previous conditions with lower frequencies (1.1, 2.4, and 4.5 Hz), as illustrated in Fig. 3.19b. This behavior is related to the competition between the interval between two pulses and the relaxation time of the artificial synapse, which can be considered metallization of the electrode, and its rate increases with higher frequencies. When the amplitude of 100 pulses on voltage is 1.5, 1, 0.7, and 0.5 V with a pulse width of 1 ms, the current decrease rate becomes even smaller in the lower voltage range, as illustrated in Fig. 3.19c, which corresponds to slow movement of diffusion flow of ions and results in a decrease in the rate of metallization. The decay of the synaptic weight of the Cu/Ag@AgCl/Cu core-shell IL artificial synapse device is shown in Fig. 3.19d. To obtain the forgetting curve, presynaptic input pulses were applied with $V = 1.5$ V and pulse width = 1 ms by keeping the device in the LRS state. As a result, the postsynaptic current is monitored with time.

This experimental part is based on the demonstration of device bending, which can open a gateway for future IL device structures to intergrade in soft electronics. The bending and flexible nature of the device was due to the usage of the main component of the Ag@AgCl core-shell electrolyte and polydimethylsiloxane (PDMS) substrate, as shown in Fig. 3.19e. The bending state current was obtained by applying 100 repetitive pulses of 1.5 V and -1.5 V in the positive and negative voltage regions, respectively, with a pulse width of 1 ms, as shown in Fig. 3.19e. The flexible nature of the device helps to achieve stable bending performance and can be used as a synaptic device. This study opens a gateway for soft and liquid-switching media for electronic synapses.

Figure 3.20a shows the neuromorphic simulation structure. The input image data based on CIFAR-10 are used for training and testing. The simulation is composed of six convolutional neural networks and two fully connected layers[53], as shown in Fig. 3.20a. The 100 continuous input pulses of amplitude +1.3 V and -1.3 V, respectively, with a pulse width of 1 ms were applied to investigate the current change in the positive and negative regions, as shown in Fig. 3.20b.

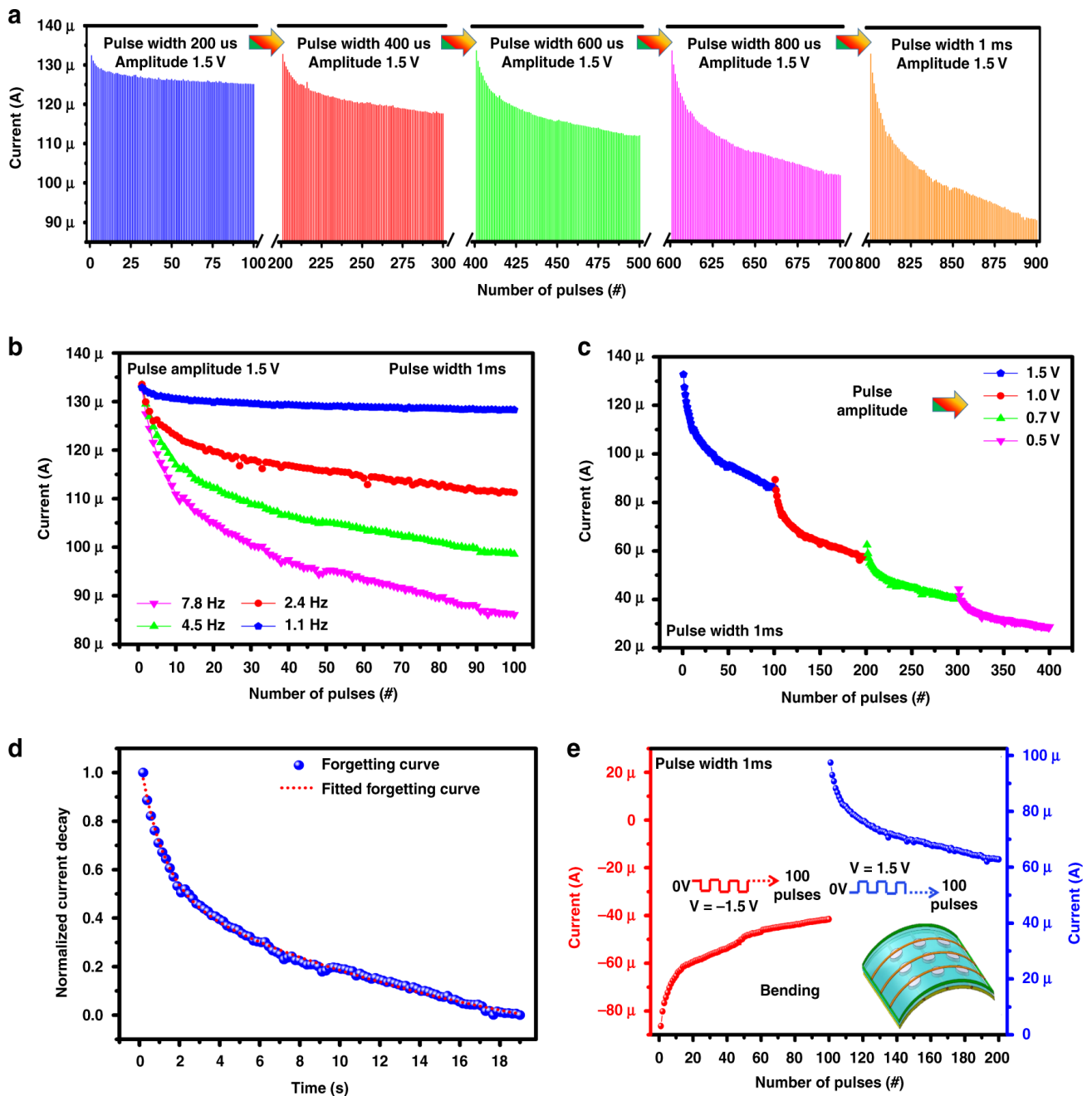


Figure 3.19. (a) Plasticity characteristics of the artificial synapse with different pulse widths of 200 μ s, 400 μ s, 600 μ s, 800 μ s, and 1 ms. (b) Frequency response at 1.1, 2.4, 4.5, and 7.8 Hz. (c) The different pulse amplitude responses at 1.5, 1.0, 0.7, and 0.5 V. (d) The forgetting curve of the neuromorphic device. (e) Bending test of the device under a continuous pulse train.

The data given in Fig. 3.20b were applied to perform deep learning, to investigate the system accuracy using DNN_NeuroSim_V2.129. The analog weight nonlinearities are ~ 3.74 for a positive pulse current and 4.17 for a negative pulse current for the data given in Fig. 3.20b, and the cycle-to-cycle variation is measured as 0.003. As the simulation result shows in Fig. 3.20c, the maximum network learning accuracy converges to 85% under 200 epochs.

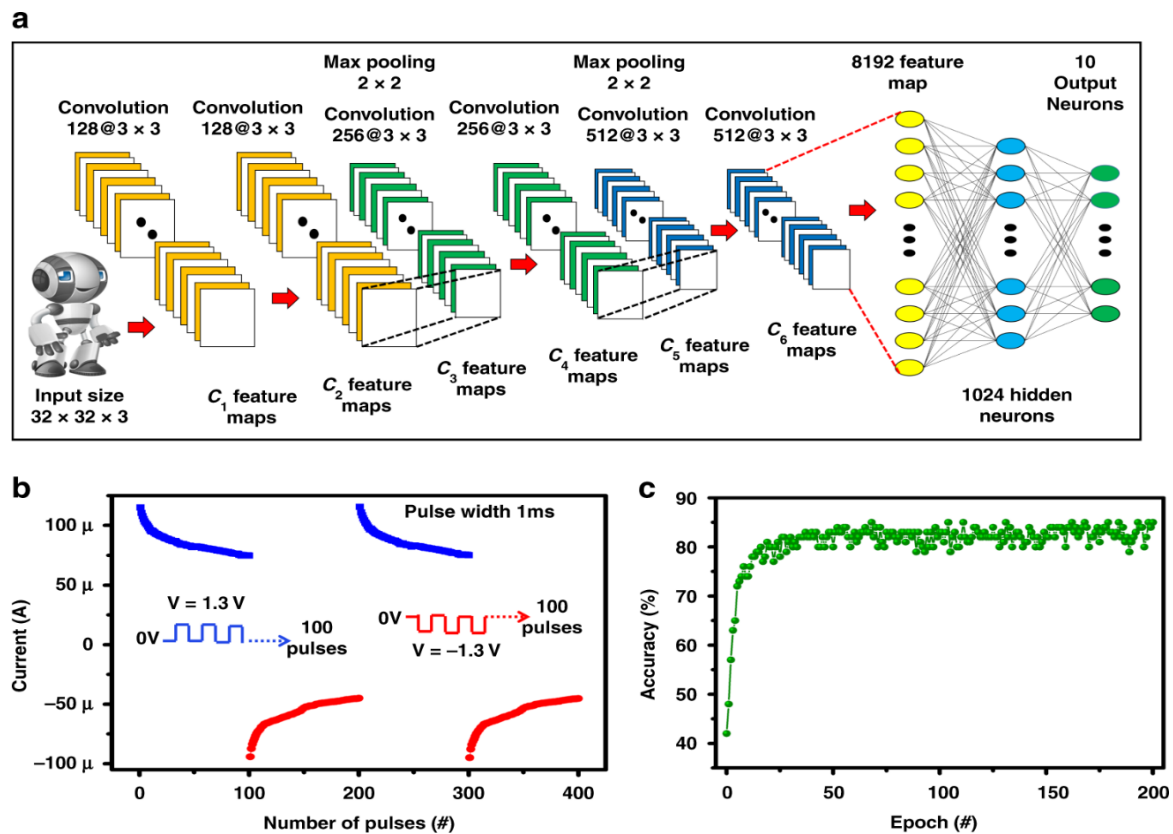


Figure 3.20. (a) The convolutional neural network. (b) Synaptic plasticity under a continuous pulse train. (c) Simulated accuracy of each epoch during training

This mechanism part, as shown in Fig. 3.21, illustrates only the flow of Cu ions in a working mechanism of core shell-based IL. The multistate resistive switching is due to the movement of Cu ions, which can be regulated by tuning the amplitude of the applied voltage. The multistate resistive switching characteristics of the core shell-based device are illustrated in Fig. 3.21, in which a positive voltage sweep (V_{cc}) was applied on the top electrode to the anode Cu electrode and the ground was applied to the bottom cathode Cu electrode.

During forward voltage sweep $0 \text{ V} \rightarrow 1.5 \text{ V}$, initially at $V_{cc} = 0$, there is no movement of Cu ions, and the device remains in the HRS state. If $V_{cc} > 0 \text{ V}$, then the core-shell IL device shows turn-off behavior. The IL device with “ON” and “OFF” states depend solely on the time during which conduction filaments form between the anode and cathode. During the $V_{cc} > 0 \text{ V}$ state, Cu^{++} ions start entering an ionic solution and the diffusion flux helps to increase the flow of ions. When the voltage range is between $V_{cc} < \text{threshold voltage } (V_{th})$, ions move toward the cathode and, at the same time, a very small amount of Cu^{++} ions react with OH^- ions at the anode, resulting in the formation of $\text{Cu}(\text{OH})_2$ (oxidation) and releasing $2e^-$. At a voltage state of $V_{cc} = V_{th}$, the Cu^{++} ions move toward the cathode and accept $2e^-$, which results in a reduction of Cu at the cathode, as illustrated in Fig. 3.21.

At the same time, the presence of Ag@AgCl core-shell nanoparticles restricted the movement of Cu^{++} ions, which became the main reason for multistate resistive switching. In this whole process, ionic flux saturates, because ion transportation proceeds with the diffusion of concentration gradient flux and a decrease in current appears beyond a critical point. During reverse voltage sweep $1.5 \text{ V} \rightarrow 0 \text{ V}$, movement of Cu ions increases at a certain value of voltage and then the movement of ions decreases, due to which breakage of the conduction filament occurs and the off state at voltage state $0 \text{ V} < V_{\text{cc}} < V_{\text{th}}$ was due to diffusive flux and concentration gradient flux increases until ions are depleted on the Cu electrode resulting in the creation of a higher resistance value at $V_{\text{cc}} = 0 \text{ V}$. This process will repeat during every voltage sweep, which results in the multistate resistive switching behavior.

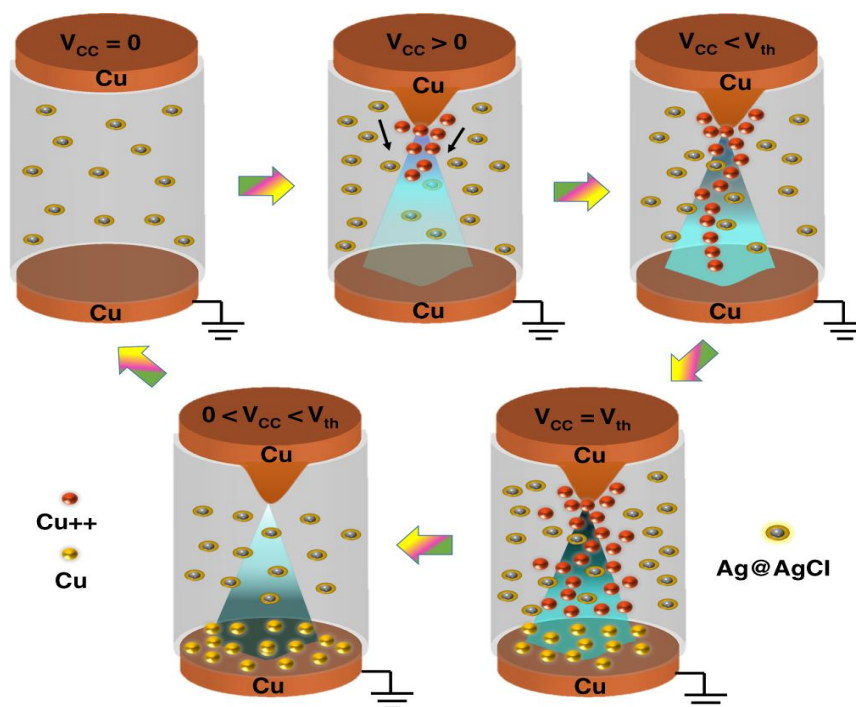


Figure 3.21. The working mechanism of the core-shell soft ionic liquid neuromorphic device

3.5.4 Summary

In conclusion, this study has proposed a core-shell soft IL-resistive memory device for electronic synapses with a Cu/Ag@AgCl/Cu structure. The mechanism of the core shell-based device is highly dependent on ion concentration polarization, which is the main reason for synaptic behavior. Synaptic plastic behavior was observed in both positive and negative voltage regions to investigate the pulse width, frequency, and pulse amplitude. The mechanical bending test demonstrates stable synaptic behavior. We are sure that core-shell IL devices can open a gateway for the development of a highly efficient and soft brain-mimicking system.

Chapter 4 Sensors

4.1 Biocompatible Organic Humidity Sensor Based on Natural Inner Eggshell Membrane

In environment sensing, there are various factors to be detected like humidity level[11, 12, 65, 92-96], temperature[97], various gases (NH_3 , H_2S , etc.)[65], and light intensity[9, 10]. In these features, a humidity sensing is widely investigated by many researchers[65, 98]. Sensors based on impedance and capacitance responses are the best choice for humidity sensing due to low cost, easy fabrication, and nominal time response[98], which can detect amount of water content in environment with following parameters like impedance[65], capacitance[65] and resistance[65, 98]. To fabricate a humidity sensor, the various materials are studied like, graphene, organic, inorganic, organic-inorganic nano-composite, and other composites[99].

For an eco-friendly, low cost and high-performance devices, many researchers are exploring natural materials, for example, humidity sensing layer and substrate using onion membrane[100], piezoelectric nanogenerator using onion skin[101], silk fiber applied in electronic devices and non-volatile resistive memory[102], and fish scale based piezoelectric nanogenerator[103]. Hence, a biomaterial can be obtained from a hen egg, and it is widely using as food in the world. It can be applied in different applications like egg albumen as an active layer for non-volatile resistive memory[104], a high-performance electrode for super capacitor using carbonized eggshell membrane[105], a biosensor to determine the glucose using inner eggshell membrane (IESM)[106], and piezoelectric flexible nanogenerator using IESM[107].

Although the IESM is structured with natural multilayer cross-linked fibers, it is not applied for a humidity sensor[92]. The natural biomaterials available in our daily life have potential to be employed in sensing applications as they can opens a new possibility towards bio-compatible electronic devices. Many researchers are focusing on transferable, wearable, and implantable electronic devices on thin substrates, which are highly flexible and light in weight[92]. Moreover, such substrates are used only to support device printed on them with no sensing properties and additional sensing layer is required to be top printed on electrodes[92].

For these attributes, natural biological organic materials available in our daily life are very attractive for sensing in wearable electronic devices. In this expectation, to achieve good results, the various printing methods are utilizing for high performance and transferable wearable devices[92]. The conventional printing methods utilized to transfer wearable electronic devices are very complex and damage may occur while transferring to arbitrary shaped substrate. While an IESM is ultra-thin with thickness of $\sim 19 \mu\text{m}$, it is allowed to transfer to any arbitrary shaped substrate. The IESM can be transfer in a single step to an arbitrary shape substrate without causing any damage.

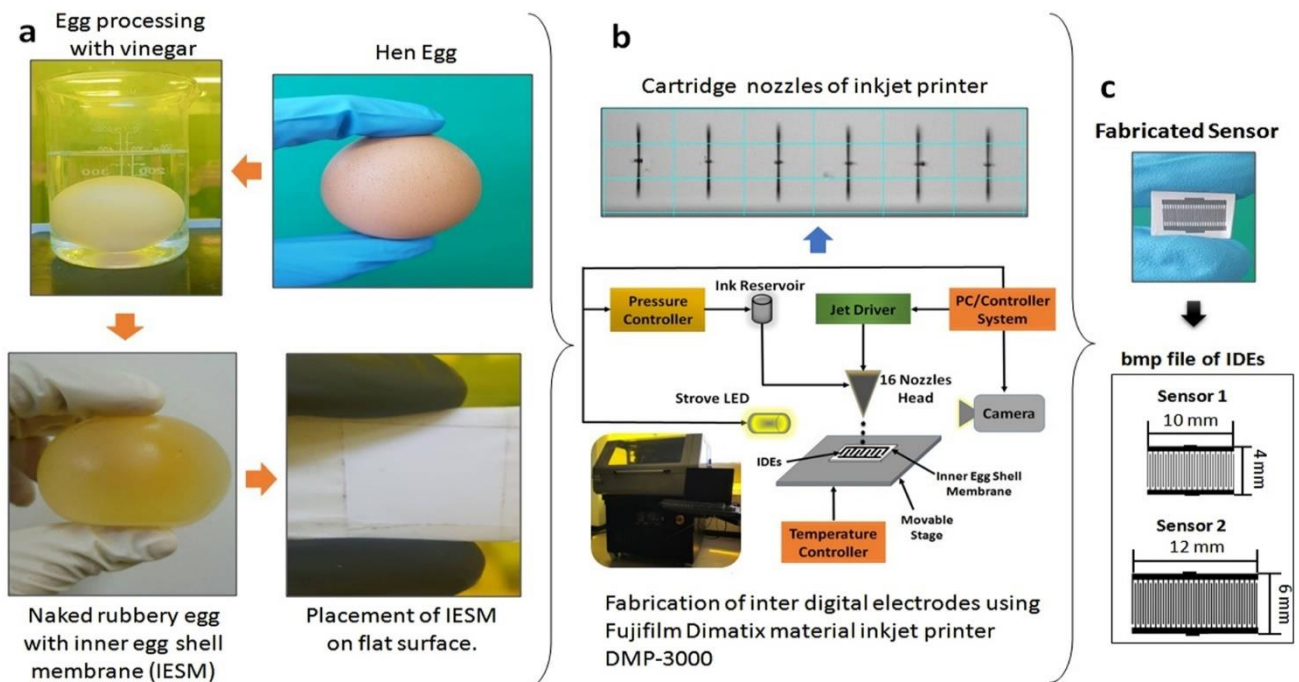


Figure 4.1. (a) The Processing of the IESM. (b) The wave shape of printing nozzles of the Fujifilm DMP-3000 inkjet printer. (c) Dimension of the IDEs and Printed IDEs on the surface of the IESM using inkjet printer.

The proposed humidity sensor is fabricated by using the IESM as an active sensing layer and substrate. The IESM is contacted with the egg albumen and an external contact with the eggshell minerals[108]. Especially, the IESM has fibrous and porous structure, which is a suitable to absorb a permeable solvent like water; hence it can be used as a humidity sensing active layer. To get a signal from the IESM, we fabricated inter digital electrodes (IDEs) pattern with finger width of $100 \mu\text{m}$ and spacing of $100 \mu\text{m}$ through Fujifilm Dimatix DMP-3000 material as shown in Fig. 4.1. The fabricated sensor is tested with homemade humidity sensing setup, which has an impedance and capacitance response range from 0% RH to 90% RH, and this bio-compatible humidity sensor achieves a response time (T_{res}) of $\sim 1.99 \text{ sec}$ and a recovery time (T_{rec}) of $\sim 8.76 \text{ sec}$ using sensor 1 and T_{res} of $\sim 2.32 \text{ sec}$ and T_{rec} of $\sim 9.21 \text{ sec}$ using sensor 2.

4.1.1 Materials and Methods

Fresh egg was processed using white vinegar. The humidity sensing electrodes were patterned on the surface of the IESM using the Ag nanoparticle ink with 50% dispersion in triethylene glycol monomethyl ether (TGME). Ethanol and de-ionized water were used for cleaning purpose and purchased from sigma Aldrich. The silver (Ag) conductive epoxy CW2400 was used for connecting wires and purchased from circuitworks. Dry nitrogen gas (N_2) was used as dehumidification.

The manual separation of the IESM can be done, but it is difficult to obtain the IESM as it is tightly bonded to the mineral shell[92]. The eggshell is made of calcium carbonate crystals. It consist of a porous structure, that is why IESM is called semi permeable membrane[92]. IESM can be easily extracted by dipping the egg in vinegar. The IESM processing is given in Fig. 4.1a as we dipped the egg in vinegar at room temperature 28 °C. During reaction tiny bubbles of CO_2 will be released on the surface of vinegar, as a result it will release carbon dioxide (CO_2)[92]. Then, the naked rubbery egg will remain at the end after 3 days. We make a small hole on the surface of the IESM and pour out the yolk and albumen. The IESM was cleaned with 20 ml ethanol and 30 ml de-ionized water and place it on a flat surface in a high-tension wet state to remove all the water trapped inside the membrane and make it dry at room temperature as shown in Fig. 4.1a. To fabricate the proposed sensor 1 and sensor 2 on the surface IESM, the IDEs were designed using EAGLE version 7 in dxf format. The design file was converted into bmp file format using ACE 3000 and exported to Dimatix Drop manager software, which converts bmp into ptn format. The ptn file was loaded into software-controlled Fujifilm Dimatix DMP-3000 material inkjet printer. The Ag ink was loaded in 10 pL 16 nozzles cartridge with diameter of 9 μm . The 30 V were applied on cartridge nozzles for a stable printing with drop spacing of 20 μm as shown in Fig. 4.1b and c temperature of the printing platform was controlled at 30 °C through software control system attached with the inkjet printer. IESM was pasted on a flat PET and wrinkles were removed using a tissue paper and it was fixed at its position using tape. The proposed sensor was fabricated by printing IDEs on the surface of IESM through Fujifilm Dimatix DMP-3000 material inkjet printer. The IESM was selected due to good moisture sensitivity, and it can easily detect a small change of humidity. The applied IDEs were designed as electrode finger width of $\sim 100 \mu m$ and electrode space of $\sim 100 \mu m$ as shown in Fig. 4.1c, and these parameters were optimized through experimental process to achieve a high sensitivity of the IESM. The IESM were cracked at high temperature annealing due to shrinking of organic nature of thin membrane. That's why fabricated IDEs are cured at low annealing temperature for longer time duration at 30 °C for 1 hour as given in Fig. 4.1a.

4.1.2 Characterization

Different characterization techniques are used to investigate the chemical and structure composition of IESM. The SEM has been powerful tool for characterizing fundamental physical properties and surface morphology of the samples. The morphology of IESM can be studied by coating sample with platinum (Pt) sputter using Pt 20 mA 120 mode with Scanning electron microscopy (SEM) Jeol JSM-7600F. The damages may occur on the surface of an IESM during fabrication process. For this reason, the fabricated sensor was observed with optical microscope after each step to make sure that, IESM was intact, and IDEs were properly fabricated with the DMP-3000 inkjet printer. 2D and 3D nano profile of top electrode and IESM was analyzed with NV-2000 Universal non-contact surface profiler for roughness measurement in phase shifting interferometry (PSI) mode. The Fourier transform infrared spectroscopy (FTIR) spectra of an IESM were recorded on a Bruker IFS 66 V spectrometer by using the potassium bromide (KBr) pellet, at a resolution 4 cm^{-1} . EDS mapping is performed to confirm the element-by-element composition of IESM using TESCAN MIRA 3 STEM.

Hen egg is shown in Fig. 4.2a, which insure that IESM is present between egg albumen and eggshell. The IESM is consisted of an intricate lattice network of fibers[92]. A network-like structure is perceived in the natural IESM with $10\text{ }\mu\text{m}$ scale at $\times 500$ magnification as shown in Fig. 4.2b. This indicates that the IESM is consisted of cavities and pores of diameter $5\text{ }\mu\text{m}$ and has highly crosslinked fibers of protein with diameter $0.5\text{--}1.5\text{ }\mu\text{m}$. Figure 4.2c shows the microscopic image of the patterned IDEs. The 2D and 3D nano profile of the IDEs is illustrate as shown in Fig. 4.2c and d, which ensures that electrodes are properly fabricated with the inkjet printer. Figure 4.2f shows the surface morphology of IDEs with magnification level of $10\text{ }\mu\text{m}$, which ensures that the electrodes are properly fabricated on the surface of IESM. The cross sectional of an IESM is shown in Fig. 4.3a with magnification level of $20\text{ }\mu\text{m}$, which indicate that dried IESM have thickness of $\sim 19\text{ }\mu\text{m}$. The variability of the thickness of dried IESM is presented in Fig. 4.3a with mean value (μ) of $19.67\text{ }\mu\text{m}$, standard deviation (σ) of $0.94\text{ }\mu\text{m}$ and variance (σ^2) of $0.89\text{ }\mu\text{m}$. These results shows that the thickness of the dried IESM is almost uniform with small value of standard deviation as shown in Fig. 4.3a. The 2D and 3D nano profile of the printed IDEs is shown in Fig. 4.2c and d, which indicates that printed electrodes have roughness of 197.33 nm and the IDEs are uniformly fabricated. The height profile of IDEs is shown in Fig. 4.2e, which indicate that average height of the Ag nanoparticle-based IDEs is $\sim 1.77\text{ }\mu\text{m}$.

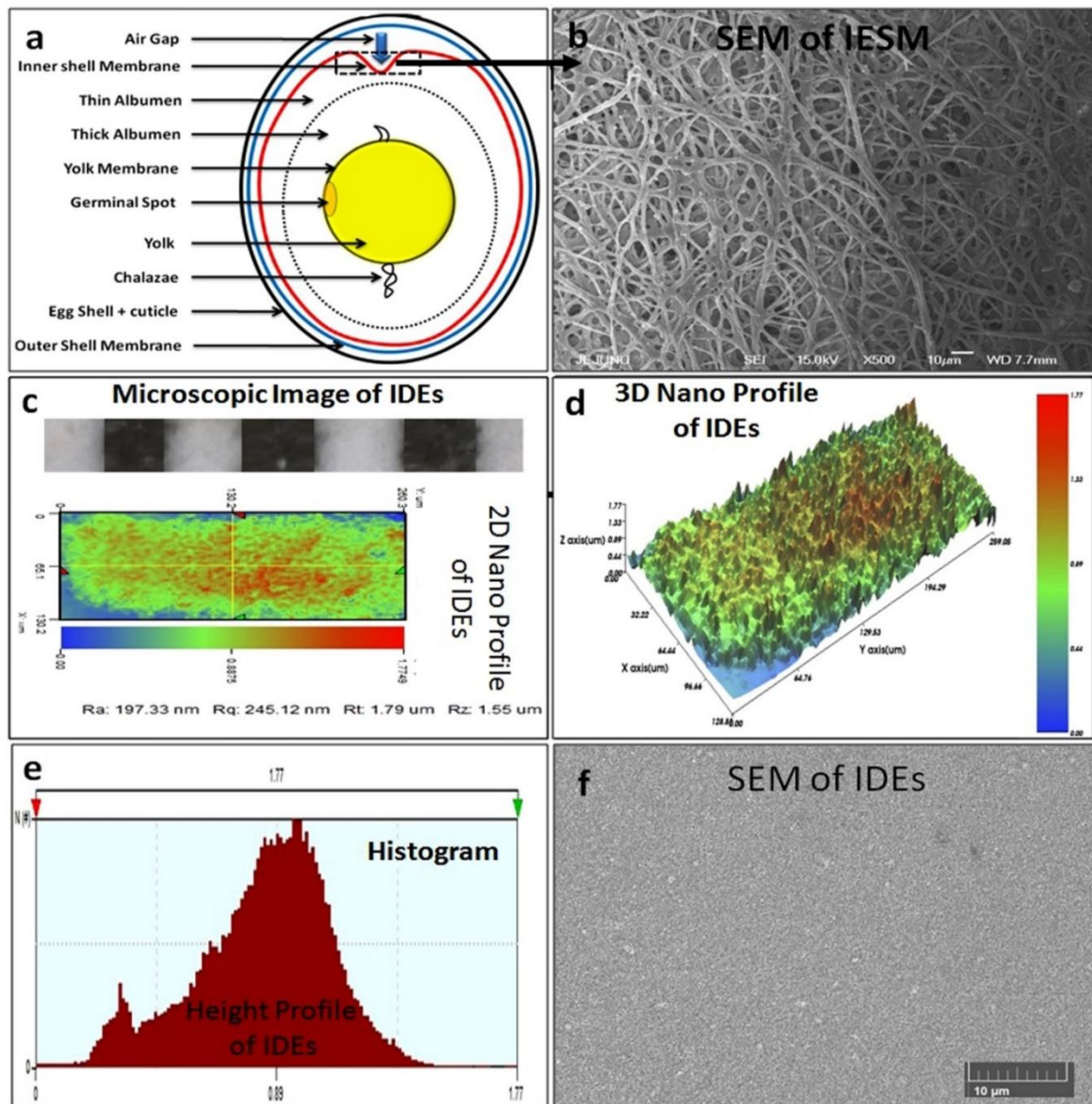


Figure 4.2. (a) Structural image of hen egg. (b) FESEM image of IESM. (c) Microscopic image of printed IDEs showing electrode width of 100 μm and electrode spacing of 100 μm . 2D surface roughness of 197.33 nm and (d) 3D surface nano profile with thickness of 1.77 μm . (e) Histogram of height for nano profile of IDEs. (f) SEM image of the IDEs.

The Fourier transform infrared spectroscopy-potassium bromide (FTIR-KBr) spectra of IESM showed the characteristic absorption peaks related to the organic structure of the membrane. In the FTIR spectra of an IESM shown in Fig. 4.3b, the amide and protein characteristic peaks are found as three highly intense peaks. Amide I show two sharper bands of C=O stretching vibrations at 1650 cm^{-1} , amide II shows NH in plane bending and CN stretching at 1440 cm^{-1} , and amide A shows NH stretching vibration at 3400 cm^{-1} . An absorption band shows stretching vibration of C-S bonds appeared at 670 cm^{-1} , which is associated with cysteine-rich proteins of an IESM fibers[92]. A sharp absorption peak of eggshell was also present at 875 cm^{-1} which shows out of the plane bending vibration of (CO_3^{2-})[92].

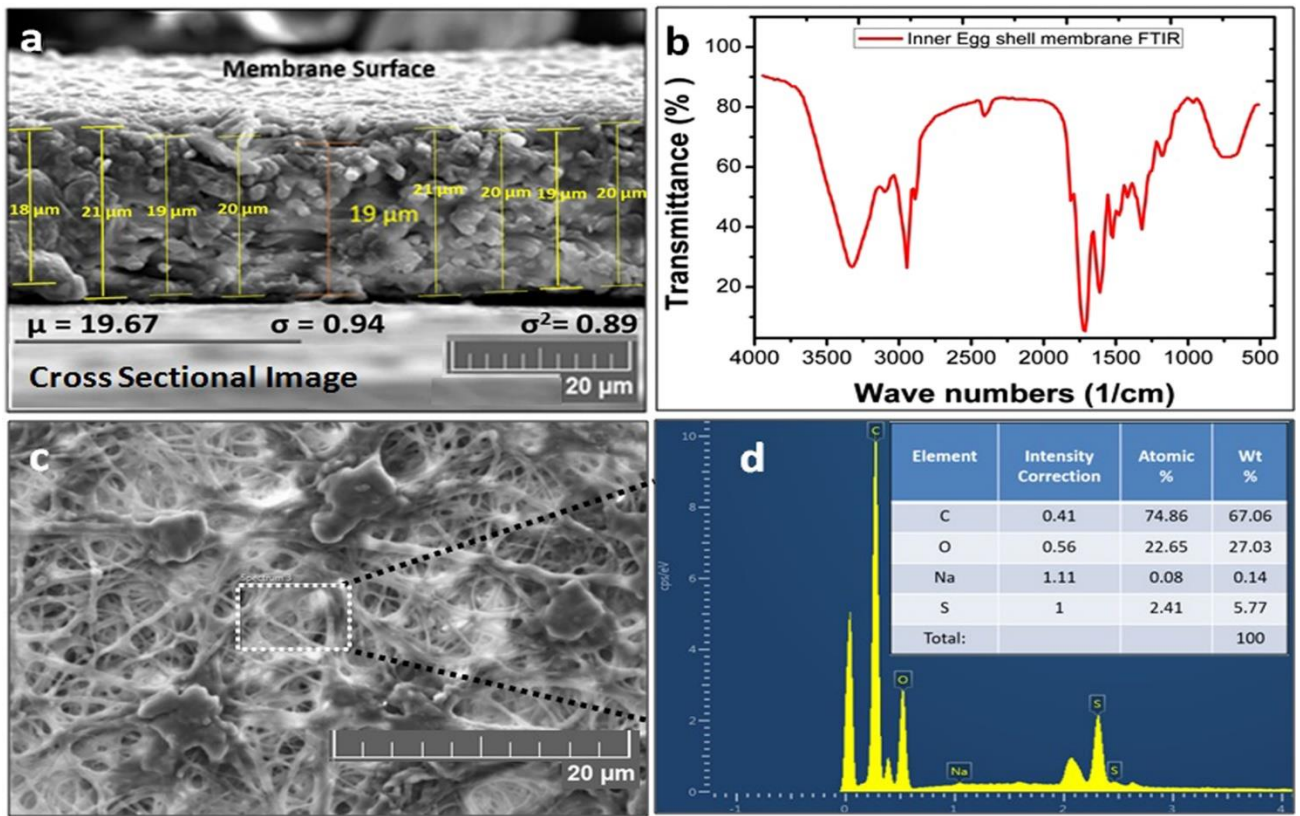


Figure 4.3. (a) Cross sectional image of IESM. (b) FTIR of the IESM. (c) Surface morphology of the IESM using TESCAN MIRA 3. (d) The EDS representation of the IESM and insert image showing element composition of the IESM.

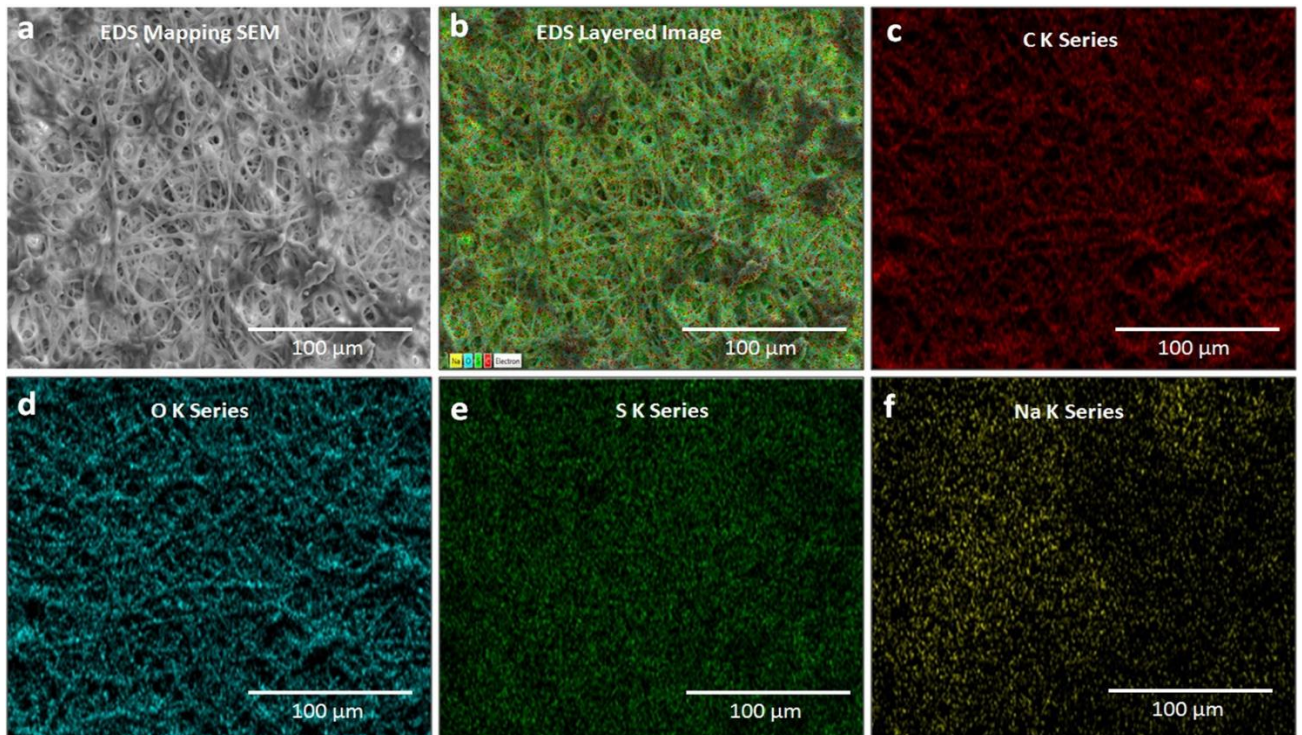


Figure 4.4. (a) EDS mapping SEM image of IES. (b) EDS layer image, and element mapping of the IESM representing as (c) C K series, (d) O K series, (e) S K series, and (f) Na K series.

The elemental composition on the surface of IESM can be confirmed by energy dispersive X-ray spectroscopy (EDS) as depicted in Fig. 4.3c with magnification of 20 μm . The EDS energy dispersive analysis of X-ray spot profile of the IESM clearly shows peaks of C, O, S and Na as inset shown of Fig. 4.3d. EDS mapping of the IESM is performed with TESCAN MIRA 3. As EDS SEM image is shown in Fig. 4.4a, it shows the magnification level of 100 μm and Fig. 4.4b shows the EDS layered image which insurances the presence of carbon series with weight 67.06%, Oxygen series with weight 27.03%, Sulfur series with weight 5.77%, and Sodium series with weight 0.14% as shown in Fig. 4.4c–f. EDS confirms the presence of carbonyl, amino protein, and carboxyl group as we discussed in FTIR of IESM.

4.1.3 Result and Discussion

Humidity setup consist of airtight homemade humidity box, HTU21D sensor with resolution 0.04% RH, accuracy $\pm 2\%$ RH, temperature coefficient -0.15% RH/ $^{\circ}\text{C}$ and response time < 5 sec was used as a reference sensor. Arduino UNO is used as a controlling board and PC is used for data acquisition. The impedance of the fabricated sensor was measured with KEYSIGHT Digital U1700C handled LCR meter.

Figure 4.5 shows the block diagram of the humidity setup. The airtight humidity box covers the humidity from 0% to 100% RH respectively with reference sensor and the IESM as a sensing layer and substrate with printed IDEs used as a SUT. The reference sensor is connected with Arduino UNO and SUT is connected with LCR meter. For real time data acquisition, LCR meter and Arduino UNO are connected with PC through data line (USB port) for automatic data logging. The dry N_2 is injected for dehumidification level from 40% to 0% and the commercialized humidifier is used to increase the humidification level from 0% to 100%. The external valve is used to control the level of humidity inside airtight box using humidifier and N_2 gas. The temperature of the experiment setup was controlled at 25 $^{\circ}\text{C}$. Figure 4.5 shows the realized image of the humidity setup. Using this setup, we measured the proposed sensors. The transient response is measured with sudden increase in humidity level from 0% RH to 100% RH and then dehumidified the sensor from 100% RH to 0% RH.

The impedance response of the humidity sensor was recorded on different levels of humidity in the environment. The effect of humidity on the surface of the IESM was recorded on different frequencies as shown in Fig. 4.6. These results clearly indicate that the impedance of Sensor under test (SUT) is decreased with increase in humidity level. This behavior is consistent at 1 kHz and 10 kHz of sensor 1 and sensor 2 as shown in Fig. 4.6a–d. The increase in test frequency results in the decrease in the impedance state of the SUT.

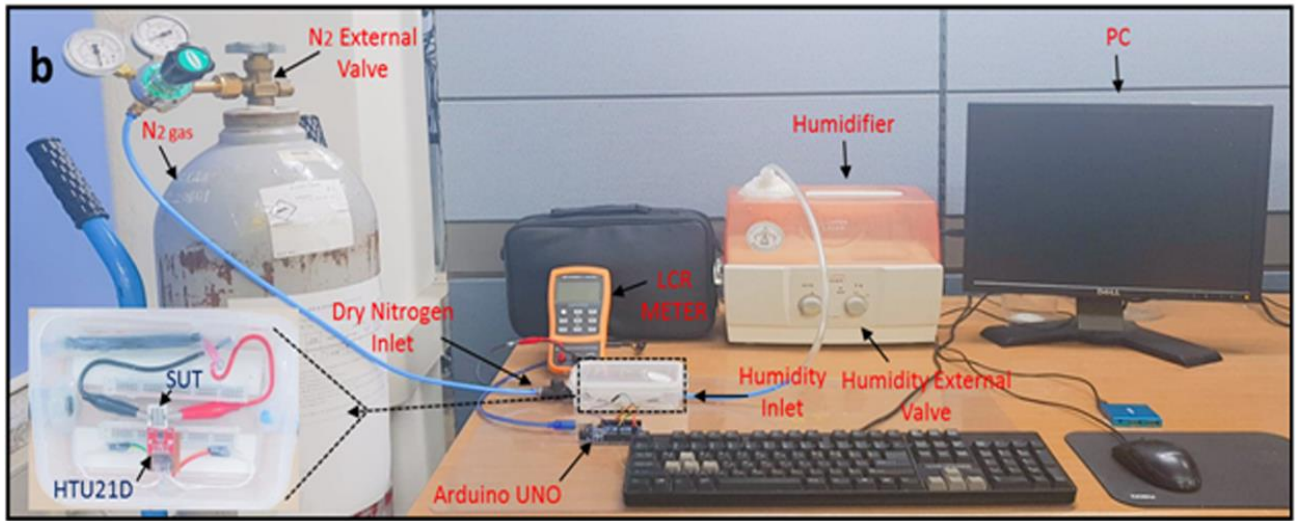


Figure 4.5. Realized image of the humidity setup using Arduino UNO, DHT21D humidity sensor, sensor under test (SUT), KEYSIGHT LCR meter, humidifier, dry nitrogen (N2), LCD, and PC.

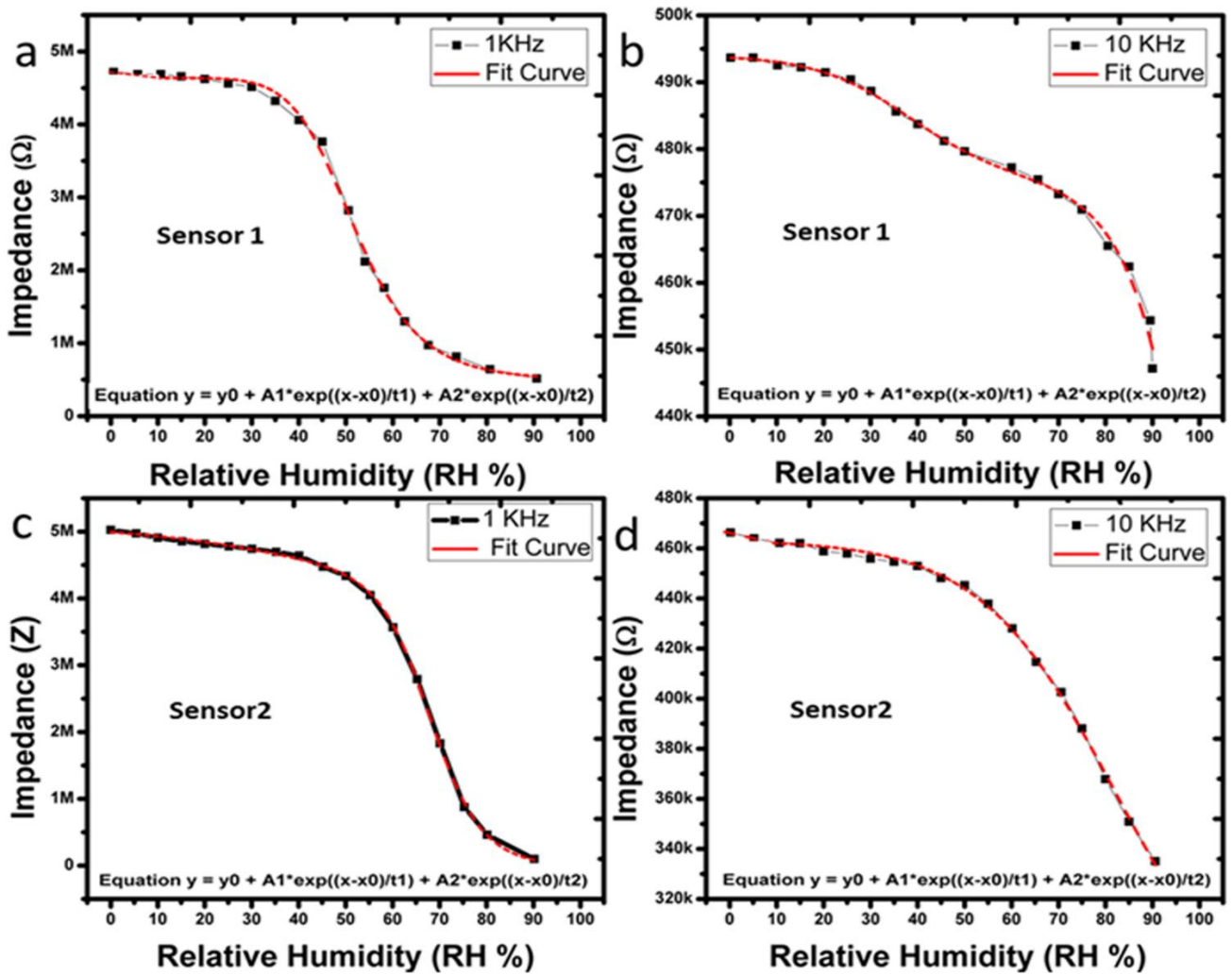


Figure 4.6. Impedance response of the sensor 1 at (a) 1 kHz and (b) 10 kHz. Impedance response of the sensor 2 at (c) 1 kHz and (d) 10 kHz.

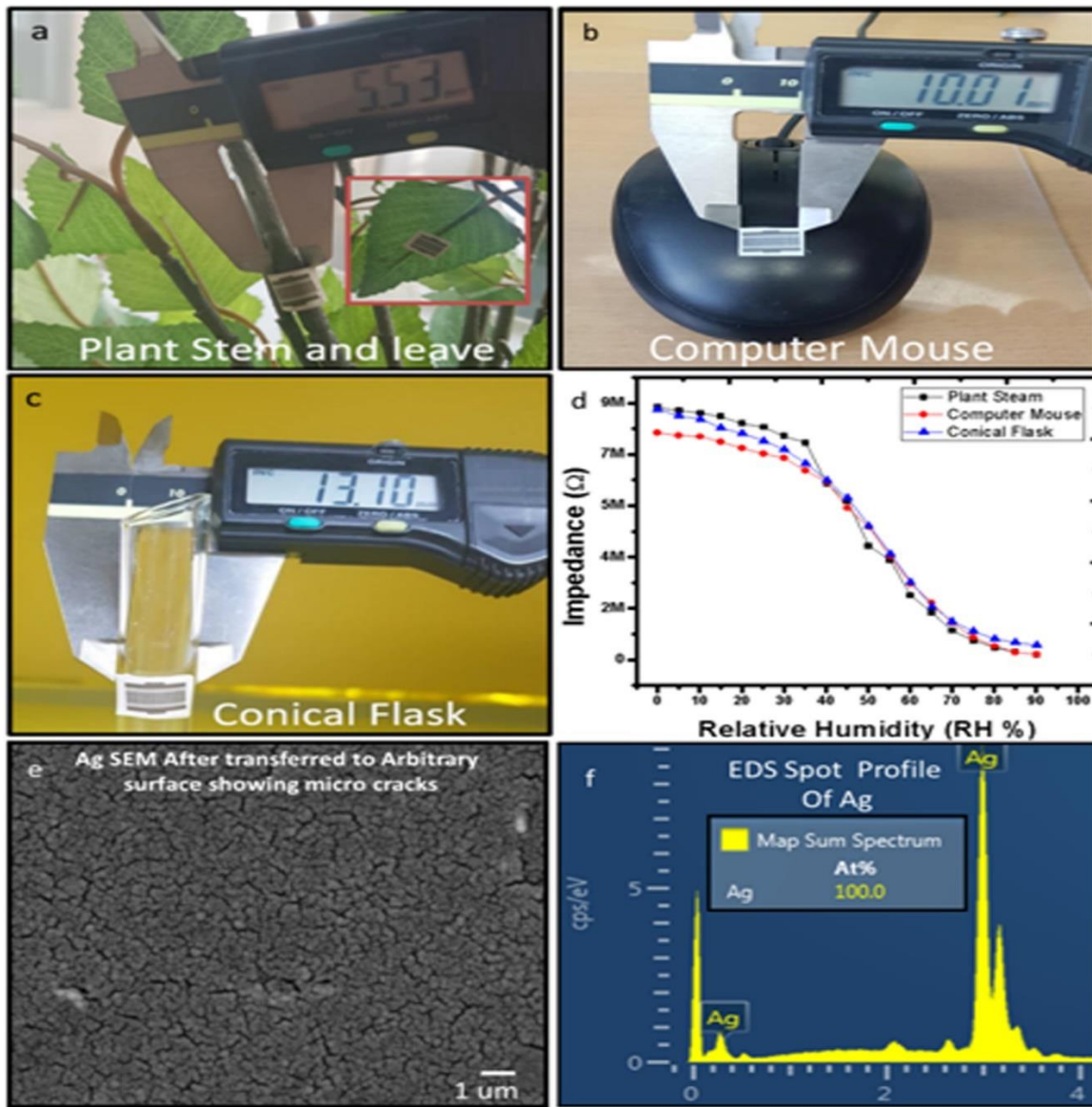


Figure 4.7. Images of the fabricated sensor on IESM transferred to various shaped as a substrate: (a) plant stem as a substrate with 5.53 mm diameter, (b) computer mouse with diameter 10 mm, and (c) round shape conical flask with diameter 13.1 mm. (d) Impedance response of IESM on transferred to arbitrary surface. (e) FESEM of IDEs after transferred to arbitrary surface. (f) EDS spot profile shows the presence of Ag in FESEM.

The fabricated sensor was mounted/transferred on the different arbitrary surfaces as a substrate. The target substrates have different uneven surfaces with different curvature, which includes plant leaf and stem, computer mouse, and conical flask as shown in Fig. 4.7a–c. The SUT is attached to different targeted surfaces with different curvature are shown in Fig. 4.7a–c. The output response of SUT shown in Fig. 4.7d is obtained from the transferred-on plant stem, computer mouse and conical flask. The impedance response of the sensor was increased due to the formation of micro cracks in IDEs after bending as shown in Fig. 4.7e. Figure 4.7 indicates that IESM can easily be transferred to an arbitrary shape substrate without causing any damage. The EDS spot profile of the IDEs after transferred to arbitrary surface is shown in Fig. 4.7f.

As shown in Fig. 4.8, the absorption of water molecules changes the dielectric coefficient, as a result change in capacitance of SUT. The capacitance of SUT increases with decrease in impedance with increase in relative humidity. The change in capacitance can be observed on different test frequencies of sensor 1 and sensor 2 as given in Fig. 4.8a–d. The intrinsic capacitance of SUT decreases with increase in test frequency range from 1 kHz to 10 kHz. This phenomenon is due to flow of leakage conduction and capacitance at higher frequencies.

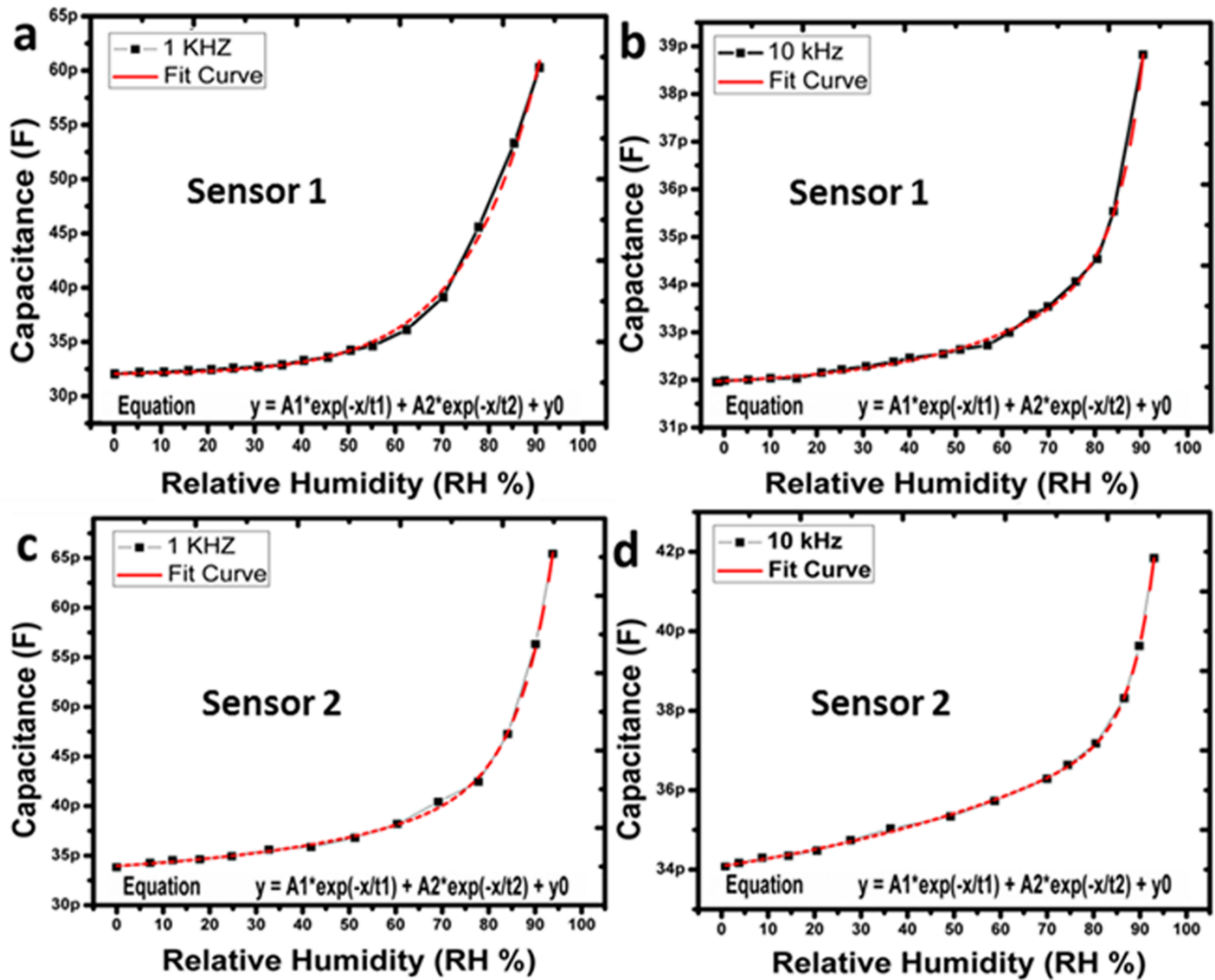


Figure 4.8. Capacitance response of the sensor 1 at (a) 1 kHz and (b) 10 kHz. Capacitance response of the sensor 2 at (c) 1 kHz and (d) 10 kHz.

The transient response of SUT is shown in Fig. 4.9, and it was recorded using breath detection system. The exhaling and inhaling act as humidification and dehumidification, respectively. The transient response of the sensor indicates that, sensor can detect sudden change in humidification levels in environment. The T_{res} and T_{rec} of sensor 1 were recorded as ~ 1.99 sec and ~ 8.76 sec, respectively as shown in Fig. 4.9a. The T_{res} and T_{rec} of the sensor 2 were recorded as ~ 2.32 sec and ~ 9.21 sec, respectively as shown in Fig. 4.9b.

The Transient response of the fabricated sensor has fast response time and recovery time, and it can be employed in the real life for the humidity sensing purpose. The stability of the fabricated sensor 1 and sensor 2 were investigated at 1 kHz and both sensors were kept in the ambient chamber for 120 min at 90% RH, at 40% RH (open air response) and 0% RH. Both sensors as shown in Fig. 4.9c,d maintained stable impedance response at 90%, 40%, and 0% RH, respectively. The sensor 1 maintained a stable impedance response with maximum 0.17% error rate as shown in Figs. 8c and 0.198% error rate was recorded in sensor 2 as shown in Fig. 4.9d.

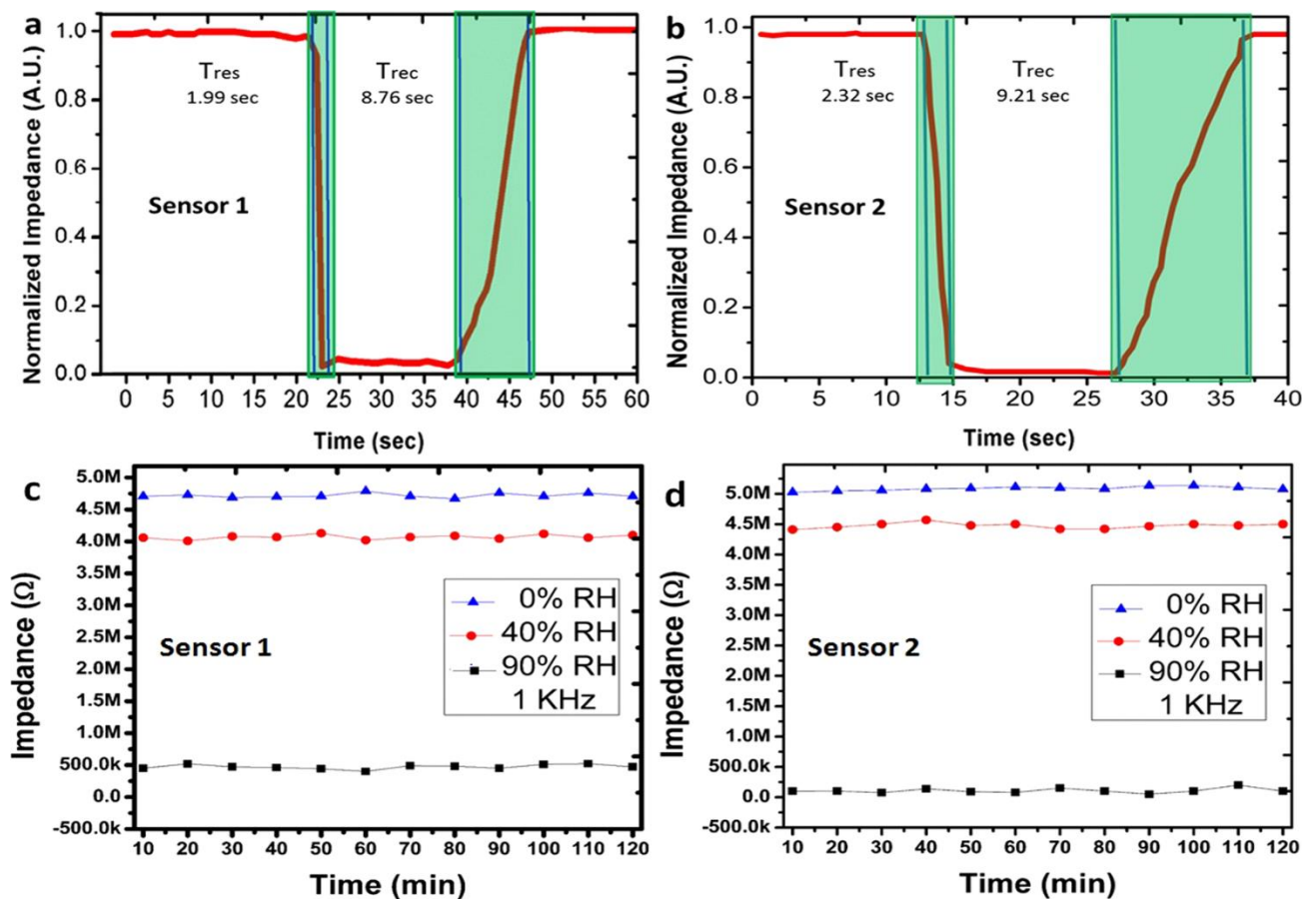


Figure 4.9. Transient response of (a) sensor 1 and (b) sensor 2. Stability on 0% RH, 40% RH (open air), and 90% RH of (c) sensor 1 and (d) sensor 2.

The proposed bio-compatible humidity sensor has been reported that the main constituent of the IESM is collagen and saccharides[92]. The chemical composition of the membrane consists of uronic acid and amino acids (alanine and glycine). The uronic acid is a product of monosaccharide in which the terminal carbon's hydroxyl group has been oxidized to carboxylic acid. It contains both aldehyde and carboxylic acid moieties and lot of hydroxyl, carbonyl, and amino functional groups[92] are present on the protein fibers of IESM to interact with moisture content present in the environment³⁷ and can be used as a humidity sensing layer.

Hence, the humidity sensing mechanism can be explained as shown in Fig. 4.10a. It is a porous structure as shown in Fig. 4.10b, which allows the flow of air and moisture and it can easily catch humidity. The structure of IESM also can be observed using NV-2000 Universal non-contact surface profiler, which indicate that IESM has surface roughness of 1.35 μm and it also confirm the average thickness between ~ 18 to 21 μm as shown in Fig. 4.10c, and d. Due to the natural multilayer crosslinked fiber structure of the IESM, its porous structure can be observed using 2D and 3D nano profile as given in Fig. 4.10c, and d. It indicates that IESM is highly porous and consist of micro spacing fibrous structure. The height profile of IESM is shown in Fig. 4.10e, which indicate that average height of the IESM is 18.24 μm . The IESM is a good insulator and in dried form its impedance value is very high, and the impedance change depends on the water content inside the IESM. The relative permittivity of water significantly differs from the dried IESM. The absorption of water molecules in the thin film of the IESM can dissolve the dried organic materials inside the cells that result in the change in impedance and ionic current flow through the IDEs.

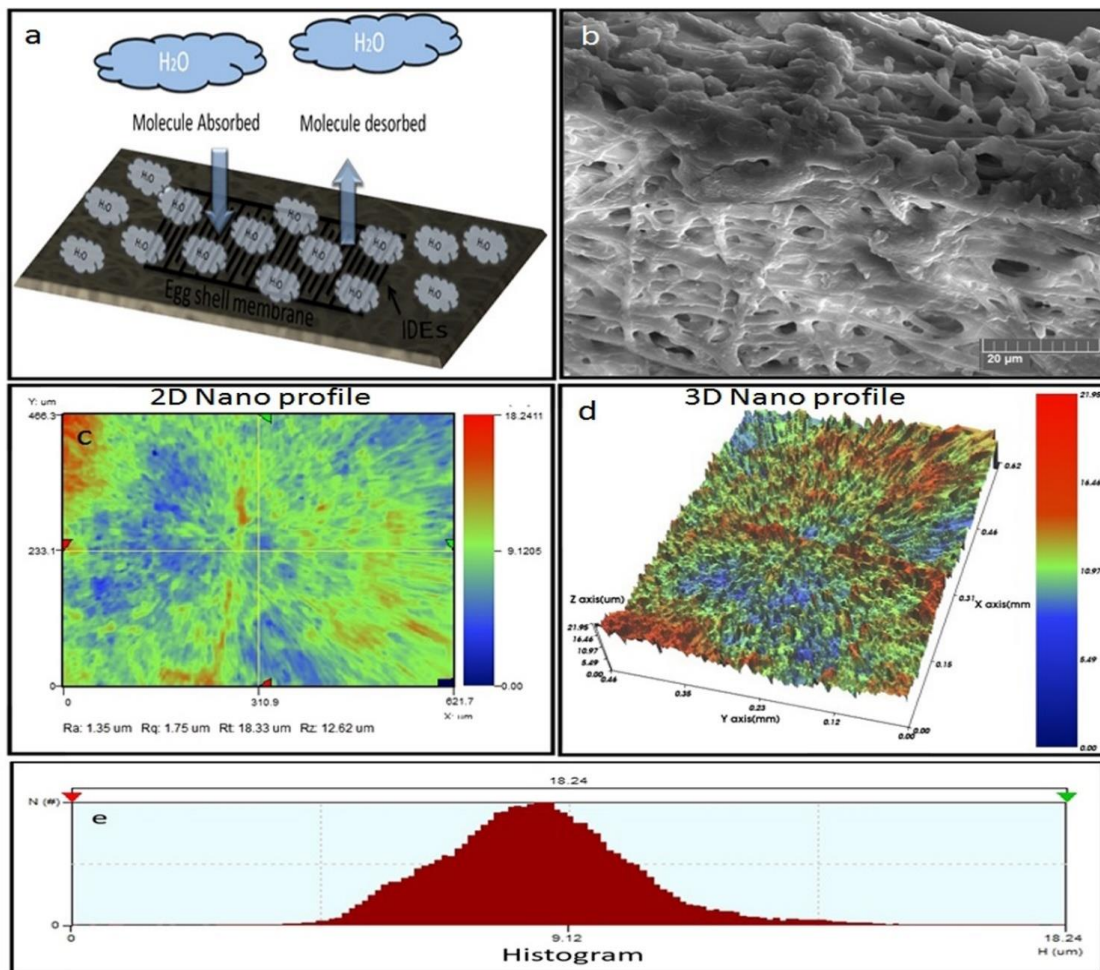


Figure 4.10. (a) Sensing mechanism of the IESM showing adsorption of water molecules and resulting ionic current flow through the thin film. (b) Cross sectional image of the IESM at 50 μm magnification, and (c) 2D and (d) 3D nano profile of IESM. (e) Histogram of IESM.

The main reason of the hysteresis in the IESM is due to the porous structure and chemical absorption. The proposed sensor 1 and sensor 2 was analyzed for the hysteresis characteristics at 1 kHz as shown in Fig. 4.11. The main reason to observe hysteresis at 1 kHz is, IESM is showing large change in impedance and capacitance at 1 kHz as compared to 10 kHz. For this characteristic, the sensor was sorted at 0% RH and then humidity level was increased to 90% and back from 90% to 0% RH. The impedance and capacitance were recorded against each humidity level during adsorption and desorption cycles. The impedance hysteresis is shown in Fig. 4.11a, and b and capacitance hysteresis are shown in Fig. 4.11c, and d of the sensor 1 and sensor 2. In each case hysteresis curve is observed from 30% RH to 80% RH.

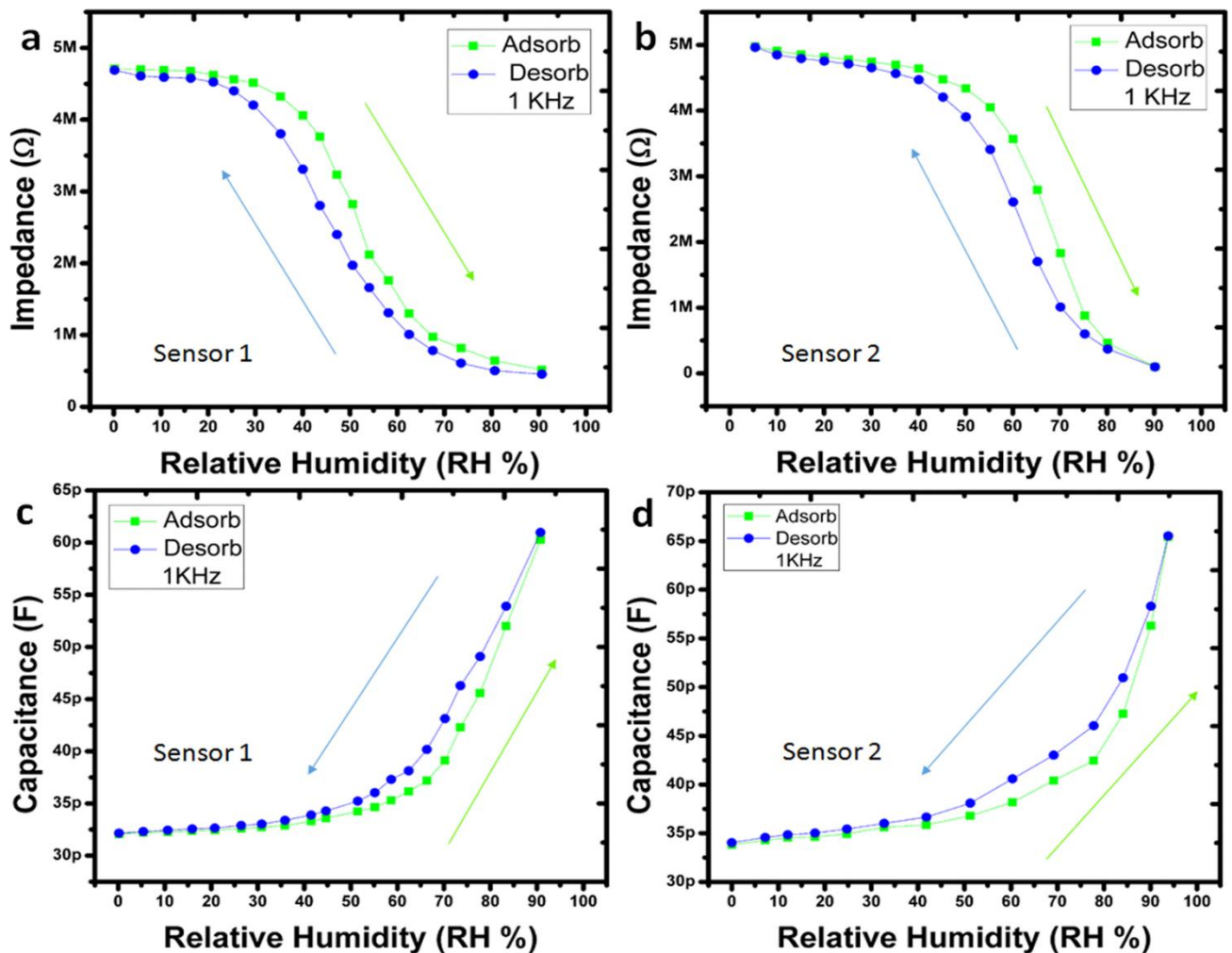


Figure 4.11. Impedance response hysteresis curve of (a) sensor 1 and (b) sensor 2 showing adsorption and desorption from RH 0–90% at 1 kHz. Capacitance response hysteresis curve of (c) sensor 1 and (d) sensor 2 showing adsorption and desorption cycle with humidity range from 0 to 90% at 1 kHz.

4.1.4 Summary

For weather monitoring applications, the paper proposed the bio-compatible humidity sensor based on IESM. This IESM applied as a humidity sensing layer and substrate using IESM. Here, inter digital electrodes (IDEs) with finger width of 100 μm and spacing of 100 μm were deposited on the surface of IESM through Fujifilm Dimatix DMP 3000 inkjet material printers for sensor 1 and sensor 2. The proposed sensor achieved a good response and recovery time, and its impedance and capacitance change are recorded from 0% RH to 90% RH. Hence, the 19 μm thin IESM could be used to replace flexible and ultra-thin substrate based on PDMS. The Possible areas of IESM were applied as ultra-thin substrate for electronic skin applications, which could be conformably transferred to different arbitrary shape surfaces. The IESM is an environment friendly and can be used as a disposable substrate for environment sensing applications.

4.2 Printable Highly Stable and Superfast Humidity Sensor Based on 2D MoSe₂

Atmosphere contains water molecules in gaseous state and creates humid conditions in the environment. Concentration of water molecules is generally measured as a relative parameter called relative humidity (RH)[92]. Temperature and humidity are interdependent and have complex and varied effects on objects[94]. Objects/substances not only get affected by the concentration of water molecules but also by the rate of change in ambience. Humidity affects (biological growth, mechanical strength, chemical degradation, building damage, metal corrosion, etc.) if not maintained in a suitable range, making its accurate measurement necessary[94]. Plants play a vital role in maintenance of hydrologic response and water stress through transpiration, taking up CO₂ and releasing H₂O cooling off the surface[94]. Thus, humidity and temperature show interdependence making accurate measurements difficult. Thus, accurate measurement of RH is perplexed and difficult as compared to other environmental factors[93].

In recent years, researchers investigated semiconducting metal oxides[93], graphene[98], carbon nanotubes (CNTs)[109], carbon quantum dots (CQDs)[110], transition metal dichalcogenides (TMDCs)[12], and composites[111]for humidity sensing applications because of ease of fabrication and low cost. However, most of these materials have intrinsic drawbacks, like metal oxides have a non-linear response, graphene has almost zero band gap energy, and TMDCs have limited detection range.

Semiconductors are synthesized from group II to VI, in which silicon Si is the most widely used material[112]. Porous silicon (PSi) gets corroded and is instable leading to restrictions in humidity sensing applications. Moisture sensing properties of gallium nitride (GaN) have been exploited in recent years and it can be employed for humidity sensing applications[113]. The crystal structure of GaN is similar to the Wurtzite (ZnS) structure[65]. The outermost layer of Gallium in a Wurtzite crystal has three bonds with underlying Nitrogen atoms, while the fourth place is readily available for reaction with ligands, especially anions. Hydrolysis of GaN is difficult and does not react with hydrochloric or nitric acids, but dissolves slowly in hot concentrated sulfuric acid[65]. Melting point of GaN is >2500 °C, these properties make it a highly stable material for humidity sensing applications. The calculated density of GaN is 6200 kg m^{-3} . Due to high electron mobility of GaN High Electron Mobility Transistors (HEMTs) are being fabricated by utilizing GaN[65]. Devices of GaN can safely operate at high terminal voltages up to 42 V due to high impedance and are preferable for low power consumption, or in other words low power dissipation. It shows a wide bandgap energy of 3.4 eV at 300 K reliable for high-voltage and temperature operations. A fast response and recovery time for adsorption of H_2O molecules on GaN was calculated $\approx 6.8 \times 10^{-3}$ s[65]. In addition, GaN shows bio-compatible properties, an extensive network of neurons was found after seeding on GaN surface, and human embryonic kidney cells were grown on AlGaIn/GaN heterostructures[114]. Thus, GaN surface facilitates neuronal cell attachment and tissue growth without specialized surface treatment. Therefore, GaN can be engaged as a highly sensitive and real time humidity sensor at bio-interfaces.

Gallium Nitride is difficult to grow utilizing conventional methods. Temperatures >800 °C are required for GaN epitaxial growth. Until 926.85 °C GaN is stable and can be stabilized in increased pressures[65]. Sputtering process deposits atoms, molecules or fragments from a target bombarded with high energy particles or ions. Magnetron sputtering process is widely used for fabrication of high quality thin films[65]. Pulsed magnetron sputtering (PMS) enables deposition and growth of dielectric materials. Pulsed sputtering process reduces the risk of DC arc events and stabilizes thin film growth with reduced defects[65]. Advantages of PMS include high deposition rate, high adhesion to substrate, uniformity of deposition and high purity[65]. Thus, enhanced structural, optical and electrical properties can be achieved through PMS coating technique[65]. In this paper, we present a highly stable, reliable and fast humidity sensor capable of all range humidity detection between 0 and 100% RH based on pulsed modulated DC magnetron sputtering of GaN on glass substrate. Interdigitated electrodes (IDEs) are printed on top of sensing layer to enhance the electrical sensitivity of the proposed sensor.

The proposed sensor shows linear impedance response towards all range humidity, capacitive and impedance sensitivity of ~ 8.53 nF/RH% and ~ 79 k Ω /RH%, respectively. A fast response and recovery time of ~ 3.5 s and ~ 9 s, respectively, was recorded with little hysteresis of $< 3.53\%$. It also has low temperature dependence; thus, sensor capabilities can be incorporated with real time bio-sensing for smart agriculture and food freshness applications. Smart agriculture not only requires conservation of water but also monitoring of soil acidity and resources for increased crop production from plants. Transpiration monitoring can help accumulate the required data through sensing network. Food quality and wastage are another concern for modern day-to-day life affecting human health especially meat products, thus, evaluation of meat freshness can be conducted via sensor attachment during packaging process. We demonstrate efficacy and suitability of proposed sensor for these applications with a low-cost sensor.

4.2.1 Materials and Methods

The Glass slide was used as substrate material after cleaning process, 20 nm buffer layer of ZnO was prepared by sputtering to improve crystal quality of GaN thin film. High purity liquid Ga target (99.99999%) with a mixture of sputtered gasses (N₂ and Ar) at 41:9 sccm flow rate was used for GaN thin film deposition. The base pressure of vacuum chamber was pumped down to 1×10^{-6} Torr to avoid any moisture influence. The substrate was preheated to 450 °C and chamber pressure was maintained at 7.5 mT with a pulse width of 70 μ s and an average power of 70 W, respectively. Resultantly, a 300 nm GaN thin film was deposited by pulsed DC magnetron sputtering process.

The IDEs were designed using EAGLE software platform in dxf format then converted to bmp format using ACE 3000 and exported to Dimatix Drop manager software. The Dimatix manager converts the bmp file into ptn format loadable to Fujifilm Dimatix DMP-3000 inkjet printer. Silver nanoparticles (Ag NPs) ink was loaded in 16 nozzle 10 pL cartridge with diameter of 9 μ m. A 30 V biasing voltage was applied on nozzles with drop spacing of 20 μ m with temperature regulation of 30 °C of the movable platform. Silver electrodes were deposited on the top of GaN thin film via inkjet printing process having 100 μ m width and 100 μ m spacing. Electrodes were cured at temperature of 120 °C for 1 h. Figure 4.12 shows schematic illustration of printing process of the humidity sensor.

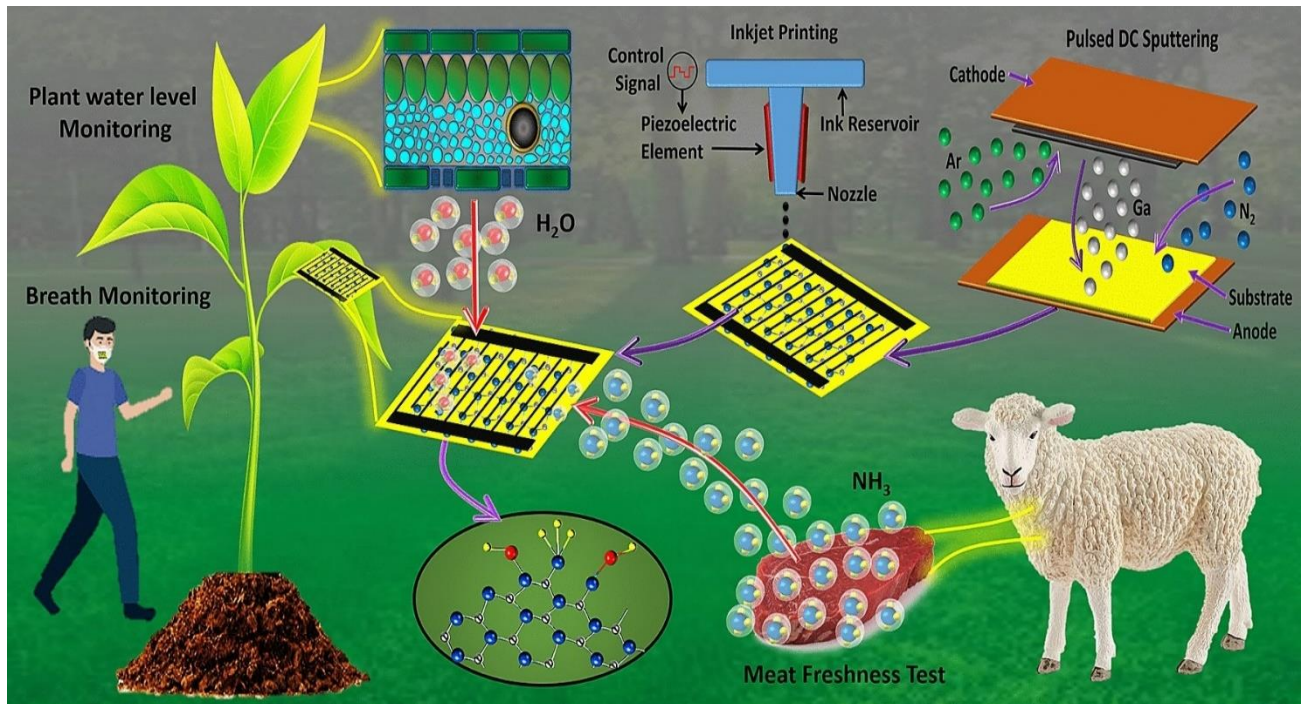


Figure 4.12. Schematic illustration of fabrication process of humidity sensor.

4.2.2 Characterization

TESCAN MIRA 3 scanning transmission electron microscope (STEM) and energy dispersive X-Ray spectroscope (EDS) were used to examine elemental composition and surface morphology of the sensing layer as well as IDEs. A STEM image of sensing layer GaN with electron beam accelerated at 15 kV and 2.5 μm sizing is shown in Fig. 4.13a confirming uniform fabrication of active layer through sputtering technique. The EDS mapped image confirms presence of Nitrogen K series and Gallium L series in Fig. 4.13b and c, respectively. After deposition of Ag IDEs on top of active GaN layer, SEM image is presented in Fig. 4.13d at magnification of 100 μm validating uniform fabrication. Rough edges of IDEs are observed after curing at 120 $^{\circ}\text{C}$. The EDS mapped images in Fig. 4.13e and f endorse presence of Silver K series and Carbon L series, respectively. A non-contact surface profiler NV-2000 was used to analyze the surface roughness and height of GaN. The 3D nano-profile arithmetic mean (Ra), RMS (Rq), and height profiles (Rz)[65] of GaN were found to be 76.85 nm, 90.01 nm and 380.86 nm as shown in Fig. 4.13g. Similarly, for surface roughness and height of IDE layers, the Ra, Rq, and Rz of Ag IDEs were found to be 3.06 μm , 3.35 μm and 11.79 μm , respectively, shown in Fig. 4.13h. These results ensure correct fabrication of GaN layer through magnetron sputtering and IDEs via inkjet printing techniques.

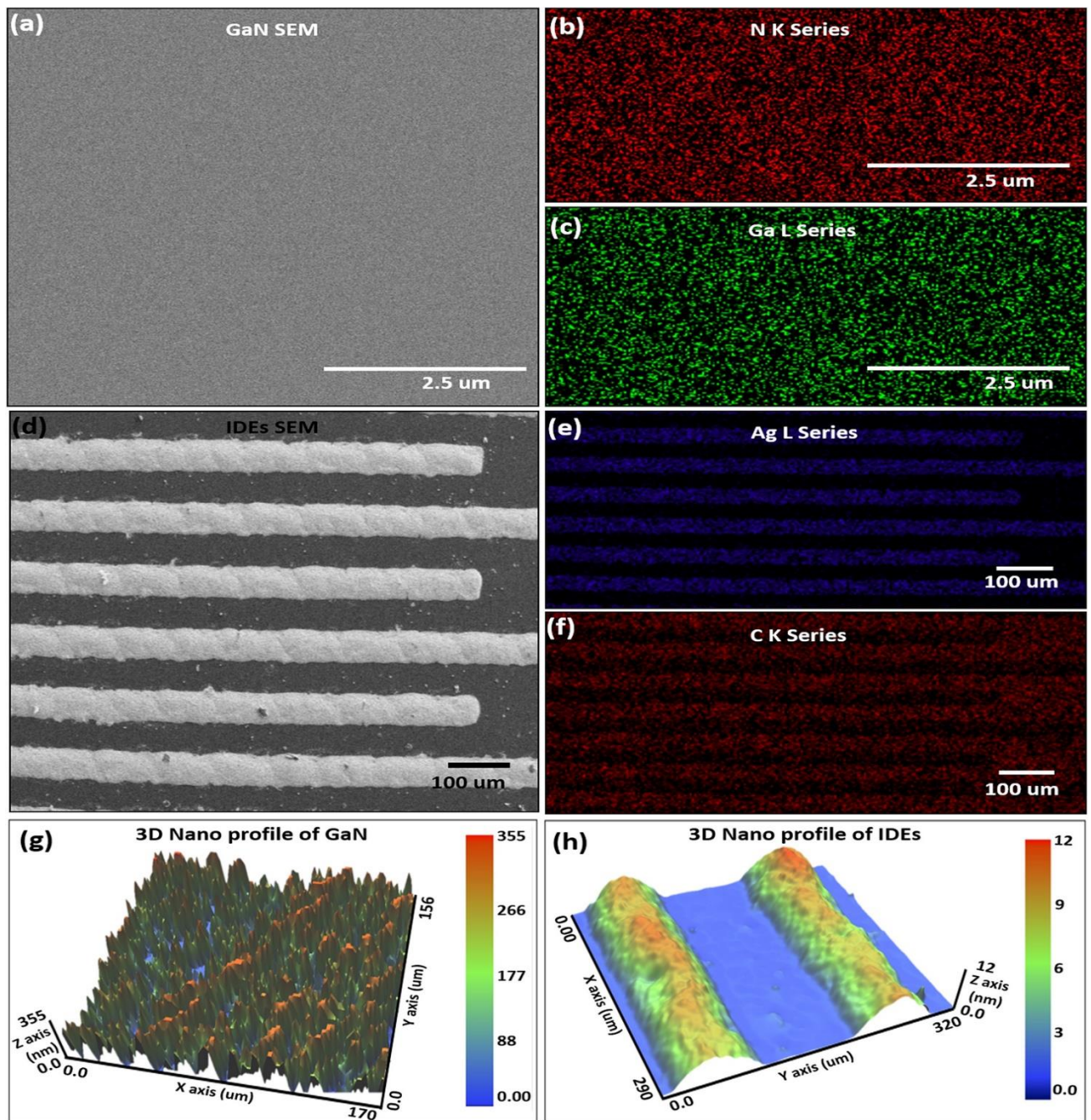


Figure 4.13. (a) STEM GaN layer, (b) nitrogen K series, (c) Ga L series, (d) STEM IDEs (e) silver L series, (f) carbon K series, nano-profile (g) GaN, and (h) IDEs.

XPS Spectrum was measured by PHI 5600 (Physical Electronics) with source of Al X-ray monochromator. XPS spectrum of GaN with having peaks of Carbon, Nitrogen and Gallium presented in Fig. 4.14a. C 1s peak was adjusted at 285.0 eV for the calibration of absolute binding energy. De-convoluted spectra with core levels of Ga 3d in Fig. 4.14b, N 1s Fig. 4.14c and O 1s Fig. 4.14d from the surface of the sample. High resolution N-1s reveals three sub peaks at 397.20 eV confirm the bonding of N–Ga and other two peaks at 394.51 and 396.2 eV correspond towards Auger Ga[65].

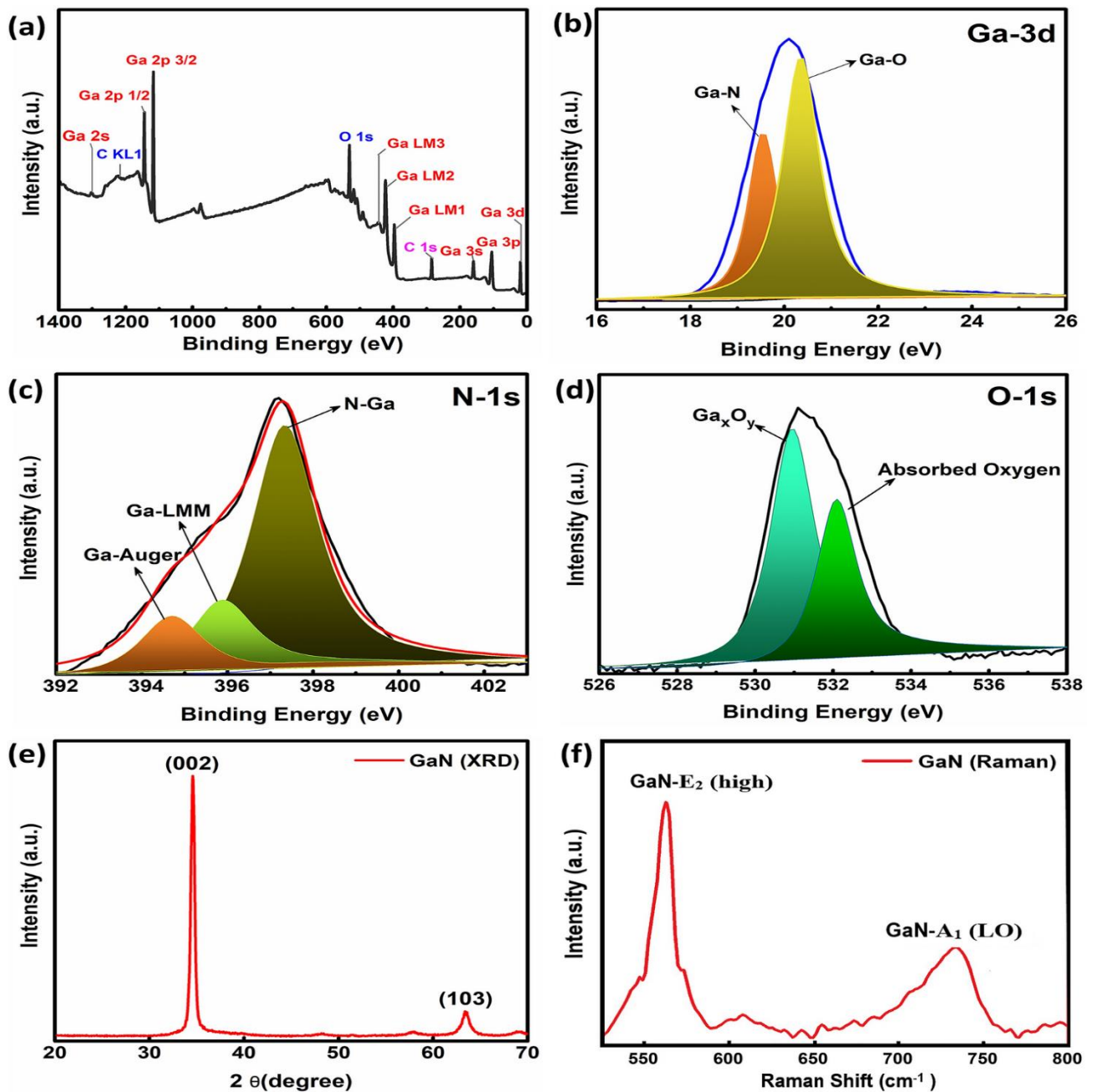


Figure 4.14. GaN sensing layer (a) Overall general XPS spectrum, (b) Ga 3d band, (c) N 1s Band, and (d) O 1s band, (e) XRD, and (f) Raman spectrum.

The dominant peak at 20.10 eV and Lorentzian fitted peak at 19.46 in high resolution are attributed towards the Ga–N and Ga–O bonds, respectively^{34,35}. X-ray diffraction pattern (XRD) was recorded by Empyrean (PANalytical) diffractometer using $\text{CuK}\alpha$ radiation of wavelength $\lambda = 1.5406$ nm in the scan range $2\theta = 20^\circ\text{--}70^\circ$ as shown in Fig. 4.14e. The diffraction peaks are labelled as (002) and (103) at angles of 34.4° and 62.4° . XRD analysis revealed the Polycrystalline structure of GaN, it has wurtzite structure with sharp and high peak of (002) c-axis orientation with FWHM of (0.4821).

The average crystallite size was calculated by Debye–scherrer approximation, which is found to be 30 nm[65]. Raman Spectrum was measured by HORIBA LabRAM HR confocal spectrometer, equipped with 800 nm length monochromator, He–Cd laser was shined on the surface of the sample with the excitation wavelength of 325 nm. RT Raman Spectra of GaN was taken which shows the two corresponding signature peaks of E2 (high) and A1 (LO) modes can be seen in Fig. 4.14f, predicts the figure prints of hexagonal wurtzite structure of GaN. Epitaxial GaN layer grown on sapphire shows the actual Raman peaks at 570.4 cm^{-1} and 736.2 cm^{-1} for E2 (high) and A1 (LO) modes, in correspondence of our Raman peaks located at 566.3 cm^{-1} and 731.5 cm^{-1} for E2 (high) and A1 (LO) modes, respectively. These relative shifts of peaks are due to the in plane compressive stress between GaN thin film on ZnO buffer layer originated because of slightly unmatched lattice constant[65].

A customized testing chamber was made for observations in change of impedance and capacitance of the sensor with increase in RH. The humidity was increased slowly from 0 to 100% RH through atomizer via ultrasonic humidifier, for dehumidification from 100 to 10% RH compressed air was used, and dry N_2 gas was used between 10 and 0% RH both controlled via electronic flow control valves. A high accuracy commercially available humidity sensor HTU21D is used as reference with response $< 5\text{ s}$, resolution of 0.04% RH and accuracy of $\pm 2\%$ RH. Electronic valves are regulated through a control board and an Arduino UNO is connected for data sampling and logging connected to computer via Universal Serial Bus (USB) cable. Block diagram is shown in Fig. 4.15a.

4.2.3 Result and Discussion

During experimentation impedance is observed by slowly varying ambient humidity conditions with intervals after variations for stabilization of response. The RH is increased from 0 to 100% with a stepping of 10%. Figure 4.15b shows the impedance response at 1 kHz frequency. The impedance at 1 kHz starts at $9\text{ M}\Omega$ at 0% RH and starts to decrease as the RH increases, till 100% RH the impedance drops down to $0.982\text{ M}\Omega$. This drop in impedance is due to cumulative sheet resistance and capacitive impedance drop. At low frequencies the capacitive impedance drops down to a certain minimum with increase in frequency, then inductive impedance overwhelms the capacitive behavior. Similarly, the capacitance of the sensing layer also shows humidity dependence. Figure 4.15b shows capacitance response as a function of RH at 1 kHz. The capacitance observed is 15.2 to 882.8 nF from 0% RH to 100% RH. The sensitivity is calculated as $79\text{ k}\Omega/\text{RH}\%$ and $8.53\text{ nF}/\text{RH}\%$ for impedance and capacitance, respectively.

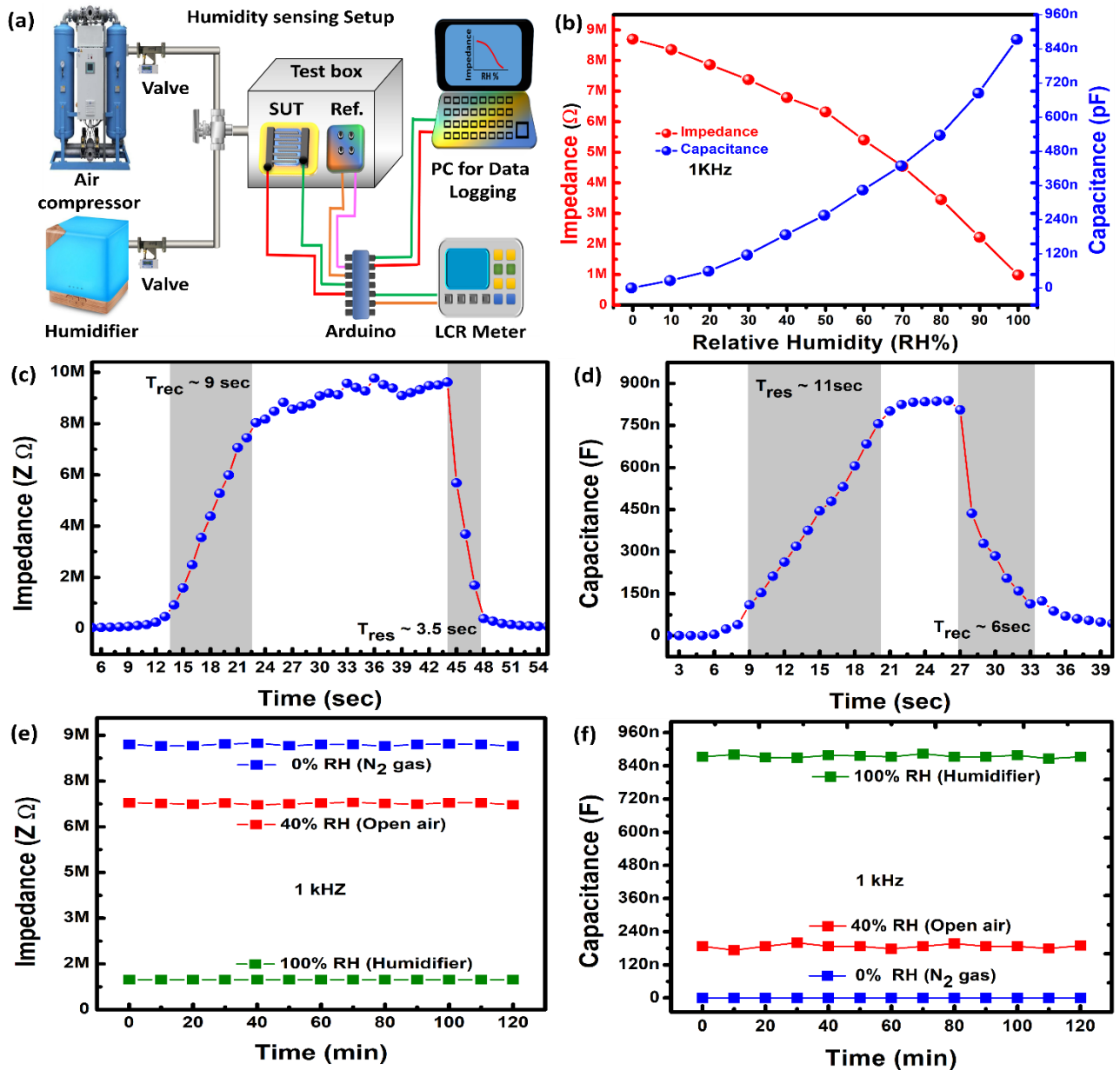


Figure 4.15. (a) Humidity test setup, (b) measured and simulated impedance and capacitance response at 1 kHz. (c) Impedance response and recovery. (d) Capacitance response and recovery. (e) Impedance stability, and (f) capacitance stability.

Sensors are also characterized by transient response facilitating examination of response (T_{res}) and recovery (T_{rec}) times upon sudden change for humidification and dehumidification process. A sudden increase in humidity through humidifier was analyzed from 0 to 100% RH and for dehumidification dry N_2 gas was utilized for change from ~100 to 0% RH. Response and recovery times for impedance are calculated to be $T_{res} \sim 3.5$ s and $T_{rec} \sim 9$ s, respectively and presented in Fig. 4.15c. Similarly, capacitance response on time scale showing $T_{res} \sim 11$ s and $T_{rec} \sim 6$ s, respectively are presented in Fig. 4.15d. Slow response and recovery time are attributed to chemical adsorption of hydronium and hydroxyl ions on GaN layer and considered a major drawback of GaN proposed sensor.

The stability tests were performed on the proposed GaN sensor by observance of impedance and capacitance response under ambient conditions for 1 kHz frequency on different humidity levels (0%, 40%, and 100%) for consecutive 120 min as shown in Fig. 4.15e for impedance and Fig. 4.15f for capacitance response. The sensor presents a stable response with insignificant error over a wide range of change in impedance and capacitance responses.

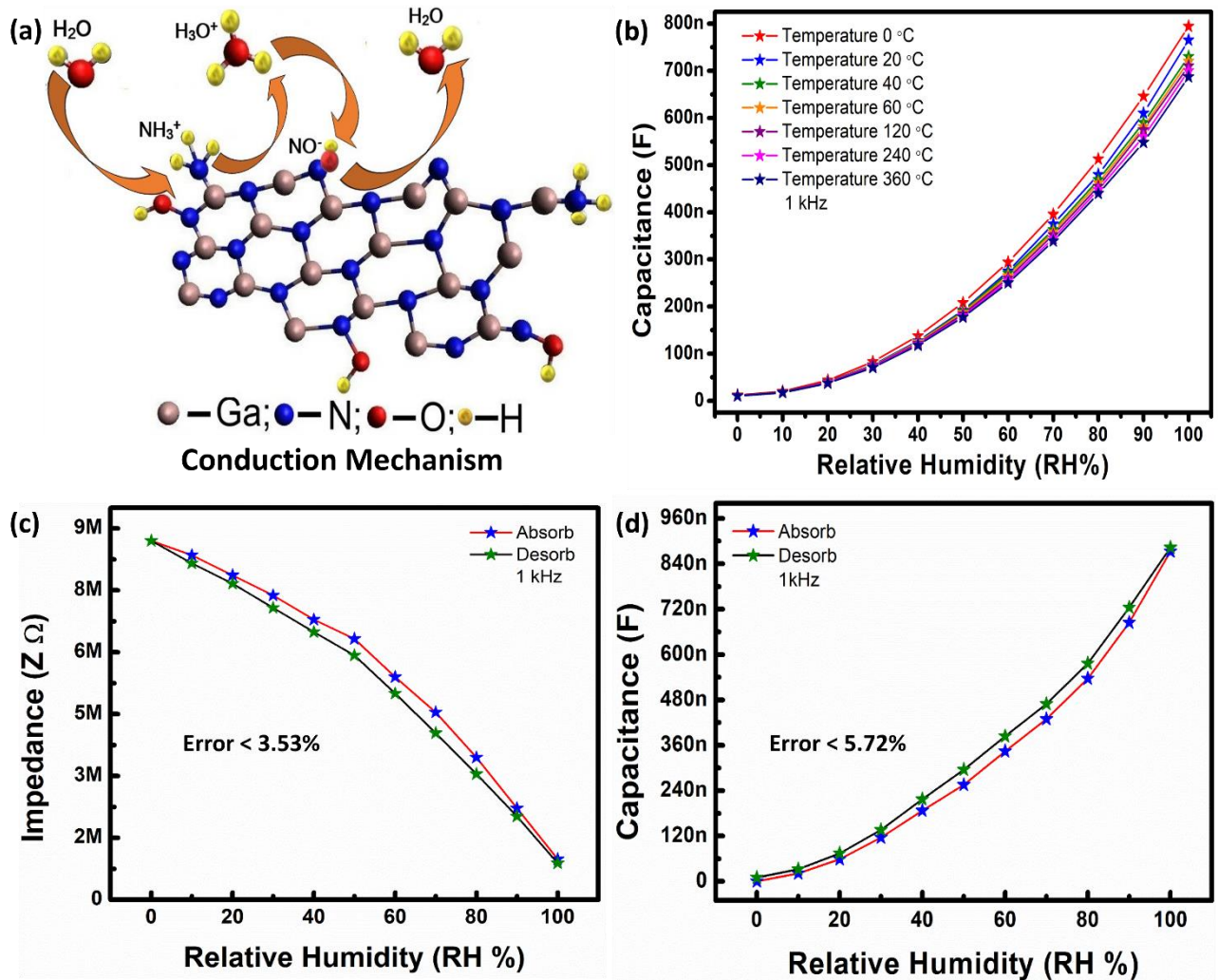


Figure 4.16. (a) chemical adsorption of water molecules on GaN sensing layer. (b) capacitance response w.r.t temperature variations. Hysteresis (c) impedance at 1 kHz, (d) capacitance at 1 kHz.

The water surface is much more acidic and hydronium ion is a strong proton donor. In presence of humid conditions, the GaN surface oxides to Ga_xO_y making additional deficiencies providing more electrically active sites for hydrogen atom adsorption[65]. Enhanced active sites increase the Fermi energy from semiconductor nature of GaN towards conduction band. The adsorption of H_2O causes the static dielectric constant of GaN ranging between 8.9 and 9.748 to increase and hence an increase in capacitance is observed at the sensor terminals. The chemical bonding of NH_4^+ and OH^- is displayed in Fig. 4.16a.

Upon energizing electrode terminals, a potential difference is created between the electrodes. Thus, an electric field is created between the electrodes originating from the higher potential surface and ending at low potential. This directional field aligns the H_3O^+ and OH^- ions in a polar molecular structure above the GaN layer. As RH increases, increase in adsorption of hydronium and hydroxyl ions is observed resultantly the electric field intensity increases. Energizing the circuit through LCR meter the parasitic capacitance between electrodes and substrate, sensing layer sheet resistance, capacitance between the electrodes, capacitance due to adsorption of hydroxyl OH^- ions on sensing layer and hydronium ions H_3O^+ ions. The change in ambient RH affects all the individual circuit elements present in the sensing device. Thus, the measured change in impedance as well as capacitance is a cumulative effect.

The GaN is stable element and has low temperature dependence. This dependence is measured between range of 0–100% RH and temperature range of 0–360 °C, plot is shown in Fig. 4.16b. Relative permittivity changes from 600 to 583, on temperature variation from 25 to 360 °C. GaN is stable in a wide temperature range. Figure 4.16b presents the simulated capacitance response at 0 °C, 20 °C, 40 °C, 60 °C, 120 °C, 240 °C, and 360 °C.

Trapping of charges/ions between the molecular gaps causes hysteresis, which is injected from/to the interfaces between semiconductor, substrate, and adsorbates. Large electric dipole of $\sim 1.8\text{D}$ are formed by water molecules under electric field and can align to form polar molecular structure. This structural alignment causes different charge trap densities and, hence causing hysteresis. The impedance and capacitance-based hysteresis characteristics are shown in Fig. 4.16c and d, respectively at 1 kHz frequency. Initially, the sensor was placed at 0% RH, then humidity level was increased from 0–100% RH, and back from 100–0% RH. Both, impedance, and capacitance of the sensor were recorded during adsorption and desorption cycles. Impedance hysteresis was calculated with an average error $< 3.53\%$ and capacitance hysteresis with average error $< 5.72\%$.

For bio sensing applications a DC bias was applied of 5 V on electrode terminals using KEYSIGHT B2902A source measurement unit apparatus to measure the flow of DC current, while an Arduino was connected with reference ammonia sensor TGS2602 for meat freshness test. Both the B2902A source measurement unit as well as Arduino were connected to a computer via USB(s) for data logging[65]. Plant growth rate is directly linked to its' water status, drought conditions can inhibit growth rate of a plant. The sensor was attached to backside of leaf as shown in Fig. 4.17a and capacitance response was recorded from 1 to 5 days as shown in Fig. 4.17b. To perform drought conditions, long term capacitive measurements were performed to estimate water quantity of soil.

A picture of attached sensor to leaf is shown in Fig. 4.17a, the zoomed image shows the cross-sectional view of leaf. The data was recorded for 5 days with sampling after 24 h, at 1 day addition of water to soil increased the uptake and release of water molecules from stomata corresponding to increase in capacitance at 1 day as shown in Fig. 4.17b. A drop in capacitance is observed as days pass by due to water evaporation from soil corresponding to decrease in capacitance shown in Fig. 4.17b. These results indicate that proposed can be employed for smart agriculture.

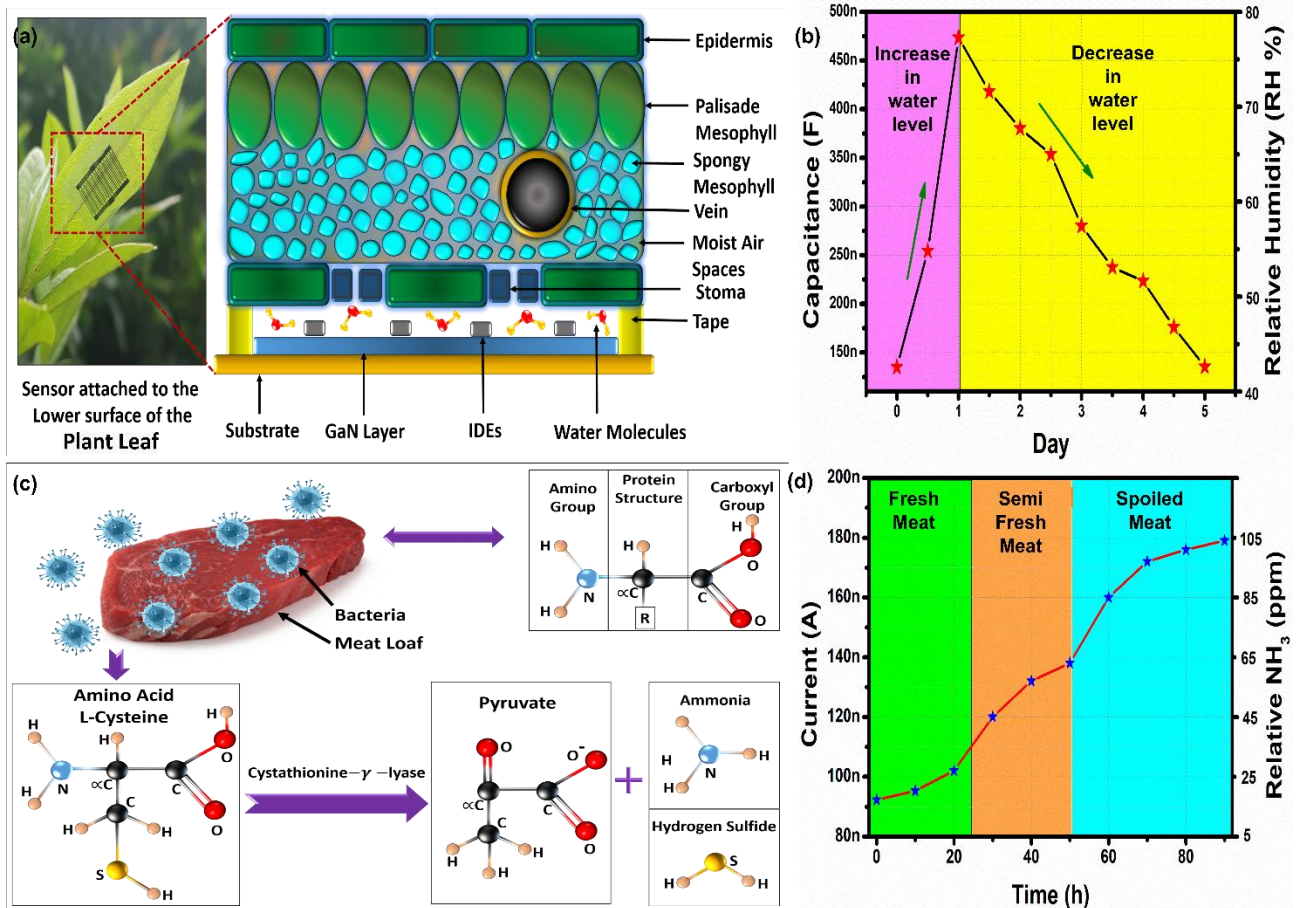


Figure 4.17. (a) Picture of sensor attached at lower side of plant leaf and cross-sectional view of leaf with sensing mechanism and (b) real time monitoring of capacitive response towards plant transpiration after water from 1 to 5 days. Meat freshness test: (c) Amino acids structure and decomposition mechanism and (d) current response w.r.t. time and freshness states.

Fresh meat was purchased from local market and placed on same day in test chamber. Meat proteins are formed by long chains of amino acids and general structure of proteins is shown in Fig. 8c. Meat decomposition starts by secretion of decomposing enzymes by bacteria. A particular type of amino acid known as L-Cysteine structure is presented in the Fig. 4.17c. Cystathionine-γ-lyase secreted by bacteria decomposed Cysteine into Pyruvate releasing ammonia (NH₃) and hydrogen sulfide (H₂S) gases. Ammonia like water auto-ionizes as well as dissolves in water to form ammonium and hydroxyl ions[65].

As the decomposition rate increases so does the concentration of ammonia as well as ammonium and hydroxyl ions in test chamber decreasing GaN sheet resistance. A 100-h duration test was conducted keeping ambient temperature at 25 °C and 40% RH level inside the test jar with sampling time of 10 h. In the first 24 h, the response of the sensor was quite small with little ammonia accumulation. The current response of the sensor stays below 110 nA till 24 h as shown in Fig. 4.17d categorized as fresh. The spoilage of meat started after 24 h due to rapid growth of microbes till 65 ppm ammonia accumulation categorized as semi fresh. After spoilage, the current response of the sensor reaches 180 nA with high ammonia concentration of 105 ppm categorized as spoiled meat. The results indicate the effectiveness of the sensor making it suitable for freshness evaluation. The results were divided into three sections as fresh, semi-fresh and spoiled according to human sensory evaluation to distinguish between freshness levels as shown in Fig. 4.17d based on odor and color during the spoilage process.

4.2.4 Summary

This work reports highly linear humidity sensor based on GaN as sensing layer, fabricated through sputtering technology and silver IDEs via inkjet printing process. The proposed sensor shows impedance sensitivity $\sim 79 \text{ k}\Omega/\text{RH}\%$ and capacitance sensitivity $\sim 8.53 \text{ nF}/\text{RH}\%$ in a range between 0 and 100% RH with hysteresis response $< 3.53\%$ and $T_{res} \sim 3.5 \text{ s}$ and $T_{rec} \sim 9 \text{ s}$. Sensor shows stable humidity response on temperature variation in a range of 0–360 °C. The sensor performance was validated through computer aided simulations. The higher stability and reliability of GaN makes its utility in real life applications.

4.3 Self-Powered Tribo and Piezoelectric Nanogenerator using Snakeskin Shed Membrane

The increasing demand of energy, researchers are trying to develop the energy harvesting devices across the world[115]. Solar cell, piezoelectric nanogenerator and triboelectric nanogenerator are in developing mode for the energy harvesting with the integration of energy storage[107, 115-117]. Solar cell is getting good efficiency, but it has dependency onto the environment[117]. However, the tribo and piezo nanogenerator are dependent onto the applied force not on environment[107, 118]. Due to that reasons researcher are more focused onto the integration of energy storage or self-powered device by using a piezo or tribo electric nanogenerator[107, 118].

In recent years, Wang group firstly invented the triboelectric nanogenerator in 2012. They give the mechanism through the electrostatic induction and triboelectrification. Researchers developed the triboelectric nanogenerator by using the novel tribo positive and electronegative materials and different device structures for efficient energy generation[119, 120]. Some researchers used the biomaterials, bio-waste materials, and polymeric waste materials for the development of environmentally friendly triboelectric nanogenerator[120, 121]. Triboelectric nanogenerator getting good efficiency but it has some limitation to integration with self-powered system due to the need of complex power management system (rectifier) which can take higher cost for manufacturing and having limitations in biomedical application due to the space between two layers.

Piezoelectric nanogenerator[121] can generate low energy than triboelectric but it has been useful for rectification free energy harvester based self-powered devices and biomedical applications like cardiac contraction force, breathing state, heart rate, blood pressure, diaphragmatic muscle movement due to its high sensibility. Researchers are trying to develop the highly sensitive piezoelectric devices by using the organic and inorganic materials[121, 122]. The ceramic based perovskite structured inorganic materials are widely used in development of piezoelectric nanogenerator[123]. Recently some researchers are developed the piezoelectric nanogenerator by using the biomaterials like cellulose, lignin, proteins,[115, 116] etc. but it all has limitations for making the piezo membrane. Some researchers used the bio membrane like eggshell membrane and tomato skin for piezoelectric nanogenerator[107, 121]. But this device having a high thickness and poor sensitivity for the piezoelectric applications. To overcome these problems, we have reported the interesting micro-patterning snakeskin shed membrane of red tongue viper snake for the development of tribo and piezoelectric nanogenerator as shown in Fig. 4.18a. The snakeskin shed membrane unfolded and folded images presents the membrane flexibility and rigidity for flexible electronics as shown in Fig. 4.18b and c.

The epidermis of snakes is a multi-layered structure made up of keratin and related proteins that may be differentiated histologically from top to bottom[124]. The epidermis is made up of three major layers: stratum basal (germinativum), stratum granulosum, and stratum corneum, which are made up of four layers of dead but completely differentiated keratinocytes and a layer of basal living keratinocytes[125]. The stratum germinativum, or inner layer, is made up of cuvoidal dividing cells that produce the protein keratin. The intermediate layer, stratum granulosum, contained a lipid-rich film that helped the skin maintain a water-permeable barrier [126, 127]. Scales cover the outer stratum corneum, which is highly keratinized. In reptiles two forms of keratin are produced: α -keratin, which is flexible, and β -keratin, which provide rigidity[128].

The presence of the highly keratinized is proving that the materials have high tribo and piezoelectric properties in this material. In this work, we have developed the tribo and piezoelectric nanogenerator by using the snakeskin shed membrane. We have performed the triboelectric nanogenerator by using snake shed electropositive material with Ag electrode and different electronegative layer with copper electrodes as shown in Fig. 4.18d. The piezoelectric experiments of proposed device were performed by using Ag electrode on both side of snakeskin shed membrane which is deposited by using a sputter as shown in Fig. 4.18e and the cross-sectional SEM image of piezoelectric nanogenerator is shown in Fig. 4.18i. The proposed devices show the efficient energy harvesting for both tribo and piezoelectric nanogenerator.

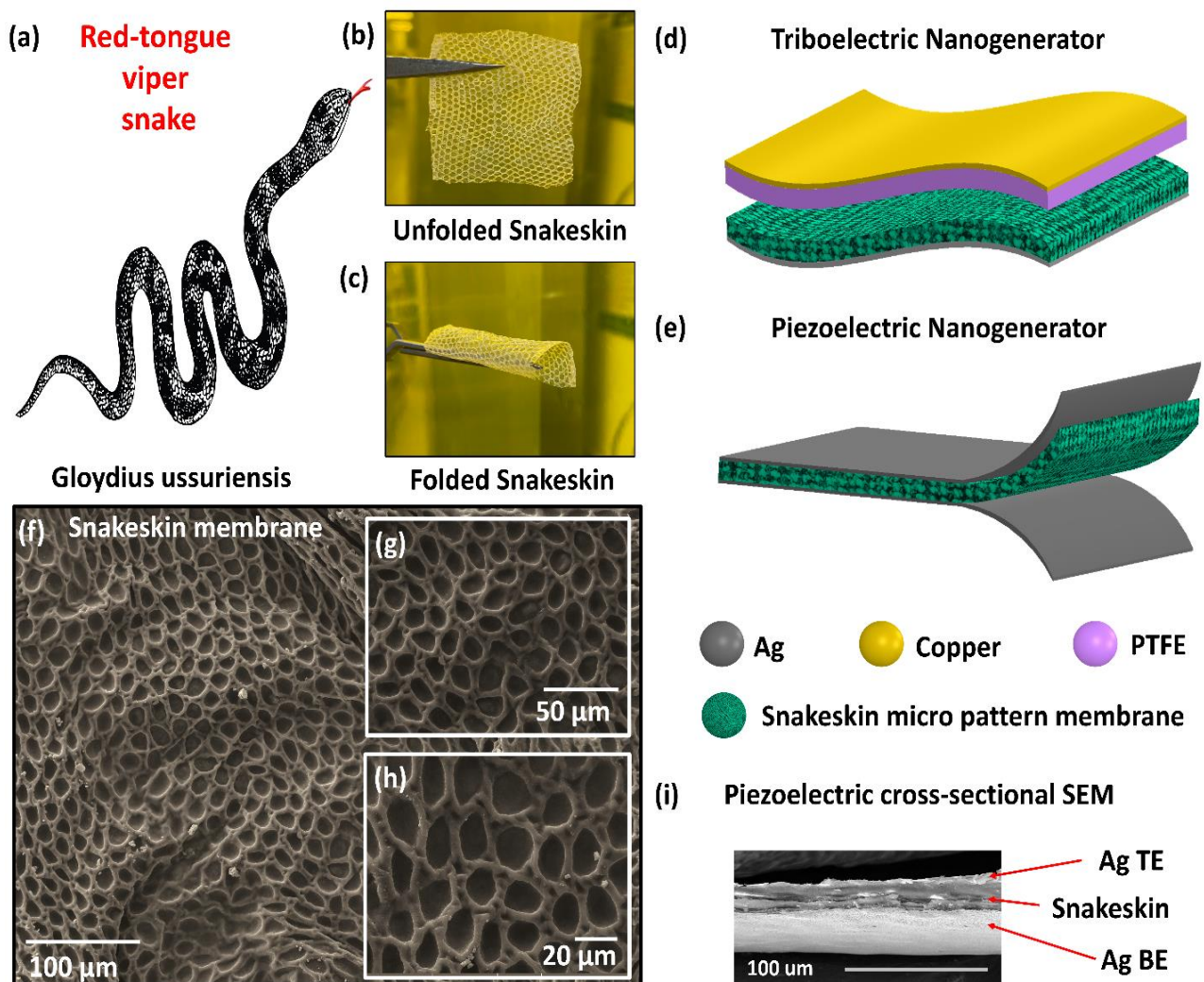


Figure 4.18. (a) The schematic of Red-tongue viper snake species gloydius ussuriensis. (b) Unfolded and (c) folded snakeskin shed membrane showing its flexibility. The schematic device structure of (d) triboelectric and (e) piezoelectric nanogenerator. The SEM image of snakeskin shed membrane at magnification level of (f) 100 μm, (g) 50 μm and (h) 20 μm. (i) The cross-sectional image of piezoelectric nanogenerator showing deposition of Ag electrodes on both sides of snakeskin shed membrane using RF sputter and, we can see the thickness of membrane ~ 10 μm.

4.3.1 Materials and Methods

The snakes are predatory reptiles with elongated, limbless bodies and extremely movable jaws that allow them to swallow food much larger than themselves. Snakes are ectothermic, amniote vertebrate covered in overlapping scales[129]. Snake species of the world consists of 31 families, 450 genera and more than 2500 species and not found in Antarctica and some large island such as Ireland, Iceland, Greenland and Hawaiian archipeiago[130]. In Korea, there are 16 species of snakes including Jeju endemic sibynophis chinensis. Red-tongue viper snake *Gloydius ussuriensis* is a venomous species of snake distributed in Korea, northeast of China and Far East of Russia[131]. The color pattern consists of a light brownish gray to blackish ground color overlaid with a series of 24-33 relatively large and usually elliptical dorsolateral blotches. Red-tongue viper usually prefer low altitude forested areas, containing swamps and marshes. They feed on small lizards like *Scincella vandenburghi* and centipedes such as *Scolopendra subspinipes mutilans*. An outdoor survey was conducted within Jeju Island. Red-tongue viper snake *Gloydius ussuriensis* was spotted accidentally at Dongbaekdongsan wetland areas (33°31'02.12" N 126°42'26.88" E) and was in the process of ecdysis (shedding of skin). We waited until complete shedding without any disturbance to the snake. This shed skin was used in this experiment. The developmental shedding of skin called ecdysis or molting. It is regular process in snakes which allow for further growth and the removal of parasites such as mites and ticks. The snake stops feeding and frequently hides or travels to a safe area before each molt. Shedding occurs from the snout to the tail and takes time, depending on the species. The micropattern structure of membrane can be observed using SEM image with magnification level of f) 100 μm , (g) 50 μm and (h) 20 μm as shown in Fig. 4.18f-h.

The device fabrication of triboelectric and piezoelectric nanogenerator can be seen in Fig. 18d and e. For triboelectric nanogenerator one side of snakeskin shed membrane was RF sputtered by Ag target as bottom electrode and membrane used as electropositive material and on the opposite side PTFE is used as electronegative material and copper is used top electrode on the top of PTFE and the distance of 6mm was kept between both electrodes as shown in Fig, 4.18d. Similarly, for piezoelectric nanogenerator Ag is sputtered on both sides of snakeskin shed membrane as top and bottom electrodes and membrane is used as piezoelectric layer as shown in Fig. 4.18e. The sputtering process of Ag on both side of snakeskin shed membrane can be verified from the cross-sectional image show in Fig. 4.18i.

4.3.2 Characterizations

The skin was smooth and white in color. Skin was not discrete; hence they are not shed separately but as a complete outer layer. We often make use of this scale for snake characteristics and taxonomic purpose. The SEM image with magnification level of 25 μm is shown in Fig. 4.19a show that snakeskin shed membrane possesses a well-organized, highly porous structure having the width of the pores from ~ 15 to $10 \mu\text{m}$. The snakeskin shed membrane spot-profile, which shows C, O, Na, Si, S, Cl and k peaks, and the inset shows the wt.% of C, O, S, Na, Si, Cl and K as 70.3, 24.3, 2.5, 0.6, 0.7, 0.9 and 0.7, respectively as shown in Fig. 4.19b.

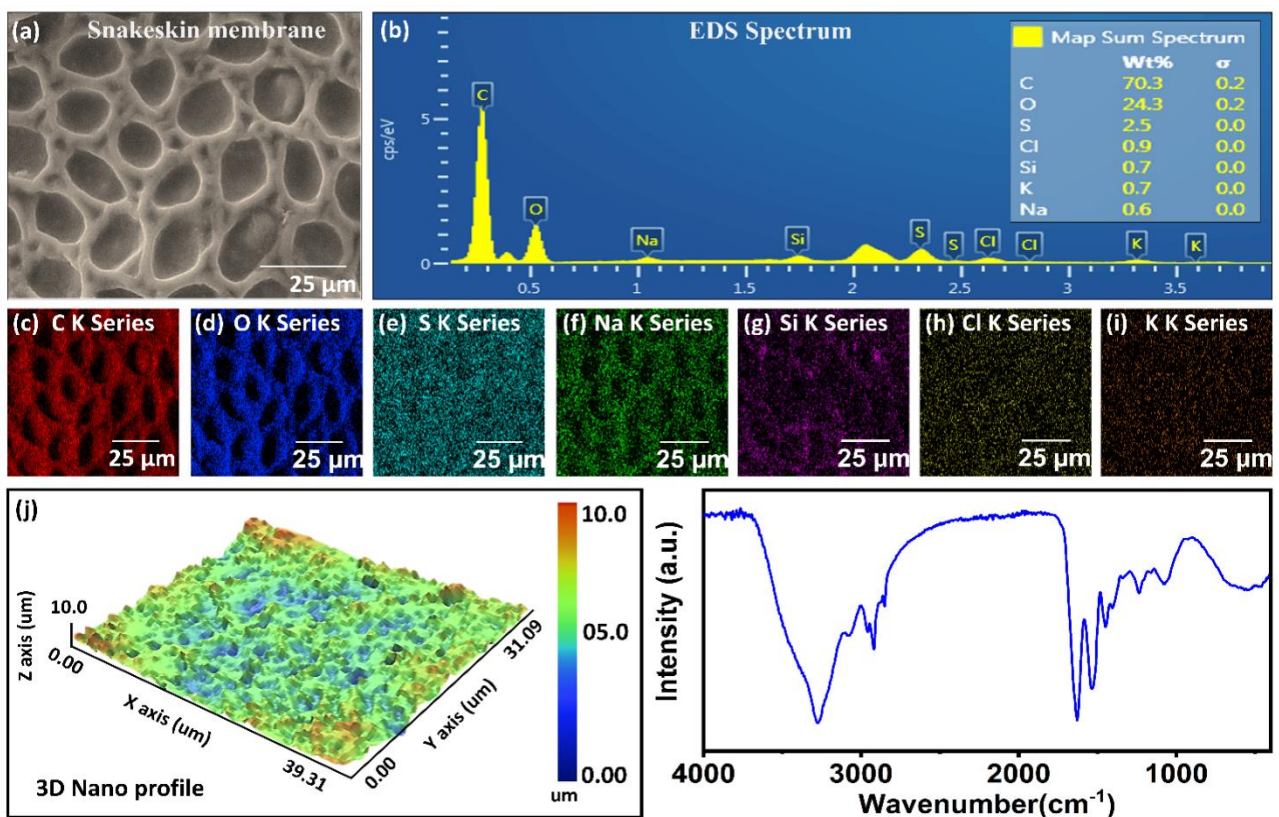


Figure 4.19. (a) The surface morphology of the snakeskin shed membrane analyzed by the SEM with a magnification of 25 μm . (b) EDS analysis of the snakeskin shed film. The insert figure presented its elemental composition. The EDS layered image of the snakeskin shed showing the (c) C K series, (d) O K series, (e) S K series, (f) Na K series, (g) Si K series, (h) Cl K series, and (i) K K series, respectively. The structural analysis for the snakeskin shed film. c) 2D and d) 3D nano-profile presenting the highly porous structure. e) FTIR analysis of the snakeskin shed, showing the existence of different functional groups.

The snakeskin shed membrane elemental analysis using EDS with a magnification of 25 μm . The EDS layered image confirm the presence of C K series, O K series, S K series, Na K series, Si K series, Cl K series and K K series as shown in Fig. 4.18c-i. The electron donating property makes the snakeskin shed membrane as a potential electropositive layer for nanogenerator applications.

The 2D and 3D nano profile of the snakeskin shed membrane is depicted in Fig. 4.18j, which confirms the natural microporous structure. Each pore has an average diameter range from 10-15 μm , while the average height of each pore is measured to be $\approx 10 \mu\text{m}$. All these characterization results verified the micropatterned porous nature of the snakeskin shed membrane. Furthermore, the flexible and microporous snakeskin shed membrane can facilitate to develop piezo electricity also.

FTIR as shown in Fig. 4.18k. The hydroxyl group is observed into the 3280 cm^{-1} . The C-H stretching of the snake shed is observed between 3100-2700. 1650-1672 band demonstrating the C=O group which is obtained from the α -Keratin and possibly of β - keratin. C-N stretching is observed at 1274 cm^{-1} . The C-N and N-H stretching demonstrating the presence of protein in material.

4.3.3 Result and Discussion

The electrical output performance was evaluated using a pneumatic air cylinder (SHINYEONG MECHATRONICS CO., LTD, C32B 16–50) to press the device in vertical direction with a 10 Hz frequency. To investigate the open circuit voltage and short circuit current of snakeskin shed membrane triboelectric nanogenerator with different electronegative materials are investigated which include cellulose, Lignin, PET, PDMS, and PTFE. The output voltage with cellulose $\sim 25 \text{ V}$, Lignin $\sim 30 \text{ V}$, PET $\sim 85 \text{ V}$, PDMS 95 V , and PTFE 120 V as shown in Fig. 4.20a and the output current with cellulose $\sim 10 \mu\text{A}$, Lignin $\sim 17 \mu\text{A}$, PET $\sim 45 \mu\text{A}$, PDMS $\sim 50 \mu\text{A}$, and PTFE $\sim 60 \mu\text{A}$ as shown in Fig. 4.20b. These results shown in Fig. 4.20a and b, clearly depicts that PTFE have most dominant output performance with snakeskin shed membrane and compared to other materials (cellulose, Lignin, PET, and PDMS). The electropositive nature of snakeskin shed membrane can be verified by performing triboelectric nanogenerator results with and without membrane by using PTFE as electronegative layer as shown in Fig. 4.20c and d. The output voltage and current without snakeskin shed membrane are $\sim 30 \text{ V}$ and $\sim 18 \mu\text{A}$, however the results with highly electropositive nature of snakeskin shows clear difference in voltage and current $\sim 120 \text{ V}$ and $\sim 60 \mu\text{A}$ as shown in Fig. 4.20c and d. The electrical output performance of the fabricated TENG is performed using snakeskin shed membrane as electropositive layer and PTFE as electronegative layer as shown in Fig. 4.20e. The results depicted that TENG with snakeskin shed membrane and PTFE as electronegative layers yielded an open circuit voltage $\sim 120 \text{ V}$, short circuit current $\sim 60 \mu\text{A}$ and maximum output power of $6 \text{ k} \mu\text{W}$. The TENG nanogenerator was further employed to charge $10 \mu\text{F}$, $4.7 \mu\text{F}$, and $1 \mu\text{F}$ capacitors, as shown in Fig. 4.21f. The charging discharging curve of the $10 \mu\text{F}$ capacitor is shown in Fig. 4.21g, and can easily charge the capacitor up to 2 V . The TENG endure performance is shown in Fig. 4.20h.

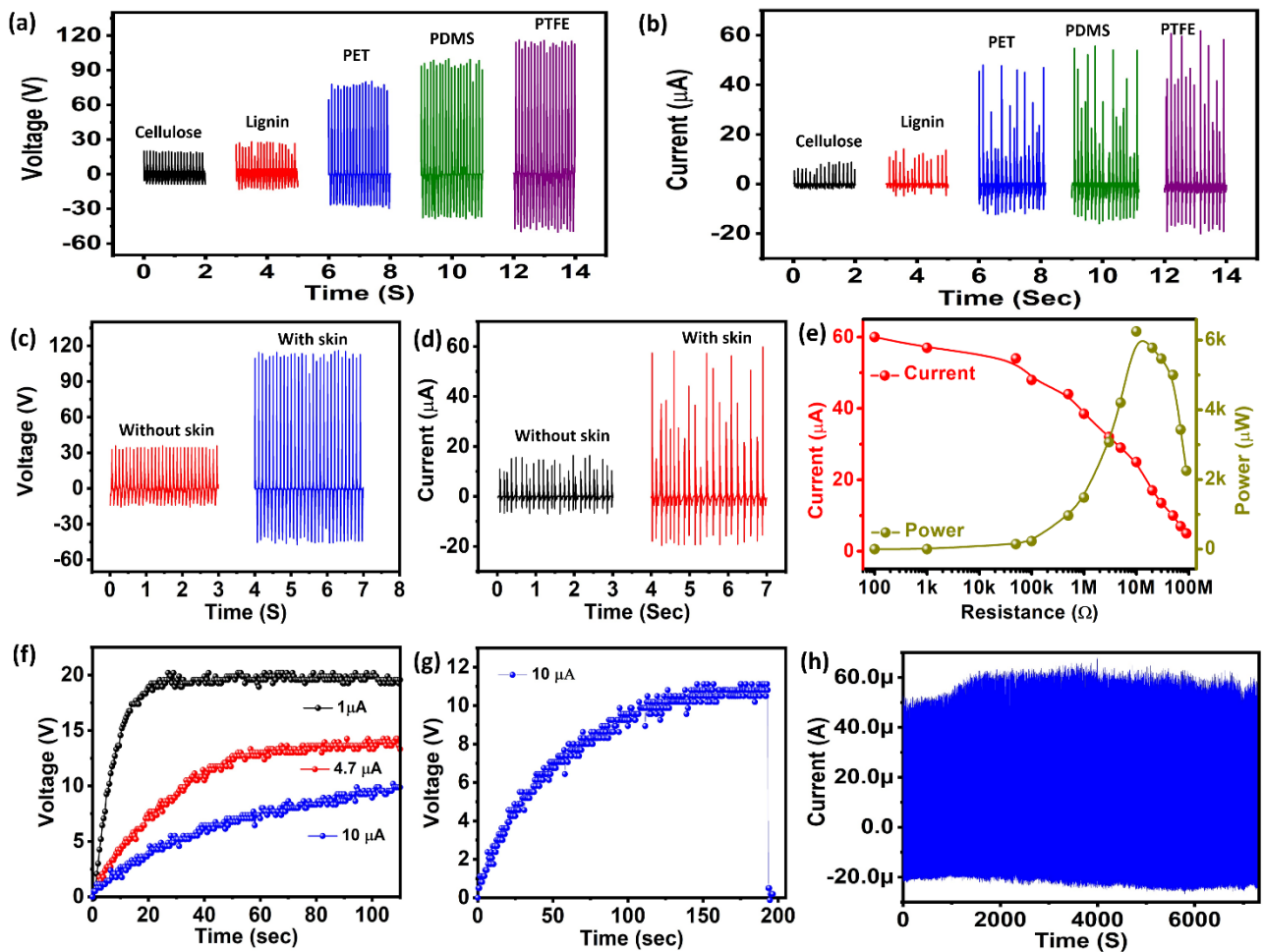


Figure 4.20. The output (a) of open circuit voltage and (b) short circuit current comparison using different electronegative layer (cellulose, Lignin, PRT, PDMS, PTFE) and snakeskin shed membrane used as electropositive layer. The output of (c) open circuit voltage and (d) short circuit current comparison using PTFE as electropositive layer and with and without snakeskin shed membrane as electronegative layer. (e) Output power of snakeskin shed membrane with PTFE at different external load resistances, (f) The charging of 10 μF , 4.7 μF , and 1 μF capacitors using snakeskin shed piezoelectric nanogenerator, (g) The charging and discharging curve of 10 μF capacitor employing snakeskin shed piezoelectric nanogenerator. (h) The current stability for more than 7300 sec.

The fabricated snakeskin shed membrane piezoelectric nanogenerator (PENG) device are fabricated based on different device sizes, which include 6 cm^2 , 9 cm^2 , 12 cm^2 and 15 cm^2 to examine the open-circuit voltage and the short circuit current using as shown in Fig. 4.21a and b. We can see that by increasing the device size 6 cm^2 to 12 cm^2 , there is significant increase in open circuit voltage from ~ 10 V to ~ 15.5 V as shown in Fig. 4.21a and short circuit current increases from 1.6 μA to 3.4 μA as shown in Fig. 4.21b. The above 12 cm^2 to 15 cm^2 doesn't show any improvement or increase in output voltage and current. There is a slight variation in the peaks of the output values of voltage and current, that may occur due to varying strain rate during pressing and releasing the air cylinder. The positive and negative peaks can be better assumed as the pressing of the device occurs due to the pneumatic air cylinder, whereas the releasing occurs because of the flexible and porous nature of the snakeskin shed membrane.

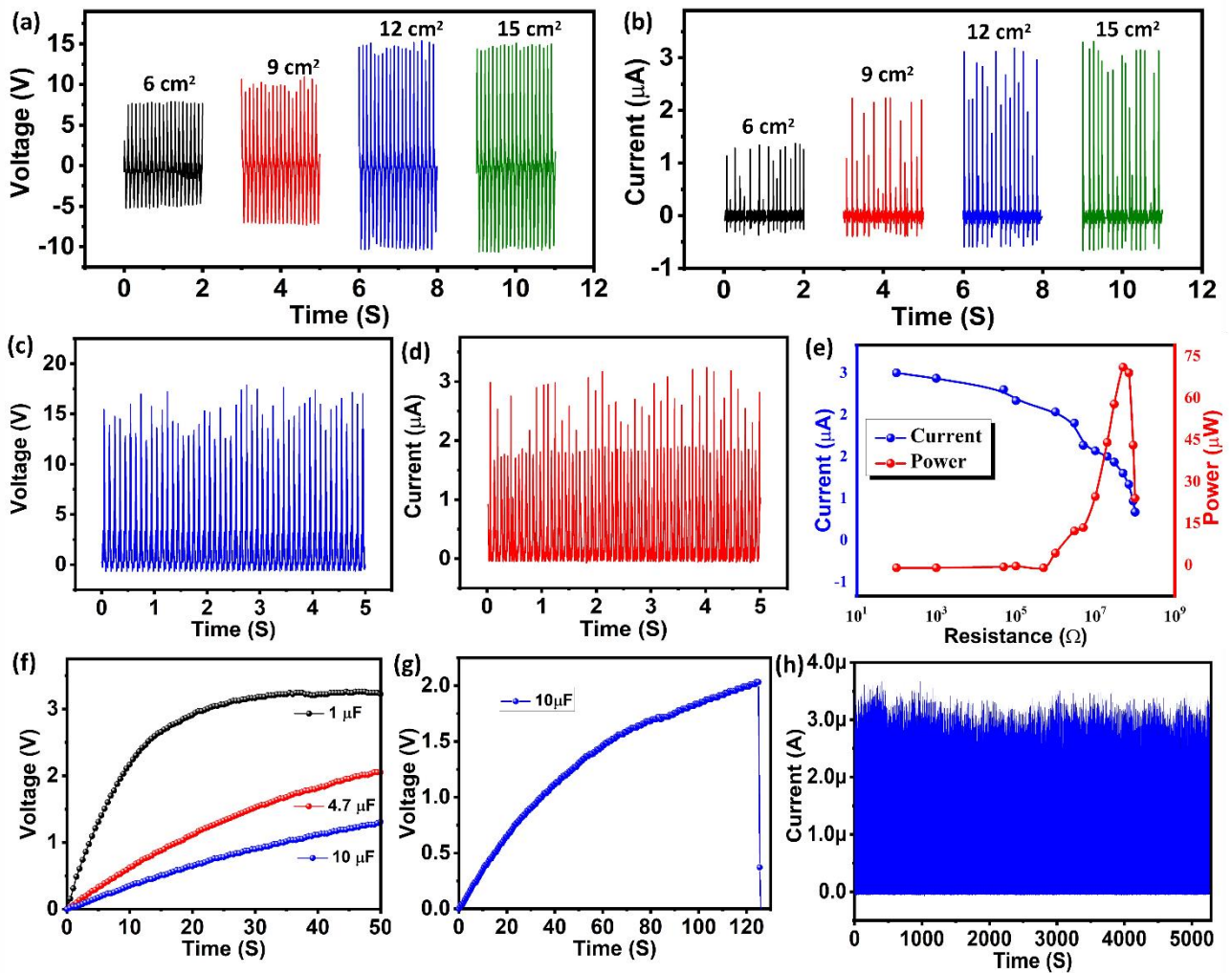


Figure 4.21. The different size of piezoelectric nanogenerators to examine the (a) open circuit voltage and (b) short circuit current. The rectification effect is examined of the snakeskin shed membrane piezoelectric nanogenerator to monitor the (c) open circuit voltage and (d) short circuit current. (e) Dependence of output current and power of piezoelectric nanogenerator of snakeskin shed membrane at different external load resistances, (f) The charging of 10 μF , 4.7 μF , and 1 μF capacitors using snakeskin shed piezoelectric nanogenerator, (g) The charging and discharging curve of 10 μF capacitor employing snakeskin shed piezoelectric nanogenerator. (h) The current stability for more than 5000 sec.

The rectified open circuit voltage $\sim 18\text{ V}$ as shown in Fig. 4.21c and short circuit current $\sim 3\ \mu\text{A}$. The snakeskin shed membrane piezoelectric nanogenerator power was measured by applying various resistances ranging from $100\ \Omega$ to $100\ \text{M}\Omega$ along the external circuitry, as the power of the device depend on the external load resistance as shown in Fig. 4.21d. It can be seen that the current decreases with increasing the load resistance. Notably, the maximum power of the TP based PENG reaches $73\ \mu\text{W}$ at the load resistance of $20\ \text{M}\Omega$. The snakeskin shed membrane piezoelectric nanogenerator was further employed to charge $10\ \mu\text{F}$, $4.7\ \mu\text{F}$, and $0.1\ \mu\text{F}$ capacitors, as shown in Fig. 4.21f. It can be seen that the device can easily charge the capacitors to drive the low-power devices. The charging discharging curve of the $10\ \mu\text{F}$ capacitor is shown in Fig. 4.21g, which shows that the snakeskin shed membrane piezoelectric nanogenerator can easily charge the capacitor up to 2 V .

The device repeatability and endurance performance of snakeskin shed membrane piezoelectric nanogenerator is performed for more than 5000 sec to ensure the device reliability to power up small electronic appliances as shown in Fig. 4.21h.

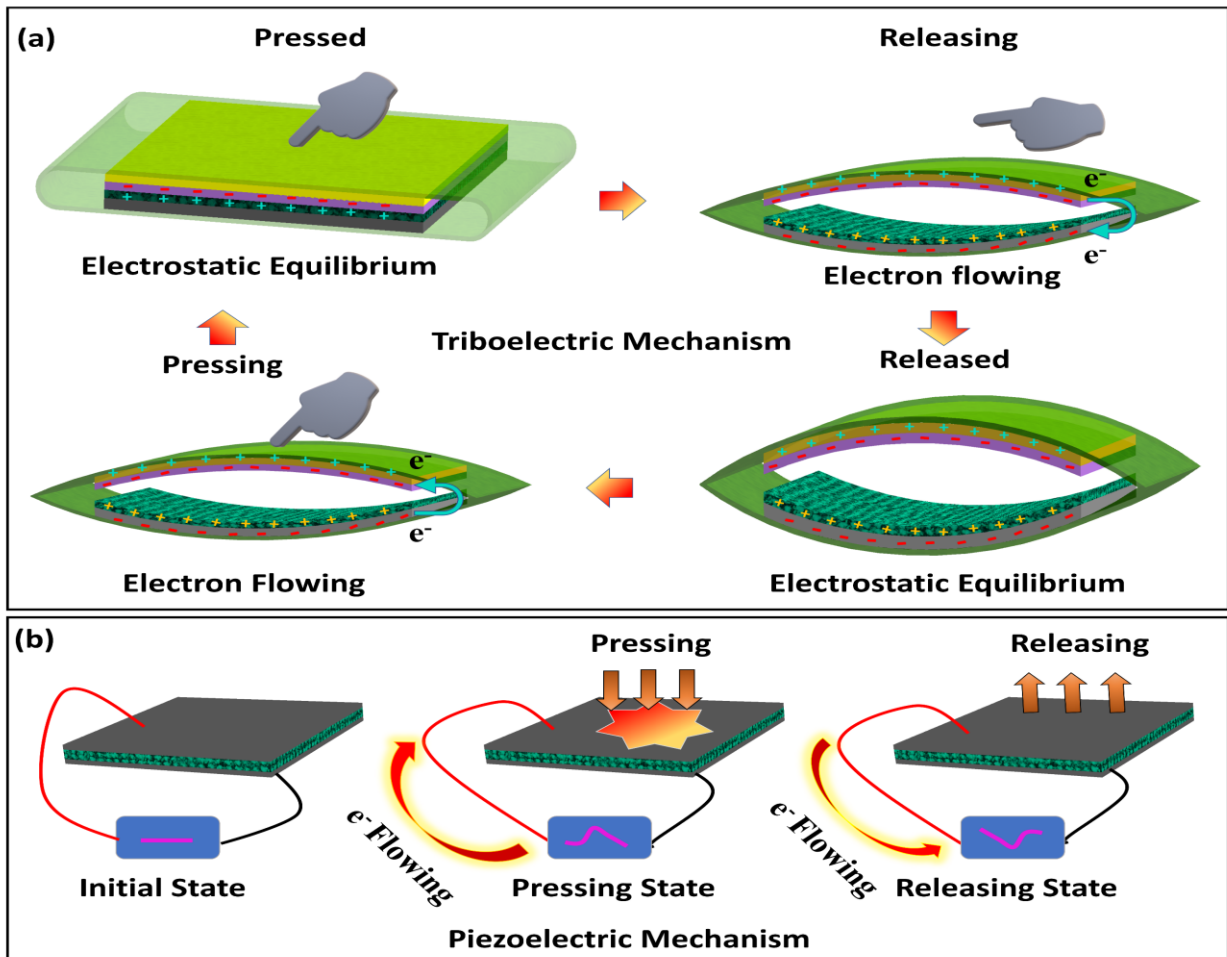


Figure 4.22. The (a) triboelectric and (b) piezoelectric nanogenerator mechanism

The working mechanism of the proposed TENG is demonstrated into the Fig. 4.22a. firstly, both electropositive and electronegative layers are coming contact to each other. The positive and negative charges will be generated on both electropositive and electronegative sides. An induced charge is produced in the top/bottom electrodes opposite the dielectric layers during the releasing process because of electrostatic induction, as shown in Fig. 22a. As a result, the charges flow in the external circuitry. A balanced state will be achieved when full separation occurs between top/bottom layers, as shown in Fig. 22a thus, no current will flow in the external circuit. When both electrodes again come closer to each other, an electric potential is re-established, while the current will flow in the opposite direction, as shown in Fig. 22a. An alternating current (AC) will be established under a constant applied force during pressing and releasing the fabricated triboelectric nanogenerator device. The working mechanism of proposed PENG is shown in Fig. 22b.

When vertical force is applied by pneumatic air cylinder, positive and negative piezoelectric potential is developed between two electrodes in the fabricated PENG device. As a result, a potential difference is generated on top and bottom electrodes. When the external path is provided, the electrons flow in the external circuitry. Further, when the external applied force is released, the electrons stop flowing. As a result, piezoelectric potential vanishes. The stored electrons flow back in opposite direction.

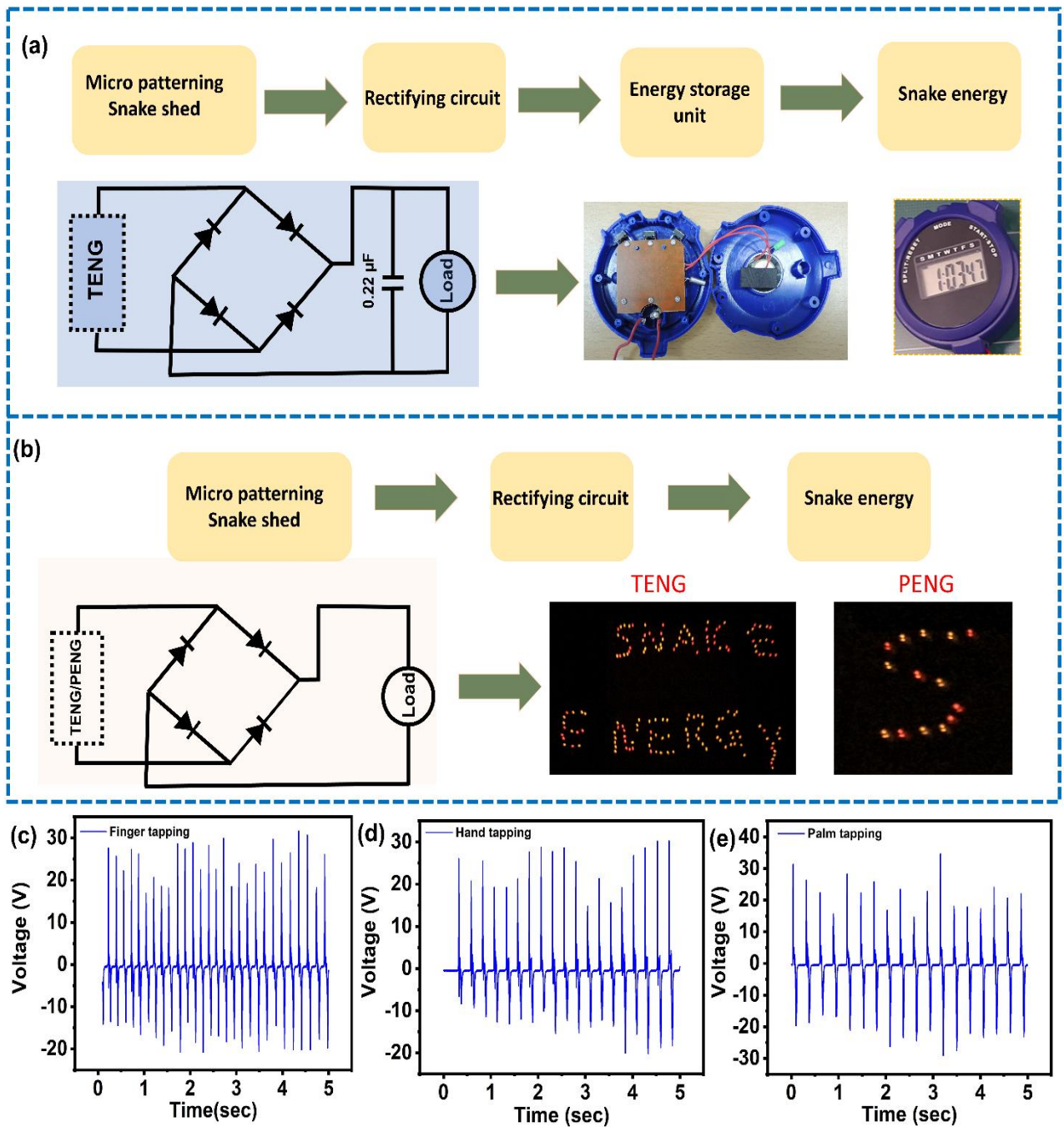


Figure 4.23. (a) The schematic circuit of TENG connections with a stopwatch and the realized image of internal connections and powering up low power stopwatch. (b) The schematic circuit of TENG connections with LEDs and Lighting of LEDs using GUA-based TENG. The bio-mechanical force excitation for piezoelectric nanogenerator. (c) Finger tapping, (d) Hand tapping and (e) Palm tapping.

To investigate the applicability and reliability of the proposed tribo and piezo electric nanogenerator, we have implemented the device for self-powering electronic applications. The real time applications were investigated by the hand excitation force. Fig. 4.23a demonstrating the circuit connection and pictorial image of smart electronic stopwatch. We have operated stopwatch by using energy storage device (2.2 μ F) and bridge rectifier with connection of triboelectric nanogenerator and it has showed the very stable performance without any degradation while operating time. Fig. 4.23b shows the connection of lighting the LEDs by using the tribo and piezoelectric nanogenerator device. The triboelectric nanogenerator shows the ability to light up the 198 LED's and the piezoelectric nanogenerator shows the 12 LEDs without any storage device. Also, we have performed the piezoelectric nanogenerator experiments by bio-mechanical energy harvesting system (Finger tapping, hand tapping, palm tapping) as shown in Fig. 4.23c-e. This all bio-mechanical pressure shows the efficient results from proposed Piezoelectric nanogenerator. This daily routine life experimental results suggesting that the proposed micropatterning snake shed based tribo and Piezo electric nanogenerator is a potential candidate for future energy harvester and self-powering applications.

4.3.4 Summary

In this paper, we have successfully applied the micropatterning snake shed for flexible tribo and piezoelectric nanogenerator. The presence of hydroxyl and carbonyl groups in snake shed is responsible for the tribo-positive properties of snake shed. The α -keratin is responsible for the flexibility, and β -keratin is responsible for rigidity of the snake shed. The dominance of α and β keratin and other proteins playing the important role for high performance in piezoelectric nanogenerator. The proposed tribo and piezo electric device shows the good ability to charge the commercially available dielectric capacitors and operated the electronic devices. The tribo and piezoelectric nanogenerator shows the higher stability. These all results suggested that the proposed micropatterning snake shed based tribo and Piezoelectric nanogenerators is a prominent candidate to develop the high performance and highly stable flexible energy harvester.

4.4 Inkjet Printed Self Healable Strain Sensor Based on Graphene and Magnetic Iron Oxide

In recent days, flexible strain sensors have got tremendous attention in the various applications such as human motion detection, health care, damage detection, characterization of structures, and exhaustion studies of materials[5]. For these kinds of applications, well established strain sensors are required. However, the micro cracks and mechanical fractures in the strain sensors are very repeatedly occurred under repeated deformation[6]. The performance of a strain sensor is susceptible to the structure damage, and this damage may cause the loss of a functionality of the sensor[5]. Therefore, it is necessary to introduce a sensor with self-healing property to improve its reliability, and to maintain its function towards the strain through its healing even though it is cut[132].

To overcome the fracture problem of the strain sensors, many research groups are exploring and developing self-healing conductors and sensors by using the various materials and nano-composites[132]. The self-healing materials are smart materials that can restore some or all of its functions after cutting or suffering by an external damage from mechanical force[133]. Their self-healing property are not only prolonging the lifetime of products but also reducing the wastage of the materials[6, 132, 133]. Especially, this function increases their reliability of the strain sensor based devices¹⁴. To cover these good advantages, self-healing mechanism and several materials have been studied[134]. In terms of materials, two types of materials have been reported in early decades with intrinsic self-healing and extrinsic self-healing properties[135, 136]. Self-healing property in intrinsic materials is due to the reversible covalent and non-covalent bonds[136, 137] while self-healing in extrinsic materials is due to microcapsules or healing agent, which heals the cracks when cracks are formed due to external strain[137, 138]. The self-healing property of these materials is not just limited to a mechanical performance. It is utilized for the various application such as conductivity, artificial electronic skin, medical devices, and soft robotics[139-141]. For the strain sensor applications, the self-healing property as well as a good electric conductivity should be satisfied[142].

Herein, this paper proposes a novel high stretchable strain sensor with the self-healing property depositing graphene and magnetic iron oxide nano-composite on the engineered self-healable polyurethane substrate through Fujifilm inkjet DMP-3000 printer at ambient conditions as shown in Fig. 4.24 of supplementary information. To include a self-healing function between graphene flake to flake, magnetic iron oxide is blended, and it has also a role to induce the magnetic force property in the nanocomposite.

Experimentally, the best graphene and magnetic iron oxide blending ratio is 1:1. This composite material shows a high mechanical and excellent self-healing property. To increase a self-healing property of the proposed sensor, the engineered self-healable polyurethane substrate is applied due to its strong self-healing function. The prepared samples maintain its strain function of 100% even after 10,000 times bending cycles, and the strain sensitivity performance of 94% recovered after cutting the sensor. The proposed strain sensor is stretchable up to 54.5%. After cutting it, the stretching factor decrease down to 32.5%, but it still working good for a strain sensor application. For these results, we are sure that this work can create a new opportunity towards the design and fabrication of a future self-healing wearable strain sensing based electronic devices.

4.4.1 Materials and Methods

Graphene flacks with average size of 100 nm, heptane solvent, magnetic iron oxide (Fe_2O_3) nanoparticles solution in heptane with 0.8–1.4% solid material was purchased from Sigma Aldrich, South Korea. To make the ink solution based on graphene, 0.5 mg graphene was dispersed in 4 ml heptane solvent. The ink was sonicated for 30 min at room temperature to make homogenous suspension. The solution was then centrifuged for 30 min at 1000 rpm to remove the big chunks and particles. The super latent was removed in a vile, which was used as the final solution for the fabrication of active layers. Magnetic iron oxide solution was used without further purification. For the best fabrication of the composite film, both inks were mixed with different blending ratios. To find the best blending ratio, different ratios of graphene and Fe_2O_3 were used, i.e., 1:0, 1:0.5, 1:1, and 1:1.5. The solution was bath sonicated for 30 min at room temperature to make homogenous composite solution and then put on shaker for 1 h. The viscosity of the composite ink was measured to be 12.35–16.9 mPa by using Viscometer VM-10A system. The surface tension was measured 41–54 mN/m by Surface electro-optics (SEO)'s contact angle analyzer. The wrinkled aluminum foil substrate was prepared by squeezing and unfolding the 60 mm × 60 mm × 10 μm aluminum foils. This methodology can create random micro ridges on the aluminum foil, which is finally suppressed by using a soft hammer as shown in Fig. 4.24a of supplementary information. After that, the wrinkled aluminum foil was attached to the glass substrate using a double-sided stick tape to caste a liquid polyurethane. The casted polyurethane was cured inside UV ozone for 5 min. The cured polyurethane was cut into different substrate sizes to use for the sensor. The prepared polyurethane substrate with the random micro ridges has several advantages as it ensures the stickiness of the active film and helps in scattering the applied strain.

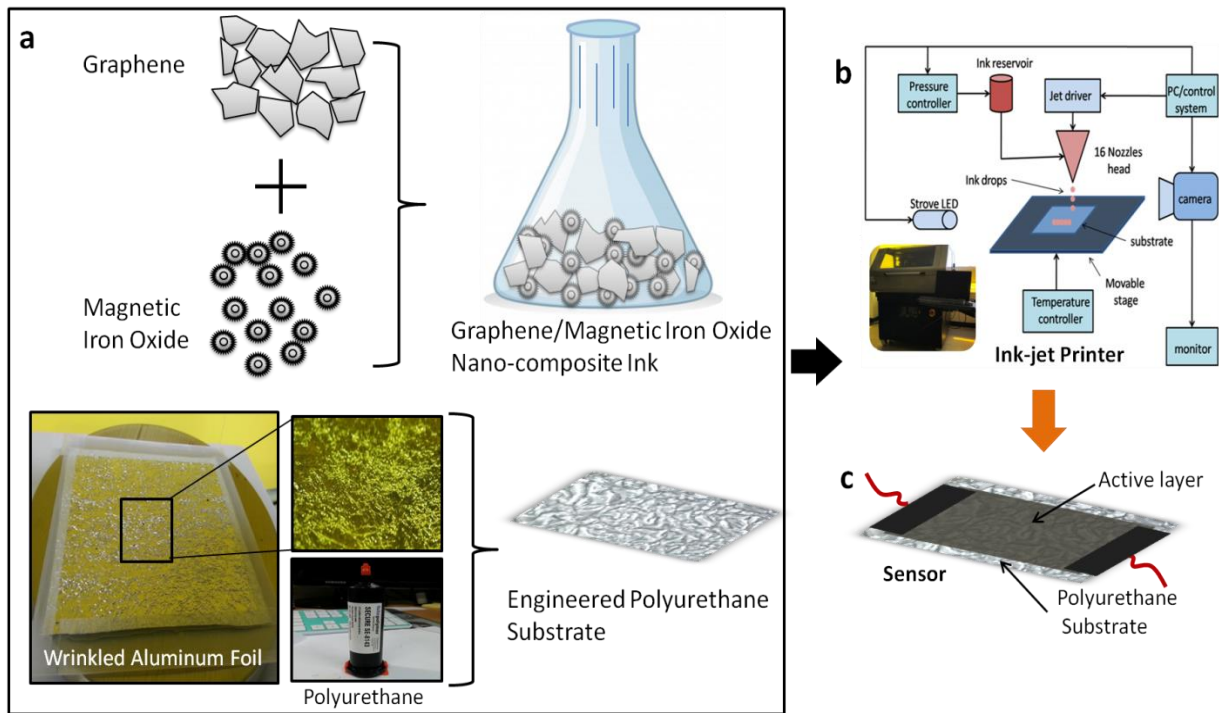


Figure 4.24. Materials preparation and step by step fabrication process. (a) Preparation of the graphene and magnetic iron oxide nano-composite and polyurethane substrate. (b) Inkjet materials printer DMP-3000 and its schematic diagram. (c) The proposed strain sensor.

The commercialized materials ink-jet printer (Fujifilm Dimatix DMP-3000) was utilized to fabricate the graphene and Fe_2O_3 nano-composite active film on the engineered polyurethane substrate. To begin with, schematic of the active layer (graphene and Fe_2O_3 nanocomposite) was designed in EAGLE 7.4.0 and converted to bitmap image format using ACE 3000 and then exported to Dimatix Drop Manager, which converts the Bitmap image file into ptn format⁵¹. The resulted file was loaded into the material ink-jet printer (DMP-3000) and the graphene/ Fe_2O_3 nano-composite ink was loaded in the cartridge containing 16 nozzles. The composite ink was deposited by using 10 pL drop size on the engineered polyurethane substrate, and the stable wave shapes for the print head was determined at 26 V, which was applied to fabricate the proposed active layer and then cured at 100 °C for 2h. The schematic diagram of the ink-jet material printer and the real image of DMP-3000 material printer shown in Fig. 4.24b. The contact pads were deposited for external circuitry interfacing and all fabrication steps of the proposed strain sensor are shown in Fig. 4.24b.

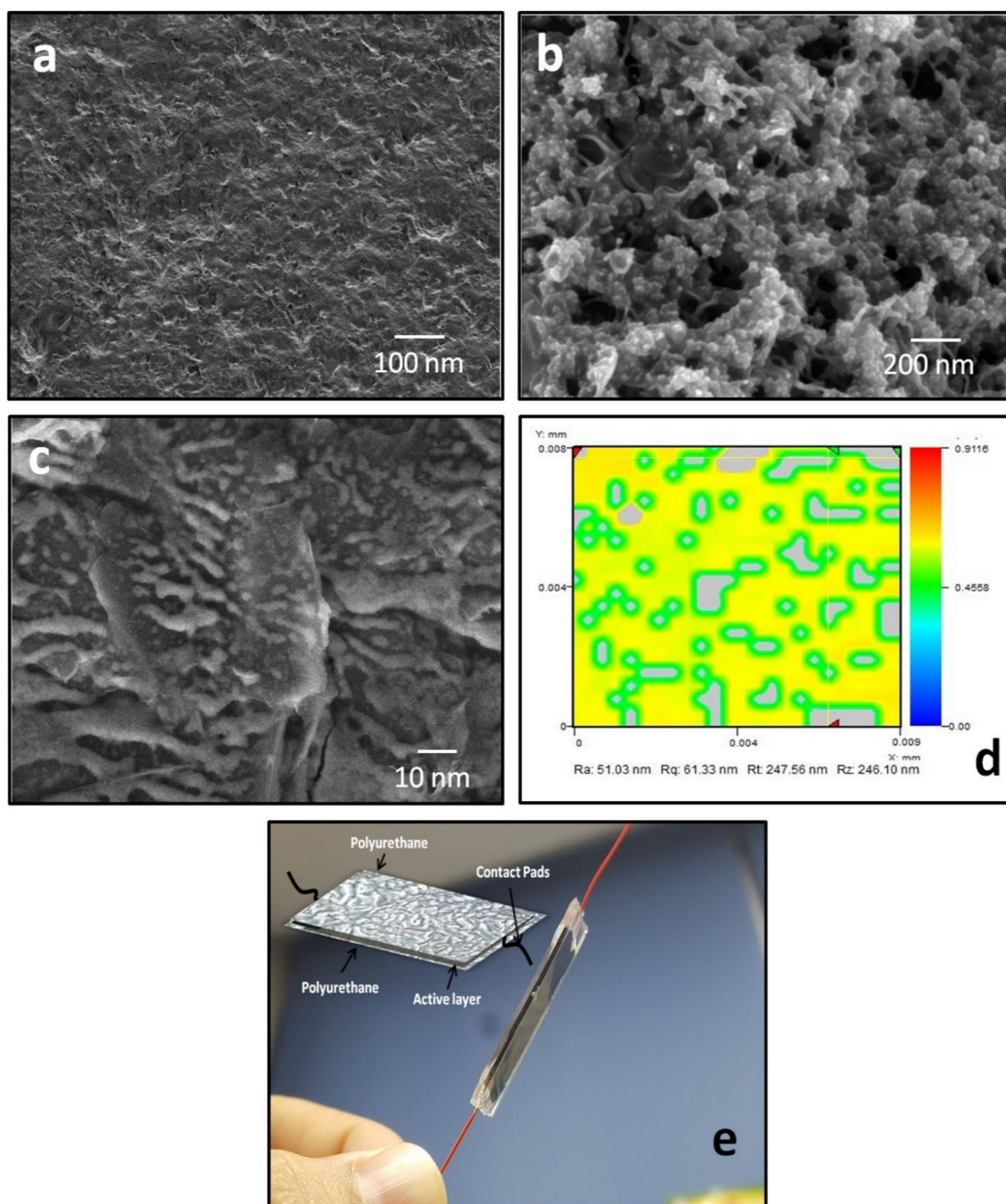


Figure 4.25. SEM Analysis of the active layer. (a) SEM image of graphene film, (b) SEM image of magnetic iron oxide film, and (c) SEM image of self-healing nano-composite film of graphene and magnetic iron oxide. (d) 3D morphology of the active layer on engineered polyurethane substrate. (e) The fabricated strain sensor based on graphene and magnetic iron oxide nanocomposite.

4.4.2 Characterizations

Field Emission Scanning Electron Microscope (TESCAN) was utilized to examine the surface morphology of graphene, Fe_2O_3 , and the active layer based on graphene and Fe_2O_3 nanocomposite. To investigate the composite active layer further. NV-2000(Universal) non-contact surface profiler with nano level accuracy was applied for roughness measurement and the 3D profile of the active layer. The nano-composite active film is spatially uniform due to the polyurethane substrate roughness as we can see in the 3D morphology image. Electrical characterizations of the sensor were performed by using Agilent B1500A Semiconductor Device and the stretching characterization were performed by homemade stretching machine while the bending tests were also performed to verify the flexible nature of the fabricated strain sensor.

4.4.3 Results and Discussion

To begin with, Field Emission Scanning Electron Microscope (TESCAN) was used to analyze the surface morphology of graphene, Fe_2O_3 , and their nano-composite active film. Fig. 4.25a shows the SEM image of graphene and confirms that the film is uniformly deposited without visible defects. Fig. 4.25b shows the SEM image of Fe_2O_3 thin film and the film is uniformly deposited, while Fig. 4.25c shows the SEM image of the graphene and Fe_2O_3 nanocomposite active film as certain crack free film, which is properly deposited over engineered polyurethane substrate through ink-jet material printer (DMP-3000). As Fig. 4.25c is the zoomed image of the active composite film, we can clearly see that both the graphene and Fe_2O_3 are present in the film. From this analysis, we confirm the uniform and equal distribution of all materials over the entire surface of the engineered polyurethane substrate. Based on graphene and magnetic iron oxide, the proposed strain sensor is fabricated on the engineered polyurethane substrate as shown in Fig. 4.25e.

To enhance the stretchability of the proposed strain sensor, the substrate roughness plays a key role in stretchable electronic devices as shown in Fig. 4.25d, and its shows the 3D morphology of the active layer on engineered polyurethane substrate. Both the tensile stress and cracks on the film surface depend on the nature of substrate. The strain endurance of the proposed thin film is enhanced by two design concepts: the substrate roughness and the addition of Fe_2O_3 . The polyurethane substrate surface pattern was manufactured by an aluminum foil, which was chosen due to the roughness feature of the surface. It increases the adhesion between the active film layer and the substrate.

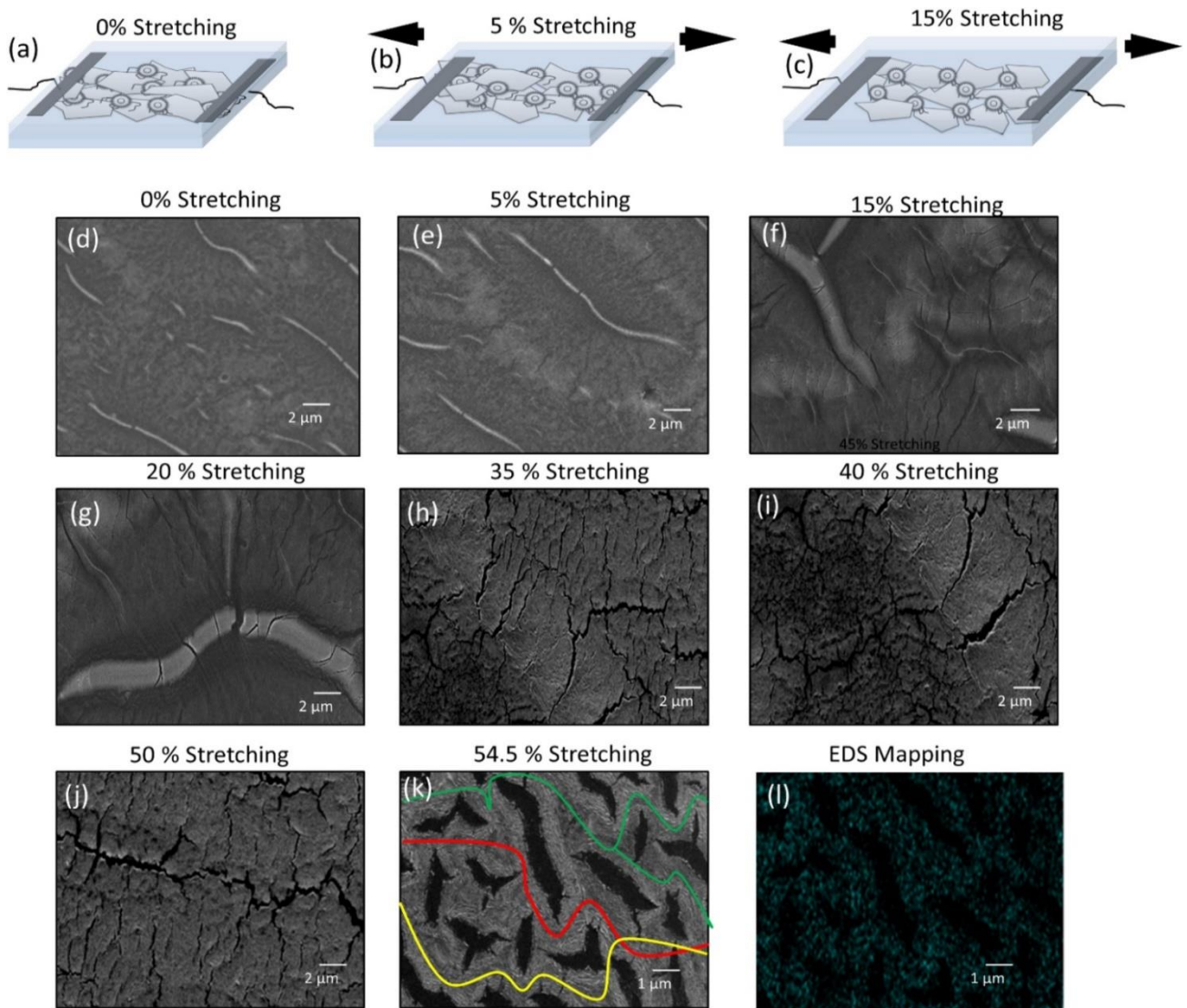


Figure 4.26. Strain detection mechanism of the proposed self-healing strain sensor. (a) Schematic illustration of the strain sensing with 0%. (b) Schematic illustration of the strain sensing with 5%, with increasing the stretching strain, the overlapping area between graphene flakes decrease those results in the increase in resistance. (c) Schematic illustration of the strain sensing with 15%, along the decreasing overlapping area between graphene flakes, small micro cracks also appear that results in the increase in the resistance of the strain sensor. (d) SEM image of the active composite film with 0% stretching. (e) SEM image with 5% stretching. (f) SEM image with 15% stretching. (g) SEM image with 20% stretching. (h) SEM image with 35% stretching. (i) SEM image with 40% stretching. (j) SEM image with 50% stretching. (k) SEM image with 54.5% stretching. (l) EDS elemental mapping after 54.5% stretching.

Fe_2O_3 has the magnetic force property, so its addition to graphene increases the stretching parameter by making the connection between the graphene flake to flake. To demonstrate the stretching effects of the proposed strain sensor, the schematic illustrations are demonstrated as shown in Fig. 4.26a–c. By applying an external tensile stress, the overlapping region between flakes decreases due to graphene flakes spaced out, and the active film resistance is increased as a function of an external tensile strain. For the external tensile strain $< 5\%$ (% increase in device length), the substrate roughness acts as the wrinkled pattern and the deformation on active film remains lower than the strain

on the substrate. The deformation on graphene/Fe₂O₃ nano-composite film remains lower than the strain force < 5% on the substrate. When the tensile strain is less than 5%, the active layer resistance increases, due to the decreasing overlapping between flakes. When the tensile strain is increased more than 5%, several small cracks appear on the nano-composite film of graphene/Fe₂O₃, which result in increase in resistance is observed due to moment of flakes as well as appearance of small cracks as shown in Fig. 4.26d–l. Here, if the stress is more increased on active layer, these cracks are nucleate due to the rough polyurethane substrate and as well presence of magnetic Fe₂O₃, and that prevents the breakdown of the active film due to its self-healing property. Since the roughness induces an inhomogeneous stress field on it, the destructive force is scattered as evidence shown in Fig. 4.26d–l. Hence, the stretchability of the active film on the micro-random ridge polyurethane substrates can be dramatically increased. Here, the stretching factor is increased due to substrate roughness and the blending of magnetic iron oxide. As magnetic iron oxide has the magnetic property, so it makes paths from flake to flake and prevent the film form breakdown. The magnetic material also performed the self-healing function on the active layer.

The resistance of the active film is increasing if the cracks size or their numbers are increasing. The electrical resistance changes in two phenomena as; (1) the resistance change is dominant due to flakes movement under 5% tensile stress, (2) for more than 5% tensile stress, the resistance changes due to the formation of cracks. Although the cracks are occurred on the active film due to increase in tensile stress, it can still operate as a strain sensor because of progressive paths transformation from initial tracks into one or several longer and narrower conductive paths, which results in increasing the film resistance as shown in Fig. 4.26k. By increasing roughness on the polyurethane substrate, the stretchability is improved as it leads to a higher density of pinning centers which help the scattering of tensile stress all over the active film.

To find the best blending ratio of graphene and magnetic iron oxide for the proposed strain sensor, we have fabricated four types of devices with different blending ratios of 1:0, 1:0.5, 1:1, and 1:1.5, and calculated the sensitivity of each ratio at different bending diameter. Under different bending diameters, the sensitivity of the devices with the same surface roughness of 0.34 was observed⁵¹. The blending ratio of 1:0 has the highest sensitivity as it has just graphene flakes, but the stretching parameter is low because there are no magnetic iron oxide nanoparticles to make them bind together, hence a change in the resistance is substantial and unstable. As shown in Fig. 4.27, we fabricated the sensor with just graphene as the active layer. It can also work as a stain sensor with a stable behavior, but the stretching behavior is less pronounced and having the high error in resistance.

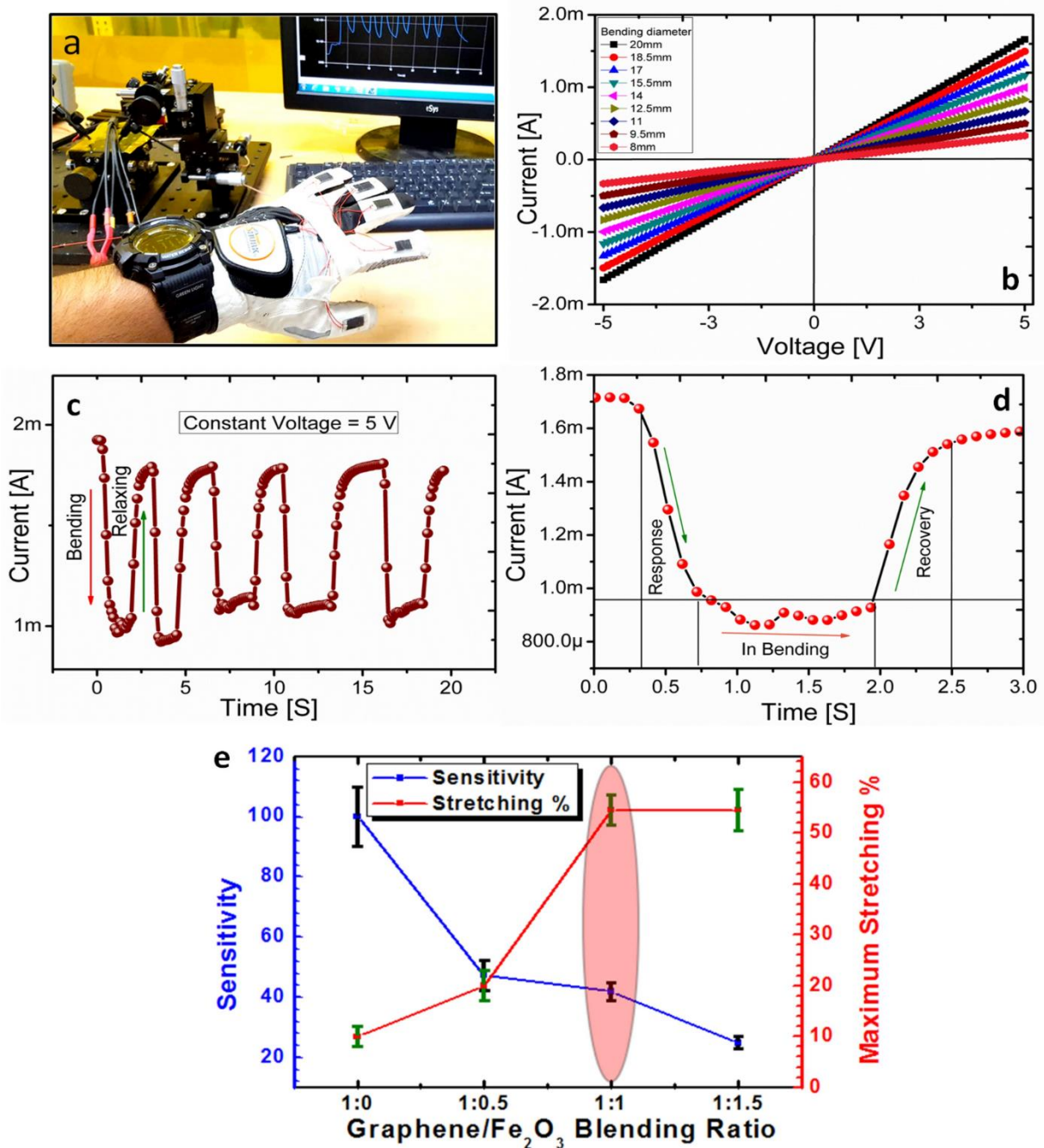


Figure 4.27. Characterization of a strain sensor based on just graphene active layer. (a) Sensors attached on a glove to record the fingers motion. (b) I–V curves by different bending diameter as shown in the inset image. (c) Bending and relaxing cycles of the sensor. (d) The response and recovery time of the sensor. (e) Sensitivity and maximum stretching % along graphene and iron oxide composite blending ratio.

Fig. 4.27a shows the realization of the device with graphene as the active layer as the strain sensor. The sensors are attached on the glove to record the motion of the fingers. Fig. 4.27b shows the I-V curves of the sensor via different bending diameters as the inset image in this figure. Through finger detection in Fig. 4.27a, the bending and relaxing cycles are measured as shown in Fig. 4.27c. Here, its response of 0.3 s and recovery time of 0.45 s are recorded as shown in Fig. 4.27d.

These results show that just graphene flakes can be used as strain sensor, but the stretching percent (%) is less. To increase the stretching parameter and reduce the error, we blend the magnetic iron oxide in graphene with different ratios. When the ratio of the magnetic iron oxide is increased, the stretching performance is increased, and the resistance error is reduced. As shown in Fig. 4.27e, 1:1 was the optimum ratio for the proposed strain sensor with a valuable sensitivity error and high stretching %. Here, the sensor with 1:0 blending ratio has the highest sensitivity error as the reason of the graphene flakes are only used. When we add the magnetic iron oxide, the sensitivity error decreased because it provides connection between flake and flake, and the stretchability also was enhanced. From this analysis, we have selected the graphene and magnetic iron oxide composite blending ratio of 1:1 for the proposed strain sensor.

To understand the proposed sensor based on graphene and magnetic iron oxide nano-composite material, the bending effect is measured along different bending diameter as the inset image shown in Fig. 4.28a. As shown in Fig. 4.28a, the electrical resistance and current are almost linearly increased under bending diameter down to 6 mm, which confirm the proposed strain sensor can be used in the finger bending detection. For this reason, we attached five sensors on a glove to test the application performance as shown in Fig. 4.27a, and we came to know that it shows stability and uniformity to the bending. Electrical resistance was changed due to the graphene flakes overlapping area-changing and cracking phenomenon in the nanocomposite film of the sensor. The data was calculated for 5 sensors at different bending diameters to investigate the error in resistance and its stability. Very low error is observed, and the maximum error is $\pm 10 \Omega$ via 6 mm bending diameter, which is negligible error. Similarly, the current via different diameter was also checked and there was uniform change in current as shown in Fig. 4.28a. The bendability test suggests that the proposed strain sensor can be used for the human body motion detection. As shown in Fig. 4.28b, the sensor was stretched up to 54.4% and there was linear change in resistance and current along different stretching %. After 54.5% stretching, it shows open circuit due to the breakdown of the composite film. However, on relaxing the stretching, it recovers its 100% efficiency due to self-healing. For a stability for a long-term strain endurance cycle, the proposed strain sensor is tested for more than 10,000 bending/relaxing cycles as shown in Fig. 4.28c and the sensor shows stable behavior without losing its performance. Figure 4d shows the stretching cycle of the proposed strain sensor. Starting from 5% stretching, the sensor was stretched step by step following 10%, 20%, and 30% and then again relaxed with the stretching following 20%, 10%, and 5%. The sensor shows a stable response and recovers to its original position. Fig. 4.28e shows the hysteresis curve of bending and relaxing as it shows stability. For these results, we can say that the proposed sensor can be used as a strain sensor for wearable electronics.

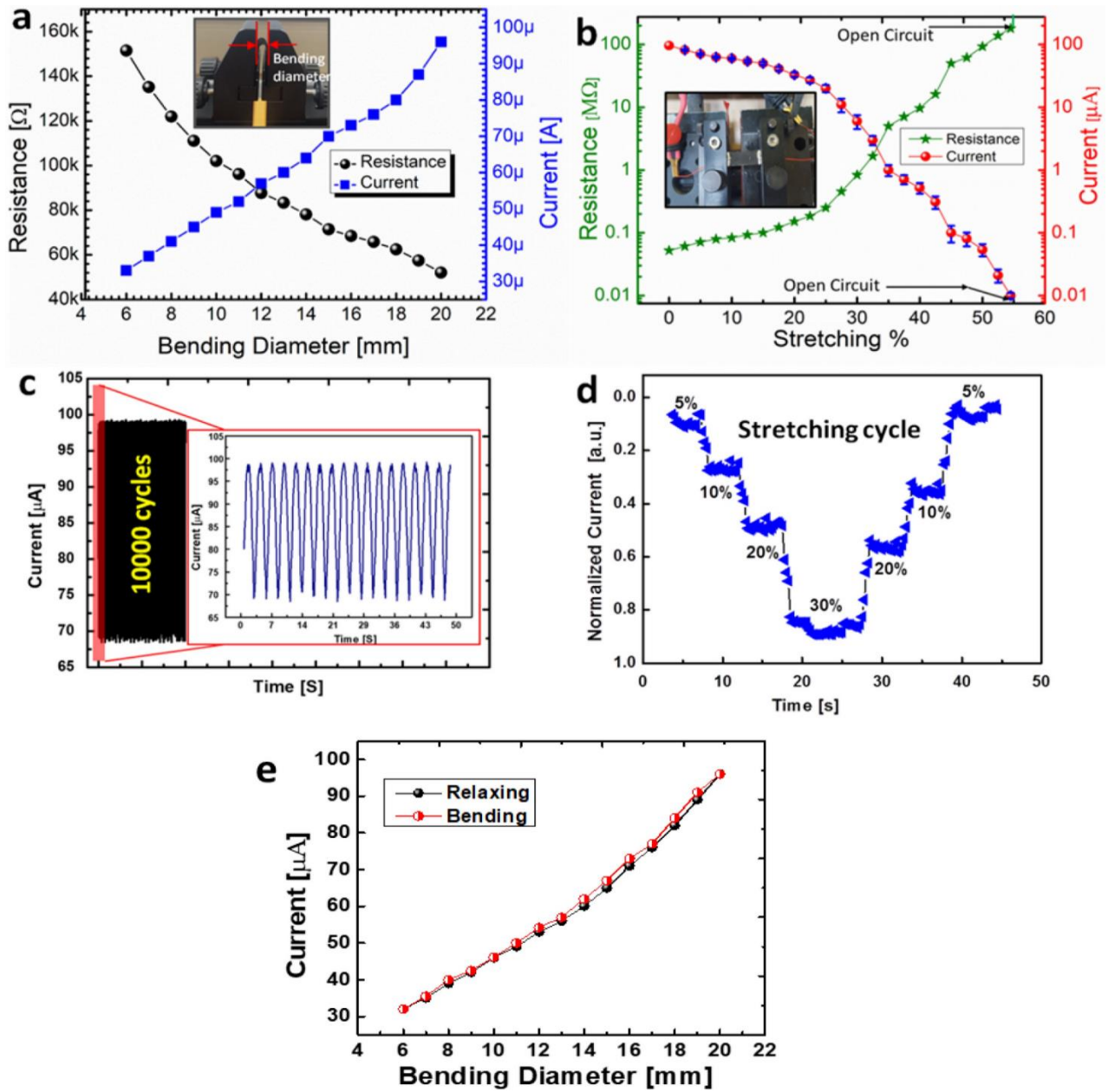


Figure 4.28. Characterization of the self-healing strain sensor with graphene and magnetic iron oxide composite film. (a) Current and resistance changes along different bending diameters as the inset image. (b) Current and resistance changes along different stretching % as the inset image. (c) 10,000 bending/relaxing cycles. (d) Normalized current variation along the stretching cycle of the proposed strain sensor. (e) Hysteresis curve of bending and relaxing.

The electrical performance of the proposed strain sensor was analyzed on different bending angles using Agilent B1500A Semiconductor Device Analyzer by applying sweeping voltage from 0 to 5 V. Fig. 4.29a shows I–V characteristics over different bending diameter (6 mm, 10 mm, 14 mm, 16 mm, and 20 mm), which shows ohmic relationship between the voltage and the resulting electrical current of the graphene/Fe₂O₃ nanocomposite. Hence, the proposed sensor can be applicable to measure the different bending angle and strength for the strain applications. For applying the strain sensor in a real-life application, we observed the stretching/releasing cycles for a long period of time.

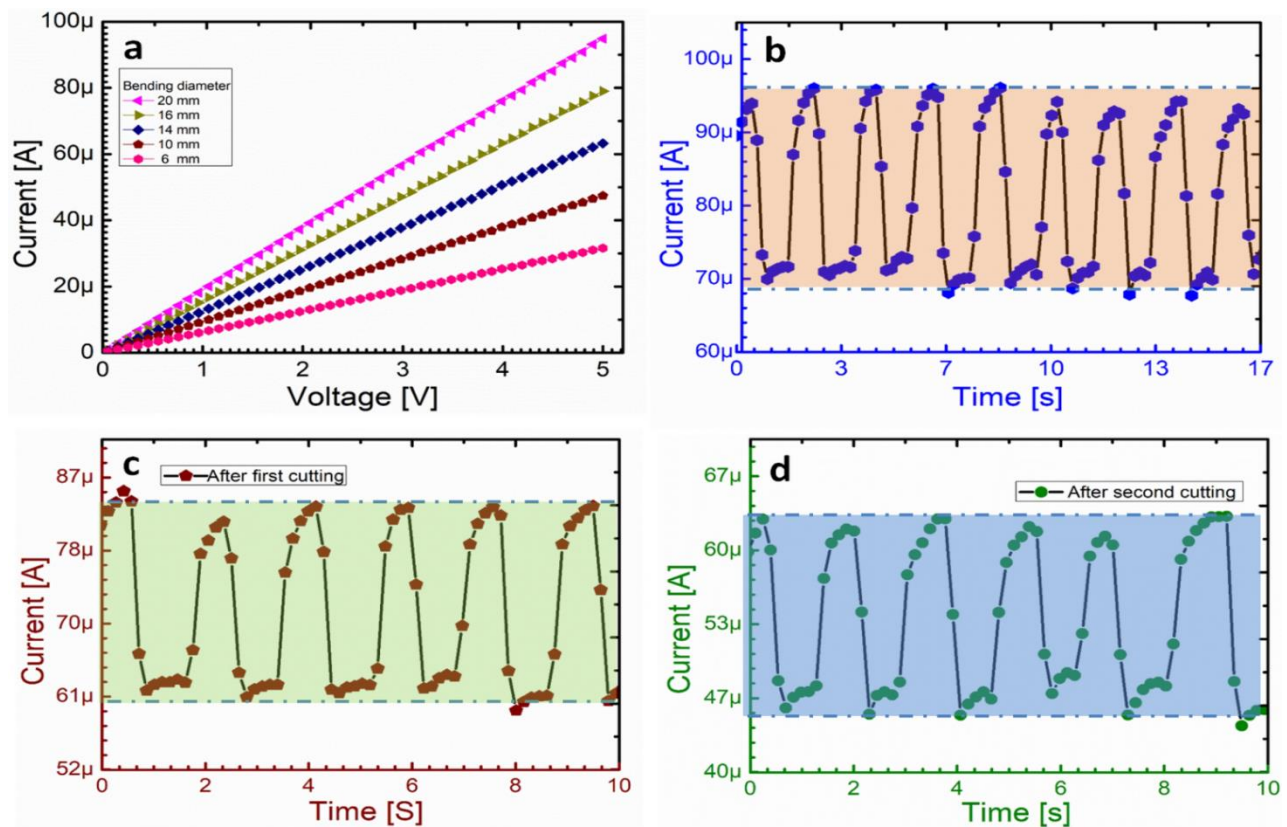


Figure 4.29. Electrical characterization of the self-healing strain sensor before and after the cutting. (a) I–V curves of the proposed self-healing strain sensor at different bending diameter. (b) Bending and relaxing cycles before cutting the proposed sensor. (c) Bending and relaxing after first cutting and the sensor recovers its 94% efficiency. (d) Bending and relaxing after 2nd time cutting and still the proposed sensor is recovered after healing

It shows a good stability with a small change of the normalized resistance during stretching/releasing cycles without any failure as shown in Fig. 4.29b. The proposed strain sensor has a good mechanical durability against the repeated elongation/relaxation cycles such as human motion. Moreover, the stability of the sensor under static loading is just drifted of 5.7Ω in the electrical resistance, when the proposed strain sensor was bent down to 8 mm for 20 min. Furthermore, the proposed sensor was placed in the 2-axis motion controlled [STM-2-TBDS] bending machine to test the stretching %. To investigate the recovery % of the proposed strain sensor after cutting it, we cut the strain sensor two times at the same place. After 1st cutting, it recovers 95% and shows stable bending and relaxing cycles as shown in Fig. 4.29c. After second time cutting at the same place, the proposed sensor recovers its 72% of the initial efficiency as shown in Fig. 4.29d, but still, it can work as a strain sensor with stable bending and relaxing cycles. After 2nd time cutting, the stretching parameter is reduced to 32.5%, which is still a high stretching % as compared to other graphene-based strain sensors⁵¹. From these results. We can say that the proposed strain sensor can be cut and reuse again and can be used as a self-healing strain sensor. The gauge factor of the device was 271.4 at 35%, hence the proposed sensor is good sensitivity.

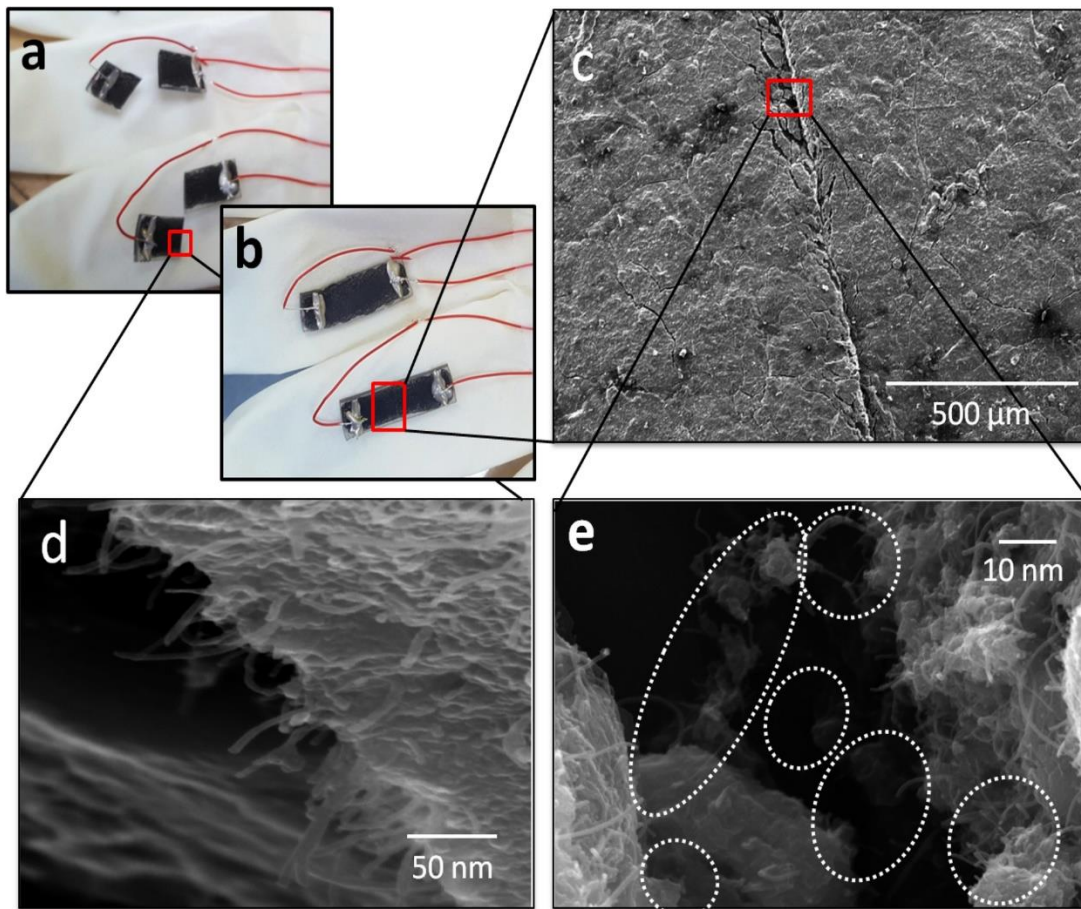


Figure 4.30. Cutting and healing of the proposed strain sensor. (a) Images of the cutting sensors. (b) Images of the sensors after self-healing and we can see that the sensors are fully healed (it can see in supplementary movie). (c) SEM image of the sensor after self-healing. (d) Cross section SEM images of the sensor after cutting it. Here, we can see both the graphene flakes as well magnetic iron oxide. (e) SEM image analysis of self-healing of the strain sensor. Here, the thread like structure and magnetic property of the magnetic iron oxide is the main reason of self-healing as shown in the SEM image.

To verify the self-healing characteristics of the proposed sensors, we cut the strain sensor in two pieces as shown in Fig. 4.30a. After combing the two pieces, it heals again without an external treatment due to two reasons: magnetic feature and healing property by the graphene and magnetic iron oxide nanocomposite in active layer and by the polyurethane in substrate, respectively, as shown in Fig. 4.30b. That is why, we are using polyurethane as a substrate which has the self-healing property, and the active layer is recovered by itself due to the presence of the magnetic iron oxide nanoparticles. As we have the evidence form SEM images in Fig. 4.30c-e, the magnetic iron oxide has the thread like structure due to its magnetic property. This results in the self-healing property of the active layer. We can also confirm this behavior from the SEM images of just graphene and with magnetic iron oxide structures. The healing time is depending on the angle at which the sensor parts are placed head-to-head after 100% cutting as shown in Fig. 4.30a, and b. On varying the healing angle, the response time of healing will be variable. But if the healing angle is constant, the response of healing time will also be constant.

Figure 4.31a, and b show the SEM images of just graphene as the active layer. Here, we can see that there are just graphene flakes and no threads. But for the SEM images of the active layer with the graphene and magnetic iron oxide as shown in Fig. 4.31c, and d. We can clearly see the graphene flakes and the magnetic iron oxide thread like structure, which is the main reason for self-healing property of the fabricated strain sensor.

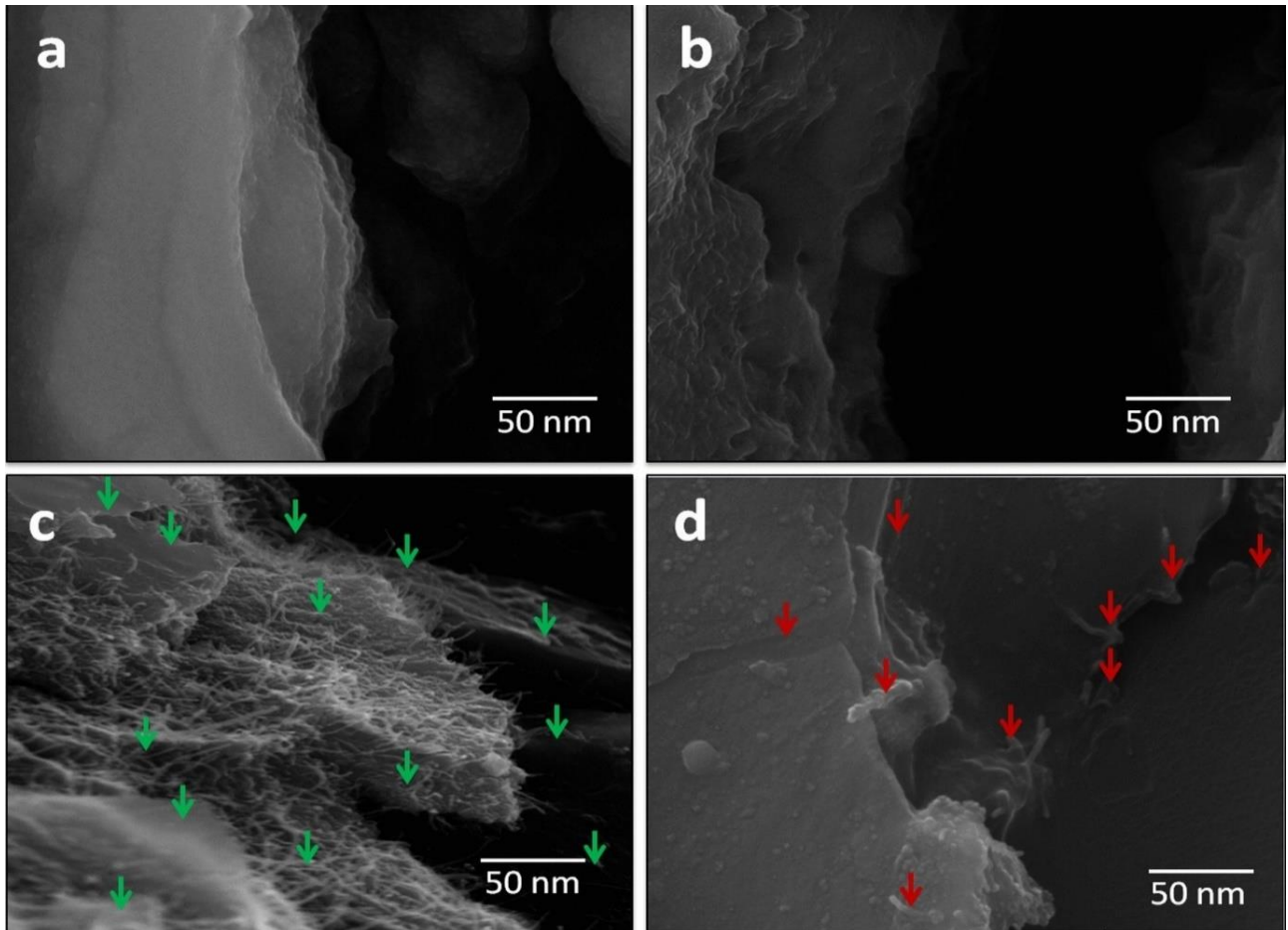


Figure 4.31. Comparison of the SEM of the films without and with Fe_2O_3 . (a) SEM of the film without Fe_2O_3 , where, in this SEM image, we can see the graphene flakes, clearly. (b) SEM image after cutting the film. Here, we can see the layered structure based on graphene flakes without Fe_2O_3 . (c) SEM image of the composite film can clearly see graphene and Fe_2O_3 . Here, in this image, the green arrows present the graphene flakes covered with Fe_2O_3 . (d) SEM image of the composite film can also clearly see graphene and Fe_2O_3 . Here, we can see the graphene flakes and the red arrows shows the Fe_2O_3 .

To figure out the sensing mechanism of the strain sensor based on graphene/ Fe_2O_3 nano-composite active film, the structural changes in the film under different levels of strain were examined to examine the effect of stretchability. As shown in Fig. 4.26a-c, the cracking phenomenon is illustrated on initial stretching, the fractures and the overlapping graphene flakes area variations are firstly occurred on the film. After certain value of strain, the cracking propagation becomes a second dominant process on the surface of active film, due to the crack density and their width are increased as shown in Fig. 4.26g-l, which corresponds the main reason of the exponential increase in its electrical resistance.

On smooth polyurethane case, a large number of the cracks were occurred on the surface of active film. In result, the strain endurance was reduced. Over 15% stretching case, the film was fully broken which indicated open circuit behaviors. To overcome the film breaking phenomena on smooth surface over 15% stretching, we have created roughness on the surface of polyurethane. As compared to smooth surface, rough polyurethane surface shows increase in stretchability range from 15 to 54.5%. The small number of cracks were appeared on the active layer during stretchability, which helps to maintain the overlapping area and contact resistance of the graphene flaks network determine the conductivity between the neighboring flakes. During compression or tension strain the overlap area between neighboring flakes becomes smaller or larger, which results in change in the resistance of the film. The magnetic property of Fe_2O_3 is utilized in with graphene for the self-healing of the active film. The Fe_2O_3 helps to connects the graphene flakes due to its magnetic force property and the stretchability is increased dramatically. Besides that, the polyurethane substrate has also the self-healing property, so due to Fe_2O_3 and polyurethane substrate the strain sensor has the self-healing property. The proposed strain sensor can be cut and reuse again and again. When the strain force is applied, the connected joints among the graphene flakes are decreased and the conductive paths are reduced as shown in Fig. 4.26 and change in electrical resistance is occurred. However, on releasing the strain force, the active film gets recover again due to magnetic iron oxide and polyurethane substrate. These mechanisms suggest that the graphene flakes and magnetic iron oxide composite are suitable for self-healing strain sensor applications.

4.4.4 Summary

In this paper, a novel self-healing high stretchable strain sensor was proposed, which could be operated after cutting it. The proposed strain sensor was fabricated depositing graphene and magnetic iron oxide nanocomposite on the engineered self-healable polyurethane substrate through the commercialized inkjet printer. To improve a self-healing function of the active sensing layer, the graphene/magnetic iron oxide composite was applied, the best graphene and magnetic iron oxide composite blending ratio is 1:1. The proposed sensor had a high mechanical property, a good sensitivity towards strain, and an excellent self-healing property. The proposed sensors have maintained its operating sensitivity over bending cycles on human fingers and a 94% of its operating sensitivity was recovered even after cutting the sensor. The proposed strain sensor was stretchable up to 54.5%. After cutting the sensor, its stretching factor decrease down to 32.5%.

Chapter 5 Conclusions and Future Work

This short chapter presents the overall conclusions of the thesis dissertation and highlights the contribution made in the Printed and Flexible Electronics fields.

5.1 Overview and General Conclusions

Printed and Flexible electronics is a new technology that enables low cost and large area devices, it is emerging in the present electronics industry to cover the cost and technological gaps associated with conventional electronic processing and application demands. The demands of low-cost, flexibility, and low temperature processing forcing the research and industry to work on this new emerging branch of electronics.

Printed electronics is relatively new field, hence facing problems of fabrication techniques, materials for device as well as for encapsulation of the electronic devices to make them reliable. In past two decades, big efforts have been made in substituting the organic, inorganic semiconductors, silicon dioxide insulator and the metals for organic materials. Apart from the material exploration for the new devices, fabrication techniques are also under investigation to enable them for effective fabrication. Some fabrication techniques are matured and been adopted by the electronic industry such as inkjet, spin coater and screen printing, however some techniques are under research yet. In this thesis work spin coater, screen printer, spray coating and Inkjet printer are used for the fabrication of devices. Materials including organic and inorganic are synthesized for the low-cost fabrication techniques and their deposition is confirmed with characterizations. This dissertation contributes to the Research and Development R&D community to address the challenges in the fabrication process of all-printed electronic devices and circuits. Main contributions are listed as below:

1. Asymmetric memristor is introduced that allow current in one direction and blocks the reverse current same as diode. By utilizing this device in crossbar memory array, it significantly minimizes the sneak currents problem. Memristor based on ZnO and Fe₂O₃ heterojunction on ITO coated PET substrate is fabricated through spin coating technique. This device provides highly asymmetric resistive switching behavior to block sneak current and can be used in crossbar passive memories (ReRAM).

Another memristor based on ionic liquid PAA:Na⁺:NaOH in a cylindrical channel using PDMS. This technique provides a gateway for soft and flexible memory devices.

2. The one directional memory structure has great importance for the implementation of hardware neural network. To achieve this objective, we have proposed two different device structures (1) ITO/ZnO/GaN/Ag and (2) ITO/Ge₂O₃. These device structures provide multistate resistive switching behavior and on the same time these devices can block sneak current. Further we have performed STDP, SRDP and convolutional neural network simulation. These devices shown stable neuromorphic behavior. On the other hand, soft neuromorphic circuits have great deal of importance in a field of soft and flexible electronics. We have proposed two soft and flexible structures for the investigation of neuromorphic behavior: (1) Cu/BMIM FeCl₄ : H₂O/Cu in a cylindrical channel and (2) Cu/Ag@AgCl/Cu in a 2x2 crossbar array structure. The soft memory devices has shown stable performance against the input signal of different frequencies, pulse width, and different voltages. The long-term memory behavior of these devices shown good stability for longer time.
3. In last section, we have proposed three different kind of sensor which include, humidity sensor, self-powered triboelectric and piezoelectric nanogenerator. The biocompatible inner eggshell membrane with highly porous structure used as substrate and humidity sensing layer and micro spacing inter digital electrodes are fabricated using inkjet printer. The inner eggshell membrane shown stable performance with fast and recovery time. In second work, we have proposed temperature independent and stable humidity sensor using GaN. This sensor is used for the monitoring of plant water level and meat freshness level monitoring. The self-powder devices have great deal of importance to power nano power electronic devices. We have proposed snakeskin shed membrane to fabricate triboelectric and piezoelectric nanogenerator. The triboelectric and piezoelectric nanogenerator has shown stable performance to power LEDs, calculator and also, we can monitor human movements (finger, wrist, tapping and walking). In last part, we have proposed self-healable strain sensor and it was fabricated using inkjet printer. The proposed sensor had a high mechanical property, a good sensitivity towards strain, and an excellent self-healing property. The proposed sensors have maintained its operating sensitivity over bending cycles on human fingers and a 94% of its operating sensitivity was recovered even after cutting the sensor. The proposed strain sensor was stretchable up to 54.5%. After cutting the sensor, its stretching factor decrease down to 32.5%.

5.2 Future Work

At the end of each chapter there is summary of the section where the achieved performance is discussed with their numerical values. Every device, circuit and system have to be improved by mean of fabrication technique, fabrication process or by changing material. In future, these devices especially can be investigated for better performance and reliability. Specifically, memristors presented in this work on different substrates with different materials can be improved for high retention time, endurance, and off/on ratio. Asymmetric memristor can enhance the ReRAM area significantly and the device can be investigated further for the performance and reliability. Apart from the performance improvement, integration with the exiting CMOS technology is still an issue for real time printed electronics applications. Conventional CMOS technology is based on three-terminal transistor while the resistive switch is two-terminal device that needs different circuit design strategy. The memristor technology has been regarded as an emerging technology for realizing neuromorphic computing systems. Compared with the CMOS, the memristor exhibits an I-V hysteresis (Chua, 2014), which makes it possible to change conductance states gradually, like the biological synaptic weight. In Future new materials and devices structures can be explored to improve the synaptic behavior to memorize synaptic data for longer time. In the sensors section, humidity sensor can be improved for their response time by adding some new material having hydrophobic nature. A nanogenerator is a type of technology that converts mechanical energy as produced by small-scale physical change into electricity. A nanogenerator has two typical approaches: piezoelectric, and triboelectric nanogenerators. Both the piezoelectric and triboelectric nanogenerators can convert mechanical energy into electricity. The triboelectric and piezoelectric nanogenerator performance can be improved by exploring the new materials with stable performance for longer time. Self-healable strain sensors have become one of the most vigorously studied research fields as they enable the gateway for the new generation portable and wearable electronic sensors to monitor strain. Stretchable and wearable self-healable strain sensors have been intensively studied in recent years for applications in human motion monitoring. However, achieving a high-performance strain sensor with self-healable property with high stretchability, ultra-sensitivity, and functionality, such as tunable sensing ranges and sensitivity to various stimuli, more materials are required to explore to improve its performance, even though such sensors have great importance for the future applications of wearable electronics.

Annex-A Journal Papers

1. **Muhammad Umair Khan**, Gul Hassan, and Jinho Bae: Soft ionic liquid based resistive memory characteristics in two terminal discrete polydimethylsiloxane cylindrical microchannel; *Journal of Materials Chemistry C*
2. **Muhammad Umair Khan**, Qazi Muhammad Saqib, Mahesh Chougale, Rayyan Ali Shaukat, Jungmin Kim and Jinho Bae: Soft and flexible: core-shell ionic liquid resistive memory for electronic synapses; *Microsystems & Nanoengineering*
3. Gul Hassan, Jinho Bae, **Muhammad Umair Khan**, Shaukat Ali: Resistive switching device based on water and zinc oxide heterojunction for soft memory applications; *Materials Science & Engineering B: Advanced Functional Solid-State Materials*
4. **Muhammad Umair Khan**, Gul Hassan, Muhammad Asim Raza and Jinho Bae: Highly bendable asymmetric resistive switching memory based on zinc oxide and magnetic iron oxide heterojunction: *Material Science: Materials in Electronics*
5. **Muhammad Umair Khan**, Gul Hassan, Muhammad Asim Raza and Jinho Bae: Resistive switching memory utilizing water and titanium dioxide thin film Schottky diode; *Material Science: Materials in Electronics*
6. **Muhammad Umair Khan**, Gul Hassan and Jinho Bae: Non-volatile resistive switching based on zirconium dioxide: poly (4-vinylphenol) nano composite; *Applied Physics A: Materials Science and Processing*
7. **Muhammad Umair Khan**, Gul Hassan and Jinho Bae: Flexible resistive switching memory with schottky diode function based on zinc oxide/methylene blue heterojunction; *Journal of Electronic Materials*
8. Muhammad Saqib, **Muhammad Umair Khan**, and Jinho Bae: chapter 8: Polymer Nanocomposites for Resistive Switching Memory; *Book: polymer Nanocomposite Materials: Applications in Integrated Electronic Devices, Wiley Book Chapter*
9. Qazi Muhammad Saqib, Mahesh Y. Chougale, **Muhammad Umair Khan**, Rayyan Ali Shaukat, , Jungmin Kim, Jinho Bae, Hyung Woo Lee, Jung-Im Park, Myung Sook Kim, and Byung Gul Lee: Natural Seagrass Tribopositive Material Based Spray Coatable Triboelectric Nanogenerator; *Nano Energy*
10. Rayyan Ali Shaukat, Qazi Muhammad Saqib, **Muhammad Umair Khan**, Mahesh Y. Chougale and Jinho Bae: Bio-wate sunflower husks powder recycled triboelectric nanogenerator for energy harvesting; *Energy Reports*
11. Mahesh Y. Chougale, Qazi Muhammad Saqib, **Muhammad Umair Khan**, Rayyan Ali Shaukat, and Jinho Bae: Expired Pharmaceutical Drugs as Tribopositive Material for Triboelectric Nanogenerator; *Advanced Sustainable Systems*
12. Mahesh Y. Chougale, Qazi Muhammad Saqib, **Muhammad Umair Khan**, Rayyan Ali Shaukat, and Jinho Bae: Novel Recycled Triboelectric Nanogenerator Based on Polymer-Coated Trash Soda Can for Clean Energy Harvesting; *Advanced Sustainable Systems*

13. Qazi Muhammad Saqib, **Muhammad Umair Khan**, Hyunjae Song, Mahesh Chougale, Rayyan Ali Shaukat, Jungmin Kim, Jinho Bae, Min Joo Choi, Seong Chan Kim, Ohbin Kwon, and Amine Bermak; Natural Hierarchically Structured Highly Porous Tomato Peel Based Tribo- And Piezo-Electric Nanogenerator for Efficient Energy Harvesting; Advanced Sustainable Systems
14. Qazi Muhammad Saqib, Rayyan Ali Shaukat, **Muhammad Umair Khan**, Mahesh Y. Chougale and Jinho Bae: Biowaste Peanut Shell Powder-Based Triboelectric Nanogenerator for Biomechanical Energy Scavenging and Sustainably Powering Electronic Supplies; ACS Applied Electronic Materials
15. Gul Hassan, **Muhammad Umair Khan**, Jinho Bae and Ahmed Shuja.: Inkjet printed self-healable strain sensor based on graphene and magnetic iron oxide nano-composite on engineered polyurethane substrate; Scientific Reports
16. Qazi Muhammad Saqib, **Muhammad Umair Khan** and Jinho Bae: Inner eggshell membrane-based bio-compatible capacitive and piezoelectric function dominant self-powered pressure sensor array for smart electronic applications; RSC Advances
17. Rayyan Ali Shaukat, **Muhammad Umair Khan**, Qazi Muhammad Saqib, Mahesh Chougale, Jungmin Kim and Jinho Bae: wide range and linear humidity sensor based on TiSi₂ for environment monitoring; Sensor and Actuator B
18. **Muhammad Umair Khan**, Gul Hassan and Jinho Bae: Bio-compatible and bio-degradable organic humidity sensor based on natural inner eggshell membrane with multilayer crosslinked fiber structure; Scientific Reports
19. Muhammad Awais, **Muhammad Umair Khan**, Arshad Hassan and Jinho Bae and Tahseen Elahi Chatta: Printable Highly Stable and Superfast Humidity Sensor Based on Two-Dimensional Molybdenum Diselenide; Scientific Reports
20. Chaudhry Muhammad Furqan, **Muhammad Umair Khan**, Muhammad Awais, Fulong Jiang, Jinho Bae, Arshad Hassan and Hoi-Sing Kwok: Humidity sensor based on Gallium Nitride for real time monitoring applications; Scientific Reports
21. **Muhammad Umair Khan**, Gul Hassan, Rayyan Ali Shaukat, Qazi Muhammad Saqib, Mahesh Chougale, Jungmin Kim and Jinho Bae: Wide Range and Highly Linear Signal Processed Systematic Humidity Sensor Array Based on Methylene Blue and Graphene Composite; Scientific Reports
22. **Muhammad Umair Khan**, Gul Hassan and Jinho Bae: Full range inkjet printed humidity sensor based on Fe₂O₃; Sensor and Actuator A
23. **Muhammad Umair Khan**, Muhammad Awais, Tahseen Elahi Chattha, Arshad Hassan and Jinho Bae: All printed wide range humidity sensor array combining MoSe₂ and PVOH in series; Journal of Material Science: Materials in Electronics
24. **Muhammad Umair Khan**, Qazi Muhammad Saqib, Gul Hassan and Jinho Bae: All printed organic humidity sensor based on egg albumin; Sensing and Bio-Sensing Research

Annex-B to be Submitted Papers

1. **Muhammad Umair Khan**, Chaudhry Muhammad Furqan, Jungmin Kim, Sobia Ali Khan, Qazi Muhammad Saqib, Mahesh Chougale, Rayyan Ali Shaukat, Jinho Bae, Nobuhiko P. Kobayashi, Moon Hee Kang, and Hoi-Sing Kwok: One directional engineered Gallium Nitride in-situ digital to analogue resistive memory device for electronic synapses; (submitted)
2. **Muhammad Umair Khan**, Jungmin Kim, Mahesh Y. Chougale, Chaudhry Muhammad Furqan, Qazi Muhammad Saqib, Rayyan Ali Shaukat, Nobuhiko P. Kobayashi, Jinho Bae and Hoi-Sing Kwok: Ionic liquid multistate resistive switching characteristics in a two terminal soft and flexible discrete channel for neuromorphic computing; (submitted)
3. Mahesh Y. Chougale, **Muhammad Umair Khan**, Jungmin Kim, Qazi Muhammad Saqib, Rayyan Ali Shaukat, and Jinho Bae: Brain-inspired neuromorphic resistive memory device based on silk fibroin gel for wearable intelligent electronics; (submitted)
4. Mahesh Chougale, **Muhammad Umair Khan**, Jungmin Kim, Qazi Muhammad Saqib, Rayyan Ali Shaukat, and Jinho Bae: Brain inspired Synaptic resistive switching characteristics and neuromorphic simulation in Germanium Oxide memristor for electronic synapses. (submitted)

Annex-C Patents

1. 자가치유 스트레인 센서 (Self-healing strain sensor), Jinho Bae, Gul Hassan, **Muhammad Umair khan**, Patent number: KR102225647B1.
2. 난막 발전 장치 (Egg membrane electricity generating apparatus), Jinho Bae, Gul Hassan, **Muhammad Umair khan**, Patent number: KR20210009544A.
3. 난막 습도 감지 장치 (Egg membrane humidity sensing apparatus), Jinho Bae, Gul Hassan, **Muhammad Umair khan**, Patent number: KR20210009543A.

Annex-D Reference

- [1] S. Khan, S. Ali, A. Bermak, Recent Developments in Printing Flexible and Wearable Sensing Electronics for Healthcare Applications, *Sensors* 19(5) (2019) 1230.
- [2] D. Baran, D. Corzo, G. Blazquez, Flexible Electronics: Status, Challenges and Opportunities, *Frontiers in Electronics* 1(2) (2020).
- [3] S. Khan, S. Ali, A. Khan, A. Bermak, Wearable Printed Temperature Sensors: Short Review on Latest Advances for Biomedical Applications, *IEEE Reviews in Biomedical Engineering* (2021) 1-1.
- [4] S. Khan, S. Ali, A. Khan, A. Bermak, Sensors on Nonconventional Substrates Developed through Printing Technologies, 2021 4th International Conference on Circuits, Systems and Simulation (ICCSS), 2021, pp. 202-206.
- [5] G. Hassan, M.U. Khan, J. Bae, A. Shuja, Inkjet printed self-healable strain sensor based on graphene and magnetic iron oxide nano-composite on engineered polyurethane substrate, *Scientific Reports* 10(1) (2020) 18234.
- [6] G. Hassan, J. Bae, A. Hassan, S. Ali, C.H. Lee, Y. Choi, Ink-jet printed stretchable strain sensor based on graphene/ZnO composite on micro-random ridged PDMS substrate, *Composites Part A: Applied Science and Manufacturing* 107 (2018) 519-528.
- [7] M.U. Khan, G. Hassan, J. Bae, Soft ionic liquid based resistive memory characteristics in a two terminal discrete polydimethylsiloxane cylindrical microchannel, *Journal of Materials Chemistry C* 8(38) (2020) 13368-13374.
- [8] K.-S. Kwon, M.K. Rahman, T.H. Phung, S. Hoath, S. Jeong, J.S. Kim, Review of digital printing technologies for electronic materials, *Flexible and Printed Electronics* (2020).
- [9] M.A. Raza, G. Hassan, M.U. Khan, J. Bae, All-printed Stretchable Photo-Conductive Device Fabricated on Engineered PDMS, 2018 23rd Opto-Electronics and Communications Conference (OECC), 2018, pp. 1-2.
- [10] M.U. Khan, G. Hassan, M.A. Raza, C.H. Lee, J. Bae, Inkjet printed organic-inorganic bilayer photoconductive sensor, 2018 23rd Opto-Electronics and Communications Conference (OECC), 2018, pp. 1-2.
- [11] R.A. Shaukat, M.U. Khan, Q.M. Saqib, M.Y. Chougale, J. Kim, J. Bae, All range highly linear and sensitive humidity sensor based on 2D material TiSi₂ for real-time monitoring, *Sensors and Actuators B: Chemical* 345 (2021) 130371.
- [12] M.U. Khan, M. Awais, T.E. Chattha, A. Hassan, J. Bae, All printed wide range humidity sensor array combining MoSe₂ and PVOH in series, *Journal of Materials Science: Materials in Electronics* 31(10) (2020) 7683-7697.
- [13] G. Hassan, M.U. Khan, M.A. Raza, J. Bae, All-printed organic and oxide hetero-structure device with photoconductivity, 2018 23rd Opto-Electronics and Communications Conference (OECC), 2018, pp. 1-2.
- [14] M.U. Khan, G. Hassan, J. Bae, Flexible Resistive Switching Memory with a Schottky Diode Function Based on a Zinc Oxide/Methylene Blue Heterojunction, *Journal of Electronic Materials* 49(8) (2020) 4764-4772.
- [15] M.U. Khan, G. Hassan, M.A. Raza, J. Bae, N.P. Kobayashi, Schottky diode based resistive switching device based on ZnO/PEDOT:PSS heterojunction to reduce sneak current problem, *Journal of Materials Science: Materials in Electronics* 30(5) (2019) 4607-4617.
- [16] W. Sun, B. Gao, M. Chi, Q. Xia, J.J. Yang, H. Qian, H. Wu, Understanding memristive switching via in situ characterization and device modeling, *Nature Communications* 10(1) (2019) 3453.
- [17] L. Chua, Memristor-The missing circuit element, *IEEE Transactions on Circuit Theory* 18(5) (1971) 507-519.
- [18] S. Ali, S. Khan, A. Khan, A. Bermak, Memristor Fabrication Through Printing Technologies: A Review, *IEEE Access* 9 (2021) 95970-95985.
- [19] S. Ali, A. Hassan, G. Hassan, J. Bae, C.H. Lee, Flexible frequency selective passive circuits based on memristor and capacitor, *Organic Electronics* 51 (2017) 119-127.
- [20] S. Ali, A. Hassan, G. Hassan, J. Bae, C.H. Lee, Memristor-capacitor passive filters to tune both cut-off frequency and bandwidth, 2017 25th Optical Fiber Sensors Conference (OFS), 2017, pp. 1-4.
- [21] H. Abbas, Y. Abbas, G. Hassan, A.S. Sokolov, Y.-R. Jeon, B. Ku, C.J. Kang, C. Choi, The coexistence of threshold and memory switching characteristics of ALD HfO₂ memristor synaptic arrays for energy-efficient neuromorphic computing, *Nanoscale* 12(26) (2020) 14120-14134.

- [22] G. Hassan, S. Ali, J. Bae, C.H. Lee, Flexible resistive switching device based on poly(3,4-ethylenedioxythiophene):poly(styrene sulfonate) (PEDOT:PSS)/poly(4-vinylphenol) (PVP) composite and methyl red heterojunction, *Applied Physics A* 123(4) (2017) 256.
- [23] S. Ali, J. Bae, K.H. Choi, C.H. Lee, Y.H. Doh, S. Shin, N.P. Kobayashi, Organic non-volatile memory cell based on resistive elements through electro-hydrodynamic technique, *Organic Electronics* 17 (2015) 121-128.
- [24] S. Ali, J. Bae, C.H. Lee, K.H. Choi, Y.H. Doh, All-printed and highly stable organic resistive switching device based on graphene quantum dots and polyvinylpyrrolidone composite, *Organic Electronics* 25 (2015) 225-231.
- [25] S. Ali, J. Bae, C.H. Lee, S. Shin, N.P. Kobayashi, Ultra-low power non-volatile resistive crossbar memory based on pull up resistors, *Organic Electronics* 41 (2017) 73-78.
- [26] G. Hassan, J. Bae, M.U. Khan, S. Ali, Resistive switching device based on water and zinc oxide heterojunction for soft memory applications, *Materials Science and Engineering: B* 246 (2019) 1-6.
- [27] L. Yin, R. Cheng, Z. Wang, F. Wang, M.G. Sendeku, Y. Wen, X. Zhan, J. He, Two-Dimensional Unipolar Memristors with Logic and Memory Functions, *Nano Letters* 20(6) (2020) 4144-4152.
- [28] A. Shawkat, B. Jinho, L. Chong Hyun, Flexible and stackable non-volatile resistive memory for high integration, *Proc.SPIE*, 2015.
- [29] J.D. Greenlee, W.L. Calley, M.W. Moseley, W.A. Doolittle, Comparison of Interfacial and Bulk Ionic Motion in Analog Memristors, *IEEE Transactions on Electron Devices* 60(1) (2013) 427-432.
- [30] Z. Liu, J. Tang, B. Gao, P. Yao, X. Li, D. Liu, Y. Zhou, H. Qian, B. Hong, H. Wu, Neural signal analysis with memristor arrays towards high-efficiency brain-machine interfaces, *Nature Communications* 11(1) (2020) 4234.
- [31] R. Dittmann, J.P. Strachan, Redox-based memristive devices for new computing paradigm, *APL Materials* 7(11) (2019) 110903.
- [32] G. Di Martino, A. Demetriadou, W. Li, D. Kos, B. Zhu, X. Wang, B. de Nijs, H. Wang, J. MacManus-Driscoll, J.J. Baumberg, Real-time in situ optical tracking of oxygen vacancy migration in memristors, *Nature Electronics* 3(11) (2020) 687-693.
- [33] B. Mohammad, M.A. Jaoude, V. Kumar, D.M. Al Homouz, H.A. Nahla, M. Al-Qutayri, N. Christoforou, State of the art of metal oxide memristor devices, *Nanotechnology Reviews* 5(3) (2016) 311-329.
- [34] M.U. Khan, G. Hassan, M.A. Raza, J. Bae, Bipolar resistive switching device based on N,N'-bis(3-methylphenyl)-N,N'-diphenylbenzidine and poly(3,4-ethylenedioxythiophene):poly(styrene sulfonate)/poly(vinyl alcohol) bilayer stacked structure, *Applied Physics A* 124(10) (2018) 726.
- [35] G. Hassan, M.U. Khan, J. Bae, Solution-processed flexible non-volatile resistive switching device based on poly[(9,9-di-n-octylfluorenyl-2,7-diyl)-alt-(benzo[2,1,3]thiadiazol-4,8-diyl)]: polyvinylpyrrolidone composite and its conduction mechanism, *Applied Physics A* 125(1) (2018) 18.
- [36] M.U. Khan, G. Hassan, J. Bae, Non-volatile resistive switching based on zirconium dioxide: poly (4-vinylphenol) nano-composite, *Applied Physics A* 125(6) (2019) 378.
- [37] D.B. Strukov, G.S. Snider, D.R. Stewart, R.S. Williams, The missing memristor found, *Nature* 453(7191) (2008) 80-83.
- [38] L. Zhu, J. Zhou, Z. Guo, Z. Sun, An overview of materials issues in resistive random access memory, *Journal of Materiomics* 1(4) (2015) 285-295.
- [39] Z. Zhang, Z. Wang, T. Shi, C. Bi, F. Rao, Y. Cai, Q. Liu, H. Wu, P. Zhou, Memory materials and devices: From concept to application, *InfoMat* 2(2) (2020) 261-290.
- [40] R. Wang, J.-Q. Yang, J.-Y. Mao, Z.-P. Wang, S. Wu, M. Zhou, T. Chen, Y. Zhou, S.-T. Han, Recent Advances of Volatile Memristors: Devices, Mechanisms, and Applications, *Advanced Intelligent Systems* 2(9) (2020) 2000055.
- [41] S. Munjal, N. Khare, Advances in resistive switching based memory devices, *Journal of Physics D: Applied Physics* 52(43) (2019) 433002.
- [42] F. Gül, Addressing the sneak-path problem in crossbar RRAM devices using memristor-based one Schottky diode-one resistor array, *Results in Physics* 12 (2019) 1091-1096.
- [43] L. Shi, G. Zheng, B. Tian, B. Dkhil, C. Duan, Research progress on solutions to the sneak path issue in memristor crossbar arrays, *Nanoscale Advances* 2(5) (2020) 1811-1827.
- [44] M.U. Khan, G. Hassan, J. Bae, Highly bendable asymmetric resistive switching memory based on zinc oxide and magnetic iron oxide heterojunction, *Journal of Materials Science: Materials in Electronics* 31(2) (2020) 1105-1115.

- [45] B. Vines, M.H. Rashid, Memristors: The fourth fundamental circuit element, 2009 International Conference on Electrical and Electronics Engineering - ELECO 2009, 2009, pp. II-37-II-37.
- [46] S. Lv, J. Liu, Z. Geng, Application of Memristors in Hardware Security: A Current State-of-the-Art Technology, *Advanced Intelligent Systems* 3(1) (2021) 2000127.
- [47] W. Xue, W. Ci, X.-H. Xu, G. Liu, Optoelectronic memristor for neuromorphic computing, *Chinese Physics B* 29(4) (2020) 048401.
- [48] P.W.C. Ho, F.O. Hatem, H.A.F. Almurib, T.N. Kumar, Comparison between Pt/TiO₂/Pt and Pt/TaOX/TaOY/Pt based bipolar resistive switching devices, *Journal of Semiconductors* 37(6) (2016) 064001.
- [49] K. Liao, P. Lei, M. Tu, S. Luo, T. Jiang, W. Jie, J. Hao, Memristor Based on Inorganic and Organic Two-Dimensional Materials: Mechanisms, Performance, and Synaptic Applications, *ACS Applied Materials & Interfaces* 13(28) (2021) 32606-32623.
- [50] J.G. McDaniel, A. Yethiraj, Understanding the Properties of Ionic Liquids: Electrostatics, Structure Factors, and Their Sum Rules, *The Journal of Physical Chemistry B* 123(16) (2019) 3499-3512.
- [51] S. Ohisa, J. Kido, CHAPTER 8 Applications of Ionic Liquids in Organic Electronic Devices, *Ionic Liquid Devices*, The Royal Society of Chemistry 2018, pp. 196-233.
- [52] K. Rajan, A. Chiappone, D. Perrone, S. Bocchini, I. Roppolo, K. Bejtka, M. Castellino, C.F. Pirri, C. Ricciardi, A. Chiolerio, Ionic liquid-enhanced soft resistive switching devices, *RSC Advances* 6(96) (2016) 94128-94138.
- [53] M.U. Khan, Q.M. Saqib, M.Y. Chougale, R.A. Shaikat, J. Kim, J. Bae, Soft and flexible: core-shell ionic liquid resistive memory for electronic synapses, *Microsystems & Nanoengineering* 7(1) (2021) 78.
- [54] M.U. Khan, G. Hassan, J. Bae, Resistive switching memory utilizing water and titanium dioxide thin film Schottky diode, *Journal of Materials Science: Materials in Electronics* 30(20) (2019) 18744-18752.
- [55] D. Ielmini, Brain-inspired computing with resistive switching memory (RRAM): Devices, synapses and neural networks, *Microelectronic Engineering* 190 (2018) 44-53.
- [56] J. Woo, T. Van Nguyen, J.H. Kim, J.-P. Im, S. Im, Y. Kim, K.-S. Min, S.E. Moon, Exploiting defective RRAM array as synapses of HTM spatial pooler with boost-factor adjustment scheme for defect-tolerant neuromorphic systems, *Scientific Reports* 10(1) (2020) 11703.
- [57] A.S. Sokolov, H. Abbas, Y. Abbas, C. Choi, Towards engineering in memristors for emerging memory and neuromorphic computing: A review, *Journal of Semiconductors* 42(1) (2021) 013101.
- [58] K. Mbarek, F.O. Rzig, S. Ghedira, K. Besbes, Implementation of 1T1R-based OxRRAM Memristor Model for Circuit Design and Simulation, 2019 International Conference on Control, Automation and Diagnosis (ICCAD), 2019, pp. 1-6.
- [59] C. Wu, T.W. Kim, H.Y. Choi, D.B. Strukov, J.J. Yang, Flexible three-dimensional artificial synapse networks with correlated learning and trainable memory capability, *Nature Communications* 8(1) (2017) 752.
- [60] D. Ielmini, S. Ambrogio, 16 - Neuromorphic computing with resistive switching memory devices, in: B. Magyari-Köpe, Y. Nishi (Eds.), *Advances in Non-Volatile Memory and Storage Technology (Second Edition)*, Woodhead Publishing 2019, pp. 603-631.
- [61] D. Kim, I.-J. Kim, J.-S. Lee, Memory Devices for Flexible and Neuromorphic Device Applications, *Advanced Intelligent Systems* 3(5) (2021) 2000206.
- [62] F. Zahoor, T.Z. Azni Zulkifli, F.A. Khanday, Resistive Random Access Memory (RRAM): an Overview of Materials, Switching Mechanism, Performance, Multilevel Cell (mlc) Storage, Modeling, and Applications, *Nanoscale Research Letters* 15(1) (2020) 90.
- [63] K. Moon, S. Park, D. Lee, J. Woo, E. Cha, S. Lee, H. Hwang, Resistive-switching analogue memory device for neuromorphic application, 2014 Silicon Nanoelectronics Workshop (SNW), 2014, pp. 1-2.
- [64] Z. Wang, T. Zeng, Y. Ren, Y. Lin, H. Xu, X. Zhao, Y. Liu, D. Ielmini, Toward a generalized Bienenstock-Cooper-Munro rule for spatiotemporal learning via triplet-STDP in memristive devices, *Nature Communications* 11(1) (2020) 1510.
- [65] C.M. Furqan, M.U. Khan, M. Awais, F. Jiang, J. Bae, A. Hassan, H.-S. Kwok, Humidity sensor based on Gallium Nitride for real time monitoring applications, *Scientific Reports* 11(1) (2021) 11088.
- [66] M. Tian, Y.D. Qian, C. Zhang, L. Li, S.D. Yao, I.T. Ferguson, D.N. Talwar, J.Y. Zhai, D.H. Meng, K.Y. He, L.Y. Wan, Z.C. Feng, Investigation of high indium-composition InGa_N/Ga_N heterostructures on ZnO grown by metallic organic chemical vapor deposition, *Opt. Mater. Express* 8(10) (2018) 3184-3196.
- [67] X. Zhang, Y. Zhuo, Q. Luo, Z. Wu, R. Midya, Z. Wang, W. Song, R. Wang, N.K. Upadhyay, Y. Fang, F. Kiani, M. Rao, Y. Yang, Q. Xia, Q. Liu, M. Liu, J.J. Yang, An artificial spiking afferent nerve based on Mott memristors for neurorobotics, *Nature Communications* 11(1) (2020) 51.

- [68] G. Milano, M. Luebben, Z. Ma, R. Dunin-Borkowski, L. Boarino, C.F. Pirri, R. Waser, C. Ricciardi, I. Valov, Self-limited single nanowire systems combining all-in-one memristive and neuromorphic functionalities, *Nature Communications* 9(1) (2018) 5151.
- [69] M. Prezioso, F. Merrih Bayat, B. Hoskins, K. Likharev, D. Strukov, Self-Adaptive Spike-Time-Dependent Plasticity of Metal-Oxide Memristors, *Scientific Reports* 6(1) (2016) 21331.
- [70] X. Yan, J. Zhao, S. Liu, Z. Zhou, Q. Liu, J. Chen, X.Y. Liu, Memristor with Ag-Cluster-Doped TiO₂ Films as Artificial Synapse for Neuroinspired Computing, *Advanced Functional Materials* 28(1) (2018) 1705320.
- [71] S.G. Kim, J.S. Han, H. Kim, S.Y. Kim, H.W. Jang, Recent Advances in Memristive Materials for Artificial Synapses, *Advanced Materials Technologies* 3(12) (2018) 1800457.
- [72] X. Peng, R. Liu, S. Yu, Optimizing Weight Mapping and Data Flow for Convolutional Neural Networks on Processing-in-Memory Architectures, *IEEE Transactions on Circuits and Systems I: Regular Papers* 67(4) (2020) 1333-1343.
- [73] S. Liu, W. Deng, Very deep convolutional neural network based image classification using small training sample size, 2015 3rd IAPR Asian Conference on Pattern Recognition (ACPR), 2015, pp. 730-734.
- [74] P. Chen, X. Peng, S. Yu, NeuroSim: A Circuit-Level Macro Model for Benchmarking Neuro-Inspired Architectures in Online Learning, *IEEE Transactions on Computer-Aided Design of Integrated Circuits and Systems* 37(12) (2018) 3067-3080.
- [75] T.A. Anusudha, S.S. Reka, S.R.S. Prabakaran, Memristor and its Applications: A Comprehensive Review, *Nanoscience & Nanotechnology-Asia* 10(5) (2020) 558-576.
- [76] Y. Li, L. Loh, S. Li, L. Chen, B. Li, M. Bosman, K.-W. Ang, Anomalous resistive switching in memristors based on two-dimensional palladium diselenide using heterophase grain boundaries, *Nature Electronics* 4(5) (2021) 348-356.
- [77] M.S. Chavali, M.P. Nikolova, Metal oxide nanoparticles and their applications in nanotechnology, *SN Applied Sciences* 1(6) (2019) 607.
- [78] J.J. Yang, M.D. Pickett, X. Li, D.A.A. Ohlberg, D.R. Stewart, R.S. Williams, Memristive switching mechanism for metal/oxide/metal nanodevices, *Nature Nanotechnology* 3(7) (2008) 429-433.
- [79] F.B. Fauzi, M.H. Ani, S.H. Herman, M.A. Mohamed, Dilute electrodeposition of TiO₂ and ZnO thin film memristors on Cu substrate, *IOP Conference Series: Materials Science and Engineering* 340 (2018) 012006.
- [80] S. Sakaguchi, S.-i. Todoroki, Optical properties of GeO₂ glass and optical fibers, *Appl. Opt.* 36(27) (1997) 6809-6814.
- [81] Q. Xie, S. Deng, M. Schaeckers, H.C. Lin, M. Caymax, A. Delabie, X.-P. Qu, Y.-L. Jiang, D. Deduytsche, C. Detavernier, Germanium surface passivation and atomic layer deposition of high-k dielectrics - A tutorial review on Ge-based MOS capacitors, *Semiconductor Science and Technology - SEMICONDUCTOR SCI TECHNOL* 27 (2012).
- [82] Y. Xu, G. Han, H. Liu, Y. Wang, Y. Liu, J. Ao, Y. Hao, Ge pMOSFETs with GeO_x Passivation Formed by Ozone and Plasma Post Oxidation, *Nanoscale Research Letters* 14(1) (2019) 126.
- [83] A. Prakash, S. Maikap, S.Z. Rahaman, S. Majumdar, S. Manna, S.K. Ray, Resistive switching memory characteristics of Ge/GeO_x nanowires and evidence of oxygen ion migration, *Nanoscale Research Letters* 8(1) (2013) 220.
- [84] V. Lobaz, M. Rabyk, J. Pánek, E. Doris, F. Nallet, P. Pánek, M. Hrubý, Photoluminescent polysaccharide-coated germanium(IV) oxide nanoparticles, *Colloid and Polymer Science* 294 (2016) 1225-1235.
- [85] S. Mukherjee, K. Das, S. Das, S.K. Ray, Highly Responsive, Polarization Sensitive, Self-Biased Single GeO₂-Ge Nanowire Device for Broadband and Low Power Photodetectors, *ACS Photonics* 5(10) (2018) 4170-4178.
- [86] A.R. Zanatta, Temperature-dependent Raman scattering of the Ge + GeO_x system and its potential as an optical thermometer, *Results in Physics* 19 (2020) 103500.
- [87] X. Wang, L. Duan, G. Dong, P. Wei, W. Wang, L. Wang, Y. Qiu, Synthesis and characterization of nano/micro-structured crystalline germanium dioxide with novel morphology, *Chinese Science Bulletin* 54(16) (2009) 2810-2813.
- [88] T. Prodromakis, C. Toumazou, A review on memristive devices and applications, 2010 17th IEEE International Conference on Electronics, Circuits and Systems, 2010, pp. 934-937.
- [89] Q. Zhao, Z. Xie, Y.-P. Peng, K. Wang, H. Wang, X. Li, H. Wang, J. Chen, H. Zhang, X. Yan, Current status and prospects of memristors based on novel 2D materials, *Materials Horizons* 7(6) (2020) 1495-1518.

- [90] Y. Chen, G. Liu, C. Wang, W. Zhang, R.-W. Li, L. Wang, Polymer memristor for information storage and neuromorphic applications, *Materials Horizons* 1(5) (2014) 489-506.
- [91] T. Wasilewski, J. Gębicki, W. Kamysz, Prospects of ionic liquids application in electronic and bioelectronic nose instruments, *TrAC Trends in Analytical Chemistry* 93 (2017) 23-36.
- [92] M.U. Khan, G. Hassan, J. Bae, Bio-compatible organic humidity sensor based on natural inner egg shell membrane with multilayer crosslinked fiber structure, *Scientific Reports* 9(1) (2019) 5824.
- [93] M.U. Khan, G. Hassan, M. Awais, J. Bae, All printed full range humidity sensor based on Fe₂O₃, *Sensors and Actuators A: Physical* 311 (2020) 112072.
- [94] M. Awais, M.U. Khan, A. Hassan, J. Bae, T.E. Chattha, Printable Highly Stable and Superfast Humidity Sensor Based on Two Dimensional Molybdenum Diselenide, *Scientific Reports* 10(1) (2020) 5509.
- [95] M.U. Khan, Q.M. Saqib, G. Hassan, J. Bae, All printed organic humidity sensor based on egg albumin, *Sensing and Bio-Sensing Research* 28 (2020) 100337.
- [96] M.U. Khan, G. Hassan, R.A. Shaukat, Q.M. Saqib, M.Y. Chougale, J. Kim, J. Bae, Wide range and highly linear signal processed systematic humidity sensor array using Methylene Blue and Graphene composite, *Scientific Reports* 11(1) (2021) 16665.
- [97] S. Ali, A. Hassan, J. Bae, C.H. Lee, J. Kim, All-Printed Differential Temperature Sensor for the Compensation of Bending Effects, *Langmuir* 32(44) (2016) 11432-11439.
- [98] S. Ali, A. Hassan, G. Hassan, J. Bae, C.H. Lee, All-printed humidity sensor based on graphene/methyl-red composite with high sensitivity, *Carbon* 105 (2016) 23-32.
- [99] Z. Chen, C. Lu, Humidity Sensors: A Review of Materials and Mechanisms, *Sensor Letters* 3(4) (2005) 274-295.
- [100] M. Sajid, S. Aziz, G.B. Kim, S.W. Kim, J. Jo, K.H. Choi, Bio-compatible organic humidity sensor transferred to arbitrary surfaces fabricated using single-cell-thick onion membrane as both the substrate and sensing layer, *Scientific Reports* 6(1) (2016) 30065.
- [101] S. Maiti, S. Kumar Karan, J. Lee, A. Kumar Mishra, B. Bhusan Khatua, J. Kon Kim, Bio-waste onion skin as an innovative nature-driven piezoelectric material with high energy conversion efficiency, *Nano Energy* 42 (2017) 282-293.
- [102] J. Yong, B. Hassan, Y. Liang, K. Ganesan, R. Rajasekharan, R. Evans, G. Egan, O. Kavehei, J. Li, G. Chana, B. Nasr, E. Skafidas, A Silk Fibroin Bio-Transient Solution Processable Memristor, *Scientific Reports* 7(1) (2017) 14731.
- [103] S.K. Ghosh, D. Mandal, High-performance bio-piezoelectric nanogenerator made with fish scale, *Applied Physics Letters* 109(10) (2016) 103701.
- [104] Y.-C. Chen, H.-C. Yu, C.-Y. Huang, W.-L. Chung, S.-L. Wu, Y.-K. Su, Nonvolatile Bio-Memristor Fabricated with Egg Albumen Film, *Scientific Reports* 5(1) (2015) 10022.
- [105] Z. Li, L. Zhang, B.S. Amirkhiz, X. Tan, Z. Xu, H. Wang, B.C. Olsen, C.M.B. Holt, D. Mitlin, Carbonized Chicken Eggshell Membranes with 3D Architectures as High-Performance Electrode Materials for Supercapacitors, *Advanced Energy Materials* 2(4) (2012) 431-437.
- [106] M.M.F. Choi, W.S.H. Pang, D. Xiao, X. Wu, An optical glucose biosensor with eggshell membrane as an enzyme immobilisation platform, *Analyst* 126(9) (2001) 1558-1563.
- [107] Q.M. Saqib, M.U. Khan, J. Bae, Inner egg shell membrane based bio-compatible capacitive and piezoelectric function dominant self-powered pressure sensor array for smart electronic applications, *RSC Advances* 10(49) (2020) 29214-29227.
- [108] R.A. Mensah, S.B. Jo, H. Kim, S.-M. Park, K.D. Patel, K.J. Cho, M.T. Cook, S.B. Kirton, V. Hutter, L.E. Sidney, D. Alves-Lima, H. Lin, J.-H. Lee, H.-W. Kim, D.Y.S. Chau, The eggshell membrane: A potential biomaterial for corneal wound healing, *Journal of Biomaterials Applications* 36(5) (2021) 912-929.
- [109] J.-W. Han, B. Kim, J. Li, M. Meyyappan, Carbon Nanotube Based Humidity Sensor on Cellulose Paper, *The Journal of Physical Chemistry C* 116(41) (2012) 22094-22097.
- [110] P. Chaudhary, D.K. Maurya, S. Yadav, A. Pandey, R.K. Tripathi, B.C. Yadav, Ultrafast responsive humidity sensor based on roasted gram derived carbon quantum dots: Experimental and theoretical study, *Sensors and Actuators B: Chemical* 329 (2021) 129116.
- [111] Y.A. Anisimov, R.W. Evitts, D.E. Cree, L.D. Wilson, Polyaniline/Biopolymer Composite Systems for Humidity Sensor Applications: A Review, *Polymers* 13(16) (2021) 2722.
- [112] S.-J. Kim, J.-Y. Park, S.-H. Lee, S.-H. Yi, Humidity sensors using porous silicon layer with mesa structure, *Journal of Physics D: Applied Physics* 33(15) (2000) 1781-1784.
- [113] T. Jalkanen, E. Mäkilä, A. Määttänen, J. Tuura, M. Kaasalainen, V.-P. Lehto, P. Ihalainen, J. Peltonen,

- J. Salonen, Porous silicon micro- and nanoparticles for printed humidity sensors, *Applied Physics Letters* 101(26) (2012) 263110.
- [114] A. Podolska, S. Tham, R.D. Hart, R.M. Seeber, M. Kocan, M. Kocan, U.K. Mishra, K.D.G. Pflieger, G. Parish, B.D. Nener, Biocompatibility of semiconducting AlGaIn/GaN material with living cells, *Sensors and Actuators B: Chemical* 169 (2012) 401-406.
- [115] R.A. Shaukat, Q.M. Saqib, M.U. Khan, M.Y. Chougale, J. Bae, Bio-waste sunflower husks powder based recycled triboelectric nanogenerator for energy harvesting, *Energy Reports* 7 (2021) 724-731.
- [116] Q.M. Saqib, R.A. Shaukat, M.U. Khan, M. Chougale, J. Bae, Biowaste Peanut Shell Powder-Based Triboelectric Nanogenerator for Biomechanical Energy Scavenging and Sustainably Powering Electronic Supplies, *ACS Applied Electronic Materials* 2(12) (2020) 3953-3963.
- [117] S. Liu, J. Yuan, W. Deng, M. Luo, Y. Xie, Q. Liang, Y. Zou, Z. He, H. Wu, Y. Cao, High-efficiency organic solar cells with low non-radiative recombination loss and low energetic disorder, *Nature Photonics* 14(5) (2020) 300-305.
- [118] M.Y. Chougale, Q.M. Saqib, M.U. Khan, R.A. Shaukat, J. Kim, D. Dubal, J. Bae, Expired Pharmaceutical Drugs as Tribopositive Material for Triboelectric Nanogenerator, *Advanced Sustainable Systems* n/a(n/a) (2021) 2100205.
- [119] Q.M. Saqib, M.Y. Chougale, M.U. Khan, R.A. Shaukat, J. Kim, J. Bae, H.W. Lee, J.-I. Park, M.S. Kim, B.G. Lee, Natural seagrass tribopositive material based spray coatable triboelectric nanogenerator, *Nano Energy* 89 (2021) 106458.
- [120] M.Y. Chougale, Q.M. Saqib, M.U. Khan, R.A. Shaukat, J. Kim, J. Bae, Novel Recycled Triboelectric Nanogenerator Based on Polymer-Coated Trash Soda Can for Clean Energy Harvesting, *Advanced Sustainable Systems* 5(10) (2021) 2100161.
- [121] Q.M. Saqib, M.U. Khan, H. Song, M.Y. Chougale, R.A. Shaukat, J. Kim, J. Bae, M.J. Choi, S.C. Kim, O. Kwon, A. Bermak, Natural Hierarchically Structured Highly Porous Tomato Peel Based Tribo- and Piezo-Electric Nanogenerator for Efficient Energy Harvesting, *Advanced Sustainable Systems* 5(7) (2021) 2100066.
- [122] A.S. Dahiya, F. Morini, S. Boubenia, K. Nadaud, D. Alquier, G. Poulin-Vittrant, Organic/Inorganic Hybrid Stretchable Piezoelectric Nanogenerators for Self-Powered Wearable Electronics, *Advanced Materials Technologies* 3(2) (2018) 1700249.
- [123] R. Ding, M.-C. Wong, J. Hao, Recent advances in hybrid perovskite nanogenerators, *EcoMat* 2(4) (2020) e12057.
- [124] L. Alibardi, L. Dalla Valle, A. Nardi, M. Toni, Evolution of hard proteins in the sauropsid integument in relation to the cornification of skin derivatives in amniotes, *Journal of Anatomy* 214(4) (2009) 560-586.
- [125] C. Chang, P. Wu, R.E. Baker, P.K. Maini, L. Alibardi, C.M. Chuong, Reptile scale paradigm: Evo-Devo, pattern formation and regeneration, *The International journal of developmental biology* 53(5-6) (2009) 813-26.
- [126] L. Landmann, Keratin formation and barrier mechanisms in the epidermis of *Natrix natrix* (Reptilia: Serpentes): An ultrastructural study, *Journal of morphology* 162(1) (1979) 93-125.
- [127] M.-C.G. Klein, S.N. Gorb, Epidermis architecture and material properties of the skin of four snake species, *J R Soc Interface* 9(76) (2012) 3140-3155.
- [128] J.E. Baio, M. Spinner, C. Jaye, D.A. Fischer, S.N. Gorb, T. Weidner, Evidence of a molecular boundary lubricant at snakeskin surfaces, *Journal of The Royal Society Interface* 12(113) (2015) 20150817.
- [129] Y. Katsu, K. Matsubara, S. Kohno, Y. Matsuda, M. Toriba, K. Oka, L.J. Guillette, Jr., Y. Ohta, T. Iguchi, Molecular Cloning, Characterization, and Chromosome Mapping of Reptilian Estrogen Receptors, *Endocrinology* 151(12) (2010) 5710-5720.
- [130] M. Banjade, Y.-H. Jeong, S.-H. Han, Y.-K. Kim, B.S. Kim, H.-S. Oh, First report on the reproduction of captive Chinese many-toothed snake (*Sibynophis chinensis*) in Jeju Island, South Korea, *Journal of Ecology and Environment* 44(1) (2020) 6.
- [131] M.R.K. Lambert, Er-Mi Zhao, Adler, K. (1993): *Herpetology of China*. 1-522. ISBN: 0-916984-28-1. Price US\$ 60.00. Society for the Study of Amphibians and Reptiles (Contributions to Herpetology no. 10), USA, *Amphibia-Reptilia* 16(4) (1995) 423-424.
- [132] C.-Z. Hang, X.-F. Zhao, S.-Y. Xi, Y.-H. Shang, K.-P. Yuan, F. Yang, Q.-G. Wang, J.-C. Wang, D.W. Zhang, H.-L. Lu, Highly stretchable and self-healing strain sensors for motion detection in wireless human-machine interface, *Nano Energy* 76 (2020) 105064.
- [133] B. Guo, X. Ji, X. Chen, G. Li, Y. Lu, J. Bai, A highly stretchable and intrinsically self-healing strain sensor produced by 3D printing, *Virtual and Physical Prototyping* 15(sup1) (2020) 520-531.
- [134] S. Wang, M.W. Urban, Self-healing polymers, *Nature Reviews Materials* 5(8) (2020) 562-583.

- [135] S.J. Garcia, Effect of polymer architecture on the intrinsic self-healing character of polymers, *European Polymer Journal* 53 (2014) 118-125.
- [136] B. Willocq, J. Odent, P. Dubois, J.-M. Raquez, Advances in intrinsic self-healing polyurethanes and related composites, *RSC Advances* 10(23) (2020) 13766-13782.
- [137] S. Paolillo, R.K. Bose, M.H. Santana, A.M. Grande, Intrinsic Self-Healing Epoxies in Polymer Matrix Composites (PMCs) for Aerospace Applications, *Polymers* 13(2) (2021).
- [138] L.F. Fan, M.Z. Rong, M.Q. Zhang, X.D. Chen, Repeated Intrinsic Self-Healing of Wider Cracks in Polymer via Dynamic Reversible Covalent Bonding Molecularly Combined with a Two-Way Shape Memory Effect, *ACS Applied Materials & Interfaces* 10(44) (2018) 38538-38546.
- [139] S. Latif, S. Amin, S.S. Haroon, I.A. Sajjad, Self-healing materials for electronic applications: an overview, *Materials Research Express* 6(6) (2019) 062001.
- [140] Y. Cao, Y.J. Tan, S. Li, W.W. Lee, H. Guo, Y. Cai, C. Wang, B.C.K. Tee, Self-healing electronic skins for aquatic environments, *Nature Electronics* 2(2) (2019) 75-82.
- [141] E. Roels, S. Terryn, F. Iida, A.W. Bosman, S. Norvez, F. Clemens, G. Van Assche, B. Vanderborcht, J. Brancart, Processing of Self-Healing Polymers for Soft Robotics, *Advanced Materials* n/a(n/a) (2021) 2104798.
- [142] W. Yang, J. Song, X. Wu, X. Wang, W. Liu, L. Qiu, W. Hao, High-efficiency self-healing conductive composites from HPAMAM and CNTs, *Journal of Materials Chemistry A* 3(23) (2015) 12154-12158.